FEDERAL INSTITUTE FOR GEOSCIENCES AND NATURAL RESOURCES (BGR), HANNOVER, GERMANY

GEOLOGICAL SURVEY AND MINES DEPARTMENT (GSMD), ENTEBBE, UGANDA

TECHNICAL COOPERATION

with

U G A N D A

GEOTHERM Project

Detailed surface analysis of the Buranga geothermal prospect, West-Uganda

Final Report

Compiled by: Christopher Stadtler, Vincent Kato, Michael Kraml, Norbert Ochmann & Uwe Schäffer

Commissioned by: Federal Ministry for Economic Cooperation and Development, Germany (Bundesministerium für wirtschaftliche Zusammenarbeit und Entwicklung, BMZ)

BMZ Project No.: 2002.2061.1

Date: April 2007

Contents:

Appendix:

Abbreviations:

ARGeo	African Rift Geothermal Development Facility
asl	above (mean) sea level
BGR	Federal Institute for Geosciences and Natural Resources
BMZ	Federal Ministry for Economic Cooperation and Development
DGPS	Differential Global Positioning System
GEF	Global Environment Facility
GMT	Greenwich Mean Time
GSMD	Geological Survey and Mines Department
GTZ	German Technical Cooperation
IAEA	International Atomic Energy Agency
ICEIDA	Icelandic International Development Agency
MEMD	Ministry of Energy and Mineral Development
PEPD	Petroleum Exploration and Production Department
SP	Self Potential
SRTM	Shuttle Radar Topography Mission
TEM	Transient Electromagnetic
UNEP	United Nations Environment Programme
UNU-GTP	United Nations University Geothermal Training Programme
UTM	Universal Transverse Mercator
VES	Vertical Electrical Sounding
WB	World Bank

Executive summary

The geothermal potential of Uganda has been explored since early 1950s but not been used by now. To reach a further step on the way to utilisation of the geothermal resources, the Ugandan Ministry of Energy and Mineral Development (MEMD) through the Geological Survey and Mines Department (GSMD) and the Federal Institute for Geosciences and Natural Resources (BGR), Germany, initiated a project with the title "Detailed surface analysis of the Buranga geothermal prospect, West-Uganda", which started in the end of 2004.

The project is part of the GEOTHERM programme, a technical cooperation programme of the German government. It promotes the use of geothermal energy in partner countries, by kicking off development at promising sites. It supports various countries worldwide. East Africa is the major regional focus of the programme. BGR on behalf of the Federal Ministry for Economic Cooperation and Development (BMZ) started the programme in 2003.

The objective of the GEOTHERM project in Uganda was to raise the development status of the Buranga geothermal prospect by geoscientific investigations to reach a pre-feasibility status in the future. A pre-feasibility study is the base for planning of exploration wells and for further development of the geothermal site. The evidences presented in this final project report have reached farer than the original objective i.e. they allow already now the planning of exploration wells (see below).

The components of the GEOTHERM project in Uganda were:

- surface exploration at Buranga geothermal prospect and
- "on the job" training if necessary (due to extended training at international training centres like UNU-GTP in Iceland, the Ugandan geothermal working group already consists of experts in all geoscientific disciplines)

The Buranga hot springs are situated in the Albertine Rift (western branch of the East African Rift) within the Semliki National Park in Bundibugyo district between Semliki River to the west (borderline to the Democratic Republic of Congo) and Rwenzori Massif to the east. The hot springs are located in a swamp within the tropical rain forest a few hundred meters west of Bwamba fault, which forms the western flank of the Rwenzori Massif.

The observation that after strong earthquakes local displacements of the hot springs as well as changes of the individual flow rates had occurred, suggests that the activity of the Buranga hot springs is strongly related to an active fault system and that these tectonically active faults might provide the migration paths for the hydrothermal fluids. An alteration zone related to an exposed fault running close to and parallel to Rwenzori border fault containing gypsum indicates fluid flow along this fault. This reinforces earlier evidence that the Bwamba fault is the major pathway for fluids as indicated by carbonates detected in the fault breccia in a shallow exploration well drilled in early 1950s.

Structural analysis based on lineament mapping of satellite images revealed the fracture pattern of Rwenzori mountains which is much more complex and detailed than previously published.

In the region of the Albertine Rift, where Buranga is located, no geological surface indications for volcanic activity or intrusive dikes were found so far which could act as a heat source for the thermal water. However, from carbon isotopic composition of CO_2 an indication of a mantle source for the gas released at Buranga hot springs was found. Additionally, analyses of (fossil) travertine indicate that the source of the involved CO_2 is compatible with a volcanic origin and that also the fossil travertine deposits were formed under the current thermogene conditions and precipitated in isotopic and chemical equilibrium. A mantle source for the gases was further confirmed by helium isotopic analyses of Buranga hot spring gas indicating a contribution of >30% mantle helium. These findings imply that a still hot actively degassing magma body exists in the subsurface of Buranga area. This magmatic body serves most likely as heat source of the hot springs. Hence the task of active ground geophysics was to detect and delineate this magmatic intrusion. The known high seismicity (over 500

local earthquakes per month) suggested that Buranga provides excellent requirements to apply seismology.

The microearthquake activity around Rwenzori was studied in order to delineate an assumed magmatic intrusion. 4185 earthquakes have been localized in the period January to August 2006. The majority of the localised events exhibit a focal depth between 10 and 30 km; the deepest events occur at depths of about 55 km. Very few earthquakes occur within the northern part of the Rwenzori block and most events do not seem to be related to the main border faults.

The strongest P-wave velocity anomaly (-9 %) in 10 km depth is located directly south of the Buranga hot springs. The centre of the anomaly is situated below the surface trace of the Bwamba fault (Fig. 6.3). If the dip angle of the Bwamba fault continues also at depth with about 60°W, it can be assumed that the centre of the anomaly is situated within the Precambrian basement.

The low velocity anomaly coincides with the aseismic region within the northern Rwenzori block which could be a further indication that the reduction in velocity is caused by temperature effects in the subsurface of this region. High temperatures would not allow rocks to develop stress levels that are high enough to be released as earthquakes (ductile behaviour).

At shallow depth (1-3 km) the results show that a large low-velocity anomaly exists in the north-western section of the region under investigation. It is interesting to note that the Buranga hot springs are located at the boundary of this anomaly at the transition between “slow” and “fast” regions. The low-velocity anomaly broadens at greater depths (> 5 km) and their position is dislocated towards the centre of the northern Rwenzori block. The anomalies tend to become stronger at depth.

The results of the tomography clearly reveal definite low velocity anomalies. Taking into account the findings of geochemistry, which clearly show that mantle helium and volcanic CO_2 are released at Buranga hot springs, the most plausible conclusion for the observed velocity reductions are high temperature anomalies. These temperature anomalies could be a result of a hot actively degassing magma intrusion, which may serve as a heat source for the hot springs.

By combining all findings a conceptual model for the Buranga geothermal prospect was developed which is presented in more detail in Chapter 6 (Fig.6.2). The four major components of the geothermal system addressed in the conceptual model are: a) recharge, b) sufficient permeability allowing fluid flow, c) a heat source and d) a seal on top of the geothermal reservoir. In the case of Buranga (a) the recharge area for the thermal water is located in the high Rwenzori Mountains (precisely defined by new isotope hydrology data). (b) The permeability is provided by fractures in particular by the Bwamba fault where the water is heated up along its several km long migration path in depth. (c) Additional heat is provided by the magmatic heat source leading to reservoir temperatures of around 160°C (solute and gas geothermometry) and an upflow of the fluids. The thermal water emanates with temperatures of up to 98°C at the Buranga hot springs and can be explained by mixing between a sulphate-chloride fluid and dilute bicarbonate water. (d) Sealing of the fault may occur when the pressure drop in the ascending fluid leads to precipitation of e.g. carbonate minerals (a smectite clay alteration zone is expected to be present along the fault in the depth-range of the reservoir).

On the basis of the presented conceptual model a possible drilling location should be located within the projected zone of major velocity reduction found in the tomographic inversions (yellow contour in Fig. 6.3). In combination with the geochemical results the low velocity zone is interpreted as the major heat source of Buranga geothermal system.

According to the hydrological results the Bwamba Fault is the major pathway for the geothermal fluids. Therefore the Bwamba Fault is the drilling target. To enhance the chances to encounter zones of highest permeability the drilling location should be at the intersection of Bwamba- and perpendicular faults known from structural interpretation (Fig.6.3). Additional advantage is seen in the fact that the suggested site is outside the Semliki National Park, close to the road and still situated within the area of the geophysical survey done in 2005 within the presented project (Fig.6.1).

Two concepts of exploratory drilling can be suggested:

- shallow gradient holes followed by a deep exploration well
- or take a higher risk and drill a deep exploration well right away (Fig. 6.3).

The shallow temperature gradient wells would be useful to investigate the upper part of the seal of the geothermal system, could confirm an enhanced geothermal gradient above the magmatic intrusion and help to determine the dip angle of the target faults. The deep exploration well should reach the Bwamba fault at depth below the seal (in ca. 2000 m) where high flow rates and reservoir temperatures of up to 160°C are expected.

1. Introduction

Power generation in Uganda is dominated by hydropower. Uganda has a total electricity generating capacity of 397 MW, mainly generated by a single source on the River Nile (380 MW). About 17 MW are supplied by a few small hydropower plants. The electrification rate is very low, with grid access of only 9% of the population for the whole country and 3% in rural areas. Additional 1% of the population provides itself with electricity by using generators, car batteries and solar photovoltaic systems. The electricity demand is estimated to be growing at a rate of 7–8% per annum resulting in a need for an increase in power generation.

The Government of Uganda is studying ways to meet the increasing energy demand by other indigenous energy sources than hydropower. To realise these plans, the government gives geothermal energy a high priority. Uganda's potential for geothermal power generation is estimated at about 450 MW. The most promising geothermal areas are Katwe, Kibiro and Buranga (Fig. 1.1) which are situated in West-Uganda in the Albertine Graben, a part of the western branch of the East African Rift System. The three areas were chosen as priority areas because their volcanic and tectonic features are indicators for geothermal heat sources and high permeability.

As a consequence, the Ugandan Ministry of Energy and Mineral Development (MEMD) through the Geological Survey and Mines Department (GSMD) and the Federal Institute for Geosciences and Natural Resources (BGR), Germany, initiated a project with the title "Detailed surface analysis of the Buranga geothermal prospect, West-Uganda", which started in the end of 2004. The objective of this geothermal project was to raise the development status of the Buranga geothermal prospect by geoscientific investigations to reach a pre-feasibility status in the future. This will provide the base for planning of exploration wells. The project cooperated with the GTZ (Deutsche Gesellschaft für Technische Zusammenarbeit) within the scope of the „Energy Advisory Project".

The geothermal project was carried out within the framework of the GEOTHERM Programme, a technical cooperation programme of the German government. The programme promotes the use of geothermal energy in partner countries, by kicking off development at promising sites. It supports various partner countries worldwide, particularly in regions with high geothermal potential. East Africa is the major regional focus of the programme. BGR on behalf of the German Federal Ministry for Economic Cooperation and Development (BMZ) started the programme in 2003.

The activities of the GEOTHERM Programme in East-Africa are part of the African Rift Geothermal Development Facility (ARGeo), which was established by the six East African countries Djibouti, Eritrea, Ethiopia, Kenya, Tanzania and Uganda together with United Nations Environment Programme (UNEP) in 2003. They decided on measures to promote the systematic development of geothermal energy use in the region. ARGeo, with support from UNEP, the Global Environment Facility (GEF), the Governments of Germany, Iceland and other countries aims to accelerate geothermal energy investments by both public and private sectors. This will displace diesel-based production and lead to the reduction of greenhouse gases. This initiative shall provide working examples for other private sector investments in the region. ARGeo will address barriers for geothermal energy use through a combination of technical assistance including institutional strengthening, and a transaction advice fund to foster public investments in geothermal electricity production and private sector participation.

The Ugandan government will apply for support through ARGeo for development of a geothermal power plant at the most promising prospect (Katwe, Kibiro or Buranga) in Uganda. The geothermal prospects Katwe and Kibiro are under study by MEMD with the support of the World Bank (WB) and the Icelandic International Development Agency (ICEIDA).

Figure 1.1: Geothermal prospects of Uganda: Katwe, Kibiro and Buranga

2. Background information about Buranga geothermal prospect

A brief review is given in the following chapter about the status of investigation at the beginning of the GEOTHERM project in Uganda.

2.1 Regional setting

Buranga is situated within the Albertine Rift which forms the northernmost part of the western branch of the East African Rift System (Fig. 2.1, Hochstein, 2005).

In contrast to the eastern branch of the East African Rift the seismic activity in the western branch is significantly higher (Fig. 2.2, Midzi et al., 1999) and the volcanic activity is remarkably lower (Fig. 2.1, Hochstein, 2005). Due to the low volcanic activity also the geothermal prospects with high-enthalpy resources are sparse (Fig. 2.1, Hochstein, 2005).

Additionally the compositions of the Upper Pleistocene to recent volcanic rocks in Uganda (see discussion of ages in Kampunzu et al., 1998) are carbonatitic and alkali-basaltic (i.e. silica-undersaturated katungites, ugandites and mafurites) implying deep-reaching feeding systems via diatremes and dikes and rapid rise to the surface. Therefore, no significant crustal magma chambers are expected in Uganda which are common e.g. in Kenya and Ethiopia. In the eastern branch high amounts of high differentiated trachytes, phonolites and alkali-rhyolites were erupted during caldera-forming events proving the existence of shallow-

level silicic magma chambers which are known to be favourable heat sources for geothermal systems. Figure 2.3 illustrates the occurrence of volcanic rocks at the earth surface which are belonging to the Toro-Ankole volcanic province. The individual volcanic fields from North to South are: Rusekere or Kasekere, Fort Portal, Kyatwa or Ndale, Katwe-Kikorongo, Bunyaruguru or Kichwamba, and Katunga.

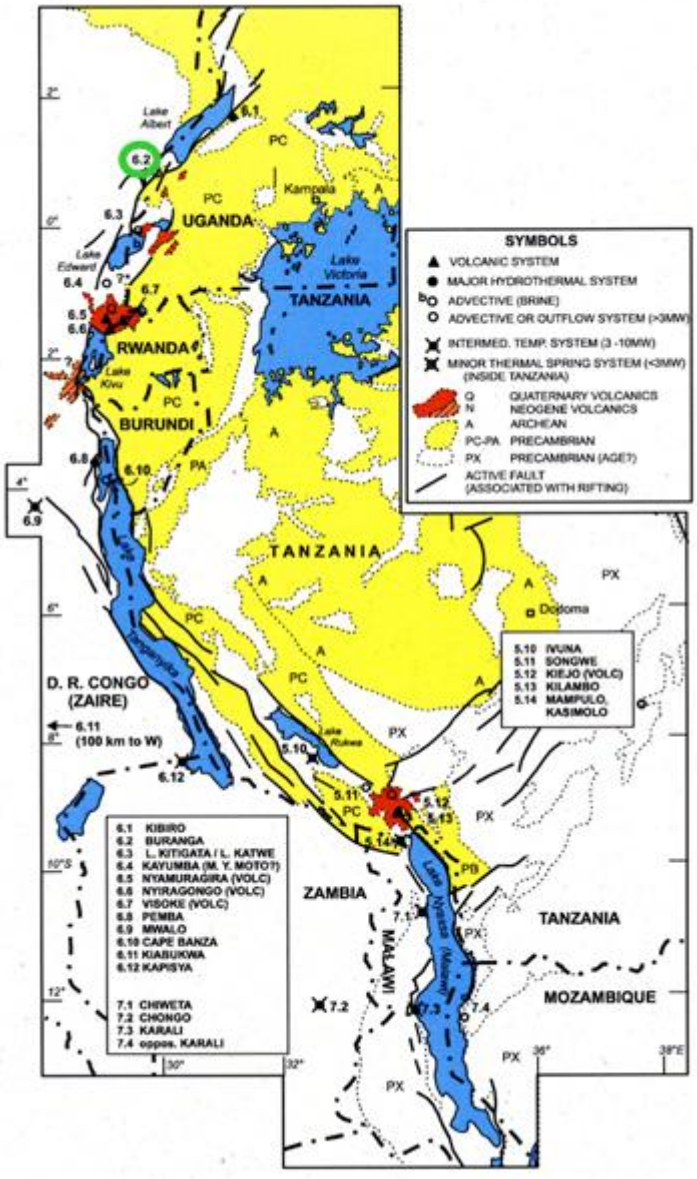

Figure 2.1: Western branch of the East African rift with geothermal prospects (Hochstein, 2005). Buranga is marked with a green circle

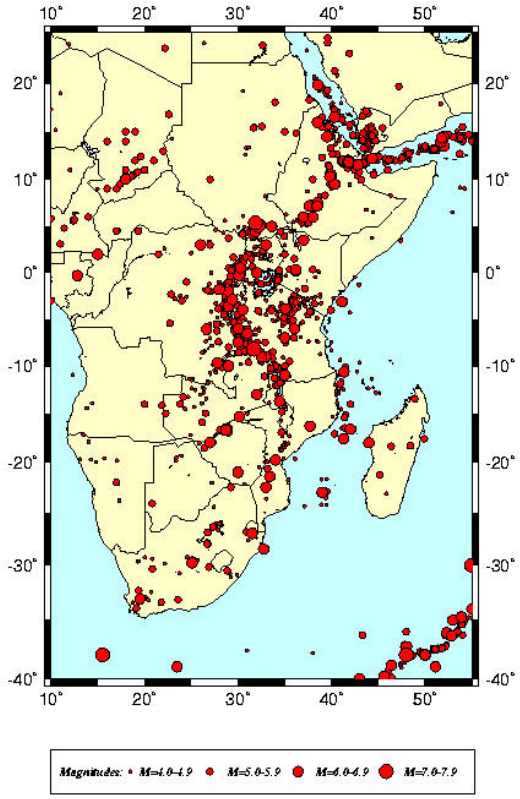

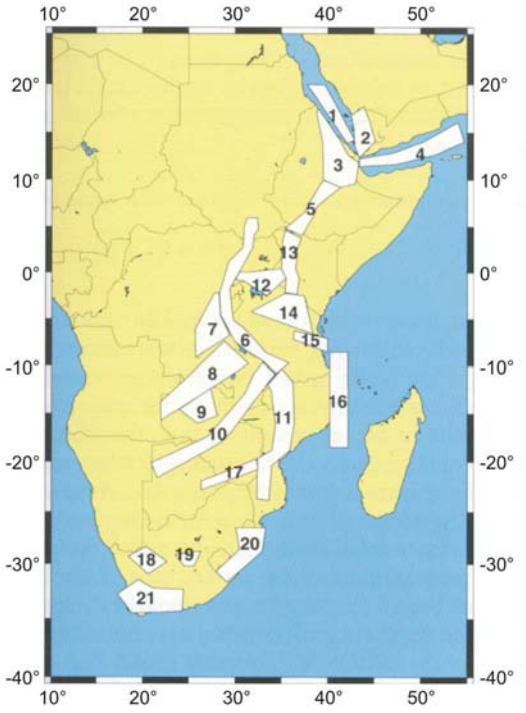

Source zones	Mlow	Mupp	β	λ
6 (West-rift)	4.5	7.8	2.08	3.17
13 (Kenya)	4.5	7.4	1.37	0.14
5 (Ethiopia)	4.5	6.8	1.33	0.39

Figure 2.2: Seismic activity in the different parts of the East African rift (Midzi et al., 1999). M_{low} = lower bound magnitude; M_{upp} = maximum expected upper bound magnitude; β=ln(10)×b-value; b-value = slope of magnitude-frequency relation; λ = activity rate (annual number of earthquakes above the lower bound magnitude)

Furthermore, magmatic bodies of significant size were detected by an aeromagnetic survey in the subsurface of the rift sediments (Fig. 2.3). These magmatic intrusions are at least partly cooled (most likely below Currie temperature) and in remarkable distance to Buranga and Kibiro, respectively. But also still hot intrusions are known to drive active sublacustrine hydrothermal systems e.g. below Lake Tanganyika (Tiercelin et al., 1989 and 1993).

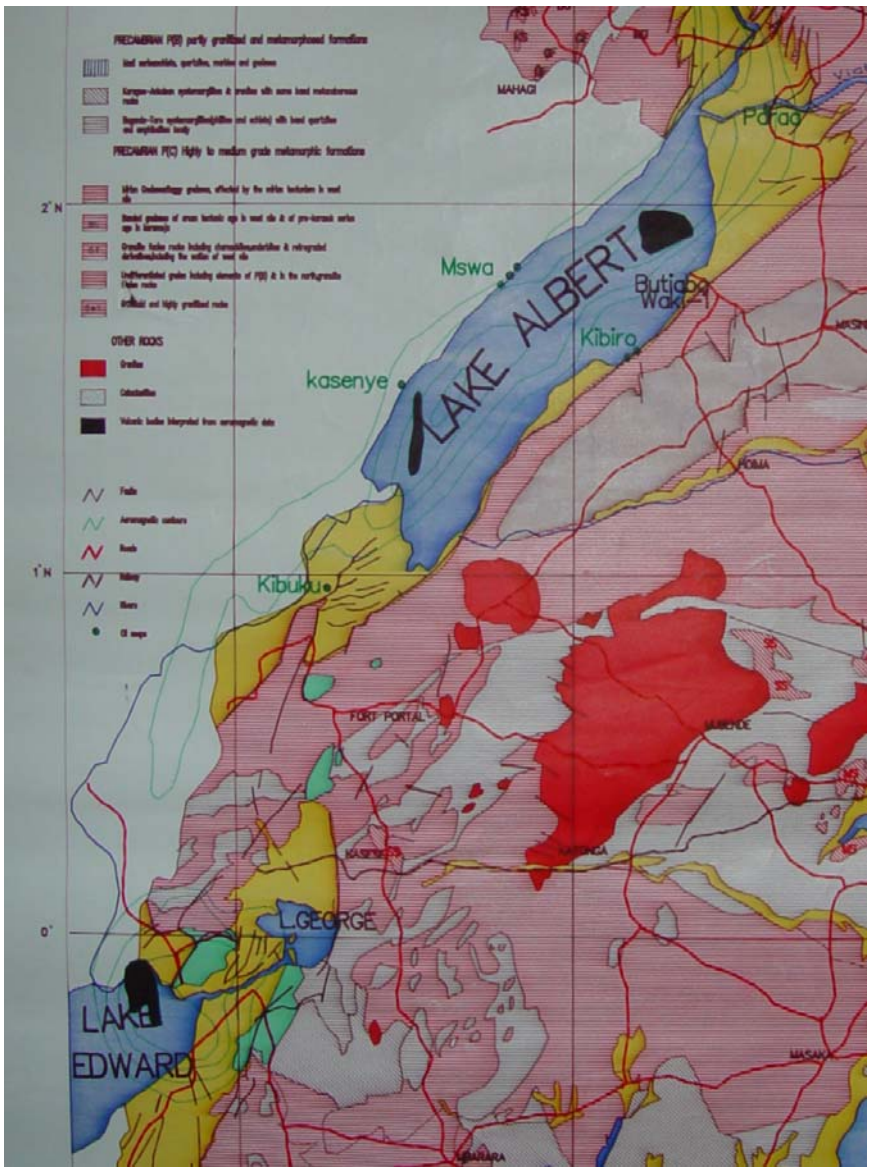

Figure 2.3 Part of geological map of western Uganda showing the Precambrian basement in red and grey colours, the Albertine rift with lakes and Cenozoic sedimentary infill in yellow colour, and the Quaternary volcanic fields in green colour. Green lines: aeromagnetic contour lines; black areas: magmatic intrusives interpreted from aeromagnetic data in subsurface of Lake Albert and Lake Edward (GSU 1962; aeromagnetic survey by Kenting Earth Sciences, Ontario, Canada)

The young undifferenciated silicate rocks of the Toro-Ankole volcanic province are explained by partial melting of metasomatised mantle material and mixing processes of kimberlitic and carbonatitic melts (Lloyd et al., 1991). The strongly silica-undersaturated magmas are highly enriched in K, Ti and associated incompatible elements. The extrusive carbonatites are the exclusive rock types of the Fort Portal and small Rusekere volcanic field but occur also in significant quantities in the Katwe-Kikorongo field. The chemical compositions of the carbonatites are also characterised by a strong enrichment of incompatible elements like Sr, Ba and the LREE (Barker & Nixon 1989). Strontium isotopic compositions show typical mantle values between 0.7039 and 0.7042 and carbon and oxygen isotope compositions are between -2 and -12‰ relative to PDB and between +10 and +26‰ relative to SMOW, respectively (see discussion in Barker & Nixon, 1989 and Chapter 5.2).

Sr, Nd and Pb isotopic compositions of Fort Portal and Rusekere lavas suggest an origin for the carbonatites involving melting and mixing of HIMU and EM1 mantle components contained within an isotopically heterogeneous deep asthenospheric mantle plume (Bell & Tilton 2001). However, mainly based on helium isotopic data of olivine from Virunga and Bukavu alkaline lavas the plume originates from shallow depth (lithospheric upper mantle) below the western branch of the East African rift (Pik et al., 2006).

Despite of contradicting evidence about the depth of origin of the mantle plume it is important to note that the still recently rising plume (e.g. Zeyen et al., 1997; Nyblade et al., 2000; Bailey & Collier, 2000) can deliver heat sources in form of magmatic intrusions and acts as driving force for tectonic processes e.g. uplift, seismicity and related active faulting which is important for fracture controlled fluid flow and surface drainage patterns.

The main trends in seismicity of the western part of the East African rift system are fairly clear from previous studies, which used teleseismic stations (e.g., DeBremaeker. 1959; Sykes & Landisman, 1964; Wohlenberg, 1969; Fairhead & Girdler, 1971). For better understanding the structure and development of the Rwenzori Mountain region of the East African rift system Maasha (1975b) carried out a micro-earthquake survey for a three month period in 1973 using four portable seismographs. He found that the Rwenzori region is the most seismically active area in Uganda. In the Rwenzori region the spatial trends of the micro-earthquakes are correlated with the major rift faults and volcanic zones on the eastern side of the Rwenzori Massif. The study gave several indications for active faulting along the Rwenzori border faults and only one event pointing to an active fault perpendicular and within the Rwenzori Massif. The seismicity is shown to extend beneath and transverse to the Rwenzori Mountain block, with hypocentral depths ranged between 0 and 40 km. Elsewhere in the studied region, composite focal mechanism solutions show dip slip motion along steeply dipping planes (Bwamba, Ruimi-Wasa, and Nyamwamba faults). The extensional axes trend in east-west direction. The motion tends to raise the mountain block relative to the surrounding country. A focal mechanism, determined at the junction of the northern and southern Rwenzori, indicates that the northern portion is being uplifted with respect to the southern block. A later study considering the major earthquakes between 1966 and 1994 (Upcott et al., 1996) again finds evidence for active faulting at the Bwamba fault in an upper crustal level. The recent earthquake of 2001 was analysed by Babirye (2003).

In the study of Upcott et al. (1996) – mainly based on gravity data – the authors have modelled the sediment thicknesses in the along-axis segmented Albertine rift which reaches in the South Albert basin maximum values of 5.5 km and decreases towards the northern tip of the Rwenzori horst (Fig. 2.4). There the South Albert basin terminates against the Semliki basin whose sediments are briefly characterised in section 2.3. The resulting tectonic model which is additionally based on aeromagnetic data shows five 25 to 65 km wide and 80 to 100 km long rift segments separated by cross-rift ramps or normal faults.

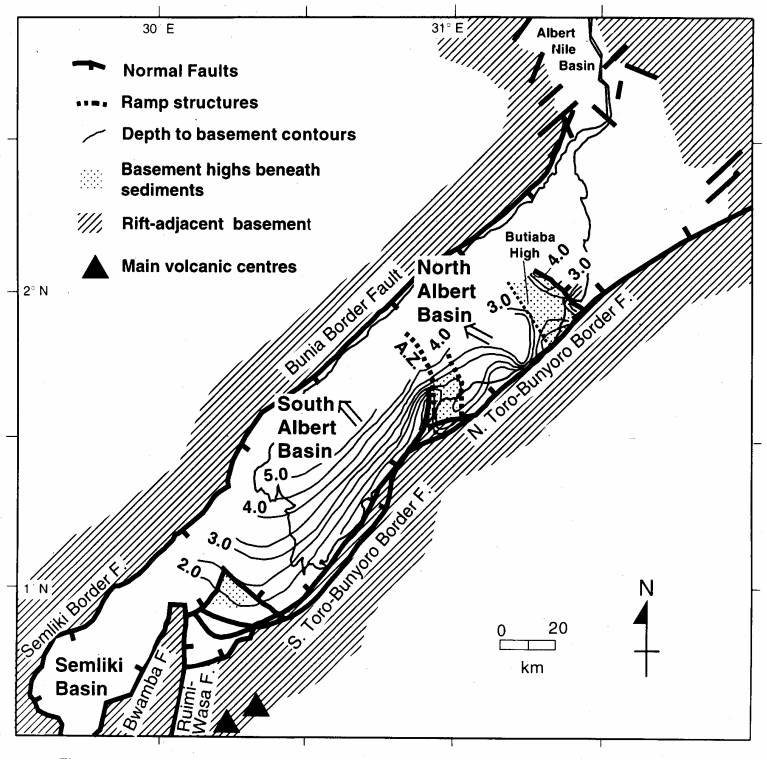

Figure 2.4: Segmented Albertine rift with amongst others Semliki basin bound by Semliki border fault to the west (D.R. Congo) and Bwamba fault to the East (Upcott et al., 1996)

Recent investigations by Dozith & Mugisha (2004) further unravelled the structural status and development of the Albertine graben. These authors explain the uplifted Rwenzori mountain ranges as a result of isostatic compensation by the sediment masses accumulated in the rift.

The Rwenzori mountain range with heights of up to 5109 m is about 115 km long and up to 64 km wide in its central part. It is permanently snow-capped and has 43 named glaciers distributed over six mountains with a total area of fife square kilometres which is about half the total glacier area in Africa. Additionally high elevated lakes (Kitandara lakes 4027 m; Lake Vert 4300 m; Lake Bujuku ca. 3500 m a.s.l.) and rivers (Bujuku; Butawu which originates from Kitandara lakes and their glaciers; Kuruguta; Mubuku) are the result of high annual precipitation reaching 2000 mm per year (recorded in ca. 4600 m a.s.l., Kato, 2000). The Precambrian basement in the northern part of Rwenzori consists mainly of different types of gneisses whereas the southern part shows significant intercalations of amphibolites, quartzites, phyllites etc. (GSU, 1962).

2.2 Geothermal features at Buranga

The geothermal surface manifestations of Buranga are situated at the western foot of the northern part of Rwenzori mountains within the rift sediments of Semliki basin in the Semuliki National Park in Bundibugyo district (Fig. 2.5 and 4.3.1).

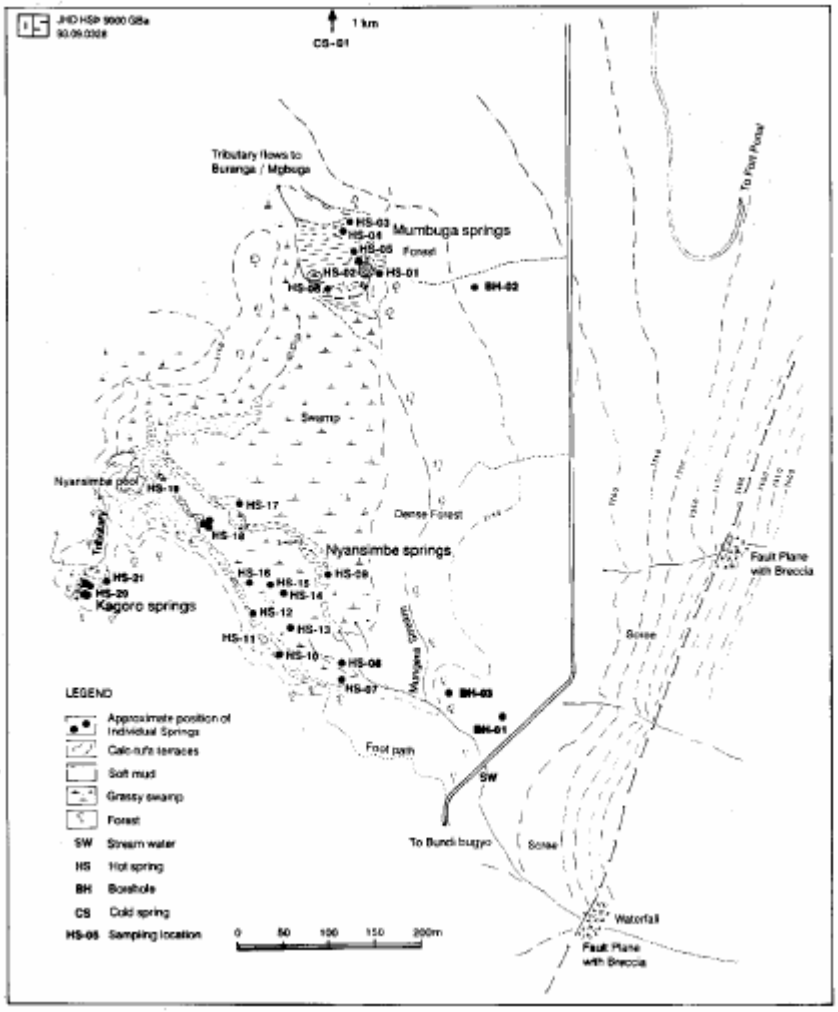

Figure 2.5: Buranga hot springs with Bwamba fault and previous sampling points (Armannsson, 1993 in: Kato, 2000)

A few hundred meters east of the hot springs the Precambrian basement rocks of the Rwenzori dip 60-65° W and strike 20-40° NNE (Bwamba fault; Fig. 2.5). The Buranga hot springs consist of 37 springs which are divided in three main groups: Mumbuga, Nyansimbe and the Kagoro springs (Fig. 2.5 and 2.6a, b, c). The groups are located along a 650 m long alignment roughly parallel to the Bwamba fault. The Mumbuga group located at the north-eastern end of the alignment consists of several hot springs which have an estimated total flow rate of about 6.5 l/s with temperatures of up to 95°C. The largest Mumbuga spring has deposited significant amounts of travertine in form of terraces and the fountain of this spouting spring is 50 cm high (artesian outflow). The Kagoro group located at the south-western end of the alignment is characterized by up to 1.5 m high travertine cones. The total flow rate in this area was estimated at about 3 l/s with temperatures between 60 and 91°C. The approximately 15 m wide and 4 m deep Nyansimbe pool is located in the centre of the alignment and is characterised by a travertine crust growing from the rim to the centre of the pool. The water temperature is 86°C with an estimated flow rate of 10 l/s. Additional hot springs in the vicinity of the pool have a total flow rate of 5 l/s. Further hot springs are located southeast of Nyansimbe pool (Fig. 2.6d). The hottest spring of Buranga with a temperature of 98.4°C is located in this area; there an estimation of the flow rate was not possible (Gíslason et al., 1994).

Additional to the various types of hot springs and travertine deposits there are other surface manifestations in Buranga area like gaseous emanations and geothermal grass.

Figure 2.6: The three main hot spring areas of Buranga: [a] largest of the Mumbuga springs, [b] Nyansimbe pool and [c] a 1.5 m high travertine cone at Kagoro springs. [d] Further hot springs southeast of Nyansimbe pool.

2.3 Previous investigations of Buranga geothermal prospect

In 1953/54 the Geological Survey of Uganda carried out a drilling programme at Buranga to determine if geothermal power could be developed. Four boreholes were drilled in Buranga (McConnell & Brown, 1954). Borehole No.1, which was sited near milestone 32 on the road to Bundibugyo, SE of the hot springs, was drilled down to a depth of 182 m. There the rift sediments consist of fine to coarse grained clastic deposits. The basement rocks were reached at 177 m, which are overlain by fault breccia and mylonite of 5 m thickness (McConnell & Brown, 1954). The highest temperature in the borehole (58°C) was observed in the fault breccia. Borehole No.2 was drilled 90 m west of the road, about 45 m south of the track to Mumbuga, to the depth of 349 m (Pallister, 1954). The borehole did not penetrate the sediments and the highest measured temperature was 66°C (Árnason, 2003). Borehole No.3 was sited 45 m west of Borehole No.1 and drilled down to a depth of 120 m. At the depth of 12m, a zone, reported as a steam zone, was hit. This resulted in a blow-out which lasted for 10 minutes. It is most likely that the blow-out was mainly due to gas rather than steam. No temperature log is available from the well but the returning drilling fluid was reported to have temperatures in the range of 49-72°C. Borehole No.3 is still flowing and the water has the temperature of 76°C (Árnason, 2003). Borehole No.4 was planned and decided to drill but no documentation has been found (Árnason, 2003).

In 1973 two Schlumberger soundings were measured at Buranga between the hot springs Mumbuga and the Bwamba fault (Fig. 2.11, Fig. 5.3.2; Maasha, 1975a). Sounding S1 was located approximately 180 m west of the road to Bundibugyo at the Sempaya visitor centre,

sounding S2 35 m west of the centre. The layout was parallel to the fault with a maximum current electrode separation of 526 m (AB/2 = 263 m). The soundings show that the resistivities of the rift sediments decrease towards the hot springs and that the high resistive basement dips to the west (Bwamba fault).

Pallister (1952) and Árnason (2003) consider that geothermal activity of the Buranga hot springs is most likely related to tectonic activity in the rift (fault controlled geothermal system). It was observed that historical earthquakes, e.g. 20th March 1966, 17th May 1966 (both magnitude 6.1-6.3, epicentres about 30 km SW of Buranga) and 6th February 1994 incl. some after shocks (magnitude 6.3, epicentre south of Fort Portal), changed the geothermal activity of Buranga. After the latter earthquake a new hot springs appeared SE of the Nyansimbe pool (Gislason et al., 1994) which shows that the seismological activity can open or reactivate flow paths for thermal water in the basement and overlying sediments. This observation was further constrained by a soil temperature survey of Buranga area done by the GSMD. The soil temperature map compiled from the measured profiles shows a high temperature anomaly which extends from the Nyansimbe pool in SE direction. The anomaly reflects the area where the hottest spring is located and the new group of hot springs opened after the earthquake from 6th February 1994.

Recent geochemical and isotope geochemical analyses were done by GSMD in cooperation with Icelandic organisations (Geosurvey and UNU-GTP) and IAEA in Vienna (e.g. Kato, 2000; Bahati et al., 2005). From isotope hydrological investigations (Fig. 2.8) it was concluded that the source of Buranga thermal water is of meteoric origin. The absence of a positive shift in $\delta^{18}O$ suggests a reasonably high permeability. The recharge cannot come from immediate neighbouring Rwenzori mountains due to the heavier isotopic composition of the local rivers. Therefore the more distant high Rwenzori mountains were suggested to be favourable recharge areas. The resulting long flow path is compatible with tritium measurements giving >50 years residence time for the thermal waters (pre-bomb-values) and a few tritium units for the local river waters.

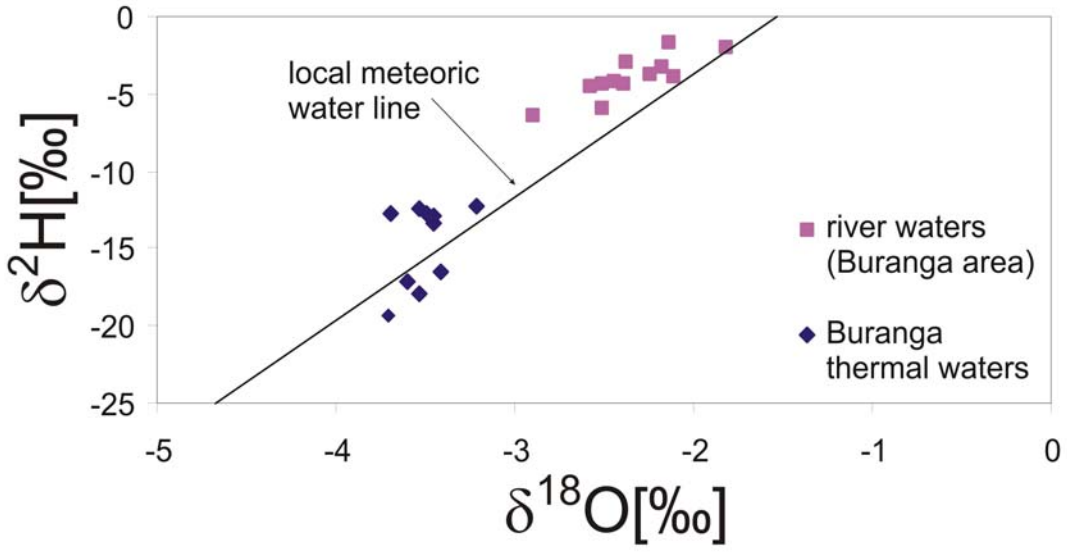

Figure 2.8: Stable isotopic composition of Buranga thermal waters and local river waters (data from Kato, 2000 and Bahati et al., 2005)

The source of salinity was traced by strontium isotopic analyses of dissolved Sr in the thermal water and different country rocks in Buranga area (Fig. 2.9). From the similar isotopic composition it was concluded that the main source of the dissolved Sr is water-rock interaction with the Precambrian basement rocks (granitic gneisses). From the same $^{87/86}Sr(H_2O)$ ratio but different Sr concentrations it was concluded that the source of salinity in Buranga

thermal waters is similar. Note the difference in isotopic ratio of dissolved Sr in comparison to Katwe hot springs which are situated within a known volcanic environment. In contrast to Katwe, there are no volcanic rocks observed at the earth surface in Buranga area (e.g. Ármannsson, 1994).

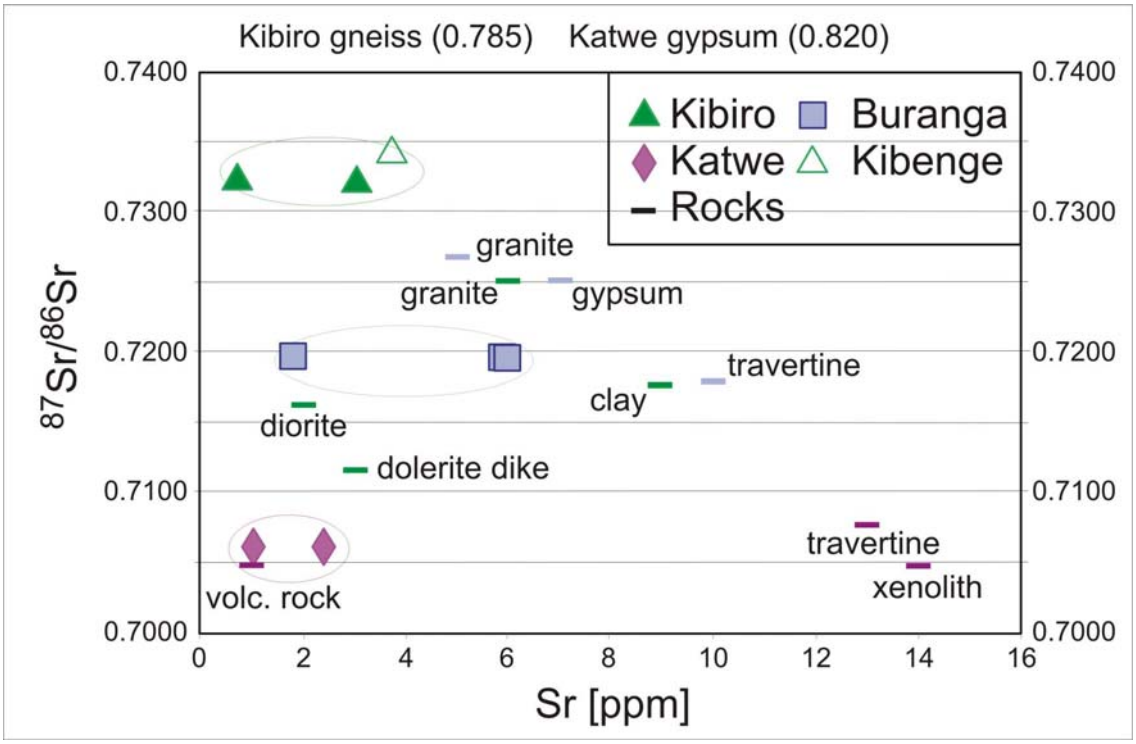

Figure 2.9: Sr isotopic composition of thermal waters and related country rocks (modified from IAEA, 2003)

Additionally the isotopic composition of dissolved sulphate was analysed as another tracer for the source of solutes in Buranga thermal waters (Fig. 2.10). From these data the sulphate of Buranga hot springs seems to come mostly from terrestrial evaporites.

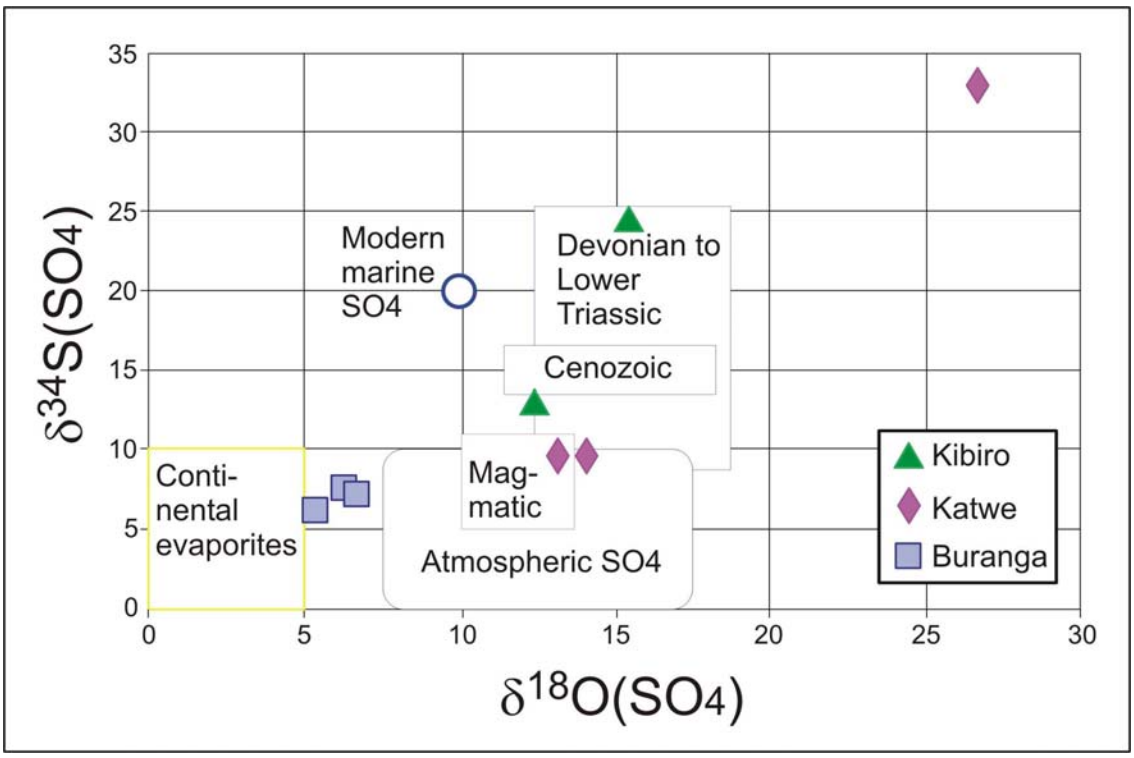

Figure 2.10: Sulphur and oxygen isotopic composition of dissolved sulphate (IAEA, 2003)

Note the difference to the magmatic Katwe sulphate of the hot springs which are situated within a known volcanic environment and the occurrence of gypsum-rich rift sediments north of Buranga (near Kibuku; Isabirye, 2000).

Geothermometry was done using isotope and solute geothermometers (Table 2.1). An additional gas geothermometer based on the CH_4/C_2H_6 ratio gave a temperature of 164°C for Buranga (Bahati et al., 2005). The causes for the differing results were intensively discussed by Ármannsson (1994), Kato (2000), IAEA (2003) and Bahati et al. (2005). It was concluded that the local reservoir feeding Buranga hot springs has actual temperatures of 120-130°C.

Table 2.1: Chemical and isotope geothermometer temperatures (°C) (Bahati et al., 2005)

Area	Site	T_{qz} [a]	T_{KMg} [b]	T_{NaK} [c]	T_{NaKCa} [d]	$T_{S^{18}O_4H_2{}^{18}O}$ [e]
Kibiro	Kibiro 5	160	148	217	220	137
	Kibiro 14	151	150	222	223	110
Katwe-Kikorongo	L. Kitagata 2	116[f]		145[f]		130
	L. Kitagata 5	134[f]		162[f]		140
Buranga	Kagoro 20	122[f]		111[f]		188
	Nyansimbe 17	104[f]		113[f]		189
	Mumbuga 5	117[f]		111[f]		212

[a] Fournier and Potter (1982).
[b] Giggenbach (1988).
[c] Arnórsson et al. (1983).
[d] Fournier and Truesdell (1973).
[e] Mizutani and Rafter (1969).
[f] Results from Ármannsson (1994).

Maasha (1975a) and Armannsson (2001) presented local conceptual models of the Buranga geothermal prospect (Fig. 3.1). The thermal water flows upward from great depth along the Bwamba fault, infiltrates the permeable sedimentary cover and forms a shallow reservoir in the subsurface of Buranga.

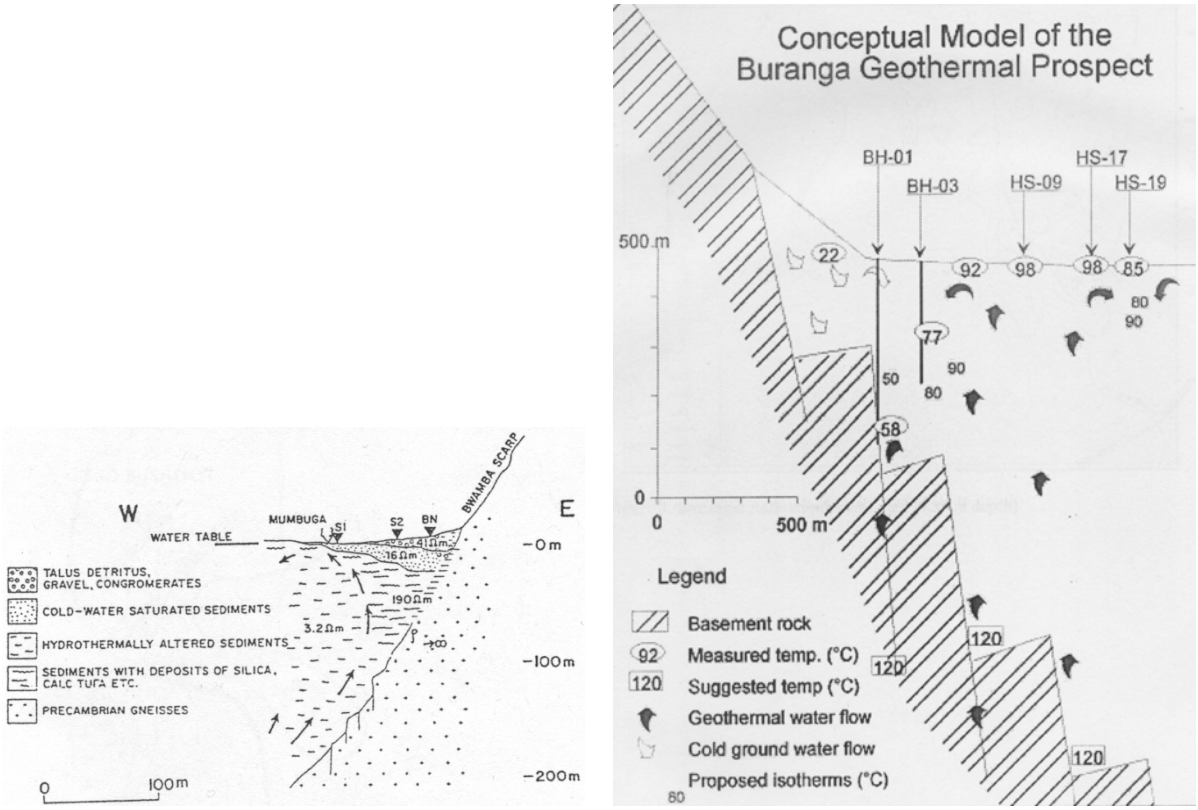

a) **b)**

Figure 2.11: Local conceptual models of a) Maasha (1975a) with interpretation of Schlumberger soundings S1 and S2 and b) Armannsson (2001), view from north

Additional studies were carried out by Bahati (1999); Bahati (2003); Bahati (2005); Bahati & Ármannsson (1995); Bahati et al. (2005); Bahati & Tugume (2005); Bazaale-Dolo (1986); Brown (1953); Dixon & Morton (1970) and Sharma (1971).

3. Exploration concept

A magmatic heat source for a geothermal system improves the probability significantly that a prospect is suitable for power generation from geothermal energy since the source provides higher temperatures and a higher longevity of the system. Most of the known geothermal prospects that are utilised for power generation are related to active volcanism or recent magmatic intrusions.

In addition to the local conceptual models in Figure 2.11, two conceptual models in regional scale for the fracture controlled reservoir of the Buranga geothermal prospect were suggested at the beginning of the project that consider the existence of a magmatic heat source (Fig. 3.1):

- Buranga is fed by meteoric fluids from high Rwenzori mountains:

Meteoric water flows in open faults down from the higher part of the Rwenzori Massif (3,000-5,000 m asl.), heats in a depth of about 2,000 m below surface (normal geothermal gradient) and up-flow occurs along Bwamba fault (density driven)

- Buranga is fed by magmatic fluids of a hidden magma chamber together with meteoric fluids of Rwenzori Massif:
  Magmatic contribution from either active magmatic intrusion below Buranga which is also the source of heat and gases or by hydraulic connection to Fort Portal volcanic field on eastern side of Rwenzori via E-W transverse faults

The idea that Buranga is fed by basinal brines (from observation of oil seeps north of Buranga) can be excluded due to existing data and is not considered.

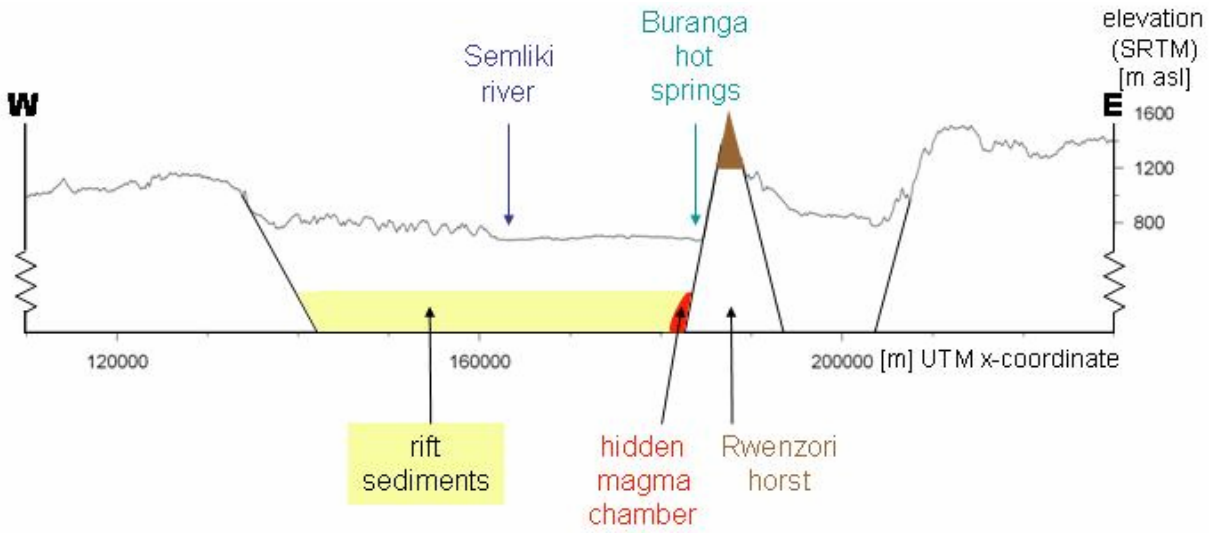

Figure 3.1: Schematic W-E cross-section through the Albertine rift showing discussed conceptual models

Analyses of geochemical samplings of hot and cold springs and gas from all over the Rwenzori region shall provide an overview over the whole system to better understand the complete system. This will assist to get indications for the origin of the thermal water of the Buranga hot springs, for the recharge area of the Buranga hot springs and for flow paths of waters.

To detect fractures that might act as migration paths for thermal water and to delineate the extent of thermal waters in the rift that could be used as geothermal reservoir, lineament mapping (remote sensing) and ground geophysical measurements will be conducted.

The existence of a magmatic heat source could be proven by geochemical studies and its location detected by seismological observation of local earthquakes that could also assist to identify active faults.

4. Methodology

For geothermal exploration of the Buranga geothermal prospect different geoscientific methods were applied: remote sensing, geochemical analyses, ground geophysical methods applied during a field survey and seismological observations registered over several months.

In this report, the UTM coordinates refer to zone 36N, ellipsoid Clarke 1880, and the geographical coordinates to WGS84.

4.1 Remote sensing

With the geological interpretation of remotely sensed data the Federal Institute of Geosciences and Natural Resources (Bundesanstalt für Geowissenschaften und Rohstoffe) has been carrying out remote sensing since the "Photo-Geology" section was founded in 1959. Digital image processing was introduced in the 1970s as satellite remote sensing with multispectral scanners and radar were brought into use.

The tasks and application areas of the remote sensing section include research and mapping for raw materials, energy resources, the environment, soil, groundwater and geological risks. Remote sensing methods are tested and improved through the use of digital image processing, GIS, multi-spectral and hyperspectral data processing methods, thermal mapping and radar technology.

4.1.1 Data sources and missions

For the present study 5 ASTER scenes have been purchased in HDF-format and a SRTM scene has been received from the “Global Land Cover Facility” (GLCF, University of Maryland, (http://glcf.umiacs.umd.edu/data/) for free of charge. The costs for one ASTER Scene (60 x 60 km ground coverage) amount about US$ 80.

4.1.2 ASTER satellite on Terra Spacecraft

Terra is the flagship of the Earth Observing System (EOS), a series of spacecraft that represents the next landmark step in NASA’s role to observe Earth from the unique vantage point of space. Focused on key measurements identified by a consensus of U.S. and international scientists, Terra enables new research into the ways Earth’s land, oceans, air, ice and life function as a total environmental system. Terra was launched into sun-synchronous Earth orbit on December 18, 1999, and started sending data back to earth in February 2000. Terra carries several instruments, e.g. the ASTER (Advanced Spaceborne Thermal Emission and Reflection Radiometer) sensors with three different subsystems.

Specifications of the Terra Spacecraft

Launch date:	December 1999	
Orbit:	705 km altitude, sun-synchronous, so that at any given latitude it crosses directly overhead at the same time each day.	
Orbit inclination:	98.3 degrees from the Equator	
Orbit period:	98.88 minutes	
Equator crossing:	10.30 a.m. (North to South)	
Ground track repeat cycle:	16 days, i.e. every 16 days (or 233 orbits) the pattern of orbits repeats itself	
Builder:	Lockheed Martin	

ASTER is a cooperative effort between NASA of the U.S.A., Japan's Ministry of Economy, Trade and Industry (METI) and Japan's Earth Remote Sensing Data Analysis Center (ERSDAC), with the collaboration of scientific and industry organizations in both countries. The ASTER instrument provides the next generation in remote sensing imaging capabilities compared with the older Landsat Thematic Mapper, and Japan's JERS-1 OPS scanner. ASTER captures high spatial resolution data in 14 bands, from the visible to the thermal infrared wavelengths; and provides stereo viewing capability for digital elevation model creation. As the "zoom lens" for Terra, ASTER data are used by other Terra and space-borne instruments for validation and calibration. ASTER is being used to obtain detailed maps of land surface temperature, reflectance and elevation. The three EOS platforms are part of NASA's Science Mission Directorate and the Earth-Sun System, whose goal is to observe, understand, and model the Earth system to discover how it is changing, to better predict change, and to understand the consequences for life on Earth.

ASTER provides data useful for a wide range of science research and applications. These include:

Land surface climatology and detection of thermal anomalies -- investigation of land surface parameters, surface temperature, etc., to understand land-surface interaction and energy and moisture fluxes

Vegetation and ecosystem dynamics -- investigations of vegetation and soil distribution and their changes to estimate biological productivity, understand land-atmosphere interactions, and detect ecosystem change

Volcano monitoring -- monitoring of eruptions and precursor events, such as gas emissions, eruption plumes, development of lava lakes, eruptive history and eruptive potential

Hazard monitoring -- observation of the extent and effects of wildfires, flooding, coastal erosion, earthquake damage, and tsunami damage

Hydrology -- understanding global energy and hydrologic processes and their relationship to global change; included is evapotranspiration from plants

Geology and soils -- the detailed composition and geomorphologic mapping of surface soils and bedrocks to study land surface processes and earth's history

Land surface and land cover change -- monitoring desertification, deforestation, urbanization; providing data for conservation managers to monitor protected areas, national parks, wilderness areas.

The ASTER instrument consists of three separate instrument subsystems. Each subsystem operates in a different spectral region, has its own telescope(s), and was built by a different Japanese company.

ASTER's three subsystems are: the Visible and Near Infrared (**VNIR**), the Shortwave Infrared (**SWIR**), and the Thermal Infrared (**TIR**).

VNIR (Visible and Near Infrared)

The VNIR subsystem operates in three spectral bands at visible and near-IR wavelengths, with a resolution of 15 m. It consists of two telescopes--one nadir-looking with a three-spectral-band detector, and the other backward-looking with a single-band detector. The backward-looking telescope provides a second view of the target area in Band 3 for stereo observations. Thermal control of the CCD detectors is provided by a platform-provided cold plate. Cross-track pointing to 24 degrees on either side of the track is accomplished by rotating the entire telescope assembly. Band separation is through a combination of dichroic elements and interference filters that allow all three bands to view the same ground area simultaneously. The data rate is 62 Mbps when all four bands are operating. Two on-board halo-

gen lamps are used for calibration of the nadir-looking detectors. This calibration source is always in the optical path.

SWIR (Short Wave Infrared)

The SWIR subsystem operates in six spectral bands in the near-IR region through a single, nadir-pointing telescope that provides 30 m resolution. Cross-track pointing (± 8.550) is accomplished by a pointing mirror. Because of the size of the detector/filter combination, the detectors must be widely spaced, causing a parallax error of about 0.5 pixels per 900 m of elevation. This error is correctable if elevation data, such as a DEM, are available. Two onboard halogen lamps are used for calibration in a manner similar to that used for the VNIR subsystem, however, the pointing mirror must turn to see the calibration source. The maximum data rate is 23 Mbps.

TIR (Thermal Infrared)

The TIR subsystem operates in five bands in the thermal infrared region using a single, fixed-position, nadir-looking telescope with a resolution of 90 m. Unlike the other instrument subsystems, it has a "whiskbroom" scanning mirror. Each band uses 10 detectors in a staggered array with optical bandpass filters over each detector element. The maximum data rate is 4.2 Mbps. The scanning mirror functions both for scanning and cross-track pointing (to ± 8.55 degrees). In the scanning mode, the mirror oscillates at about 7 Hz and, during oscillation data are collected in one direction only. During calibration, the scanning mirror rotates 90 degrees from the nadir position to view an internal black body. Because of the instrument's high data rate, restrictions have been imposed so that the average data rate is manageable by the spacecraft data management system. This restriction is a one-orbit maximum average rate of 16.6 Mbps and a two-orbit maximum average rate of 8.3 Mbps, which results in approximately a 9.3% duty cycle.

4.1.3 The Shuttle Radar Topography Mission (SRTM)

Under agreement with NASA, the USGS EROS Data Center distributes and archives SRTM data in accordance with a joint partnership Memorandum of Understanding between NASA and NGA. The SRTM Mission obtained elevation data on a near-global scale to generate the most complete high-resolution digital topographic database of Earth. SRTM consisted of a specially modified radar system that flew onboard the Space Shuttle Endeavour during an 11-day mission in February of 2000.

SRTM is an international project spearheaded by the National Geospatial-Intelligence Agency (NGA) and the National Aeronautics and Space Administration (NASA).

X-SAR/SRTM was an innovative way of collecting highly accurate topographic information using spaceborne radar instruments.

The collected radar images are converted to digital elevation models (DEMs) spanning the globe between 60° North and 58° South.

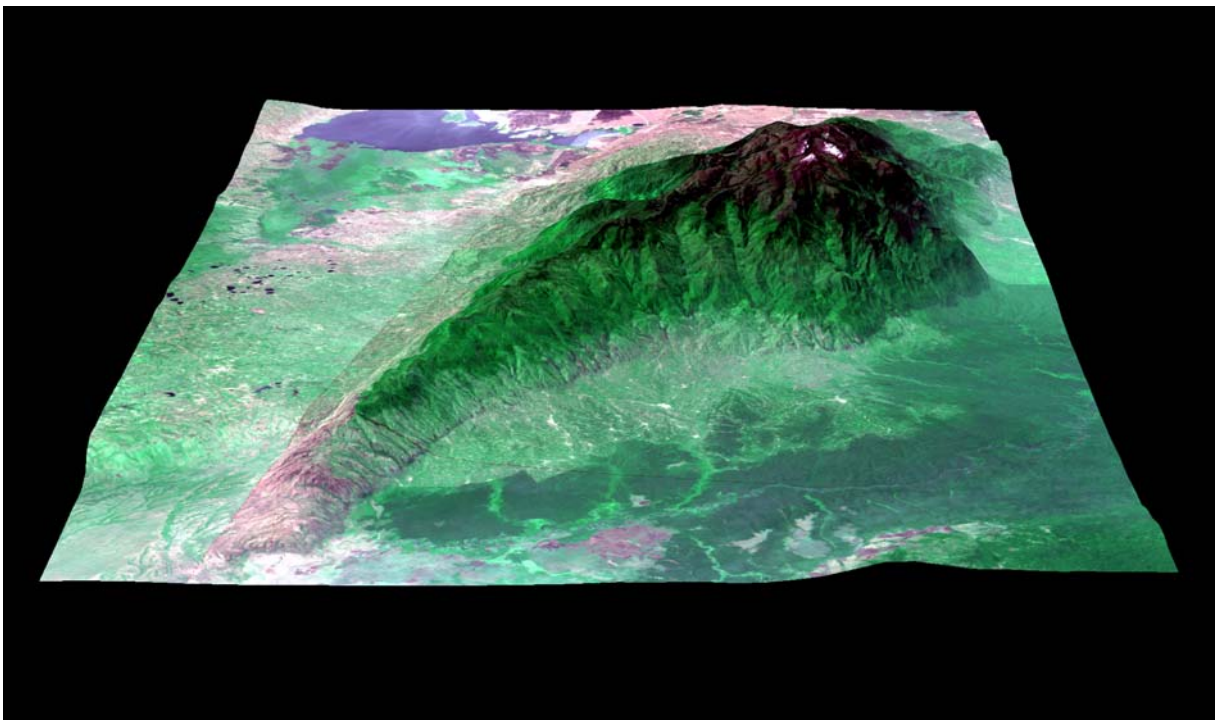

Figure 4.1.1 A 3-dimensional view of the Rwenzori Massif from space as seen from the North. The view is a combination of ASTER data (VNIR) and SRTM digital elevation data. Band combination and data processing have been chosen with respect to near natural colours. On top of the High Rwenzori the white spots represent ice and snow. Green colours are displaying vegetation.

Data processing and image processing for the “Lineament Mapping of the Rwenzori Massif” (chapter 5.1) have been carried out with ERDAS Imagine © and RSI-ENVI © software packages.

The remote sensing methodology comprises the analysis of the complex fracture pattern of the greater area of the Rwenzori Massif by visual interpretation of the ASTER-Data. The results of the investigation are demonstrated in chapter 5.1.

4.2 Geochemistry

In the following section the applied analytical methods are briefly described. It has to be noted that a careful documentation of sampling and related field observations of geological framework conditions are essential for interpretation of the data (see chapter 5.2).

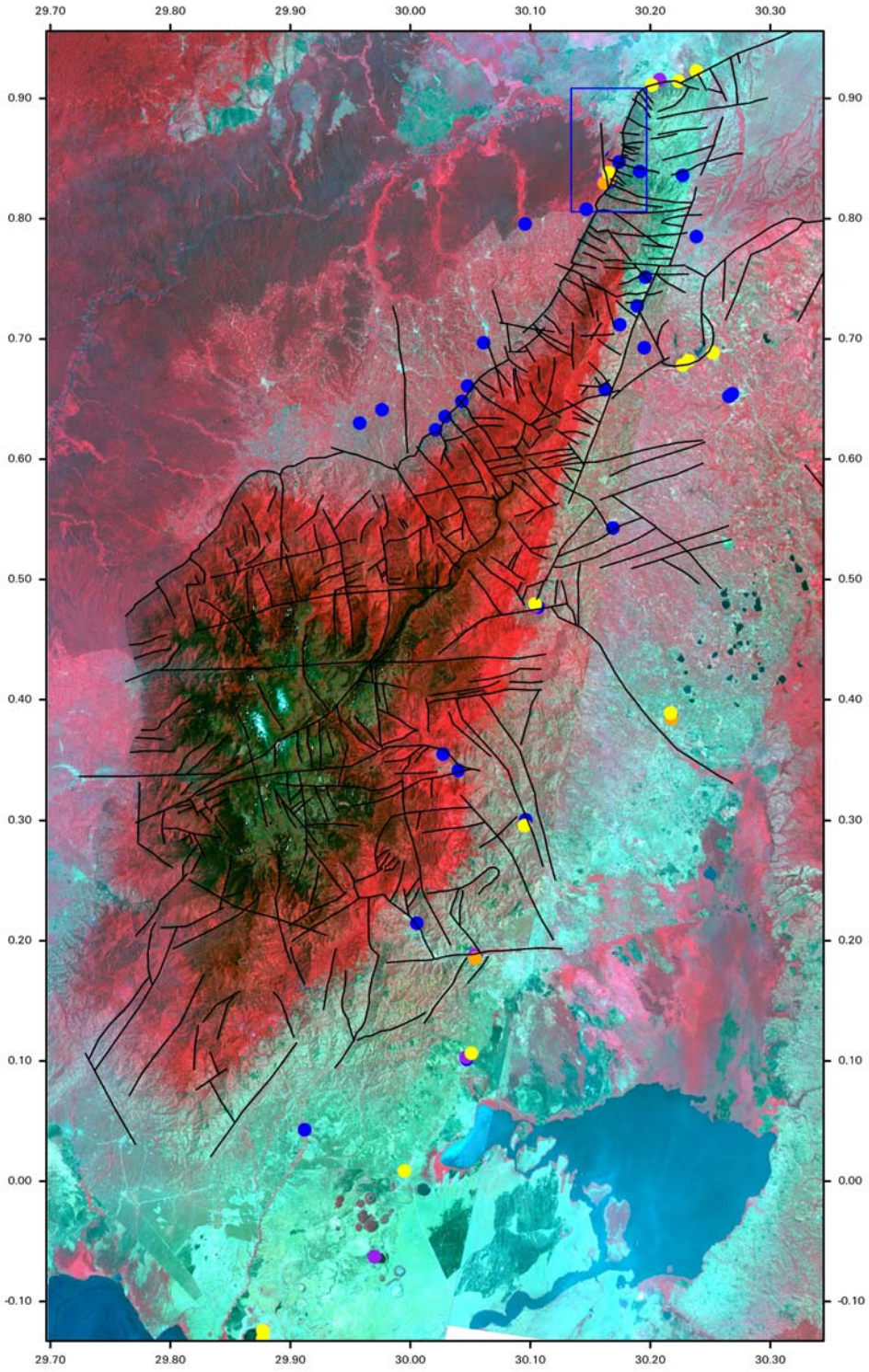

Figure 4.1: Sampling points for water (chemistry [purple] and isotope hydrology [blue]), gas (species and isotopic composition including noble gas helium [orange]) and rocks (mineralogical, chemical and stable isotopic composition [yellow]). For coordinates and analytical raw data see related Tables in Appendix A. Area of geophysical survey [blue rectangle].

The spatial distribution of the sampling points is shown in Figure 4.1 and the underlying exploration concept is described in Chapter 3.

The specific aim of the geochemical and hydrological survey was to answer the two key questions:

1) Is there an active (still hot) magmatic heat source below Buranga area and
2) Is it possible to further constrain the recharge area?

Therefore, our sampling strategy based mainly on two components:

- Sampling was done also in the far surrounding of Buranga (e.g. east of Rwenzori mountains) to get an overall view on the hydrological system and samples of known (e.g. volcanic) environment were taken for comparison
- complementing the existing data set with additional so far not applied methods to get reliable indicators for answering most important key question 1 (e.g. isotopic study of gases including noble gas helium; trace element investigations of fluids including REE; detailed isotopic and chemical travertine investigations)

4.2.1 Rock analyses

Rock samples were taken mainly from travertine deposits and Fort Portal volcanic rocks. They were analysed for their mineralogical, chemical as well as carbon and oxygen isotopic composition.

X-ray diffraction (XRD) for mineralogical composition

The mineralogical composition of the powdered samples (≈ <10µm grain size) was determined by X-ray diffraction by D. Weck in section B4.21 “Technical Mineralogy, Sedimentology” of BGR, Hannover using a Philips X’pert diffractometer PW 3710 with Cu Kα-radiation. The machine is equipped with a fixed divergence slit and a secondary graphite monochromator. The samples were run with a step size of 0.01° and a counting time of 3 seconds per step over a measuring range of 2 to 65° 2 theta.

X-ray fluorescence (XRF) for chemical composition

Sample preparation of the fused glass beads and wavelength dispersive x-ray fluorescence spectrometry (WD-XRF) using PANalytical Axios and PW2400 spectrometers, was done by F. Korte in BGR section B4.15 “Geochemistry of Rocks and Ores”.

The PW2400 spectrometer is fitted with a chromium anode x-ray tube operated at 2.7 kW. The Axios spectrometer is fitted with a rhodium anode x-ray tube also operated at 2.7 kW. Both spectrometers use SuperQ as analytical software.

Glass beads of specpure-grade chemicals and 130 certified Reference Materials (CRMs) were prepared in the same way as the samples and used for instrumental calibration. For matrix corrections the α-correction of de Jongh was applied.

For sample preparation the samples were milled to less than 40 µm particle size. To determine the loss on ignition (LOI) 1000mg of sample material was heated to 1030°C for 10 minutes. After mixing the residue with 5.0 g lithium metaborate and 25 mg lithium bromide, the mixture was fused at 1200°C for 20 minutes. Samples with LOI of more than 20% required 2.5 g lithium metaborate and 2.415 g lithium tetraborate as flux material. Pt95-Au5 crucibles and a commercial automatic fluxer (Herzog 12/1500) were used for fusion of the rapidly produced beads. The uniform elemental distribution in glass beads and reduction of matrix effects are widely acknowledged to be the advantage of fusion techniques (Török & van Grieken 1992, Török et al. 1996).

Due to time constraints of BGR/GGA labs in Hannover, Germany some sinter samples were sent to external laboratories i.e. Actlabs, Canada for analyses of chemical composition; Rafter, New Zealand and University of Tübingen, Germany for analyses of stable isotopes.

Inductive Coupled Plasma mass spectrometry (ICP-MS) for chemical composition

First samples of sinters (>0.5 g) were sent to Activation Laboratories Ltd. (Actlabs), Ancaster, Ontario Canada. Code ULTRATRACE-1 was chosen because this extraction is analyzed by ICP-MS to provide low detection limits. Upper limits are up to 20,000 times the detection limits. A list of the detection limits and further details are found on the Actlabs homepage www.actlabs.com.

Isotope ratio mass spectrometry (IRMS) for carbon and oxygen isotopic compositions

The first sample series of sinters was also sent to the Stable Isotope Laboratory (Rafter Building) of the Institute of Geological & Nuclear Sciences Limited (GNS), Lower Hutt, New Zealand. The analyses were carried out by Dr. Karyne Rogers at GNS. All measurements are normalised to V-PDB using GNS and Lincoln Marble (internal standards; Table 4.1), NBS-18 (International Standard) and NBS-19 (International Standard).

Table 4.1: Reported and measured values of internal standards

Sample	δ^{13}C PDB(CO2)	δ^{18}O PDB(CO2)
GNS Marble reported	2.06	-6.46
GNS Marble measured	2.11	-6.55
Lincoln Marble reported	-25.04	-14.59
Lincoln Marble measured	-24.99	-14.49

All data have been obtained by analysis of the samples using an automated CAPS carbonate device attached to a Europa GEO 20-20 mass spectrometer. Reaction was with phosphoric acid at 80°C to produce CO_2 for analysis. The reported precision is ±0.1‰ for δ^{13}C and δ^{18}O.

The second sinter sample series was sent to the “Geochemisches Zentrallabor” of the Institute for Geosciences (IfG), University of Tübingen, Germany. The analyses were carried out by Dr. Heinrich Taubald at IfG. All measurements were normalised to V-PDB using international standard NBS 19 (δ^{13}C = 1.95‰, δ18O = -2.20‰, relative to V-PDB).

Carbon and oxygen isotopic composition was determined using an automated Gasbench II chromatograph which is attached to a Finnigan MAT 252 isotope ratio mass spectrometer.

The external reproducibility (= standard deviation of the standards) is ±0.1‰ for δ^{13}C and ±0.15‰ for δ^{18}O. Additionally the calcium-carbonate content was analysed with an external reproducibility of ±5%.

4.2.2 Water analyses

Water samples were taken from Buranga and also from the northern tip and east of the Rwenzori. Furthermore water samples from an oil exploration well about 20 km NNE of Buranga were analysed for comparison.

Sampling

Polyethylene bottles with 500 ml and 100 ml volume were intensively cleaned in the laboratory and used for sampling of anions and cations, respectively (preferentially the hottest part of the spring fields were sampled). One millilitre of ultra pure concentrated nitric acid was filled in the 100 ml bottles to prevent precipitation of iron and related metals. Both subsamples were filtered in the field through a 0.45 µm cellulose acetate filter to remove particulate matter. In contrast to the anion samples, filtration of the acidified cation samples is essential to prevent leaching of particles (chemical pulping with HNO_3) which would severely falsify the original concentration of the dissolved solutes in the water.

Polythene bottles with 20 ml volume and polyseal caps (conical-section seals) were used for stable isotope samples after rinsing with sampled water. Most of the samples were filtered to remove particulate matter.

Analytical details of applied methods (ICP-OES; ICP-MS; IC) for solute concentrations

Full elemental analyses were done by W. Glatte in BGR section B4.16 “Hydrogeochemistry”.

Concentrations of main components Na, K, Ca, Mg, B, Li, Sr, Al, Si, Mn, Fe as well as trace elements As, Sc, Ti and V are analyzed from acidified solution with ICP-OES (inductively coupled plasma optical emission spectroscopy) based on German standard DIN EN ISO 11885 (1998).

Concentrations of other trace elements are analyzed from acidified solution with magnetic sector field ICP-MS (inductively coupled plasma mass spectrometry). With low mass resolution ($m/\Delta m = 350$) the elements Ba, Be, Cd, Cs, Hf, In, Mo, Pb, Sb, Sn, Ta, Th, Tl, U, W, Y and REE and with medium mass resolution ($m/\Delta m = 3800$) the elements Bi, Cu, Ga, Nb, Ni, Rb, Zn and Zr are analyzed. The element Rh is used as an internal standard. Further analytical details of magnetic sector field ICP-MS are described in Gäbler (2002).

For the determination of alkalinity (acid neutralizing capacity) of a water sample a 10ml aliquot of the non-acidified sample is titrated with 0.02 N HCl down to pH=4.3 (DIN 38409, 1979; Schuster, 2002). The endpoint is determined potentiometrically using a 2-cell pH-glass electrode.

For the determination of the anions Cl^-, Br^-, SO_4^{2-}, an IC method (ionic chromatography) based on German standard DIN EN ISO 10304-1 (1995) is used. The anions-peaks are detected by electrical conductivity, following neutralization of the alkaline KOH eluent with a membrane suppressor technique. H_2SO_4 is used for regenerating the system.

Isotope ratio mass spectrometry (IRMS) for hydrogen and oxygen isotopic compositions

Stable isotopic composition of waster samples was analysed in section 3 “Geochronology and Isotope Hydrology” of the Leibniz Institute for Applied Geosciences (GGA-Institute), Hannover, Germany by Dr. Robert van Geldern.

Water samples were analyzed for δ^2H using a fully automated chromium reduction system at 800°C (H/Device, ThermoFinnigan) directly coupled to the dual inlet system of a Thermo Finnigan Delta XP isotope ratio mass spectrometer. Further analytical details are given in van Geldern & Suckow (2005). Water samples were analyzed for $\delta^{18}O$ using an automated equilibration unit (Gasbench 2, Thermo Finnigan) in continuous flow mode. All samples were measured at least in duplicates and the reported value is the mean value. All values are given in the standard delta notation in permill (‰) vs. V-SMOW according to $\delta[‰] = (R_{sample}/R_{reference} - 1) \times 1000$.

Raw data were corrected for memory effect and excluded if necessary (δ^2H). The data sets were corrected for machine drift during the run and normalized to the V-SMOW/SLAP scale by assigning a value of 0 ‰ and -428 ‰ (δ^2H) / -55.5 ‰ ($\delta^{18}O$) to V-SMOW and SLAP, respectively. For normalization two laboratory standards, which were calibrated directly against V-SMOW and SLAP, were measured in each run. External reproducibility – defined as standard deviation of a control standard during all runs – was better than 0.8 ‰ and 0.06 ‰ for δ^2H and $\delta^{18}O$, respectively.

4.2.3 Gas analyses

Two different types of gas samples (glass flasks and copper tubes) were taken at Buranga geothermal prospect and for comparison e.g. also from springs of the eastern side of Rwen-

zori. The gas in the glass flasks was used for determination of the concentration and the carbon and hydrogen isotopic composition. The gas in the sealed copper tubes was used for helium isotopic measurements.

Gas species concentrations and isotopic compositions of carbon and hydrogen have been determined by M. Zimmermann and D. Laszinski in section 4.13 “Gas Geochemistry, Isotope Geochemistry” of BGR, Hannover, respectively. The analytical procedures followed the ones described e.g. in Lippmann et al. (2005).

Gas chromatography (GC) for concentrations of gas species

Major gas species and hydrocarbons were analyzed using a Varian-GC, equipped with a variety of columns and detectors. Saturated and unsaturated hydrocarbons were separated on a Silicaplot (C1-C4 components) and a CP-SIL (pentane/pentene) capillary column using He as carrier gas and were detected individually with flame ionization detectors (FID). Analytical uncertainties depend on the absolute concentration of the analyzed gas. For hydrocarbon concentrations between 1000 and 10,000 ppm the relative uncertainty is ±3%, for concentrations between 10 and 1000 ppm, ±10%, and for concentrations <10 ppm the relative uncertainty is ±20%.

Isotope ratio mass spectrometry (IRMS) for carbon and hydrogen isotopic compositions

Stable carbon and hydrogen isotope analyses of C1-C3 were performed using a Finnigan MAT Delta Plus attached to an AGILENT-GC (GC-IRMS direct inlet system). The components were separated on a Poraplot Q column (internal diameter 0.32 mm, length 25 m). Precision of measurements is <0.1‰ for $\delta^{13}C(CH_4)$ and ±3‰ for $\delta D(CH_4)$. Precision of $\delta^{13}C(C_2H_6)$ and $\delta^{13}C(C_3H_8)$ is ±0.1‰ and ±0.2‰, respectively. All values are given versus the V-PDB ($\delta^{13}C$) and V-SMOW standards (δD) in the usual δ-notation.

High resolution mass spectrometry (SMS) for helium isotopic composition

Noble gas analyses have been performed in the Helium Isotope Lab of the Institute for Environmental Physics (IUP), University of Bremen, Germany by Dr. Jürgen Sültenfuß.

Gas samples for helium isotope analysis have been taken in 20cc Cu tubes, sealed by pinch-off clamps providing extremely low leak rates.

A split (~0.001) of the sample volume was transferred to a cryo trap kept at 25K to separate Ne and He from all other gases. 3% of the sample is admitted to a quadrupol mass spectrometer (Balzers QMG112a) for analysis of Ne isotopes and ^{4}He. He is separated from Ne in a second cryo system at 14K equipped with charcoal. Subsequent heating to 45K releases only He to a high-resolution sector-field mass spectrometer (MAP 215-50). Design and system parameter allow clear separation of ^{3}He from HD-molecules leaking through metal walls. The system is calibrated by aliquots of atmospheric air. Blank, linearity and stability measurements are performed in a routine manner.

For an extended description of the analytical procedure see Sültenfuß et al. (2007).

All samples were divided and each aliquot was analysed several times (total of 29 measurements). The reported uncertainties in the ^{3}He/^{4}He ratios result partly from multiple measurements. The uncertainties of the total amount of ^{4}He are about 50% because the pressure and volumes in the Cu-tubes are poorly known. The analytical uncertainty in the determination of the Ne/He ratios is 0.001 for small values and 1% for higher ratios of the reported value.

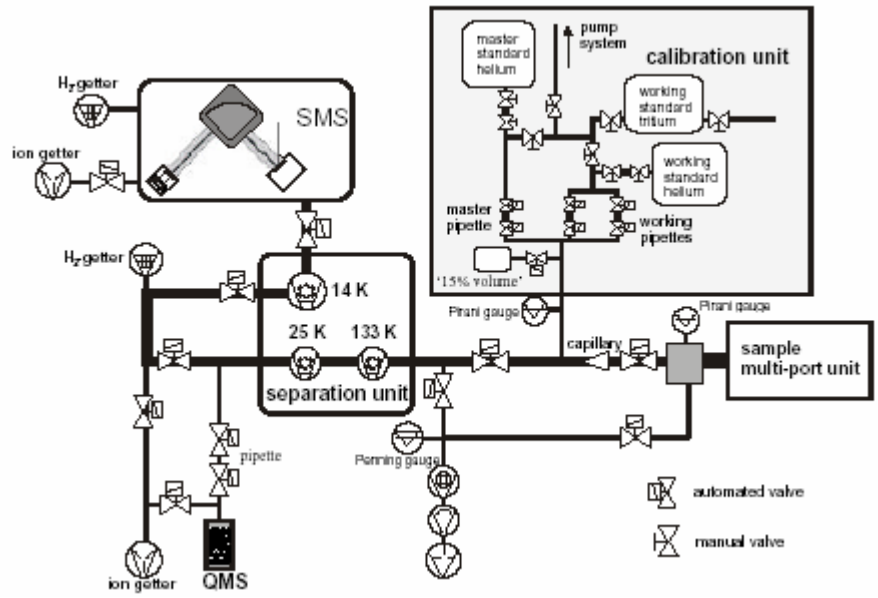

Figure 4.2: Components of the noble gas isotope facility in the Institute for Environmental Physics, University of Bremen, Germany (Sültenfuß et al. 2007)

For further details of sampling procedure and the underlying principles of noble gas geochemistry see attached presentation of introductory short course given at GSMD on 19th of July 2005 (Appendix A.8).

4.3 Geophysics

The survey area at the Buranga geothermal prospect is located in a widely difficult accessible terrain (Fig. 4.3.1). The steeply dipping escarpment of the Rwenzori Massif (Bwamba fault) borders the eastern part of the survey area. The western part is covered by dense tropical rain forest with creeks and swamps and is part of the Semuliki National Park. The hot springs are located in a swampy terrain in clearings of the rain forest. In the northern part of the survey area the rain forest is thinning out and the terrain changes to a plain covered by grass.

A first ground geophysical field survey at the Buranga geothermal prospect started on 11th of February and ended on 4th of March 2005. Geoelectrical, transient electromagnetic and gravity measurements were carried out. Stadtler & Kraml (2005) have described in detail this survey of February/March 2005.

Between May 2005 and August 2006, earthquakes were registered at several seismological stations set up in the northern part of the Rwenzori Massif. These seismological observations are reported explicitly in Rümpker et al. (2007) and additionally in Ochmann et al. (2007).

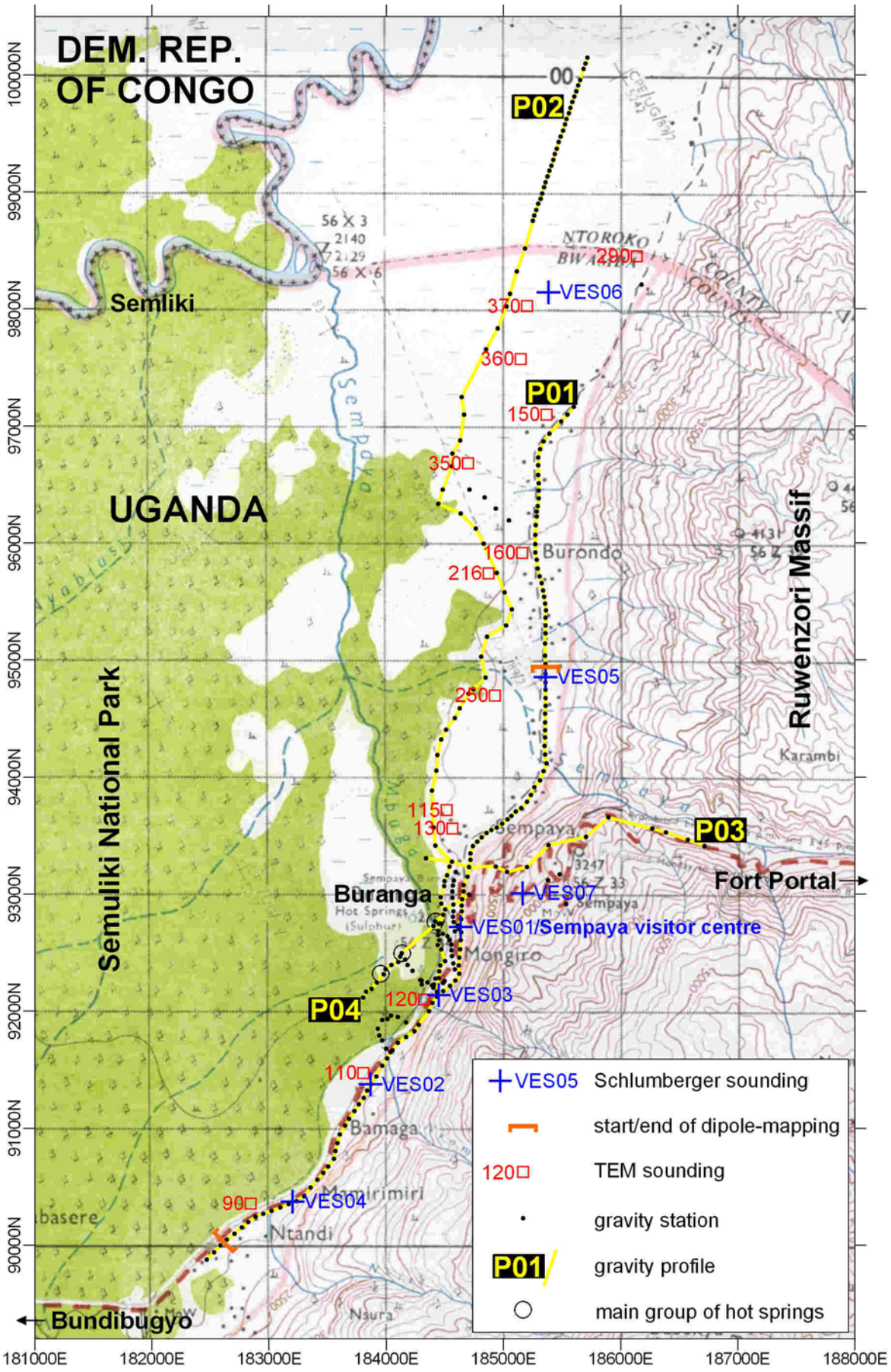

Figure 4.3.1: Survey area Buranga with the measuring points of the ground geophysical survey in February/March 2005

Direct current geoelectrics and transient electromagnetics have proven to be useful geophysical methods in geothermal exploration. The physical parameter to be determined by these methods is the specific electric resistivity (in Ωm), in this report further on called resistivity. It essentially depends on the parameters: porosity, fluid content and temperature in the subsurface. Especially the latter parameters have strong influence on the rock resistivities in geothermal areas. In fractured zones with high porosity, the bulk resistivity is principally controlled by the resistivity of the water contained in the rocks, which again strongly depends on the salinity and the temperature. The high resistivities of igneous rocks, unsaturated sediments or fresh water saturated sediments contrast with the low resistivities of fractured zones or sediments saturated by thermal water. At Buranga, thermal water may infiltrate the rift sediments through the Bwamba fault and transverse faults in the Rwenzori Massif. The dipole/dipole-mapping of the ground geophysical survey were aimed to locate transverse faults where thermal water emerges from the basement rocks and the Schlumberger and transient electromagnetic soundings to determine the depth of the dipping Precambrian basement and the extent of thermal water in the rift sediments.

In geothermal active regions thermoelectric (a few 100 mV) and electrokinetic (up to 2 V) effects are the main mechanisms in the generation of natural self potential (SP) anomalies. Temperature, resistivity, chemistry and pH of the pore fluid are the parameter which can strongly influence the streaming potential (electrokinetic potential). Generally a positive SP anomaly is generated in the direction of pore fluid flow. In the field, a positive anomaly is associated with upward flow of pore fluid, while a negative anomaly is associated with downward flow (infiltration) (Mlynarski & Zlotnicki, 2001). At Buranga, SP measurements in combination with mapping of faults could provide indications for fluid flow along faults as well as for buried faults in the rift and basement.

Gravity gives valuable information about subsurface structures. Gravity anomalies (in mGal) are caused by density variations in the subsurface, i.e. caused by geological structures like faults, fractures, variations of sedimentary thickness, densification of sediments by hydrothermal altered minerals and magmatic intrusion in sediments or basement rocks. At Buranga, the gravity measurements were aimed to determine the dip of the Bwamba fault and to locate transverse faults of the Rwenzori Massif.

Due to the high seismicity in the Rwenzori region, seismology is a valuable tool for geothermal exploration. Observations of a great amount of local earthquakes over a long time supply an excellent data base for seismological tomography (Ochmann et al., 1989). The seismological tomography was aimed to identify an active magmatic heat source in the subsurface at Buranga.

4.3.1 Direct current geoelectrical measurements

In direct current geoelectrics, e.g. Schlumberger soundings, also called vertical electrical sounding (VES), and dipole/dipole mapping, a direct current of amperage ***I*** is introduced at two points A and B at the earth‘s surface and the electrical potential ***U*** generated in this way is measured at two additional points M and N. In Schlumberger soundings, the distance ***AB*** is called current electrode spacing and ***MN*** potential electrode spacing. In dipole/dipole measurements ***AB*** and ***MN*** are the dipole length. From both measured values (***I*** and ***U***) and incorporating a so called geometric factor, which depends on the electrode positions, the apparent specific electric resistivity ρ_a (in this report just called apparent resistivity) can be calculated. In a heterogeneous medium, the apparent resistivity is furthermore influenced by the character of the heterogeneity.

The geoelectrical measurements started on February 14th and continued until March 4th 2005. The instrument used was SYSCAL-R2, manufactured by IRIS Instruments, France. The instrument can be operated conventionally (e.g. Schlumberger soundings) as well as in multi-electrode mode, i.e. processor controlled and by configuration-files/software. Two transmit-

ters were available: a 250 W transmitter powered by a 12 V car battery with maximum currents between 300 and 2500 mA (depending on the external resistance); and a 1200 W transmitter powered by a 220 V – 50 Hz generator with a maximum current of 1.5 A. The transmitter current was introduced into the ground by 1 m long steel rods. Non-polarizable copper/copper sulphate electrodes were used as potential electrodes.

Schlumberger soundings

The Schlumberger soundings were executed jointly by personal of GSMD and BGR using the SYSCAL-R2 receiver and the 250 W transmitter. The maximum current electrode spacing (AB/2) amounted to 1000 m; the potential electrode spacing (MN/2) varied between 0.5 and 50 m.

A total of 7 Schlumberger soundings were carried out (Fig. 4.3.1): 5 soundings on the road to Bundibugyo along the Rwenzori Massif, one sounding on the plain in the northern part of the survey area and one sounding within the Rwenzori Massif on the pass to Fort Portal. Table 4.3.1 summarizes the parameter of the Schlumberger soundings.

Table 4.3.1: Parameter of Schlumberger soundings

No.	East	North	max. AB/2 [m]	Direction [°N]	App. distance to Rwenzori [m]
VES01	184635	92720	750	0	150
VES02	183865	91377	1000	40	200
VES03	184445	92140	1000	45	20
VES04	183199	90376	1000	60	80
VES05	185358	94856	1000	0	300
VES06	185383	98144	1000	55	1000
VES07	185162	93010	200	0	In the mountains

The Schlumberger sounding data were processed and inverted using the software RESIXIP from Interpex, USA. The measured apparent resistivities give already qualitatively an impression about the distribution of the resistivities in the subsurface. By inversion true layer resistivities and thicknesses are determined. Thereby, a 1-d situation is assumed, i.e. the earth consists of horizontal layers infinitely extending, each with a different resistivity and thickness. In the inversion process the parameters of a starting model are iteratively adjusted until the calculated model response coincides sufficiently well to the measured data. Geoelectrical methods suffer in principle from an ambiguity and the best adjusted model finally found is just one of almost infinite equivalent models.

Dipole/dipole-mapping

The geoelectrical mapping was performed in the dipole/dipole configuration using the instrument SYSCAL-R2 and the 1200 W transmitter. The roll along technique was used, i.e. a set of measurements with dipole separations increasing from levels n=1 to 5 and a dipole length of a=100 m was taken. After completing one roll, the entire array moves further by 100 m to the next measuring point on the profile. The process is described in detail in Stadtler & Kraml (2005). Larger separations than n=5 were not feasible since the measuring signals with the dipole/dipole configuration decrease very rapidly with increasing dipole separation and decreasing resistivities in the subsurface.

At first a test survey with a dipole length of 10 m was carried out in order to instruct counterparts and casual labourers (Appendix B.2). The profile is 180 m long and extends southward from the Sempaya visitor centre along the road to Bundibugyo.

The dipole/dipole-mapping with a dipole length of 100 m was conducted then on a 6100 m long profile that starts about 2 km north of the Sempaya visitor centre and extends southward along the road to Bundibugyo (Fig. 4.3.1).

Each set of measurements were repeated several times and averaged in order to improve data quality, especially important with the weak signals of the large dipole separations. The data were inverted using the software RESIX2DI from Interpex. The program approximates the measured data matrix by a 2-dimensional finite element mesh, which is divided in rectangular cells; each cell represents then a data value in the model. The least squares error between measured data and calculated model response is minimized iteratively the inversion process. The software employs a rapid least squares inversion of apparent resistivity using the non-linear optimization techniques and the so-called quasi-Newton technique (Loke & Barker, 1996). The result is called the Zonge resistivity model.

Self potential (SP)

The natural self potential (SP) between the potential electrodes was measured simultaneously with the resistivities of the dipole/dipole-mapping with a=100 m dipole length. Since the measurements were done in roll along technique on a profile line, closed loop measurements for drift correction were not possible; as well as continuous registration of telluric and technical interfering signals at a reference line.

4.3.2 Transient electromagnetic (TEM) measurements

The TEM (transient electromagnetic or time domain electromagnetic) method makes use of the electromagnetic induction which produces eddy currents in the subsurface by abruptly turning off a current in a transmitter loop at the surface. The induced currents generate a secondary magnetic field which decays with time as the induced current diffuses in the subsurface. The decay of this secondary magnetic field is measured with help of an induction coil. With the central-loop configuration, which was used, the receiver coil is located at the centre of the transmitter loop. The decay curve as a function of time can be transformed into apparent resistivities as a function of depth.

The TEM soundings were performed by personal of the GSMD using the instrument PROTEM-67 D manufactured by Geonics Ltd., Canada. The instrument comprises a TEM67 transmitter powered by a generator, 800 m of cables for the quadratic 200 x 200 m^2 transmitter loop, a PROTEM digital receiver and a receiver coil with an effective area of 100 m^2. The instrument was operated in the central-loop configuration with repetition frequencies of 25 and 2.5 Hz with 20 time gates logarithmically spaced from 0.0881 – 6.978 ms and 0.881 – 69.78 ms respectively.

A total of 13 TEM soundings were carried out between February 24th and March 3rd 2005 (Fig. 4.3.1): 7 soundings close to the road along the Rwenzori Massif and 6 soundings located at distance to the road, mainly in the northern part of the survey area.

Unfortunately, the measured TEM data with the repetition frequency of 2.5 Hz were corrupted due to technical problems. Only the early measuring times of 25 Hz could be used, resulting in correspondingly low depths of investigation.

Processing of the TEM soundings was done by BGR using the Interpex software TEMIX XL. The program executes a 1-dimensional inversion (ridge regression), assuming an earth consisting of horizontal infinitely extending layers with different resistivity and thickness. The model parameters of a starting model are adjusted iteratively finally minimizing the least squares error between measured data and the model response.

4.3.3 Gravity

The gravity measurements and processing of raw data were performed by GSMD and PEPD (Petroleum Exploration and Production Department), a department of MEMD between February 14th and March 4th 2005, using a Scintrex CG-3 model 110196 gravity meter. The locations and the elevation of the points measured were determined with a Magellan DGPS (differential Global Positioning System) (base station and rower).

During the first days a new local base station was established at the Sempaya visitor centre, at the entrance to the Buranga hot springs (Table 4.3.2). The station is located at a distance of 7 m east of the ranger's quarter and 1.5 m from the hedge. The gravity of the new station was tied in to a base station in Karugutu.

Table 4.3.2: Coordinates, elevation (datum Arc1960) and gravity of the new base station at the Sempaya visitor centre

Station	Easting	Northing	Elevation [m]	Gravity [mGal]
Sempaya	184615.34	92703.25	689.68	977739.72

A total of 280 gravity stations were observed (Fig. 1): A long profile (P01) with 50 m station spacing was measured on the road to Bundibugyo. Profile P02 with spacings between 50 and 200 m was surveyed west of the road in the central and northern part of the area and coincides with profile P01 in the southern part. Another profile (P03) with spacings of 200 m runs along the pass to Fort Portal. A few short profiles (e.g. P04) with a 50 m station spacing were measured in the area of the hot springs.

The raw gravity data were processed with the program GRAVRED. The following parameters were used for corrections and reductions: GMT difference -3 h, projection UTM Zone 36N, ellipsoid Clarke 1880, datum Arc1960, gravity formula GRS1967, reduction density 2.67 g/cm^3. The DGPS data of base and rover stations were post processed using the program MSTAR. The accuracy of the elevation was estimated to be about 20 cm.

Additional processing of the gravity data was performed using the software OASIS MONTAJ from Geosoft Inc.. Topographic corrections were applied using SRTM data (Shuttle Radar Topography Mission) with a grid spacing of 1'' x 1'' longitude and latitude (app. 90 m).

4.3.4 Seismological observations

Deployment of seismological equipment in Buranga region to record local earthquakes was started in May 2005 with three seismological stations only (Fig. 4.3.2: Stations NTAN, KARU, ITOJ).

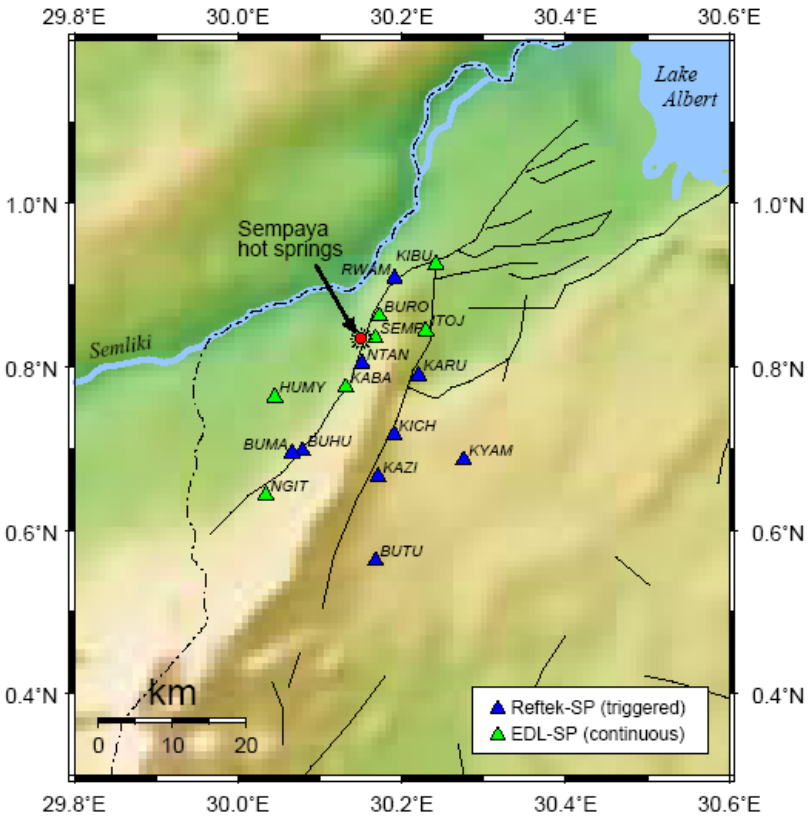

Figure 4.3.2: Map showing the distribution of stations. Note, when the project started in April 2005 only 3 sites had been occupied. By and by the number was increased to 15 stations.

These three stations were operated from May to December 2005 and revealed the very high seismicity (more than 300 local earthquakes per month) of that area, demonstrating that Buranga provides excellent pre-conditions to apply seismology. Therefore it was decided to deploy more stations: 9 stations were operated since January 2006, 15 stations since April 2006. Recording period was finished end of August, 2006. Until April 2006 only Reftek equipment was available for the project which was operated in triggered mode; after this 7 more Earth Data Logger (EDL) were deployed which operated in continuous mode. Short period 1 Hz seismometers of type Mark L-4 3D were used at every station. (The bulk of the seismological equipment was kindly provided by GFZ Potsdam, 6 seismometers were made available by Geophysical Institute of TU Berlin).

The station array covers an area of about 30 times 40 km; the distances between neighbouring stations vary between about 3 and 12 km. Note that the Buranga hot springs are marginally located at the north-western boundary of the array. A more central location of the target area with respect to the array would have been desirable but a secure operation of seismic stations to the north-west of the hot springs was not possible.

Localization of the events began in 2005 with manually picking of P- and S-phases and was continued until March 2007 (no automatic picking).

The micro-earthquake activity around Rwenzori was observed in order to provide information whether an assumed magmatic intrusion could be detected. This approach is explained in Figure 4.3.3.

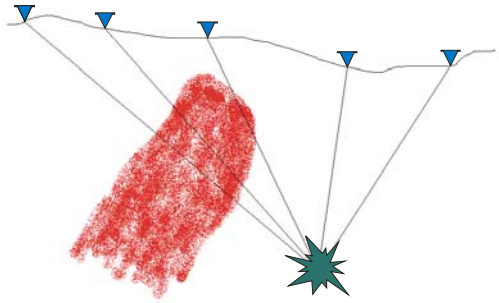

Figure 4.3.3: Seismic rays travelling from an earthquake source to recording sites at the surface can exhibit early or late arrival times depending on the velocity anomalies they have passed.

The waves of an earthquake, which happens within a homogeneous crust, travel to the recording sites at the surface. Some of the waves traverse a magmatic intrusion that has a different velocity than the homogeneous crust. If the travel time for the distance covered is corrected, the rays that passed the anomaly will arrive the sites later or earlier, depending on the intrusion's velocity. The early or late arrivals are usually called travel time residuals. These travel time residuals are used to calculate the involved velocity perturbations.

The target of the procedure is to minimize travel time residuals of P- and S-waves at the recording sites. The final solution is achieved using an iterative procedure for earthquake relocation and simultaneous determination of the velocity structure.

A tomographic inversion of travel time data was conducted in order to determine the three-dimensional structure of the P-and S-wave velocity of the crust beneath the network of stations. The tomographic method used for inverting P-wave travel times of teleseismic events was originally developed by Aki et al. (1977). Later this method was extended on local earthquakes and a major improvement of the original method was achieved with including S-waves into that inversion method. A version of that inversion method modified by Koulakov (2006) was applied.

The velocity contrast between the Precambrian crust and an assumed magmatic intrusion is difficult to estimate because many parameters (ascension temperature, age, pressure, volume, etc.) are unknown. After Kern (1978) and Landolt-Börnstein (1982) a rough mean velocity attenuation of 100 m/s (= 0.1 km/s) per 100°C may be appraised.

5. Results

5.1 Lineament mapping by remote sensing

On high-altitude aerial photographs and satellite images, one of the most obvious features are linear alignments, so called photo-linears. Recently, the term lineament has been frequently used. A most practical definition in the context of image interpretation is given by remote sensing geologists, where lineaments include structural as well as topographical alignments, natural vegetation linears, lithological boundaries, etc. These features are likely to be the surface expression of sub-surface structures. Lineaments can be detected by visual interpretation using characteristics, such as tone, colour, texture, pattern etc.

Within the scope of the project, ASTER images have been analysed for the area of the Rwenzori Massif using the software packages “ERDAS Imagine” and “RSI-ENVI”.

An automatic analysis or unsupervised classification of the satellite images for the project area using the so-called “edge detection techniques” has not been in use, because it is not practicable. Artefacts may arise due to e.g. topography, recent sedimentary cover, brightness-effects (illumination and shadows), altogether leading to misinterpretation of the results of the filtering and/or classifying routines.

Most of the commonly used sensor-systems utilise electromagnetic radiation from the visible part of the spectrum up to the microwave portion. Because radiation in this part of the spectrum (400 nm to several decimetres wavelength) cannot penetrate the ground, the remote sensing image interpretation is limited to the ground’s surface.

Due to climatic conditions, cloudless image cover of the Rwenzori Massif is extremely rare. From intensive research a series of ASTER data could be made available, where favourable and exceptional conditions exist. Fife scenes have been mosaiced leading to a complete cover of the Rwenzori Massif.

5.1.1 Structural Analysis of the Rwenzori Massif

The visual interpretation took place at different scale, directly on screen or on photoprints.

Characteristic features, e.g. representing lineaments in the greater Rwenzori Project Area are:

- active faults,
- annealed faults,
- reactivated old faults.

The entire fault pattern which has been delineated is very complex. Besides the prominent NNE striking faults which are bordering the northern Rwenzori, two major EW striking faults could be recognized north and south of the highest peaks of the massif. Regarding the high amount of lineament structures it can be expected that the entire basement block is penetrated by deep rooted fractures (Figure 5.1.1).

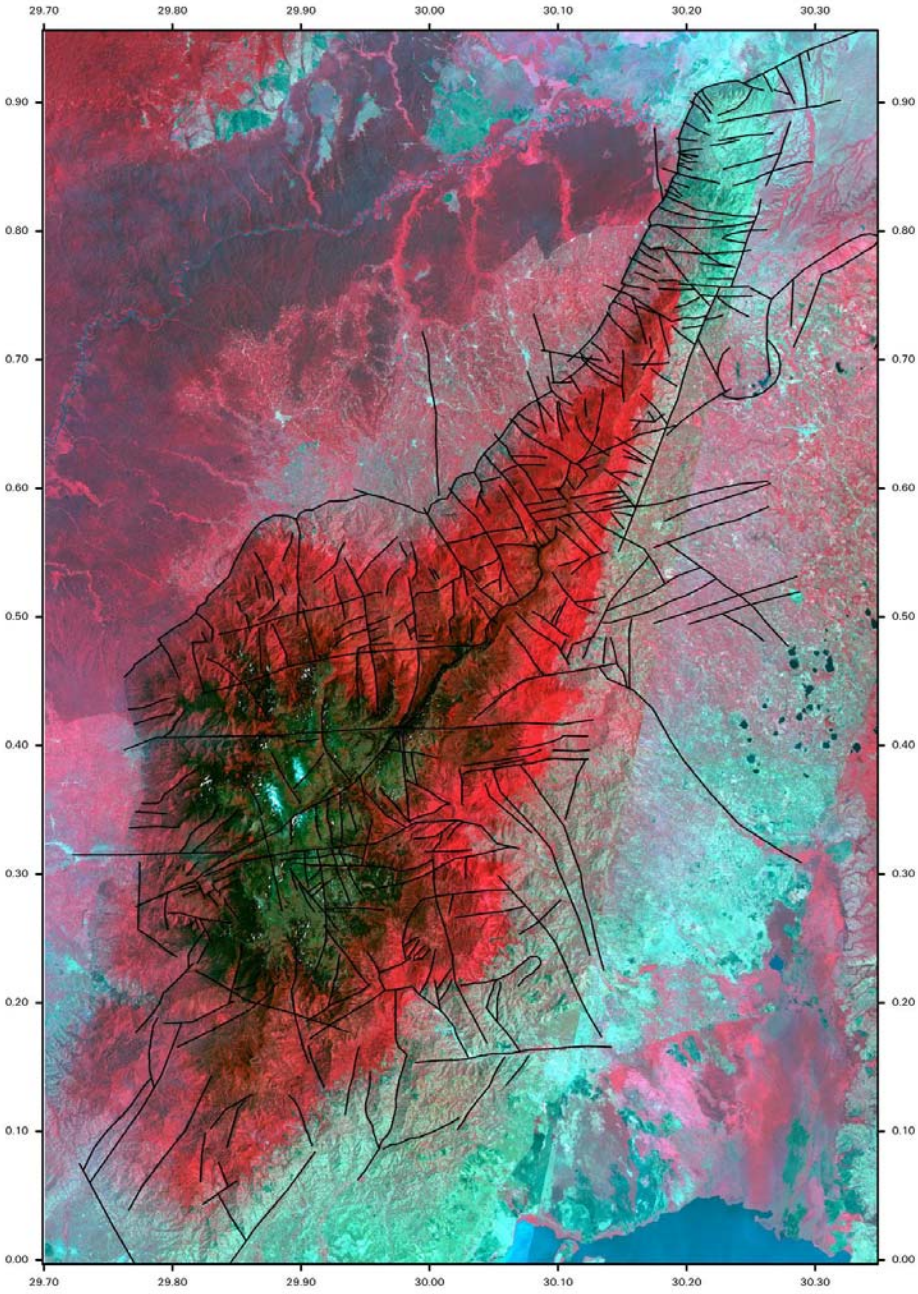

Figure 5.1.1: ASTER Satellite RGB False Colour Composite image of the Rwenzori Massif, overlain by a lineament pattern.

Band combination for the RGB False Colour Composite : Red = ASTER Band 3 (NIR), Green = ASTER Band 2 (VIS Red), Blue = ASTER Band (VIS Green). The vegetation cover appears in red colours. The High Rwenzori area, which is displayed in dark colours, is covered by bare rocks and scarce vegetation. Cyan colours of the lowland areas indicate dry vegetation. The sharp NNE striking line east of the Massif results from mosaicing of different ASTER Data from different seasons. A radiometric correction was not possible.

The majority of the EW and ENE-WSW striking faults is concentrated in the high Rwenzori and slightly north of it. In the northern Rwenzori a NW and WNW-ESE major direction can be observed.

Only very few fault systems can be observed which are prolonging from the Rwenzori Massif into the sedimentary surroundings. Those faults can be expected as very recent.

A driving force for this complicate fault pattern can not be explained by remote sensing only.

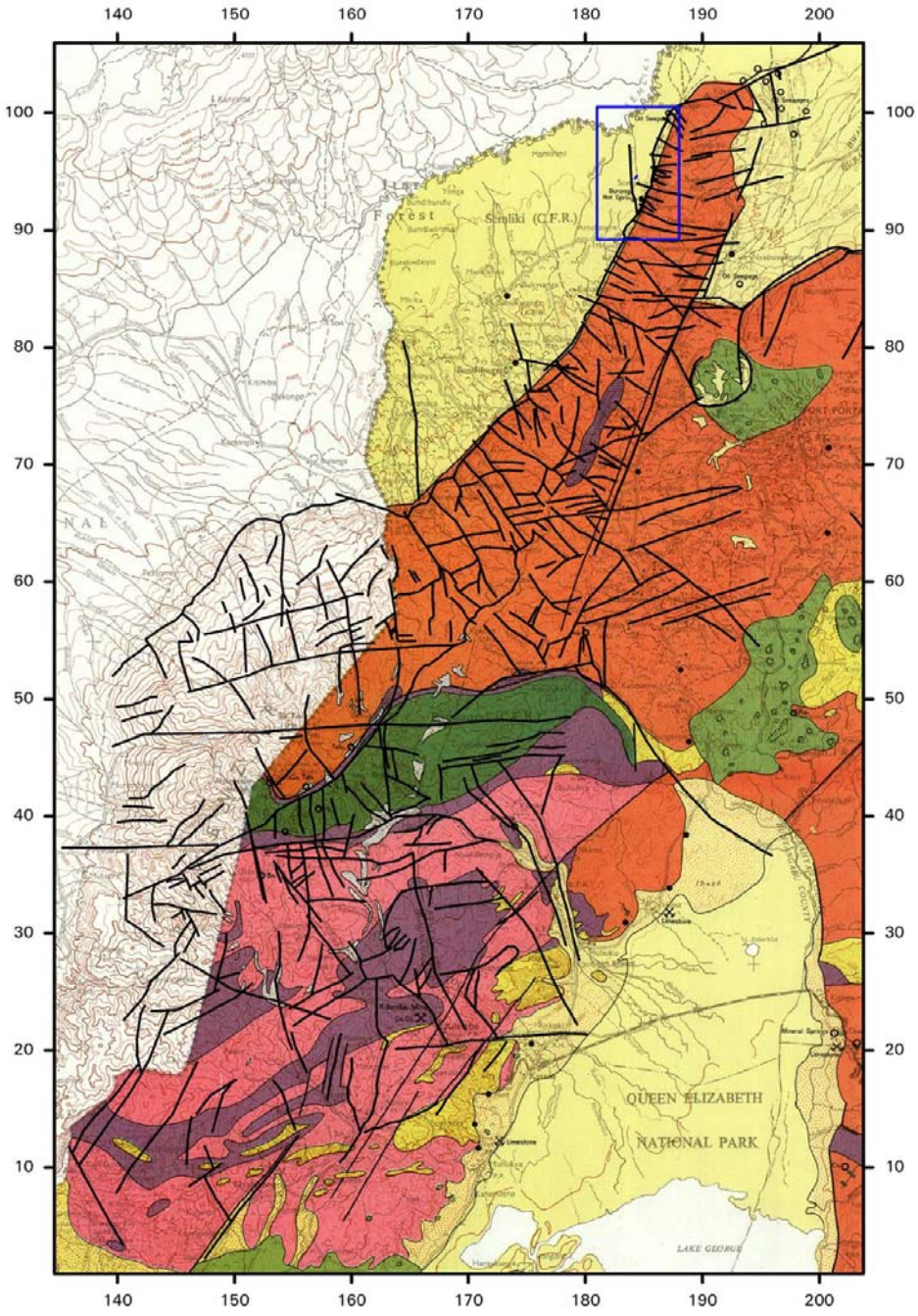

Figure 5.1.2: Geological map overlain by the lineament pattern (GSU, 1962). Blue rectangle marks the area of geophysical survey which is shown in detail in Figure 4.3.1.

Legend for Figure 5.1.2:

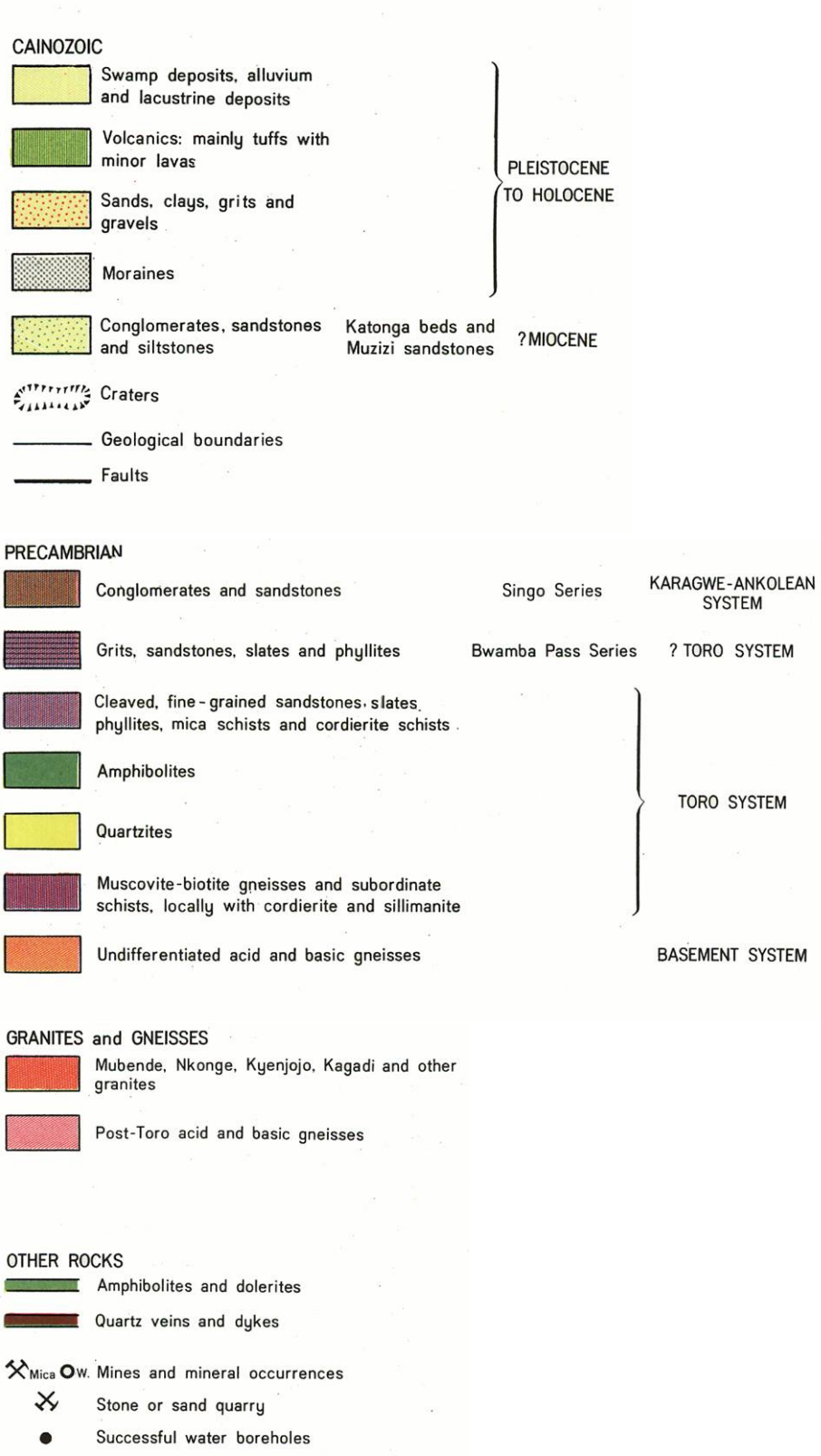

5.2 Geochemical results

In the following section the results of the applied geochemical methods are presented and discussed. Geological field observations are also noted if necessary for the interpretation. The related tables with the analytical raw data are attached in Appendix A.

5.2.1 Composition of rocks

Meteogene and thermogene travertines from known different geological environments were analysed for their mineralogical, chemical as well as carbon and oxygen isotopic composition and compared with samples from Buranga (Fig.5.1). Three groups of travertines can be distinguished (i) Buranga ($\delta^{18}O$ around 14‰) (ii) Katwe ($\delta^{18}O$ around 36‰), and (iii) all other samples ($\delta^{18}O$ around 27‰). The additionally plotted data range of Fort Portal carbonatites (Vinogradov et al. 1978) may be explained by secondary alteration because it does virtually not overlap with primary carbonatite from Ol Doinyo Lengai but is in accordance with slightly to strongly altered Lengai samples. The carbon and oxygen isotopic composition of Buranga travertine is within the field of Fort Portal carbonatites and slightly altered Ol Doinyo Lengai carbonatites.

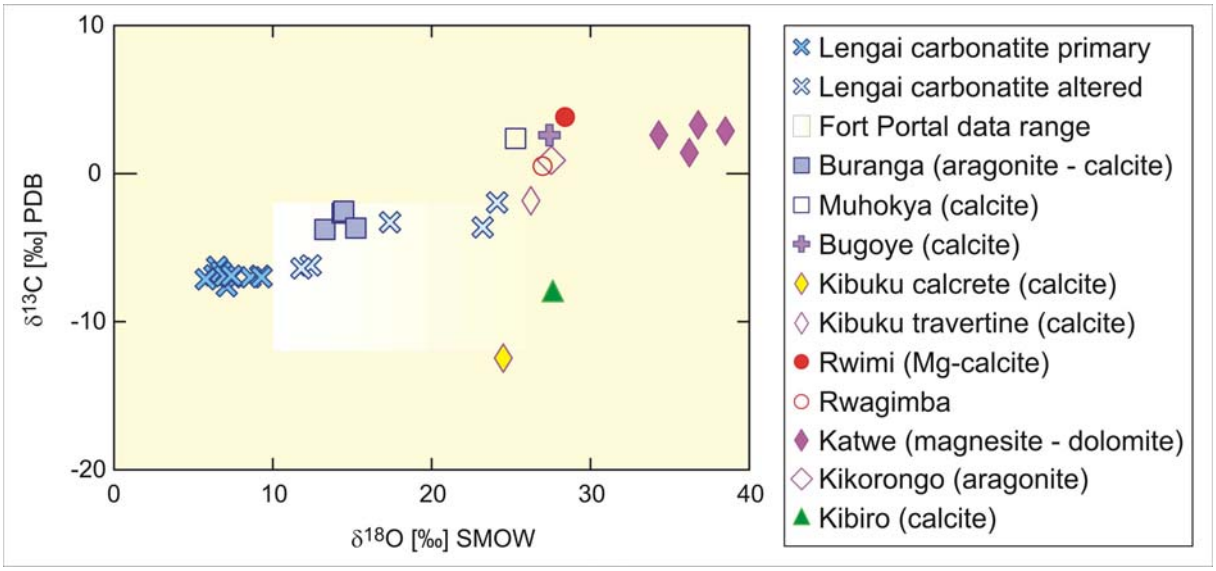

Figure 5.1: Carbon and oxygen isotopic composition of Ugandan travertines (main mineralogical composition is given in the legend). For comparison also carbonatites are plotted from Ol Doinyo Lengai, Tanzania (Keller & Hoefs 1995, Keller & Zaitsev 2006, Halama et al. 2007) and from Fort Portal volcanic field (Vinogradov et al. 1978) which is 50 km apart from Buranga.

Most recent Buranga travertine of Mumbuga spouting spring and earlier deposited travertine from the rim of the spring field as well as a specimen from GSMD museum consist mainly of aragonite and calcite (Fig. 5.1; Appendix A2). Not only the most recent travertine but also the earlier Mumbuga deposits were formed under the current thermogene conditions and precipitated in isotopic and chemical equilibrium. Oxygen isotope composition of the travertine calculated from actual spring temperature and measured $\delta^{18}O$ value of the water as well as the water temperature calculated from measured $\delta^{18}O$ compositions of travertine and water (using algorithms of O'Neil et al. 1969) are in accordance with the actual measured ones. The same type of calculation can be done for carbon isotopic composition with fractionation factors for the $CO_{2(gas)}$−$CaCO_{3(solid)}$ system given by Bottinga (1968). Also in this case the calculated values agree with the measured ones. This gives a first indication of the source of the

involved CO_2 because its calculated carbon isotopic composition (from $\delta^{13}C$ of travertine and water temperature) is compatible with a volcanic origin.

In contrast, the fossil travertine sample Kibiro received from GSMD as powder (similar tectonic environment like Buranga) cannot have formed under the high actual temperature of the Mukabiga hot spring (74°C) but indicates precipitation temperatures of 20°C calculated from $\delta^{18}O$ compositions of travertine and water (data for $\delta^{18}O$ of water from IAEA 2003). Additionally, the calculated $\delta^{13}C$ value of CO_2 (from $\delta^{13}C$ of travertine and water temperature of 20°C) points to a pure organic source of the CO_2 indicating a low temperature fluid for depositing this travertine (meteogen).

Travertines of Katwe (known volcanic environment) which were also originally sampled for comparison with Buranga consist of magnesite and dolomite. They cannot be directly compared with the calcium carbonate travertines due to different fractionation factors. However, the heavy oxygen isotopic compositions of the Katwe travertines are most likely caused by involvement of highly evaporated water from Katwe crater-lake.

Strongly different $\delta^{13}C$ values of both Kibuku samples suggest different fluids for precipitation of travertine and calcrete in the region north of Buranga. The travertine fluid must have been strongly enriched with organic CO_2 (compatible with swamp plant imprints in travertine sample) and the calcrete fluid (local meteoric water) must have been moderately enriched in organic CO_2 (mixture of atmospheric and organic soil CO_2) to explain the stable isotopic composition of these samples.

Alteration zones deliver further valuable solid samples for insights in important processes related to the geothermal system. However, in Buranga area no alteration zones were described in the literature. Therefore our search for altered samples focussed on the faults exposed in Buranga area due to the fact that faults are main fluid paths for the fault controlled geothermal system. An altered sample could be obtained from a fault breccia of an exposed local fault near Kibuku (within Precambrian basement rocks of Rwenzori; Fig.5.2a).

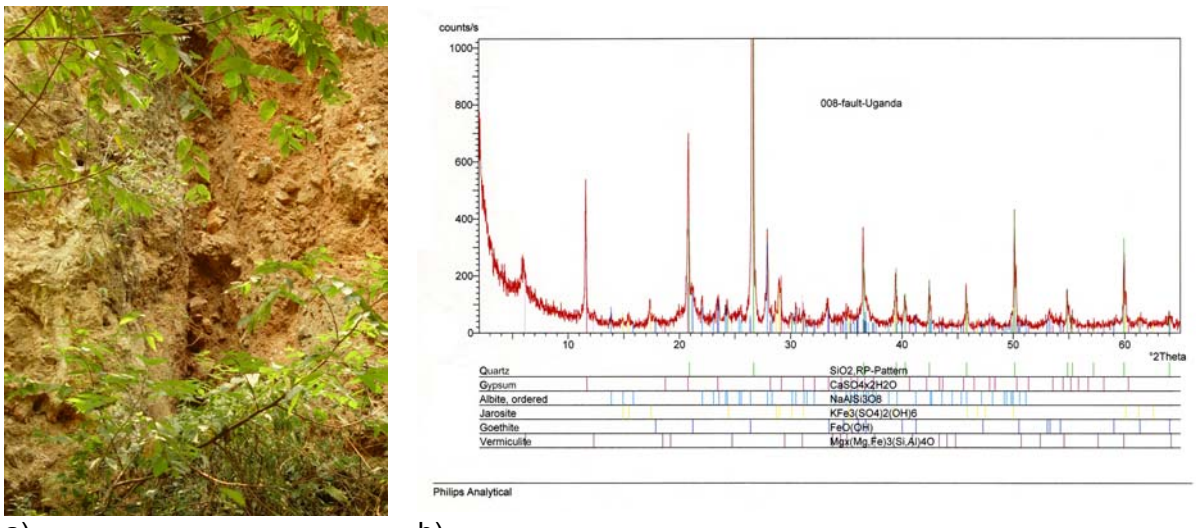

a) b)

Figure 5.2: a) Fault approximately parallel to Rwenzori border fault exposed in an erosional gully within metamorphic basement rocks near Kibuku. b) X-ray diffractogram of sampled fault breccia

Gypsum is found in the mineral assemblage of the altered rock (Fig.5.2b) which indicates fluid flow along this fault but the lack of a high-temperature mineral assemblage indicates low temperatures for this fluid. However, high-temperature mineral assemblages are expected to occur in the not exposed, deeper parts of the fault along the geothermal upflow zone.

5.2.2 Composition of waters

Water samples were taken from Buranga and also from springs east of Rwenzori mountains. The fluids were analysed for their major and trace element composition as well as stable isotopic composition of oxygen and hydrogen.

Chemical composition

Relative proportions of major anions are shown in Figure 5.3a which allows a classification of geothermal waters and a selection of suitable samples for reservoir temperature calculations. According to this triangular diagram the samples can be grouped in mixed waters (Buranga, Kibuku waterhole, Rwagimba), peripheral waters (Rwimi, shallow water sample of oil well 20 km NNE of Buranga), steam-heated waters (Kitagata), volcanic waters (Kibenge, Muhokya) and geothermal waters (deepest water sample of oil well 20 km NNE of Buranga). However, it has to be noted that the oil well samples do not represent mature geothermal fluids. The immature nature of the oil well fluids can be seen in Figure 5.3b. Additionally, down-hole temperature measurements (data in courtesy of GSMD) have found no evidence for a high geothermal gradient. It has also to be noted that Kibenge and Muhokya waters are unlike typical volcanic waters not acidic and more dilute than e.g. Buranga and Rwagimba fluids. The compositional variation of the springs around Rwenzori mountains can be explained by mixing between a sulphate-chloride fluid and dilute bicarbonate water. This mixing trend shown in the Cl versus SO_4 diagram (Fig.5.4) and in the Na-K-√Mg ternary diagram (Fig.5.3b) points to a genetic relationship of the sampled waters and to reservoir temperatures for the upflow zone of Buranga geothermal system of about 160°C.

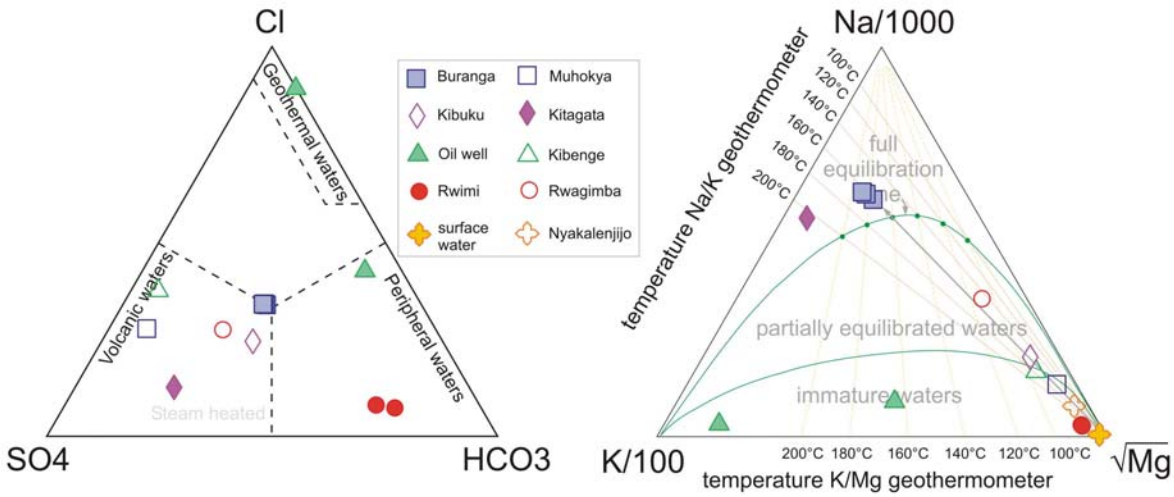

Figure 5.3: a) Cl-SO_4-HCO_3 ternary diagram and b) Na-K-√Mg ternary diagram

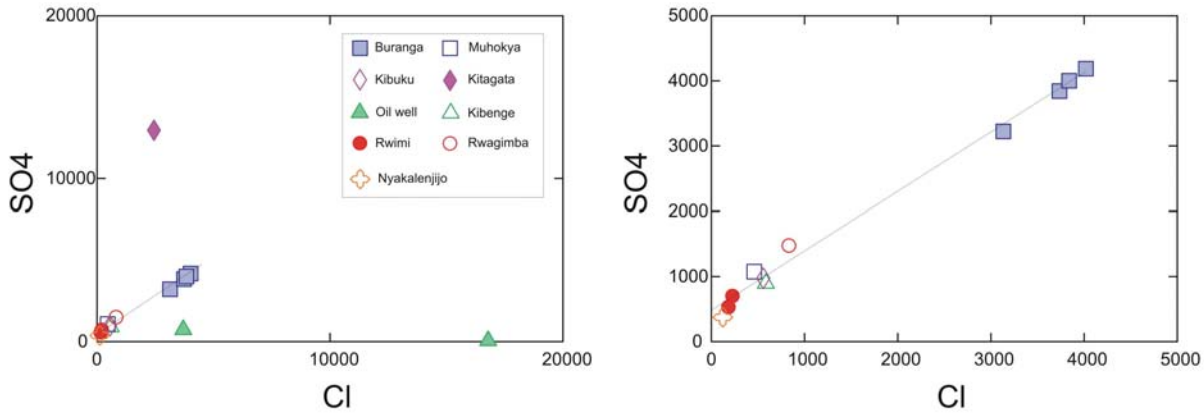

Figure 5.4: a) Cl versus SO_4 diagram [ppm] showing three different fluids (i) SO_4-rich Kitagata fluid, (ii) Cl-rich oil well fluid and (iii) Rwenzori spring fluids and b) Detail showing mixing line of Rwenzori springs (correlation coefficient R^2 = 0.99)

The genetic relationship of Rwenzori hot springs is also supported by their similar ratios of the conservative elements bromine and chlorine (Fig.5.5) pointing to the same source of salinity (note different source of salinity for oil well brines). Bromine-chlorine ratios of Rwenzori fluids (≥0.0045) are higher than seawater and Br/Cl of oil well fluids (0.0018-0.0021) are lower than seawater (0.0034; Hem 1992). Therefore the source of salinity of Rwenzori fluids is most likely silicate rock-water interaction / fluid inclusion leaching.

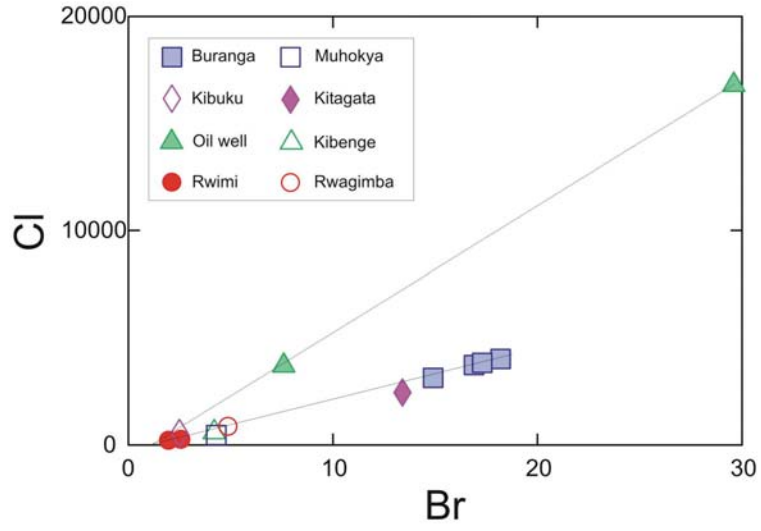

Figure 5.5: a) Cl versus Br diagram [ppm] showing the same source of salinity for Rwenzori hot and cold springs (correlation coefficient R^2 = 0.99) and a different one for oil well fluids.

Additional hints for the fluid evolution can be obtained from trace element analyses like e.g. rare earth elements (REE; Fig.5.6). The spider diagram shows a concentration range spanning two orders of magnitude and low concentrations due to the high pH of the fluids. Highest REE concentrations are found in sample Rwimi 18a which has the lowest pH. The depletion in LREE of neighbouring Rwimi 18b spring can be explained with scavenging of LREE by precipitating iron oxides-hydroxides which are only present in spring Rwimi 18b. The common feature of most analysed waters is the enrichment in light rare earth elements (LREE) compared to heavy rare earth elements (HREE). This characteristic feature is also observed in carbonatitic rocks (Bühn et al. 1999) but also at a lower concentration level in basement rocks of the upper crust and clastic sediments (McLennan 1989). Therefore it is difficult to unequivocally assign the REE pattern of the fluid to a specific REE signature of the host rock.

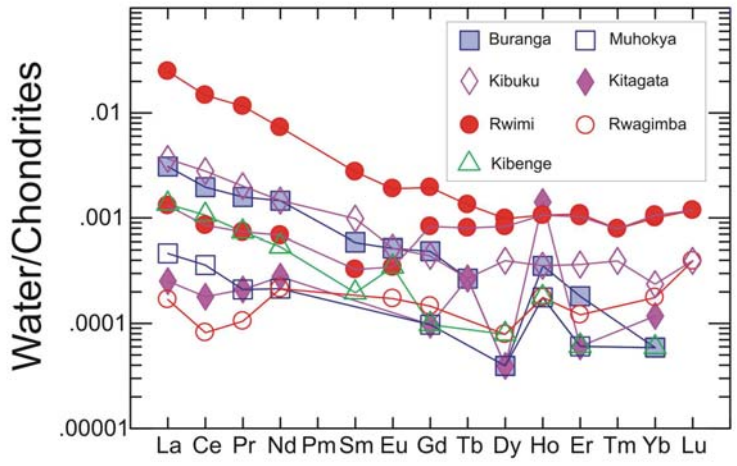

Figure 5.6: Chondrite normalised REE pattern (Sun & McDonough 1989) of water samples. LREE = La to Gd and HREE = Tb to Lu.

Additional to the evolution of the fluid the results of the isotope hydrology study will be presented in the following and solute geothermometry will be presented together with other temperature indicators at the end of this chapter.

Isotope Hydrology

Based on the previous investigations additional water samples were taken and analysed with respect to their stable isotopic composition of oxygen and hydrogen. Figure 5.7 illustrates the new and published data (see Fig. 2.8 for published data). Also in the extended data set the lack of a significant oxygen shift points to a reasonable permeability within the Buranga geothermal system (Kato 2000).

It is evident that one sample of river water (from river Mubuku which is the only sampled river with direct connection to the glacier of high Rwenzori mountains) has the same depleted isotopic composition than Buranga hot springs. Although river Mubuku flows down along the eastern flank of Rwenzori it resembles the isotopic composition of the glaciers. Similar rivers connected to the glaciers are flowing down on the western flank within the territory of D.R. Congo.

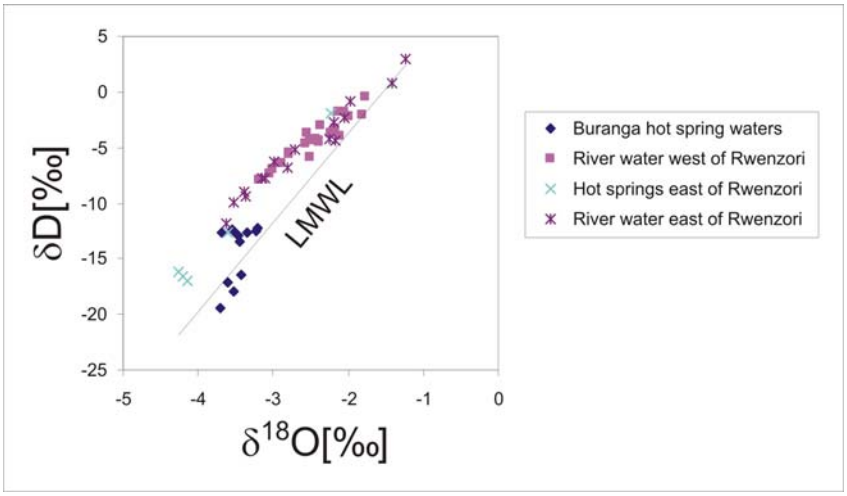

Figure 5.7: Oxygen and hydrogen isotopic composition of Rwenzori waters (LMWL = Local Meteoric Water Line). Published data are included from Kato (2000) and Bahati et al. (2005).

Those waters with depleted isotopic compositions (Fig. 5.8) are infiltrating into the deeper subsurface and flowing most likely along the active Bwamba fault to the north following the regional hydraulic gradient. Along the pathway they are heated up (and after passing an additional magmatic heat source; see below) they are ascending at Buranga.

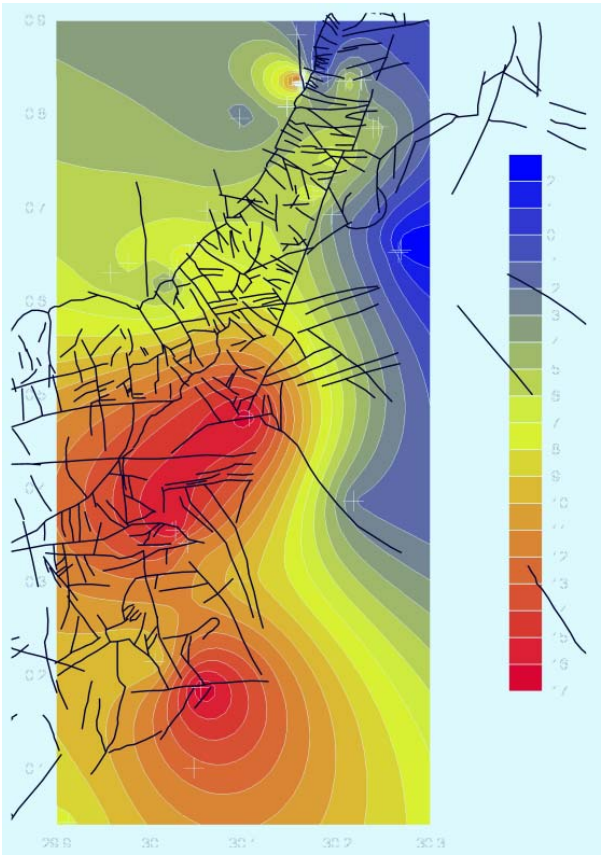

Figure 5.8: Map with grided δD values (kriging method) showing the three areas with depleted compositions (red colours): high Rwenzori, Kibenge spring east and Buranga springs west of Rwenzori.

5.2.3 Composition of gases

Two different types of gas samples (glass flasks and copper tubes) were taken at Buranga geothermal prospect and for comparison also from springs of the eastern side of Rwenzori.

Major gas species and hydrocarbons

Already from the diagram N_2 versus CO_2 it is evident that the springs around Rwenzori mountains are fed by different sources of gases (Fig. 5.9).

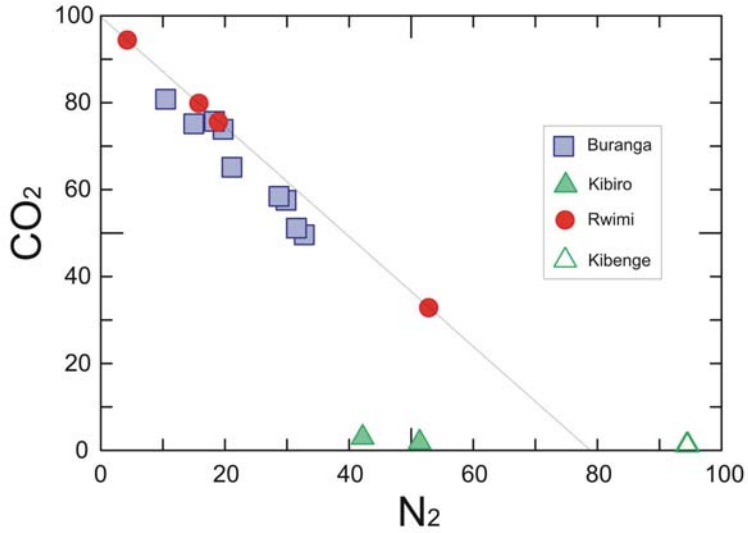

Figure 5.9: N_2 versus CO_2 diagram showing different sources of gas emanating from the sampled hot and cold springs

Especially for Rwimi and also for Buranga the data range can be explained by mixtures of pure CO_2 with atmospheric gas (air saturated water) as indicated by regression line in Figure 5.9. Due to the mixing with air saturated groundwater the gas samples from Buranga springs with lower temperature show systematically higher nitrogen concentrations. Kibenge is by far dominated by nitrogen and Kibiro consists mainly of nitrogen and methane.

Using methane and higher hydrocarbons the four hot springs with free gas emanations can further be distinguished (see Appendix A6).

Stable carbon and hydrogen isotopic composition

Carbon and carbon plus hydrogen isotopic compositions of CO_2 and CH_4 respectively can be used to trace the source of the two gas species. Figure 5.10 shows that CO_2 of Rwimi and Buranga are compatible with a volcanic source for this gas (with a more pronounced atmospheric component for Buranga compared to Rwimi). The small amount of Kibiro CO_2 (1.8-2.9%) may be explained by a mixture of atmospheric and organic CO_2 and Kibenge CO_2 (1.2%) may be mainly of organic origin.

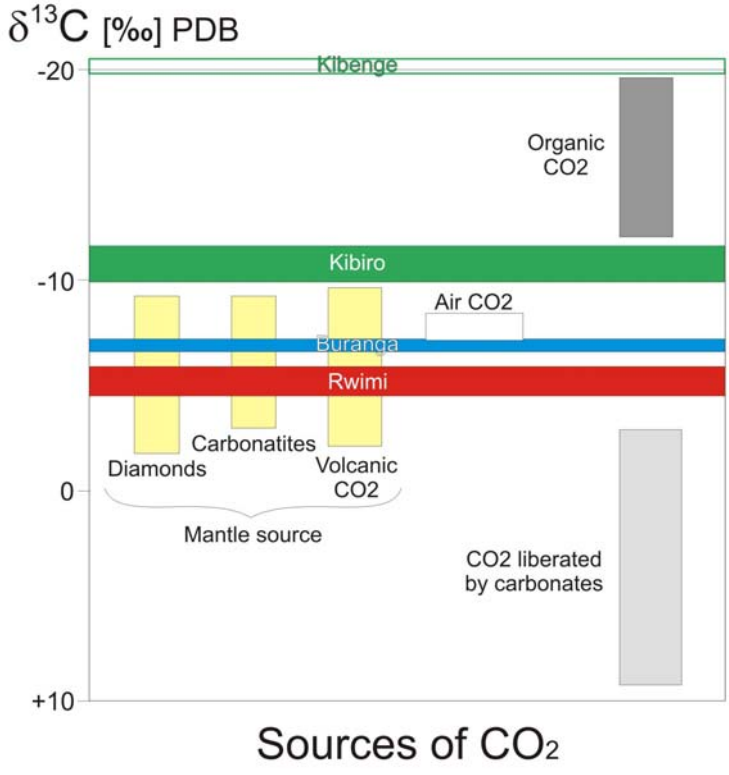

Figure 5.10: Carbon isotopic composition of CO_2 from four sampled springs (data range of CO_2 sources from compilation of Griesshaber-Schmahl, 1990)

Additionally the carbon and hydrogen isotopic compositions of CH_4 could be determined from three gas samples (Rwimi is practically CH_4-free). The results are presented in Figure 5.11. The origin of the CH_4 has implications for calculating reservoir temperatures using the methane/ethane ratio because only in the case of thermal breakdown of the higher hydrocarbons this gas geothermometer may be applied. It is evident that at most Buranga CH_4 is formed via thermal processes and therefore the boundary conditions for applying the methane/ethane geothermometer may just been met.

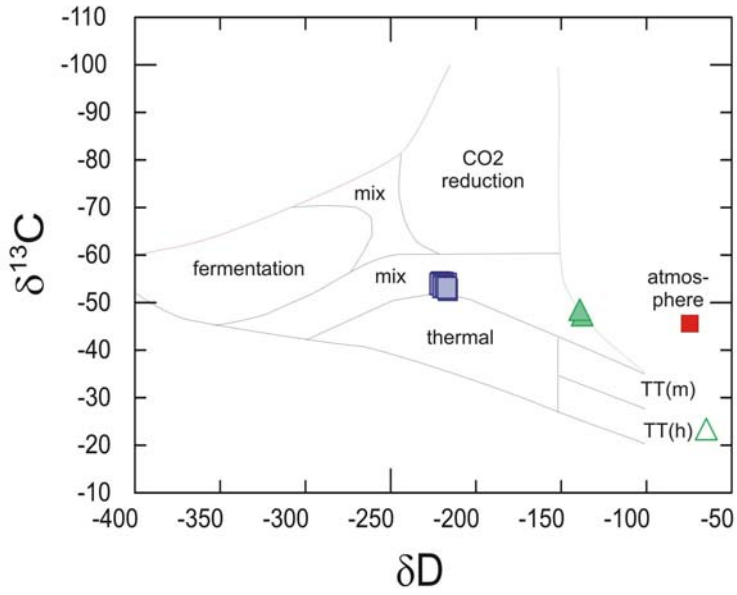

Figure 5.11: Carbon and hydrogen isotopic composition of CH_4 for Buranga (blue square), Kibiro (green filled triangle) and Kibenge (green open triangle). Red square marks atmospheric composition and fields of other CH_4 sources with different compositions are adopted from Whiticar (1990).

Helium isotopic composition

The results of helium isotopic analyses are summarised in Figure 5.12.

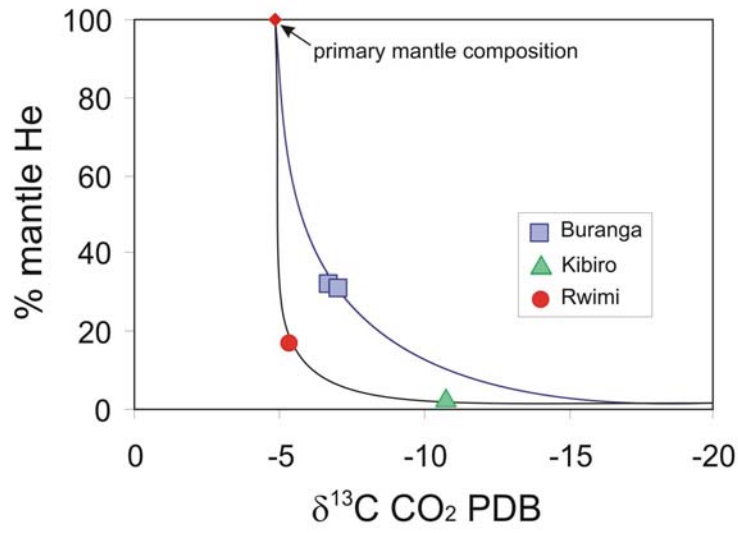

Figure 5.12: Hypothetical mixing hyperbolae of a primary mantle gas and a crustal gas component (note that mixing lines are not sufficiently defined by data points to quantitatively calculate mixing relations)

Raw helium isotopic ratios (R) were normalised with the $^3He/^4He$ isotopic ratio of the atmosphere (R_a). R/R_a values of Kibiro helium are very low (R/Ra = 0.2) which indicates nearly pure radiogenic He (crustal He, i.e. no volcanic heat source).

Rwimi spring is located at the southern end of Kyatwa or Ndale volcanic field and therefore shows a significant mantle He component (nearly 20%; R/Ra = 1.5).

Buranga is situated in a similar tectonic position than Kibiro (near a deep reaching border fault of the western rift) and the gas contains with >30% (R/Ra = 2.8) more mantle He than Rwimi implying a still hot actively degassing magma body below Buranga area.

Reservoir temperatures

The results of geothermometry are presented in Figure 5.13. Fast equilibrating SiO_2 geothermometer (Quartz) gives lowest temperatures (around 120°C) which reflect the thermal conditions of the local reservoir at Buranga. The other geothermometers (except K/Mg) are slow equilibrating geothermometers and give temperatures between 160 and 210°C (see also Fig.5.3b for combined Na/K and K/Mg). It seems most likely that those higher temperatures are meaningful because the results are in agreement despite of different boundary conditions which have to be met for applying the solute, gas and isotopic geothermometers. At least temperatures of 160°C may reflect the hotter thermal conditions of an upflow zone in some distance to Buranga.

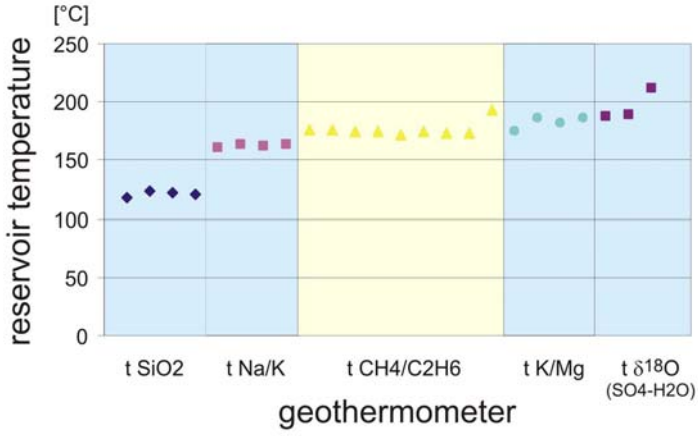

Figure 5.13: Compilation of solute, gas and isotopic geothermometers applied at Buranga using data of appendix A4 and A6 (data of isotope geothermometer are taken from IAEA 2003)

Conclusions from geochemical investigations

From geochemical and isotope geochemical investigations of rocks, fluids and gases it can be concluded that

1) fossil travertine of Buranga has also a thermogene origin and was formed under the same high temperatures than today in contrast to Kibiro where the fossil travertine gave indications of a meteogene origin
2) faults in Buranga area are major paths for fluid flow (precipitation of gypsum in fault breccia of exposed fault near Kibuku; in Bwamba fault precipitation of calcium carbonate was found in drill hole No.1 which penetrated the fault breccia in 172-173m depth; McConnell & Brown 1954)
3) Buranga fluids do not derive from basinal brines but have a similar source of salinity like the other more dilute fluids around Rwenzori mountains (possible genetic relationship)
4) mixed and CO_2 rich Buranga fluids are typical for an outflow zone but are closer to an upflow zone than the other analysed Rwenzori fluids (Fig. 5.14)
5) the recharge area of Buranga is in the high Rwenzori mountains (as formerly proposed) and could furthermore be precisely located (river Mubuku is fed by melt water of the glaciers)
6) an actively degassing magmatic body exists below the subsurface of Buranga which could be excluded for Kibiro
7) reservoir temperatures calculated with different geothermometers may reflect local thermal conditions at Buranga as well as higher temperature conditions (around 160°C) of a proposed upflow zone in some distance south of Buranga.

8) in the area of the upflow zone it would be possible to produce electricity via binary technology additional to the direct use suggested by Isabirye (2000).

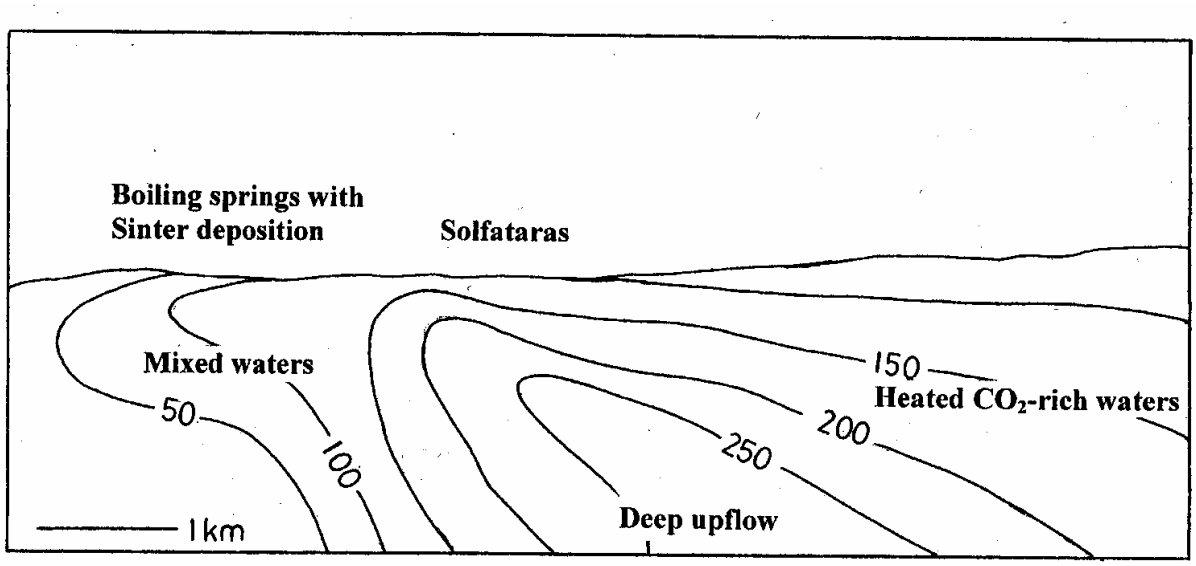

Figure 5.14: Typical temperature field (°C) of hydrothermal systems (evidence from Yellowstone, USA and North Island, New Zealand; after Henley 1996)

Figure 5.14 illustrates the hypothetical N-S cross section which could reflect the conditions in the subsurface in Buranga area. Please note that the fluids of Buranga upflow zone are not ascending to the surface (most likely due to sealing of the Bwamba fault with carbonates at a shallow level caused by pressure drop induced CO_2 degassing). Additionally, Buranga fluids are not manifesting in solfataras and the maximum upflow temperatures are most likely not exceeding 200°C. The localisation of the actively degassing magma intrusion and the related geothermal system is discussed in the following chapter.

5.3 Geophysical results

At the Buranga geothermal prospect, the terrain conditions for ground geophysical measurements are difficult in the eastern and western part that are hardly or even impossibly accessible. Due to these terrain conditions the resistivity and gravity measurements of the ground geophysical survey in February/March 2005 could only be carried out in a small zone in the rift along the Rwenzori Massif and on the pass to Fort Portal in the mountains (Fig. 4.3.1). A detailed overview of the applied methods during this field survey and the results are reported in Stadtler & Kraml (2005). In this final report the main findings about the geophysical results (resistivity and gravity) at Buranga are summarized.

The huge amount of registered local earthquakes was used to apply the seismological tomography.

5.3.1 Resistivity distribution at Buranga

The Schlumberger soundings, dipole/dipole-mapping and TEM soundings together with the inversion model results are shown in Appendix B.3. In Figure 5.3.1 the resistivity models of the three methods were projected on a profile and the models merged into a vertical resistivity section.

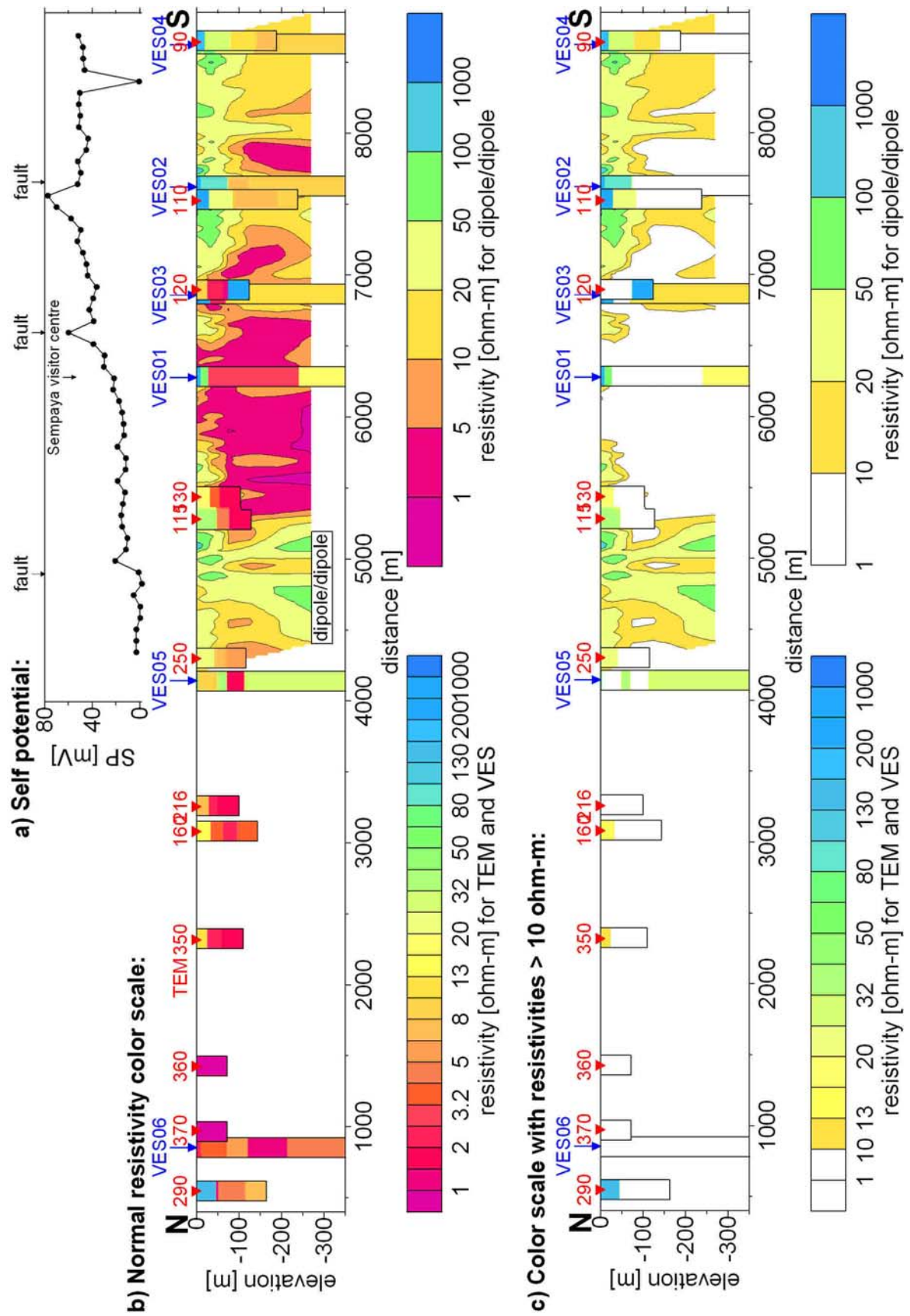

Figure 5.3.1: Resistivity distribution at Buranga. a) Self potential measurements with marked positions of transverse faults of the Rwenzori Massif. b) Resistivity models of dipole/dipole-mapping, Schlumberger and TEM soundings with normal colour scale. c) Models with colour scale for resistivities > 10 Ωm.

The resistivity methods resulted in a consistent model showing the resistivity along the Bwamba fault. Generally the resistivities in the upper 10 metres are moderate to high with values of more than 50 Ωm which is visible in the resistivity models of the Schlumberger soundings (Fig. 5.3.1b) and of the test-dipole-mapping with 10 m dipole length (Appendix B.2). The upper resistive layer is not resolved in the resistivity models of the dipole-mapping with a dipole length of 100 m due to the long dipole length and also not with TEM due to the lack of resolvability of shallow depths down to 20-30 m. The resistive layer probably reflects the water-unsaturated depositions of detritus from the Rwenzori Massif.

In the 2-d resistivity model of the dipole/dipole-mapping, two of the transverse faults of the Rwenzori Massif are reflected by the highest resistivity values of the 2-d model (> 50 Ωm) (Fig. 5.3.1b). These relatively high resistivities are visible at the northern and southern fault in the uppermost 100 m that are probably caused by deposition of detritus from the mountains that have formed alluvial fans on the rift floor in front of the faults.

The transverse faults of the Rwenzori Massif correlate with anomalies in the self potential field, which was measured along the profile of the dipole-mapping (Fig. 5.3.1a). The anomalies are small and two of them are only proven by one measuring point. This could rather be attributed to local causations in the ground at the location of the potential electrode (e.g. strong soil humidity, vegetation) than to fluid flow in the faults. In principle, the self potential field increase towards north.

With depth the resistivities along the profile (Fig. 5.3.1) decrease generally to low values predominantly below 20 Ωm, partly below 1 Ωm. In the vicinity of the Sempaya Visitor Centre and the hot springs, respectively, a high conductive anomaly was located which extends over about 2.5 km in north-south direction in the rift along the escarpment of the Rwenzori. Probably, the anomaly is mainly caused by thermal water which has infiltrated the rift sediments. This can be deduced from borehole No.3 which still produces small amounts of hot water of 62°C. The outflow is continuously but varies with rainfall which indicates that the thermal water is diluted with meteoric water.

The resistivity of the Precambrian basement of the Rwenzori Massif was determined by Schlumberger sounding VES07 (B07 in Appendix B.1) on the pass to Fort Portal in the mountains that confirmed the expectations that the basement is resistive. The resistivity soundings in the rift in the southern part of the profile (south of distance 6000 m, Fig. 5.3.1b) are located only a few 10^{th} of metres apart from the dipping basement. But only TEM sounding 120 shows a pronounced resistivity contrast in about 80 m depth which reflects the dipping resistive basement. There, the Schlumberger soundings, whose array were laid out parallel to the dipping basement, show an increase of the apparent resistivities from less than 5 Ωm to about 10 Ωm in depth which could be indications for the resistive basement. This was shown by theoretical calculations of Mundry (1979) and Keller & Frischknecht (1966) for soundings in distance to a dipping basement of infinite resistivity with the array oriented parallel to the strike. Due to the array layout, the apparent resistivities theoretically converge only to the threefold resistivity value of the low resistivities in the rift (Stadtler & Kraml, 2005). Another explanation why no high apparent resistivities in depth were encountered by the TEM and Schlumberger soundings (except TEM 120) that were measured close to the dipping basement, could be that the basement is weathered or infiltrated by thermal water through faults and fractures which lowers the bulk resistivity of the Precambrian basement.

Indications for infiltration of thermal water in rift sediments and basement could be found by the comparison between Schlumberger sounding VES01, measured in 2005, and two Schlumberger soundings S1 and S2, measured in 1973 (Maasha, 1975a). The three soundings were conducted parallel to the Bwamba fault between this fault and the hot spring group Mumbuga, sounding S1 approximately 180 m west of sounding VES01, which is located on the road to Bundibugyo at the Sempaya visitor centre, sounding S2 35 m west of VES01. The soundings S1 and S2 clearly revealed a high resistive basement which dips west at the Bwamba fault (Fig. 5.3.2). The characteristic of sounding VES01 is contradictory to S2 that

cannot be explained by the distance between the soundings. The high resistive upper part of the model of VES01 could be explained by the higher elevation and the deposition of detritus from the mountains, which is water-unsaturated and has formed alluvial fans on the rift floor that was confirmed by test-dipole-mapping at the Sempaya visitor centre. But the discrepancies in depth this could only be explained by either incorrectness of the data or by infiltration of thermal water that proceeded in the last 30 years which considerably decreased the bulk resistivity of the sediments close to the Bwamba fault or even the basement rocks.

The TEM and Schlumberger soundings in the northern part of the survey area (Fig. 5.3.1b, distance up to 3500 m) revealed that the resistivities in depth are similar or even lower than the values encountered at the conductive anomaly in the vicinity of the hot springs. The soundings are located in the flooding plain of the river Semliki which has deposited fluvial deposits consisting of fat, black clay. These deposits are infiltrated by mineralized water that is chemically identical to thermal water of the Buranga hot springs. Obviously, the thermal water of the hot springs is infiltrating the rift sediments north of the springs, following the general hydraulic gradient in the rift towards north.

In Figure 5.3.1c the colour scale of the resistivities is amended by deleting colours and contours of resistivities that are below 10 Ωm. This visualises that most of the encountered resistivities in the subsurface of Buranga are low, not only in the geothermally active area close to the Buranga hot springs but also in the geothermally non-active area in the northern part of the survey area. These almost everywhere detected low resistivities in the subsurface result in difficulties in the interpretation of the data and in a reduction of the depth of investigations of the applied resistivity methods.

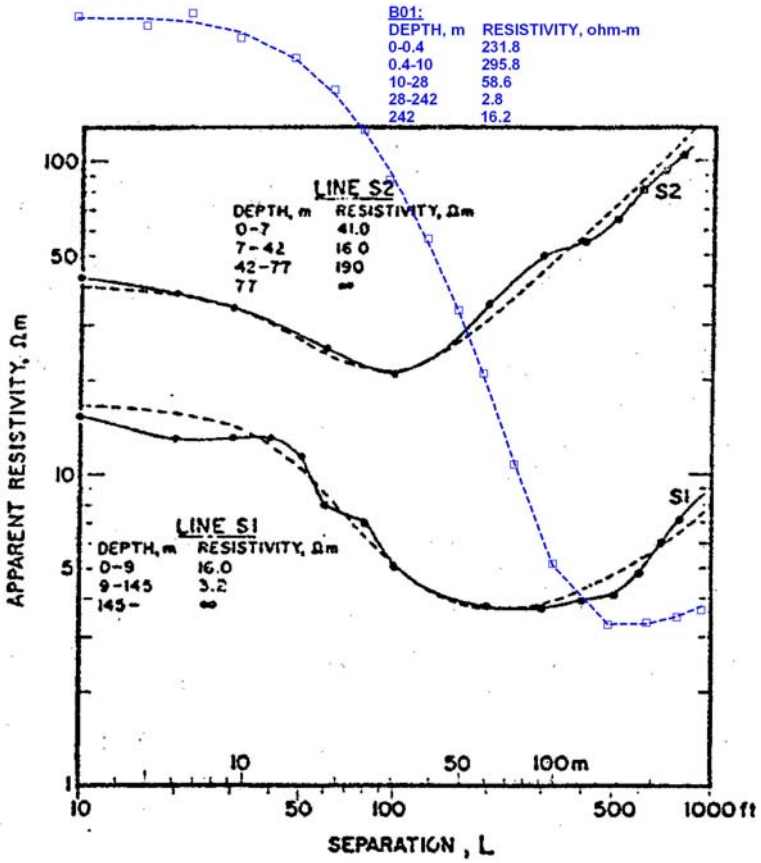

Figure 5.3.2: 3 Schlumberger soundings measured between Bwamba fault and hot springs Mumbuga. S1 and S2 were measured in the year 1973, B01 (VES01) in 2005. Distance from VES01 (which is located on the road to Bundibugyo) to S1 is approximately 180 m west, from VES01 to S2 35 m west. The data points are measured apparent resistivities, the dashed lines represent the theoretical fit to the model shown in the corresponding table (modified after Maasha, 1975a)

5.3.2 Gravity field of the Buranga area

The measured Bouguer gravity field at Buranga (Fig. 5.3.3a) is dominated by a strong regional trend which strikes approximately 30° NNE in accordance to the strike of the Bwamba fault. The gravity values decreases from -144 mGal on the pass to Fort Portal to -182 mGal in the northern part of the survey area. The trend is caused by the density contrast between the dipping Precambrian basement at the Bwamba fault and the rift sediments. The measured gravity data in the rift mainly reflect the distance to the basement. Short wavelength anomalies of interest are covered by the dominating regional trend.

The regional trend was approximated by a first order trend surface calculated by least squares fitting of the grid values (Fig. 5.3.3b) and removed from the Bouguer gravity data to reduce the influence of the dipping Precambrian basement. However, this residual gravity field (Fig. 5.3.3c) generally still decrease with distance from the basement, but short wavelength anomalies get visible.

From this residual gravity field of the profiles P01, P02 and P04, an additional 2nd order polynomial was removed (Fig. 5.3.4) to more emphasise short wavelength anomalies. A pronounced short wavelength, negative anomaly on profile P01 which is also reflected by a low in the topography (distance 5300 m), coincides with a transverse fault of the Rwenzori Massif south of the Sempaya visitor centre. This negative anomaly, which seems to extend towards NNW, is also reflected in the gravity field of the profiles P02 and P04 (blue, dashed line in Fig. 5.3.4). Although on P04, the anomaly is just indicated by a few data points, due to a gap of data coverage between the hot spring groups Mumbuga and Nyansimbe pool as a result of the swampy ground there.

The transverse fault of the Rwenzori Massif, north of Sempaya, is represented by a positive gravity anomaly and by a high in the topography (distance 3200 m of P01) which both are probably caused by deposition of a large alluvial fan of higher density. With distance to the Massif (P02), no indications for the fan are found in the gravity field, since the course of the profile follows the western periphery of the alluvial fan. A similar characteristic of gravity and topography is visible at distance 1900 m of P01 where a transverse fault could be located. The most southern transverse fault (distance 6600 m) is reflected by a high in the topography but not in the gravity field. The alluvial fans in front of the transverse faults of the Rwenzori Massif are also visible in a change of vegetation in the topographic map (Fig. 3.3.1). In the northern part of P02 the gravity decrease continuously which could be an indication for an increase of the thickness of the rift sediments. This would be in accordance with the investigations of Upcott et al. (1996) (Chap. 2.1, Fig. 2.4) that the thickness of the rift sediments increases toward Lake Albert, although these investigations omitted the rift west of the Rwenzori Massif.

The gravity profile P03 (Fig. 4.3.1) on the pass to Fort Portal were measured roughly perpendicular to the strike of the Rwenzori which provided the possibility to estimate the influence of the dipping angle of the Bwamba fault on the gravity field. The modelling is reported in detail in Stadtler & Kraml (2005). The modelling showed that the strong decrease of the gravity field towards the rift could be explained by arbitrary dip angles of the Bwamba fault between 30 and 90°. A high dip angle together with a high density of the rift sediments explains the gravity field nearly as well as a shallow dip angle together with a low density of the rift sediments. For a more significant modelling the profile had to be extended into the rift and additional information (e.g. density of rift sediments) is needed to constrain the density model.

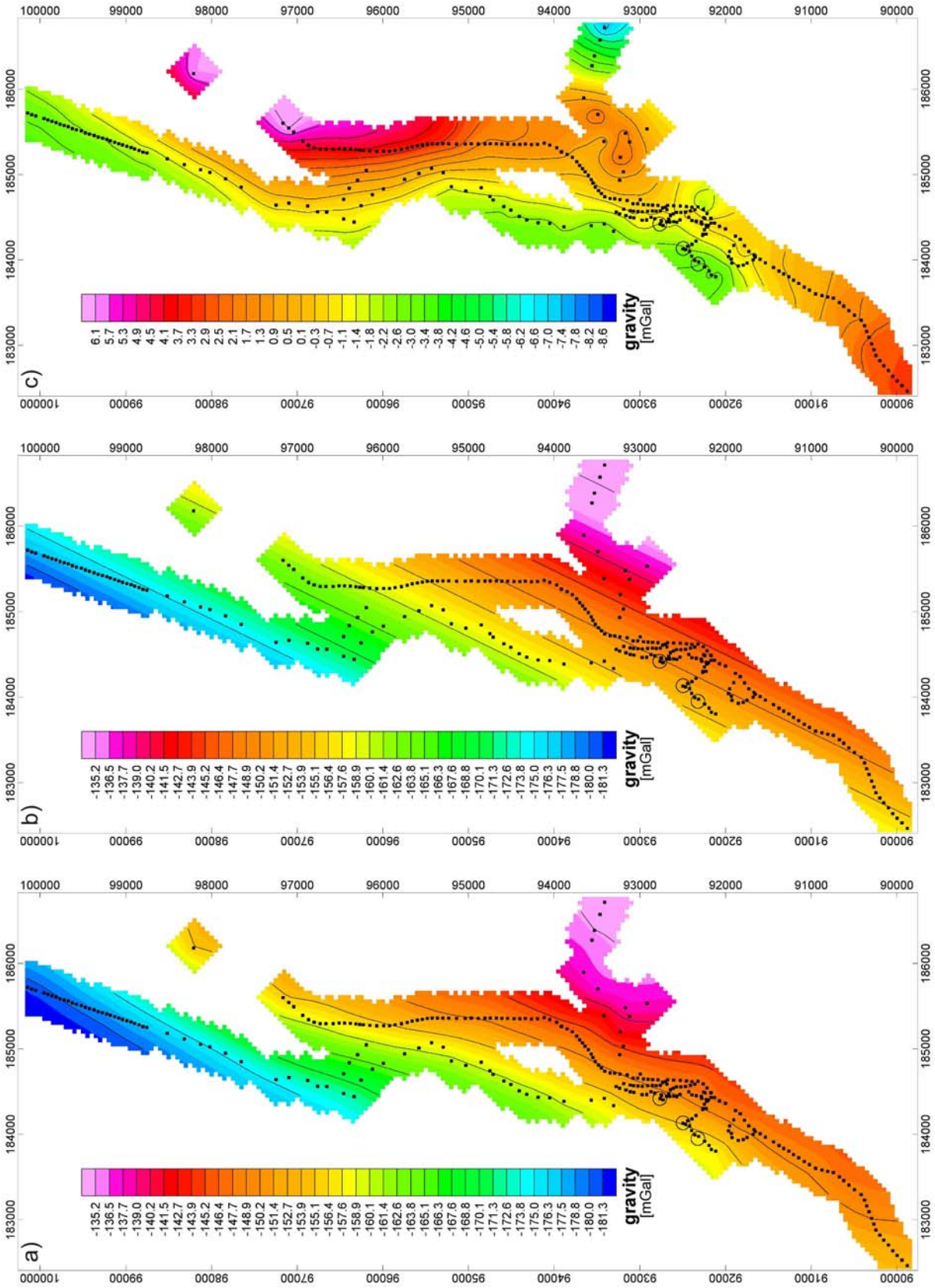

Figure 5.3.3: a) Measured Bouguer gravity field of Buranga with a reduction density of 2.67 g/cm³; dot: gravity station, circle: main group of hot springs, contour interval: 5 mGal, b) regional trend approximated by a first order trend surface, c) residual gravity field after removing of the regional trend; contour interval: 0.8 mGal

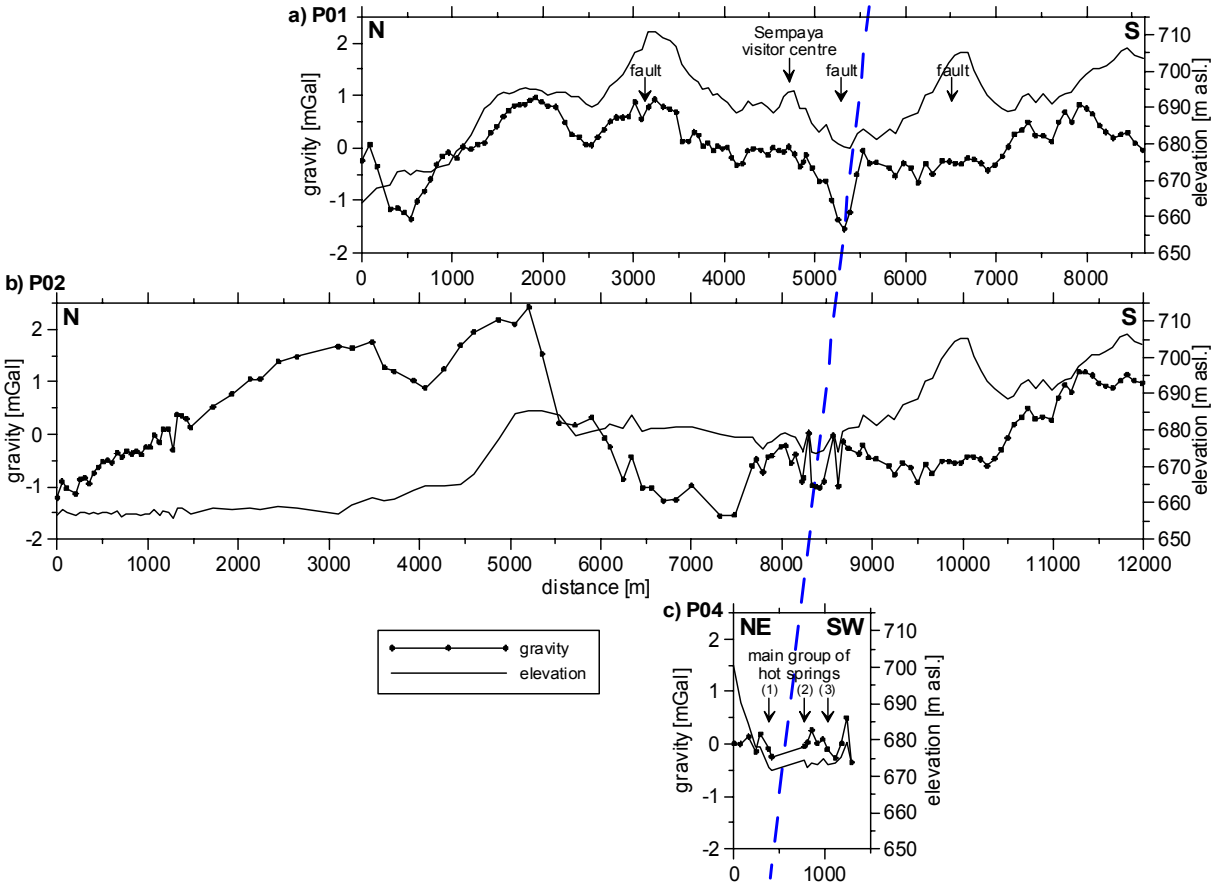

Figure 5.3.4: Elevation and residual gravity field (after removing of a 2nd order polynomial) of the gravity profiles P01, P02 and P04. a) Profile P01 on the road to Bundibugyo with locations of transverse faults of the Rwenzori Massif. b) Profile P02 aside of the road to Bundibugyo (the southern parts of P01 and P02 are identical). c) Profile P04 on the line where the main group of hot springs are situated: (1) Mumbuga, (2) Nyansimbe pool, (3) Kagoro. The blue, dashed line marks the location a negative gravity anomaly that is visible in all profiles.

5.3.3 Earthquake localization and travel-time tomography

Figure 5.3.5 shows the location of earthquakes that have been recorded in March 2006. The active stations are marked as black triangles. The majority of events had a focal depth between 10 and 30 km; some exhibited less and few greater depths. Interestingly, no earthquakes are located within the northern part of the Rwenzori block; all of the events are outside of the marginal faults (Bwamba (west) and Ruimi-Wasa (east) faults (indicated as black solid lines in Fig. 4.3.2 and 5.3.5). The surface locations of faults were obtained from existing Geological Maps (GSU, 1962).

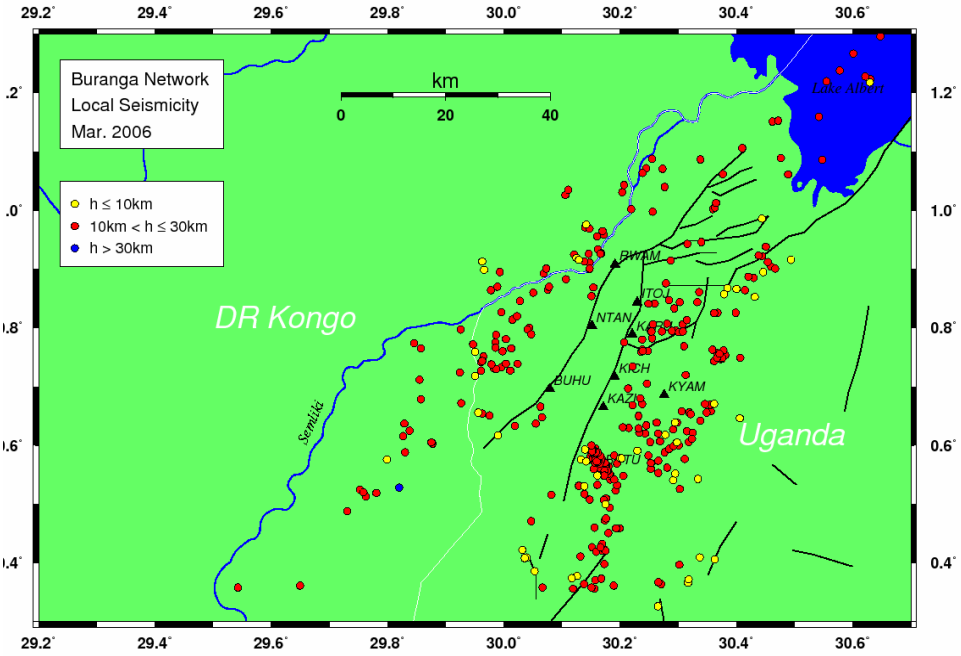

Figure 5.3.5: Location of local earthquakes in March 2006. Operating stations are marked as triangles. Different colours of epicentres indicate different focal depths.

A very similar distribution of epicenters found for the previous month February 2006 is shown in the upper left part of Figure 5.3.6. The upper right and lower left sections present vertical sections of the focal depths. These sections reveal the principal focal depths from 10 to 30 km mentioned before.

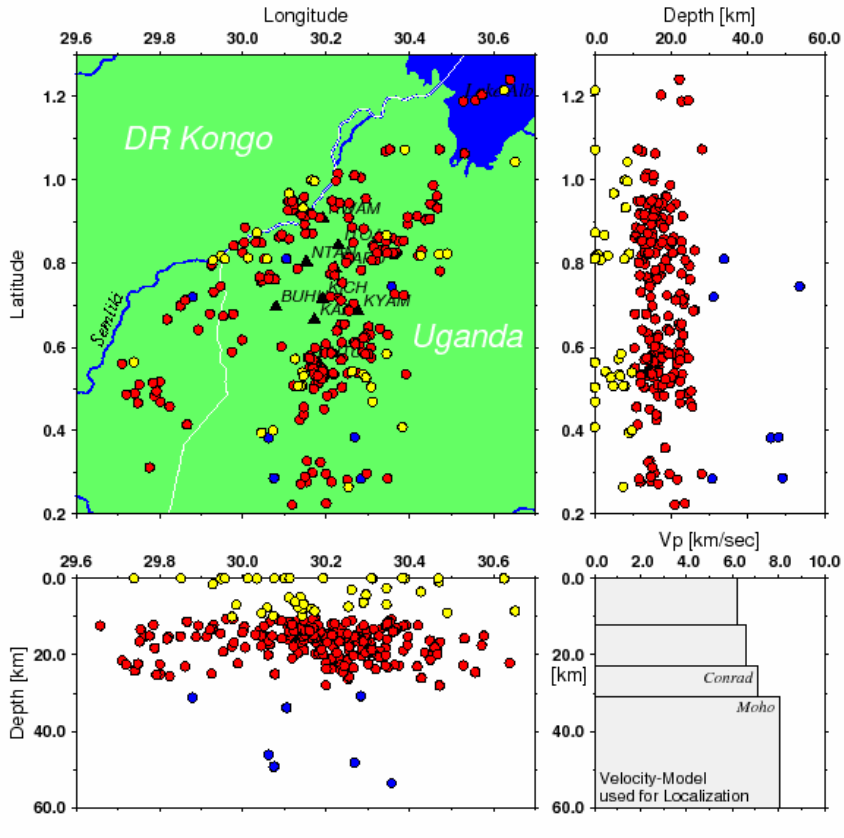

Figure 5.3.6: The distribution of local earthquakes in Feb. 2006 is shown in upper left map. The vertical sections (upper right and lower left) present a projection of focal depths.

The temporal distribution of the seismic activity for the time span considered is given in Figure 5.3.7. Within this period of two months a total number of 760 local earthquakes had been recorded which gives an average activity of 13 events per day. But from the histogram it can easily be seen that the activity rate is not more or less constant. There are days without any event as well as a day (24th March) with 55 earthquakes. Interestingly, these many events are clustered in time and space. These earthquakes are located close to the station BUTU (Fig. 5.3.5 and 5.3.6) and occurred in a swarm-like activity. This behaviour was observed there not only once but all over the recording period. Moreover, this area abounded with the strongest events in that period (two M=4.8 events). These aspects may be used to discuss the possible nature and origin of the seismic activity with respect to their tectonic or magmatic origin (Maasha, 1975b).

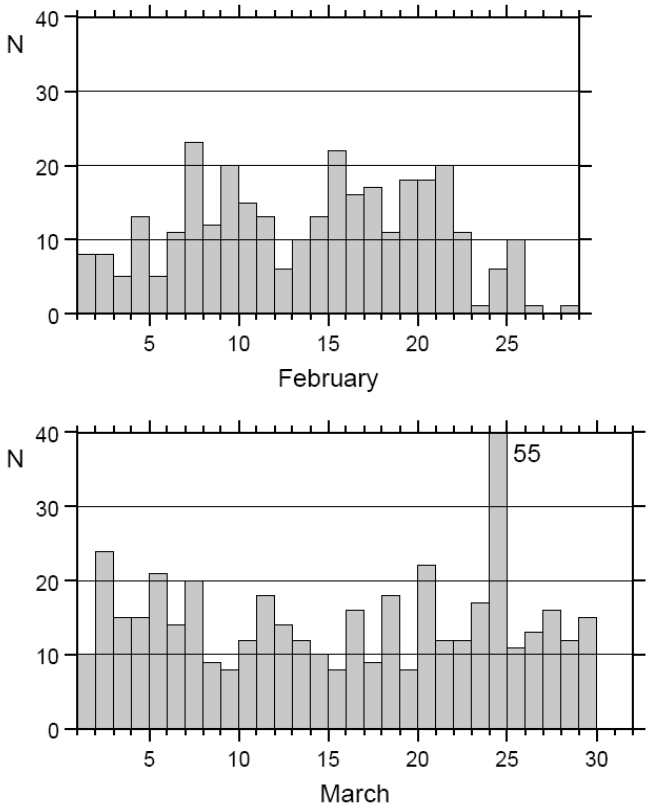

Figure 5.3.7: Chronological histograms of 760 located earthquakes in February and March 2006. Average activity is 13 events per day, but the activity is often clustered in space and time and earthquakes occur as swarm.

This is true for the latter events but the majority of earthquakes are believed to be of tectonic origin because of their spatial distribution and their waveforms. A classification could be done using a frequency magnitude relation (e.g. Mogi, 1967).

It is a common observation by the residents of this district that the greatest numbers of earthquake are felt during the rainy season (Maasha, 1975b).

The project data from northern Rwenzori can support this observation of seasonal variations in seismicity. A data statistics is only provided for February and March 2006; a very similar results would have been achieved for the whole time span.

The times of operation for each station of the Buranga network in 2006 are given in Figure 5.3.8.

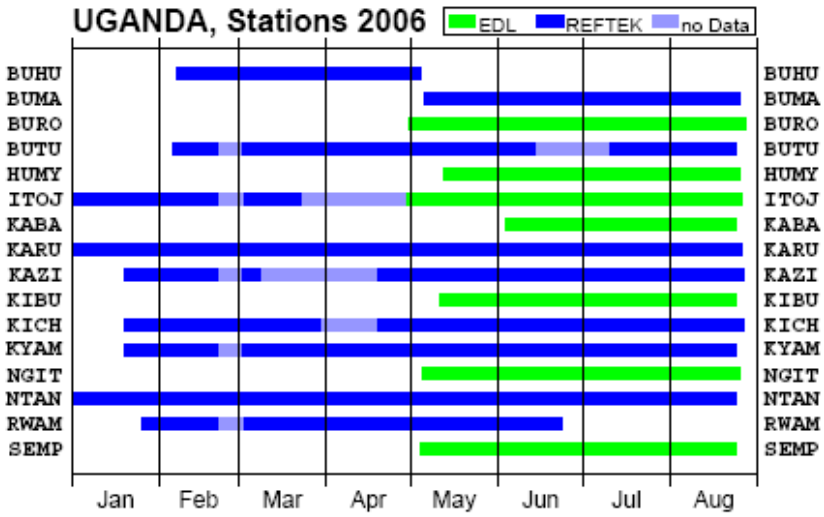

Figure 5.3.8: Times of operation for stations of the Buranga network during 2006.

The Reftek (Reftek format) and EDL (mini-seed format) data was converted into the SEISAN data format which can be used by the standard SEISAN program for earthquake analysis and event localization (the software is available free of charge at the University of Bergen, Earth Science department, http://www.geo.uib.no/seismo/-software/software.html).

The Reftek triggered data are used as a basis to identify suitable events for further analysis and to select time windows from the EDL continuous data stream. Before standard event-localization routines can be applied, the picking of P and S wave arrival times is a necessary and time consuming step. For most events, both, local P- and S-wave arrival times were determined.

In total, 49721 phase readings (P- and S-wave arrival times), corresponding to 4185 events, were determined. On average, more than 500 events per month were included in the analysis.

Preliminary localization of hypocenters

The program HYPOCENTER (Lienert et al., 1986; Lienert & Havskov, 1995), as part of the Seisan package, is used for hypocenter localization. The 1-D velocity model used for the initial determination of hypocenters is given in Table 5.1. P-velocities that are slightly faster than those of the IASPEI standard earth model (Kennett, 1991) are used. A constant P/S-velocity ratio of 1.74 is assumed. Tests reveal that moderate changes of the initial velocity model do not have significant effects of the results of the 3-D tomographic velocity inversion described below.

Table 5.1: Velocity model used for the initial determination of hypocenters

Depth (km)	Vp (km/s)	Vs (km/s)
0.0	6.2	3.6
12.0	6.6	3.8
23.0	7.1	4.1
31.0	8.05	4.63
50.0	8.25	4.71
80.0	8.5	4.9

While the 1-D velocity model gives a first impression of the location of hypocenters, it certainly represents the true velocity variations insufficiently. Seismic event locations based on regional 1-D velocity-depth sections can have bias errors caused by travel-time variations within different tectonic provinces and due to ray-paths crossing boundaries between tectonic provinces with different crustal and upper mantle velocity structures. The Rwenzori mountain range is characterized by gneisses of relatively high velocity, whereas the neighbouring regions to the

North and West are characterized by slower velocities due to sedimentary layers in the rift (Schlüter, 2006).

A velocity model with relatively high values of P-wave velocity (6.2 km/s) close to the surface was used for the localization of hypocenters. While this 1-D model probably represents a valid approximation for the eastern section of the region of interest, the velocities in the western section are likely overestimated. It is noted here, that a highly improved localization of the seismic events as well as a 3-D velocity model will result from the application of the tomographic inversion.

Figure 5.3.9 shows locations of earthquakes that have been recorded during the operation of the network. The stations are marked as triangles. The majority of events exhibit a focal depth between 10 and 30 km; the deepest events occur at depths of about 55 km.

For most events, the error of localizations is in the order of about 2-3 km. 80% of all hypocenters exhibit localization errors that are smaller than 5 km. The source-time error for most events is smaller than 0.4 sec. About 80 % of events exhibit a source time error smaller than 0.8 sec.

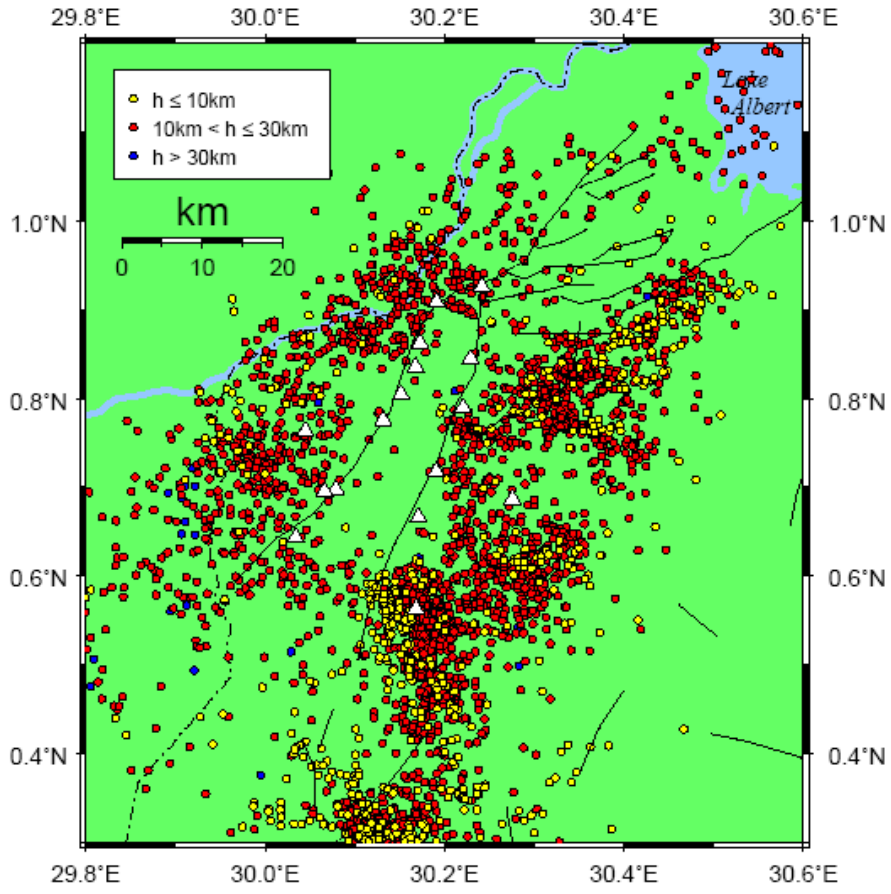

Figure 5.3.9: Results of the preliminary determination of hypocenters (4185) based on the 1-D velocity model given in Table 5.1. Stations are marked by triangles. Different colours of epicenters indicate different focal depths. Black solid lines indicate locations of surface faults.

Comparison with mapped near-surface faults

Obviously, few earthquakes occur within the northern part of the Rwenzori block; most events occur outside of the surface expressions of the main marginal faults, the Bwamba fault (west) and the Ruimi-Wasa fault (east), as indicated by the black solid lines in Figure 5.3.9 and 5.3.10.

Events lining the flanks of the Rwenzori range are connected by earthquakes along an east-west trending line near 0.6N, thus separating the northern and southern blocks of the Rwen-

zori range. This is in agreement with observations by Maasha (1975b). Further to the south, most earthquakes are located to the east of the mountains.

From Figure 5.3.9, there is no obvious strong correlation between the surface expressions of known faults and epicentre locations. The events seem to be arranged in clustered form and relatively diffuse rather than along linear structures. In part this may be due to the relatively large error ($\approx \pm 3$ km) in locating events which occur outside of the array of stations. However, before a more detailed analysis of hypocenters can take place we first continue with the tomographic inversion of the travel-time residuals and the derivation of a 3-D velocity model.

Active-faults and traveltime tomography

A tomographic inversion of the travel-time data was performed to determine the three-dimensional (3-D) structure of the P-and S-wave velocity of the crust beneath the network of stations. The method of travel-time inversion for local earthquakes used here is based on recent developments by Koulakov & Sobolev (2006) and Yakovlev et al. (2007).

The initial velocity model for the tomographic inversion is the same as the 1-D velocity model used for the preliminary localization of hypocenters (Table 5.1). A total number of 2051 events were included in the inversion. This is about half of the total number of events (4185) recorded and identified during the operation of the network. The reduction results in part from the requirement that only those events are used for the inversion for which at least 8 phase readings were determined. This means that each event was recorded by at least 4 stations if both, P and S-wave arrival times were identified. The inversion includes 28644 rays (14445 P-rays and 14199 S-rays) resulting in an average number of about 14 phase readings per event. A further requirement is that the distance between the epicentre and the centre of the array should be less than about 110 km. This is to exclude distant events for which the localization error is relatively large.

In the course of the tomographic inversion (during each step of the iteration) a 3-D velocity model is derived first. Then, on the basis of the improved velocity model, the earthquake hypocenters are re-calculated. The iteration procedure ends when the difference between the new and the previous results becomes insignificant.

Re-localization of earthquakes

In Figure 5.3.10, we show hypocenters before and after re-localization. One obvious effect of the re-localization is the stronger clustering of events near, for example, station BUTU or northeast of station KYAM. Events to the west of the Rwenzori range have shifted slightly to the west, now following the course of the Semliki river more closely. This may indicate that the river itself follows partly the surface expression of an active fault. After re-localization, there exists an almost aseismic area to the west of stations SEMP, NTAN, KABA - close to the location of the hot springs. Furthermore, shallow and deep events near station BUTU are more consistently separated after re-localization. This indicates that these events correspond to a dipping active fault plane, striking north-south.

(a) initial distribution of events

(b) after tomographic inversion and re-localization

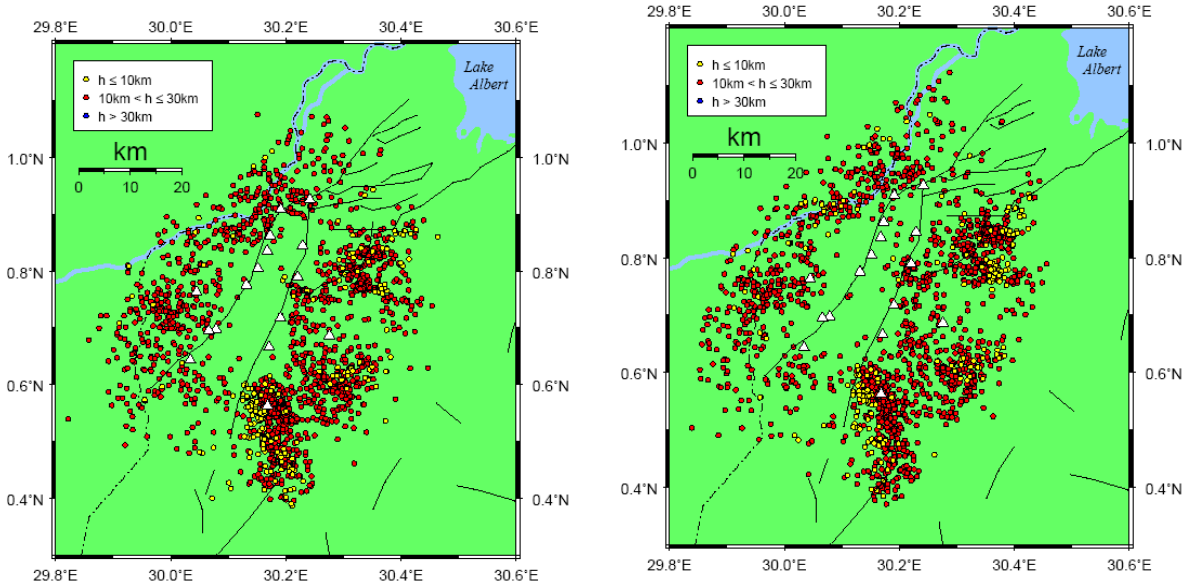

Figure 5.3.10: The re-localization of epicentres (circles) after tomographic inversion. Different colours of epicentres indicate focal depths. Stations are marked by white triangles.

Detailed analysis of the velocity structure

Figure 5.3.11 presents the data subset that was used for the tomographic inversion (same as Fig. 5.3.10). The section does not show the first locations of the hypocenters but the relocation results as described above. The vertical sections help to imaging the dense ray coverage inside the investigation area.

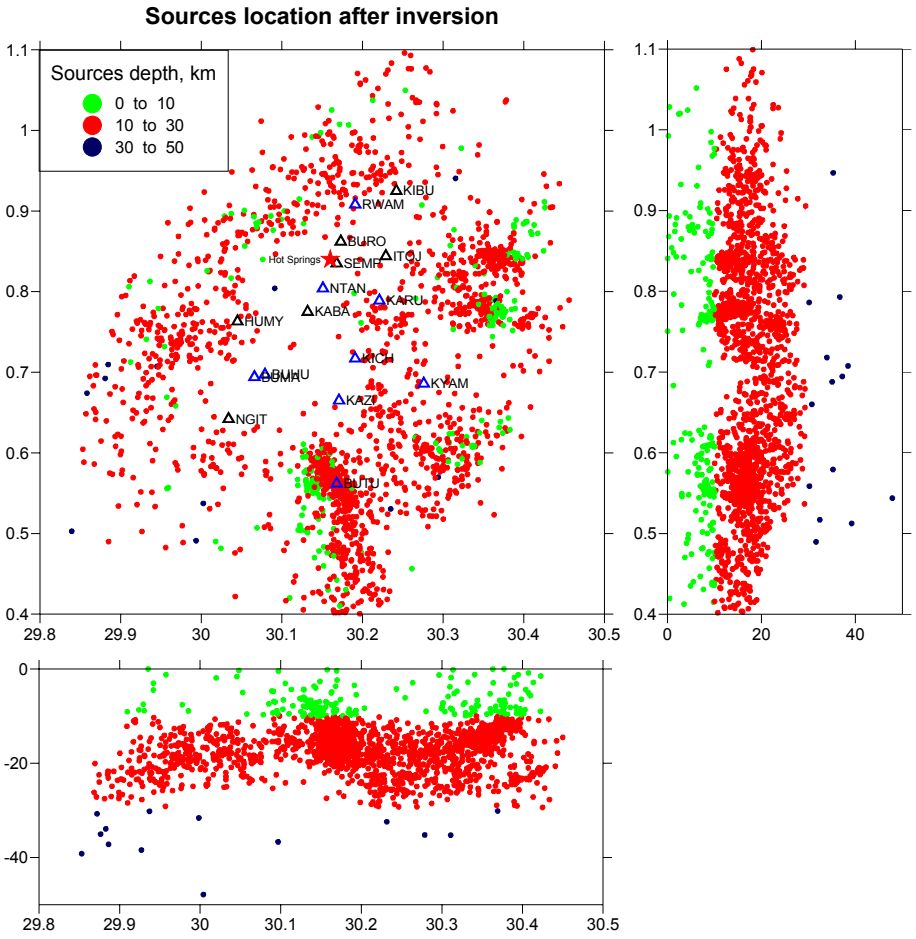

Figure 5.3.11: A data subset of 2051 events was used for this inversion meaning a total number of ca. 28644 P- and S-rays passed the investigated area. Note that the map does not show the initial locations but the hypocenters after inversion.

Generally the P-wave results may be considered more reliable due to larger uncertainties in the determination of S-wave arrival times. Therefore, the P-wave results are basically discussed. The S-wave results can be found in the Rümpker et al. (2007). The tomographic inversion results in refined earthquake locations as well as in 3-D velocity perturbations with respect to the initial 1-D model. Examples for horizontal sections of P-wave velocity anomalies at a depth of 1 to 15 km are given in Figure 5.3.12. Detailed results for additional depths and for P- and S-wave anomalies are given in Rümpker et al. (2007).

At shallow depth (1-3 km) the results show that a large low-velocity anomaly exists in the north-western section of the region under investigation. It is interesting to note that the Buranga hot springs are located at the boundary of this anomaly at the transition between slow and fast regions. The low-velocity anomaly broadens at greater depths (> 5 km). This is similarly seen in the vertical tomographic sections shown in Fig. 5.3.14. The faster velocities to the east of the hot springs are located beneath the northern block of the Rwenzori range.

A smaller, well resolved low-velocity anomaly is found near the eastern station of KARU. The anomalies appear to remain separated down to a depth of about 7.5 km. To the south some additional individual anomalies can be found. They merge to a large, more centrally-located, low-velocity anomaly at a depth of about 10 km.

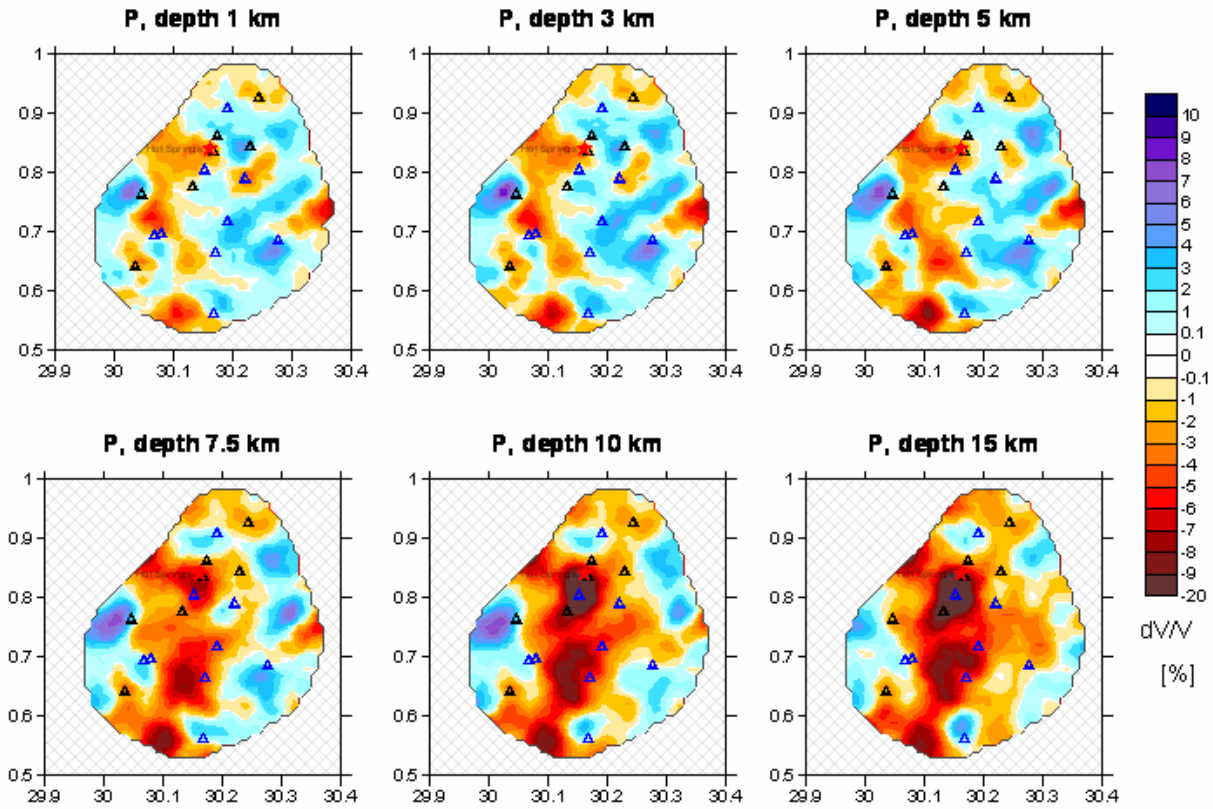

Figure 5.3.12: The anomalies of P-velocities presented in horizontal sections in different depth levels. Velocity anomaly with respect to the initial velocity model (Table 5.1).

In relation to the location of the hot springs there are several interesting observations that can be derived from this survey. The hot springs are located above the boundary between relatively slow and fast regions in the crust at depth range between 0 and 7 km. The low velocity anomaly broadens beneath this depth range and connects with other smaller anomalies to the east and south. Also, the region to the west/south-west of the hot springs is almost aseismic and it coincides with a low velocity anomaly in the crust (Fig. 5.3.9 and Fig. 5.3.10).

Low velocity anomalies are visible at all depths levels. They are relatively strong at shallow depth (1-5 km) and are arranged close to the Bwamba fault, the margin of the Rwenzori Mountains. At shallow depth they are outside of the Rwenzori block. Their position does not coincide with the hot springs; they are not directly beneath them. Two unconnected low velocity anomalies are clearly visible south of the springs of which the northern anomaly seems to have a bigger size.

At greater depth low velocity anomalies are still observable but their position was dislocated towards the centre of the Rwenzori block. The anomalies are as strong as at shallower level. The given statements can also be observed in the vertical section in Figure 5.3.14.

Absolute velocities are difficult to estimate from tomographic inversions, as true maximum amplitudes of the anomalies are usually underestimated. The velocity anomalies in the subsurface could be caused be temperature effects but this effect on P- and S-wave velocities is difficult to derive. After Kern (1978) and Landolt-Börnstein (1982) the velocity reduction may be estimated at about 0.1 km/s per 100°C. In the tomographic inversion given here, a 10 % anomaly corresponds to about 0.7 km/s change in P-wave velocity and 0.4 km/s change in S-wave velocity.

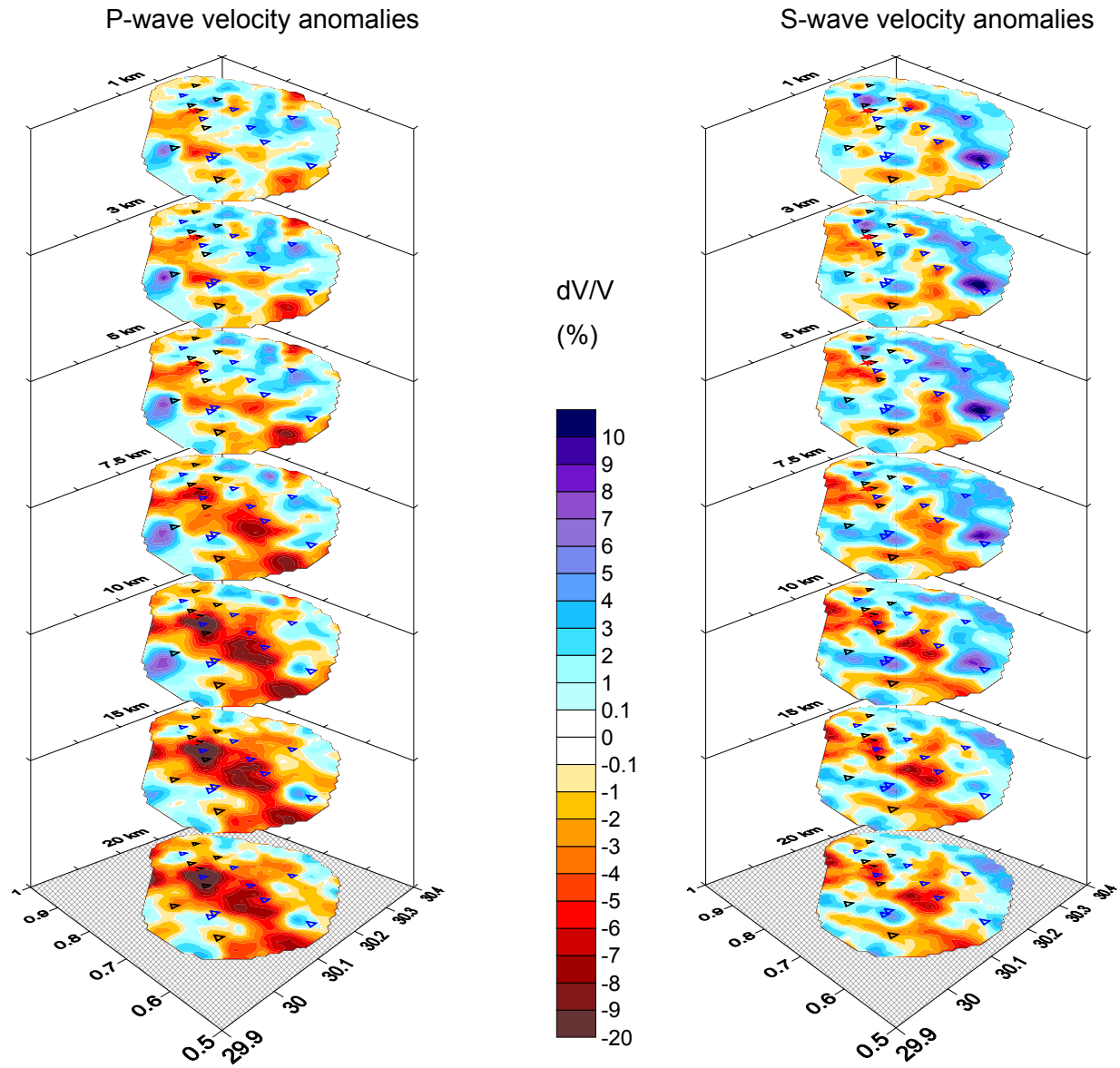

Figure 5.3.13: The anomalies of P- and S-velocities are presented as a quasi 3-D section.

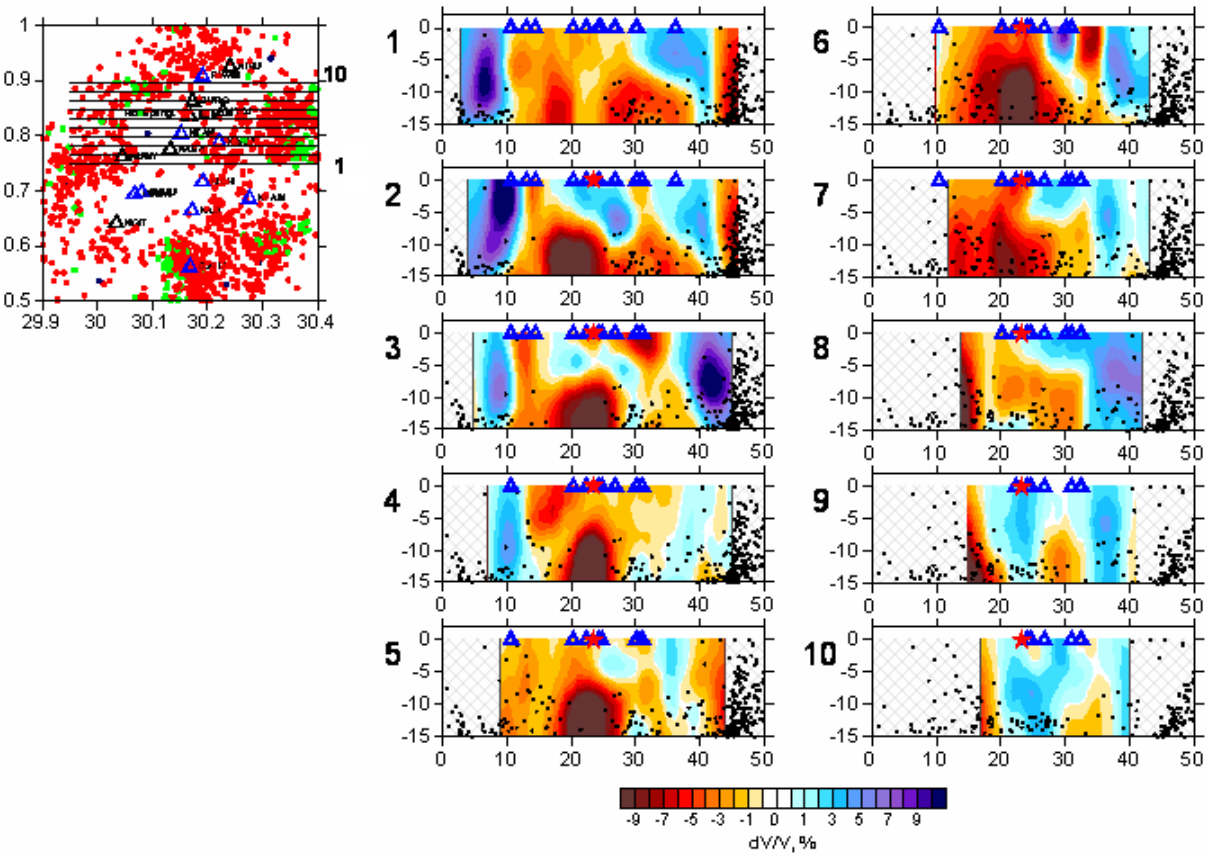

Figure 5.3.14: The anomalies of P-velocities presented in vertical sections. The East-West sections are marked on the map in the upper left corner. The projected position of the hot springs is marked with a star and section 6 closely traverses the position of the springs. Blue triangles indicate seismological stations projected into the vertical plane. Black dots mark neighbouring hypocenter locations projected into the vertical plane.

6. Conclusions and conceptual model

The survey area at the Buranga geothermal prospect is only partly accessible because of the terrain conditions with the steeply dipping escarpment of the Rwenzori Massif and dense tropical rain forest with creeks and swamps. Due to these conditions, the ground geophysical measurements (resistivity and gravity) of the field survey in February/March 2005 were restricted to a small zone along the Rwenzori Massif.

However, the resistivity methods (Schlumberger soundings, dipole/dipole-mapping and TEM soundings) result in a consistent model showing the resistivity along the Bwamba fault. In the vicinity of the hot springs a high conductive anomaly was located which extends over about 2.5 km in north-south direction in the rift along the escarpment of the Rwenzori Massif. The anomaly is probably caused by thermal water which has infiltrated the rift sediments which could be concluded from observations of borehole No.3 that still produces small amounts of hot water of 62°C. Indications for proceeding infiltration of hot water in the local rift sediments at the Buranga hot springs in the last 30 years could be derived by comparison of Schlumberger soundings from 1973 (Maasha, 1975a) and 2005 at the same location (Fig. 5.3.2). Dynamic processes are also indicated by changes in activity and location of the hot springs.

Thermal water has also infiltrated the rift sediments north of the Buranga hot springs in the northern part of the survey area. This observation is supported by the fluid chemistry of a waterhole in Kibuku area. There, the fluvial deposits of the Semliki river, infiltrated by thermal water, cause low resistivities in the subsurface which are similar to those measured in the vicinity of the hot springs. These almost everywhere detected low resistivities in the subsur-

face of the survey area prevent a clear distinction between geothermal active and non-active areas.

The gravity field of the Buranga geothermal prospect is strongly influenced by the density contrast between dipping Precambrian basement and rift sediments. Due to the sparsely gravity data coverage in the survey area, the regional field is only partly observed which restricts field separation to emphasize short wavelength anomalies of interest. Nevertheless, a pronounced negative, short wavelength anomaly was located which coincides with a transverse fault of the Rwenzori Massif south of the Sempaya visitor centre detected by lineament interpretation of satellite data. The anomaly is striking in NNW direction towards the hot springs. The fault direction is in agreement with the direction of the soil temperature anomaly and of a lineament from remote sensing. The negative gravity anomaly could be an indication for a fracture zone of lower density and higher permeability where hot water could rise and infiltrate the rift sediments.

The difficult terrain conditions at Buranga and the resistivity pattern along the Bwamba fault resulted in the decision to focus on seismological measurements and not to support other ground geophysical measurements since seismology seems to be the most promising geophysical method to investigate and assess Buranga under the given boundary conditions.

The seismological results revealed that in the subsurface of the Rwenzori region large, strong velocity anomalies exists which reduce significantly the local travel velocity of seismic waves. Taking into account that isotope geochemical results clearly proved that mantle helium and volcanic CO_2 are released at Buranga hot springs, it could be concluded that the reduction in velocity could be caused by high temperature anomalies. These temperature anomalies could be a result of a hot actively degassing magma intrusion, which may serve as a heat source of the hot springs.

The strongest P-wave velocity anomaly (-9 %) in 10 km depth is located directly south of the Buranga hot springs (Fig. 6.1). The centre of the anomaly is situated below the escarpment of the Bwamba fault. If its dip of about 60°W continues in depth, it can be assumed that the centre of the anomaly lies within the Precambrian basement. The low velocity anomaly coincides with the aseismic region which could be a further indication that the reduction in velocity is caused by temperature effects in the subsurface of this region. High temperatures would not allow rocks to develop stress levels that are high enough to be released as earthquakes (ductile behaviour).

The size of the low velocity anomalies is in the same order as the magmatic intrusives which were interpreted from aeromagnetic data in the subsurface of Lake Albert and Lake Edward (Fig. 2.3). However, it has to be noted that general difficulties exist to separate the effects of temperature-related velocity reductions from those related to changes in rock type, i.e. the sedimentary infill of the rift in shallow depth levels.

Because of the clear indications for an active magmatic intrusion which could serve as heat source for the hydrothermal system in the subsurface of the Buranga geothermal prospect, a magmatic body was included in the conceptual model (Fig. 6.2). The model is integrated in a 3-D satellite image as vertical section along the Bwamba fault. It has to be considered that the section is vertical, although the fault has a dipping angle (60°W at Buranga).

The recharge area for the thermal water, which emanates at the Buranga hot springs, is located in the high Rwenzori region (proven by isotope hydrological investigation). The meteoric water is descending in the subsurface and flowing towards Buranga most likely along the Bwamba fault. The missing tritium in the thermal water of Buranga (IAEA 2003) indicates a long flow path. The higher temperatures in the subsurface of Buranga, caused by the magmatic intrusion, additionally heats up the meteoric water, which is then forced to rise along the Bwamba fault and the identified transverse fault cutting the rift sediments. The thermal water emanates with temperatures of up to 98°C at the Buranga hot springs which are located within the rift sediments. The convectively rising fluid takes only a short way through the sediments in the upper depth level (mainly through fractures) because the source of salinity is mainly water-rock-interaction with basement rocks but not with sediments. Further-

more, it can be concluded that the thermal water has partly infiltrated the rift sediments and formed a local shallow reservoir (detected by resistivity measurements) with maximum temperatures around 120°C as e.g. indicated by the fast equilibrating SiO_2 geothermometer. This water is tapped by borehole No.3 which does not reach the Precambrian basement. The low outflow of the borehole is however mixed with cold surface water (=> reduced temperature of around 60°C and reduced salinity compared to Buranga hot springs) as evidenced by much higher discharge rates in the rainy seasons. The fluids discharging at Buranga hot springs do not show significant seasonal variations in flow rate because the geothermal system is fault controlled and recharged continuously from far distance (small variations in precipitation in high Rwenzori region).

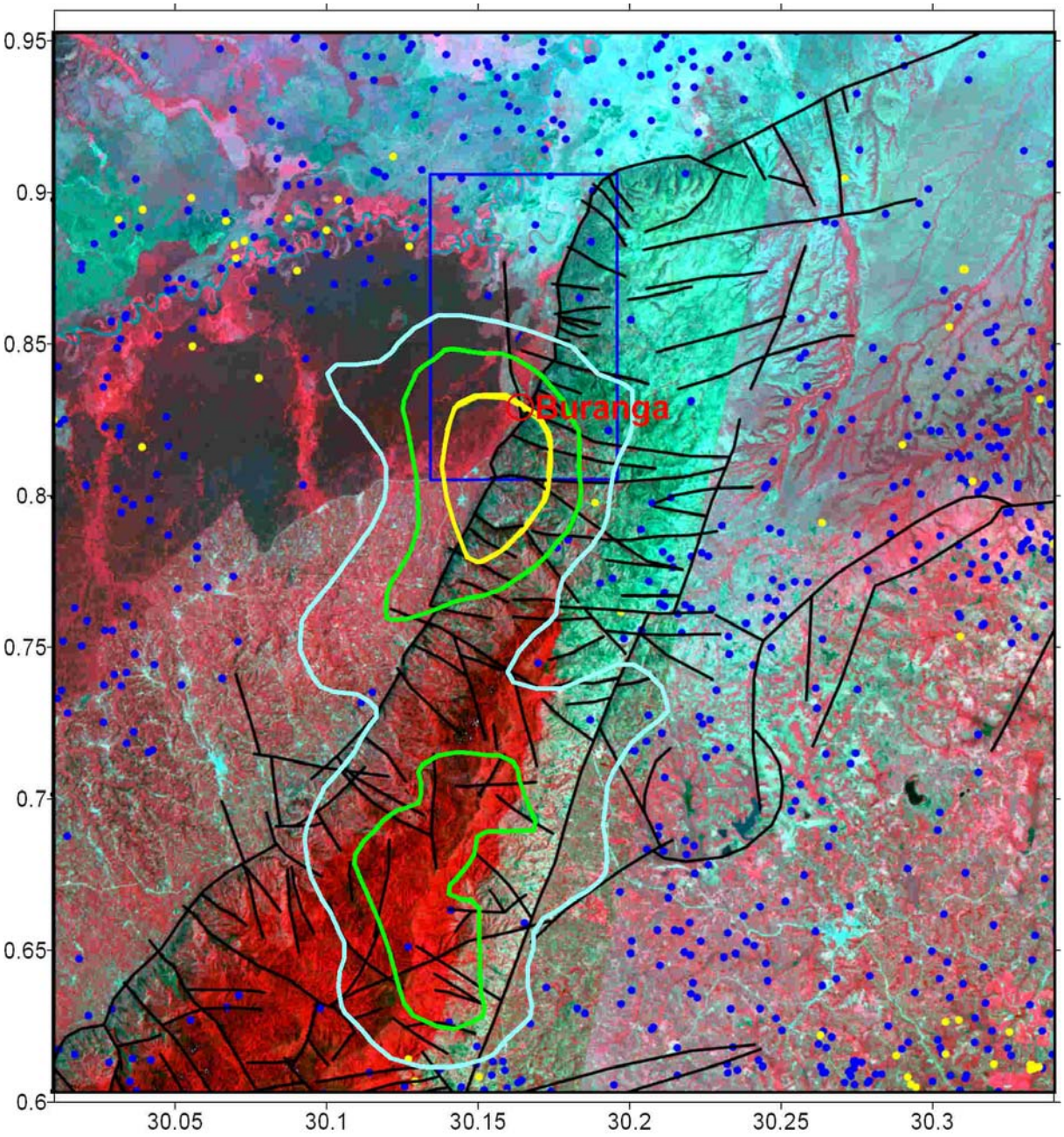

Figure 6.1: Northern part of the ASTER Satellite image of the Rwenzori Massif (Fig. 5.1.1), overlain by the lineament pattern and anomalies of P-velocities in 10 km depth (Fig. 5.3.12) derived from seismic tomography (light-blue: -3 % dV/V, green: -6 %, yellow: -9 %). Blue rectangle marks the area of the geophysical survey (Fig. 4.3.1). Dots represent relocated epicentres; different colours indicate different focal depth (Fig. 5.3.10).

The reservoir temperatures estimated from solute, gas and isotopic geothermometers cover a broad temperature range between about 110-210°C (including published data). Additionally to the local shallow reservoir at Buranga, it could be concluded that higher temperatures in the subsurface south of Buranga (upflow zone) could be expected, probably around 160°C, because of the proven existence of a heat source for the thermal water which emanates at the Buranga hot springs. This temperature would be sufficient for power generation with binary technology at the Buranga geothermal prospect.

The promising project results suggest that the Buranga geothermal prospect is appropriate for further development of a geothermal power plant.

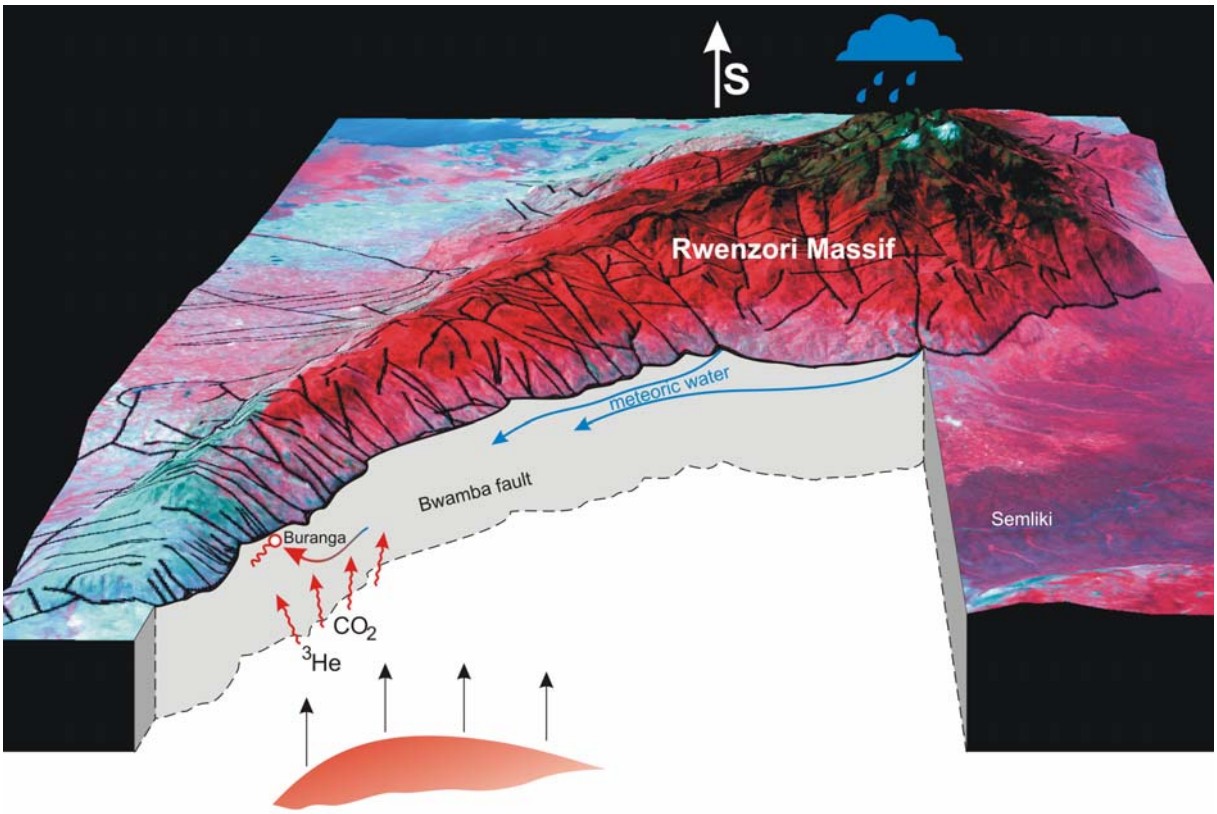

Figure 6.2: A 3-dimensional view of the Rwenzori Massif from space as seen from the North overlain by a lineament pattern and integrated conceptual model (vertical section along the Bwamba fault) of the Buranga geothermal prospect (not to scale).

7. Recommendations

The amount and quality of existing geoscientific data allows a characterisation of the Buranga geothermal system. Therefore there is no need for further extended surface exploration which would not significantly enhance the knowledge of the prospect.

A possible drilling location should be located within the projected zone of major velocity reduction found in all tomographic inversions (yellow contour in Fig. 6.3). In combination with the geochemical results this zone is interpreted as the major heat source in the investigated area.

According to the hydrological results the Bwamba Fault is the major pathway for the geothermal fluids. Therefore the Bwamba Fault is the drilling target. To enhance the chances to encounter zones of highest permeability the drilling location should be at the intersection of Bwamba- and perpendicular faults known from structural interpretation (Fig. 6.3).

To further identify the precise drilling location additional analysis of local structural data (strike and dip of relevant faults) is strongly recommended.

Additional advantage is seen in the fact that the suggested site is outside the Semliki National Park, close to the road and still situated within the area of geophysical survey done in 2005 (Fig. 6.1).

Two concepts are to be considered:

- shallow gradient holes followed by a deep exploration well
- or take a higher risk and drill a deep exploration well right away.

The first concept gives additional information on the dip angle of the Bwamba Fault in depth, possibly the transverse faults, on the geothermal gradient and additional geologic and geochemical information (fluid composition, alteration mineral assemblage zones etc.). This concept reduces the risk but needs more investment and time.

The second concept is also feasible if a somewhat higher risk is accepted.

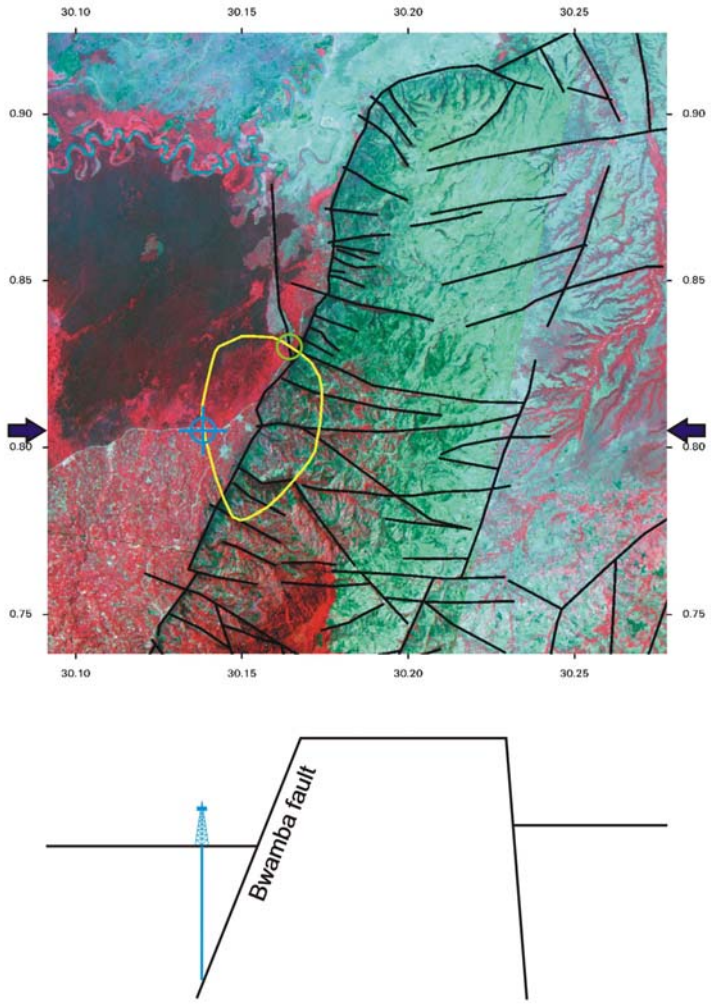

Figure 6.3: Schematic cross section with proposed drilling location (also shown on the satellite image). Bwamba fault would be reached in 2 km depth if dip angle is constantly 60°

References

Aki, K., Christofferson, A. & Huseby, E.S. 1977. Determination of the Three-Dimensional Structure of the Lithosphere. J. Geophys. Res., 82, 277-296

Ármannsson, H. 1994. Geochemical Studies on Three Geothermal Areas in West and Southwest Uganda. Final report. Geothermal Exploration UGA/92/002, UNDEST/GSMD report

Ármannsson, H. 2001. Isotope Hydrology for Exploring Geothermal Resources; End of Mission Report. National Energy Authority of Iceland, IAEA Project UGA/8/003

Árnason, K. 1994. Recommendations for Geophysical Studies on Three Geothermal Areas in West and South-West Uganda. Report under the project Geothermal Exploration UGA/92/002, UNDEST/GSMD

Árnason, K. 2003. Geothermal exploration in the Buranga geothermal field in West Uganda. Island Geosurvey, ISOR, Report

Babirye, G.P. 2003. Moment tensor inversion for the June 29, 2001 earthquake in the western arm of the East African Rift valley. In: Individual Studies by Participants at the International Institute of Seismology and Earthquake Engineering, 39, 125-135

Bahati, G. 1999. Geochemical exploration of the Katwe-Kikorongo, Buranga and Kibiro geothermal areas, Uganda

Bahati, G. 2003. Geothermal energy in Uganda, country update. International Geothermal Conference, Reykjavik, 2003, 48-53

Bahati, G. 2005. Preliminary environmental impact assessment for the development of Katwe and Kibiro geothermal prospects, Uganda. MSc thesis University of Iceland

Bahati, G. & Ármannsson, H. 1995. The chemistry of waters in the Buranga and Kibiro geothermal fields, West Uganda. In: Water-Rock Interaction by Y. K. Kharaka and O.V. Chudaev, A.A.Balkema/Rotterdam/Brookfield/1995

Bahati, G., Pang, Z., Armannsson, H., Isabirye, E.W. & Kato, V. 2005. Hydrology and reservoir characteristics of three geothermal systems in western Uganda. Geothermics, 34, 568-591

Bahati, G. & Tugume, F. 2005. Uganda geothermal energy country update. Proceedings World Geothermal Conference 2005.

Bailey, D.K. & Collier, J.D. 2000. Carbonatite-melilitite association in the Italian collision zone and the Ugandan rifted craton: significant common factors. Mineralogical Magazine, August 2000, 64 (4), 675-682

Barker, D.S. & Nixon, P. H. 1989. Hight-Ca, low-alcali carbonatite volcanism at Fort Portal, Uganda. Contrib Mineral Petrol (1989), 103, 166-177

Bazaale-Dolo As, 1986. Preliminary interpretation of chemical results of thermal discharges of western and northern Uganda. Geothermics, 15, 749-758

Bell, K. & Tilton, G.R. 2001. Nd, Pb and Sr Isotopic Compositions of East African Cabonatites: Evidence for Mantle Mixing and Plume Inhomogeneity. Journal of Petrology, 42 (10), 1927-1945

Bottinga, Y. 1968. Calculation of fractionation factors for carbon and oxygen isotopic exchange in the system calcite-carbon dioxide-water; J. Phys. Chem., 72, 800-808

Brown, J.M. 1953. Report on the Buranga Hot Springs, Toro, Uganda. Geological Survey of Uganda, Report JMB/12

Bühn, B., Rankin, A.H., Radtke, M., Haller, M. & Knöchel, A. 1999. Burbankite, a (Sr, REE, Na, Ca)-carbonate in fluid inclusions from carbonatite-derived fluids: Identification and

characterization using Laser Raman spectroscopy, SEM-EDX, and synchrotron micro-XRF analysis. American Mineralogist, 84, 1117-1125

DeBremaeker, J. 1959. Seismicity of the West African rift valley, J. Geophys. Res., 64, 1961-1966

Dixon, C.G. & Morton, W.H. 1970. Thermal and mineral springs in Uganda. Geothermics Special Issue 2, 1035-1038

DIN 38409, 1979. Deutsche Einheitsverfahren zur Wasser-, Abwasser- und Schlammuntersuchung; Summarische Wirkungs- und Stoffkenngrößen (Gruppe H) Bestimmung der Säure- und Basenkapazität (H7)

DIN EN 1484, 1997. Wasseranalytik, Anleitung zur Bestimmung des gesamten organischen Kohlenstoffs (TOC) und des gelösten organischen Kohlenstoffs (DOC), Deutsche Fassung EN 1484: 1997

DIN EN ISO 10304-1, 1995. Wasserbeschaffenheit; Bestimmung der gelösten Anionen Fluorid, Chlorid, Nitrit, Orthophosphat, Bromid, Nitrat und Sulfat mittels Ionenchromatographie; Teil 1: Verfahren für gering belastete Wässer (ISO 10304-1: 1992) Deutsche Fassung EN ISO 10304-1: 1995

DIN EN ISO 11885, 1998. Wasserbeschaffenheit, Bestimmung von 33 Elementen durch induktiv gekoppelte Plasma-Atom-Emissionsspektrometrie (ISO 11885: 1996) Deutsche Fassung EN ISO 11885: 1997

Dozith, A. & Mugisha, F. 2004. Structural Analysis of the Albertine Graben Western Uganda. Petroleum Exploration and Production Department, Uganda. Abstract in Proceedings, The East African Rift System: Development, Evolution and Resources, Addis Ababa, Ethiopia, 20.-24. June 2004

Fairhead, J.D., & Girdler, R.W. 1971. The seismicity of Africa, Geophys. J. Roy. Astron. Soc., 24, 271

Gäbler, H.-E. 2002. Applications of magnetic sector ICP-MS in geochemistry. Journal of Geochemical Exploration, 75, 1-15

Gíslason, G., Ngobi, G., Isabirye, E. & Tumwebaze, S. 1994. An Inventory of Three Geothermal Areas in West and Southwest Uganda. Geothermal Exploration UGA/92/002, UNDEST/GSMD, a draft report

Griesshaber-Schmahl, E. 1990. Helium and Carbon Isotope Systematics in Groundwaters from W.Germany and E.Africa. Dissertation University of Cambridge, 211 pp. 3/5/1990

GSU 1962. Fort Portal – Explanation of the Geology, scale 1:250,000, sheet N.A. 36-13, Geological Survey of Uganda, Entebbe, 1st Edition 1962/reprinted 1970

Halama, R., McDonough, W.F., Rudnick, R.L., Keller, J. & Klaudius, J. 2007. The Li isotopic composition of Oldoinyo Lengai: Nature of the mantle sources and lack of isotopic fractionation during carbonatite petrogenesis. Earth and Planetary Science Letters, 254, 77-89

Hem, J.D. 1992. Study and interpretation of the chemical characteristics of natural water. U.S. Geological Survey Water-Supply Paper 2254, 263 pp. (3rd edition)

Henley, R.W. 1996. Chemical and physical context for life in terrestrial hydrothermal systems. In: G.R. Bock & J.A. Goode (Eds.) Evolution of Hydrothermal Ecosystems on Earth (and Mars?), Ciba Foundation, Wiley & Sons, Chichester, UK, pp. 61-82

Hochstein, M.P. 2005. Heat transfer by hydrothermal systems in the East African Rift. Proceedings World Geothermal Conference 2005

Holmes, A. 1964. Principals of physical geology, University of Edinburgh, pp. 1069-1074

IAEA 2003. Isotope hydrology for exploring geothermal resources. IAEA TC-Project, UGA/8/003, Terminal Report

Isabirye Mugadu, E. 2000. Geothermal energy in the development of Uganda. Proceedings World Geothermal Conference 2000, 229-235

Kampunzu, A.B., Bonhomme, M.G. & Kanika, M. 1998. Geochronology of volcanic rocks and evolution of the Cenozoic Western Branch of the East African Rift System. Journal of African Earth Sciences, 26 (3), 441-461

Kato, V. 2000. Geothermal field studies using stable isotope hydrology. Case studies in Uganda and Iceland. Geothermal Training in Iceland 2000, Reports of the United Nations University Training Programme: 189-216

Kennett, B.L.N. (Ed.) 1991. IASPEI 1991 Seismological Tables. Research School of Earth Sciences, Australian National University

Kern, H. 1978 The effect of high temperature and high confining pressure on compressional wave velocities in Quartz-bearing and Quartz-free igneous and metamorphic rocks. Tectonophysics, 44, 185-203

Keller, G.V. & Frischknecht, F.C. 1966. Electrical methods in geophysical prospecting. Pergamon Press

Keller, J. & Hoefs, J.1995. Stable Isotope Characteristics of Recent Natrocarbonatites from Oldoinyo Lengai. In: K. Bell, J. Keller, Carbonatite Volcanism, Springer, 1995, pp. 113-123

Keller, J. & Zaitsev, A. 2006. Calciocarbonatite Dykes at Oldoinyo Lengai, Tanzania: the Fate of Natrocarbonatite. The Canadian Mineralogist, 44, 857-876

Koulakov, I., & Sobolev, S.V. 2006. Moho depth and three-dimensional P and S structure of the crust and uppermost mantle in the Eastern Mediterranean and Middle East derived from tomographic inversion of local ISC data. Geophysical Journal International, 164, 1, 218-235

Landolt-Börnstein 1982. Zahlenwerte und Funktionen aus Naturwissenschaft und Technik. Springer Verlag

Lienert, B.R.E., Berg, E. & Frazer, L.N. 1986. Hyocenter: An earthquake location method using centered, scaled, and adaptively least squares. BSSA, 76, 771-783

Lienert, B.R.E. & Havskov, J. 1995. A computer program for locating earthquakes both locally and globally. Seismological Research Letters, 66, 26-36

Lippmann, J., Erzinger, J., Zimmer, M., Schloemer, S., Eichinger, L. & Faber, E. 2005. On the geochemistry of gases and noble gas isotopes (including ^{222}Rn) in deep crustal fluids: the 4000 m KTB-pilot hole fluid production test 2002-03. Geofluids, 5, 52-66

Lloyd, F.E., Huntingdon, A.T., Davies, G.R. & Nixon, P.H. 1991. Phanerozoic volcanism of SW Uganda: a case for regional K and LILE enrichment beneath a domed rifted continental plate. In: Magmatism in Extensional Structural Settings by A.B. Kampunzu and R.T. Lubala, pp. 23-72, Springer-Verlag, Berlin

Loke, M.H. & Barker, R.D. 1996. Rapid least-square inversion of apparent resistivity pseudosections by a quasi-Newton method. Geophysical Prospecting, 44, 131-152

Maasha, N. 1975a. Electrical resistivity and microearthquake surveys of the Sempaya, Lake Kitagata, and Kitagata geothermal anomalies, Western Uganda. Proceedings Second United Nations Symposium on the Development and Use of Geothermal Resources, San Francisco, 20.-29. May 1975, 1103-1112

Maasha, N. 1975b. The Seismicity of the Rwenzori Region in Uganda. Journal of Geophysical Research, 80 (11), 1485-1496

McConnell, R.B. & Brown, J.N. 1954. Drilling for geothermal power at Buranga Hot Springs, Toro. First Progress Report. Geological Survey of Uganda, Unpub. report No. JMB/17 (RBM/16)

McLennan, S.M. 1989. Rare Earth Elements in Sedimentary Rocks: Influence of Provenance and Sedimentary Processes. In: B.R. Lipin & G.A. McKay (Eds.) Geochemistry and Mineralogy of Rare Earth Elements. Reviews in Mineralogy, 21, 169-200

Midzi, V., Hlatywayo, D.J., Chapola, L.S., Kebede, F., Atakan, K., Lombe, D.K., Turyomurugyendo, G. & Tugume, F.A. 1999. Seismic hazard assessment in Eastern and Southern Africa. Annali di Geofisica, 42 (6), 1067-1083, December 1999

Mlynarski, M. & Zlotnicki, J. 2001. Fluid circulation in the active emerged Asal rift (east Africa, Djibouti) inferred from self-potential and Telluric–Telluric prospecting. Tectonophysics, 339 (3-4), 455-472

Mogi, K. 1967. Earthquakes and fractures. Tectonopysics, 5, 35-55

Mundry, E. 1979. Geoelektrische Modellkurven für vertikale Störungen. NLfB Hannover, archive No. 0080147, unpub. Report, 68

Nyblade, A.A., Owens, T.J., Gurrola, H., Ritsema, J. & Langston, C.A. 2000. Seismic evidence for a deep upper mantle thermal anomaly beneath East Africa. Geology, 28 (7), 599-602

Ochmann, N., Hollnack, D. & Wohlenberg, J. 1989. Seismological Exploration of the Milos Geothermal Reservoir, Greece. Geothermics, 18, 4, 563-567

Ochmann, N., Lindenfeld, M., Barbirye, P. & Stadtler, C. 2007. Microearthquake survey at the Buranga geothermal prospect, Western Uganda. Proceedings of the 32nd workshop on geothermal reservoir engineering, Stanford University, Stanford, California, January 22-24, SGP-TR-183

O'Neil, J.R., Clayton, R.N. & Mayeda, T.K. 1969. Oxygen isotope fractionation in divalent metal carbonates. J. Chem. Phys., 51, 5547-5558

Pallister, J. W. 1952. Buranga Hot Springs, Toro, Uganda. Geological Survey of Uganda. Unpub. report No. JWP/14

Pallister J.W. 1954. Drilling for geothermal power at Buranga Hot Springs, Toro; Second Progress Report. Geological Survey of Uganda, Report No. JWP/26

Pik, R., Marty, B. & Hilton, D.R. 2006. How many mantle plumes in Africa? The geochemical point of view. Chemical Geology, 226 (2006), 100-114

Rümpker, G., Lindenfeld, M. & Yakovlev, A. 2007. Seismological data analysis, earthquake localization and travel-time tomography. GEOTHERM Project: Detailed surface analysis of the Buranga geothermal prospect, West-Uganda. Report, University of Frankfurt

Schlüter, T. 2006. Geological Atlas of Africa. Springer-Verlag Berlin Heidelberg

Schuster, R. 2002. Maßanalytische Bestimmungen in der Wasseranalytik. In: Höll, K., Wasser: Nutzung im Kreislauf, Hygiene, Analyse und Bewertung (Hrsg. Grohmann, A.), de Gruyter, Berlin, New York

Sharma D.V. 1971. Geothermal Energy; Report on the Preliminary Survey of Thermal Anomalies of Western Uganda for the possible development of Geothermal Energy. Report No. DVS/3, Geological Survey & Mines Department, Uganda.

Stadtler, C. & Kraml, M. 2005. Geophysical and geochemical investigations at the Buranga hot springs, Albertine Rift, Uganda. GEOTHERM Project: Detailed surface analysis of the Buranga geothermal prospect, West-Uganda. Interim Report, Hannover, BGR, 0125802

Sültenfuß, J., Roether, W. & Rhein, M. 2007. The Bremen Mass Spectrometric Facility for the Measurement of Helium Isotopes, Neon, and Tritium in Water. International Symposium on Quality Assurance for Analytical Methods in Isotope Hydrology, IAEA Proceedings, IAEA-CN 119-7, in press

Sun, S.s. & McDonough, W.F. 1989. Chemical and isotopic systematics of oceanic basalts: implications for mantle composition and processes. In: A.D. Saunders & M.J. Norry (Eds.) Magmatism in oceanic basins. Geol. Soc. Lond. Spec. Pub., pp. 313-345

Sykes, L. R. & Landisman, M. 1964. The seismicity of East Africa, the Gulf of Aden and the Arabian and Red seas. Bull. Seismol. Soc. Amer., 54, 1927-1940

Tiercelin, J.J., Thouin, C., Kalala, T. & Mondeguer, A. 1989. Discovery of sublacustrine hydrothermal activity and associated massive sulfides and hydrocarbons in the north Tanganyika trough, East African Rift. Geology, 17, 1053-1056

Tiercelin, J.J., Pflumio, C. Castrec, M. Boulegue, J., Gente, P., Rolet, J., Coussement, C., Stetter, K.O., Huber, R., Buku, S. & Mifundu, W. 1993. Hydrothermal vents in Lake Tanganyika, East African Rift System. Geology, 21, 499-502

Török, S.B., Labar, J., Injuk, J. & van Grieken, R.E. 1996. X-ray Spectrometry. Anal. Chem., 68: 467R-485R

Török, S.B. & van Grieken, R.E. 1992. X-ray Spectrometry. Anal. Chem., 64: 180R-196R

Upcott, N.M., Mukasa, R.K., Ebinger, C.J. & Karner, G.D. 1996. Along-axis segmentation and isostasy in the Western Rift, East Africa. Journal of Geophysical Research, B, Solid Earth and Planets, 101 (2), 3247-3268

van Geldern, R. & Suckow, A. 2005. Correction strategies in deuterium analysis using chromium reduction. Geochimica et Cosmochimica Acta, 69 (10) Supplement 1, Goldschmidt Conference Abstracts 2005, A866

Vinogradov. V.I., Krasnov, A.A. Kuleshov, V.N. & Sulerzhitskiy, L.D. 1978. $^{13}C/^{12}C$, $^{18}O/^{16}O$, and ^{14}C concentrations in the carbonatites of the Kalyango volcano (East Africa) (in Russian). Izv. Akad. Nauk. SSSR, Ser. Geol., 6, 33-41

Whiticar, M.J., 1990. A geochemial perspective of natural gas and atmospheric methane. Org. Geochem., 16 (1-3), 531-547

Wohlenberg, J. 1969. Remarks on the seismicity of East Africa between 4°N-12°S and 23°E-40°E. Tectonophysics, 8, 567-577

Yakovlev, A.V., Koulakov, I.Yu. & Tychkov S.A. 2007. Moho depths and three-dimensional velocity structure of the crust and upper mantle beneath the Baikal region, from local tomography. Russian Geology and Geophysics, 48 (2), 204-220

Zeyen, H., Volker, F., Wehrle, V., Fuchs, K., Sobolev, S.V. & Altherr, R. 1997 Styles of continental rifting: crust-mantle plumes. Tectonophysics, 278, 329-352

Hannover, 16.04.2007

Appendix

A.1 to A.8 Geochemistry

B.1 Schlumberger soundings

B.2 Test dipole/dipole mapping

B.3 TEM soundings

Appendix A.1: Coordinates of rock samples

	UTM Clarke 1880		WGS84		
Sample ID	**easting**	**northing**	**long**	**lat**	**Sample type**
Kbk007	near Kbk006	near Kbk006	near Kbk006	near Kbk006	rock
Bu001	184418	92769	30.16486	0.83826	rock
Kbk006	192617	102127	30.23840	0.92288	rock
Kbk008	190950	101185	30.22344	0.91435	rock
LKa009	152330	-13743	29.87718	-0.12415	rock
LKa010	152304	-14483	29.87694	-0.13083	rock
Mh014	171689	11782	30.05091	0.10645	rock
Mh015	165465	962	29.99506	0.00869	rock
Bg016	176634	32743	30.09526	0.29585	rock
Rw017	177588	53078	30.10376	0.47959	rock
Rm018b	190206	43062	30.21705	0.38913	rock
FPV019	191860	75469	30.23176	0.68198	rock
FPV020	191322	75058	30.22693	0.67826	rock
FPV021	194139	76193	30.25222	0.68861	rock
Kbk022	188470	100842	30.20118	0.91124	rock

Appendix A.1 continued: Coordinates of water chemistry samples

Sample ID	**easting**	**northing**	**long**	**lat**	**Sample type**
BuW 001	184418	92769	30.16486	0.83826	water
BuW 002	184133	92497	30.16230	0.83580	water
BuW 003	183950	92324	30.16066	0.83424	water
BuW 004	184425	92277	30.16492	0.83381	water
LKtW 011	162670	-6704	29.96998	-0.06057	water
KbW 012	172004	21030	30.05373	0.19001	water
MhW 013	171201	11651	30.04653	0.10527	water
RwW 017	177588	53078	30.10376	0.47959	water
RmW 018a	190216	43096	30.21714	0.38943	water
RmW 018b	190206	43062	30.21705	0.38913	water
KbkW 023	189219	101535	30.20790	0.91750	water
BRW-I-602	202895	100419	30.33068	0.90751	water
BRW-II-1497	202895	100419	30.33068	0.90751	water

Appendix A.1 continued: Coordinates of water isotope samples

Sample ID	easting	northing	long	lat	Sample type
Rwe-1 (Muhokya)	171252	11231	30.04699	0.10147	water
Rwe-2 (Nyamugasane)	156204	4768	29.91195	0.04307	water
Rwe-3 (Kibenge)	172079	20728	30.05440	0.18728	water
Rwe-4 (Nyamwamba)	166620	23757	30.00540	0.21464	water
Rwe-5 (Rwimi)	190284	42802	30.21775	0.38678	water
Rwe-6 (Mubuku)	170486	37828	30.04007	0.34178	water
Rwe-7 (Isebwe)	176747	33263	30.09627	0.30055	water
Rwe-8 (Nyakalenjijo)	169074	39332	30.02739	0.35536	water
Rwe-9 (Rwagimba)	177883	52809	30.10641	0.47716	water
Rwe-10 (Rwiimi)	177883	52809	30.10641	0.47716	water
Rwe-11 (Nsoja)	184839	60076	30.16881	0.54285	water
Rwe-12 (Mpanga)	184149	72798	30.16256	0.65780	water
Rwe-13 (Mugunu)	195617	72173	30.26550	0.65221	water
Rwe-14 (Small stream)	187081	80511	30.18884	0.72751	water
Rwe-15 (Wasa)	192602	86887	30.23836	0.78516	water
Rwe-16 (*Mumbuga)	184493	92468	30.16553	0.83554	water
Rwe-17 (*Mumbuga)	184493	92468	30.16553	0.83554	water
Rwe-18 (*Stream)	184561	91920	30.16615	0.83059	water
Rwe-19 (*Nkisi)	182391	89408	30.14668	0.80788	water
Rwe-20 (*Kirumira)	176710	88063	30.09570	0.79569	water
Rwe-21 (*Tokwe)	172843	77125	30.06106	0.69684	water
Rwe-22 (*Rugo)	171357	73153	30.04774	0.66094	water
Rwe-23 (*Ngitte)	170819	71782	30.04292	0.64855	water
Rwe-24 (*Nyauka)	169274	70343	30.02906	0.63554	water
Rwe-25 (*Kuka)	168393	69120	30.02116	0.62449	water
Rwe-26 (*Ndugutte)	163411	70975	29.97644	0.64122	water
Rwe-27 (*Lamia)	161339	69743	29.95785	0.63008	water
Rwe-28 (Kisina)	187870	83171	30.19590	0.75155	water
Rwe-29 (Itojo)	191309	92525	30.22672	0.83610	water
Rwe-30 (Stream)	187352	92892	30.19119	0.83939	water
Rwe-31 (*Ssempaya)	185435	93774	30.17398	0.84735	water
Rwe-32 (Mitomi)	185486	78772	30.17453	0.71179	water
Rwe-33 (Samusenge)	187762	76668	30.19497	0.69279	water
Rwe-34 (Mugu)	195924	72431	30.26826	0.65454	water

* = located on western side of Rwenzori

Appendix A.1 continued: Coordinates of gas samples

Sample ID	easting	northing	long	lat	Sample type
Kibiro	305971	185102	31.25587	1.67386	gas
BuG003	184042	92036	30.16149	0.83163	gas
BuG001	184511	92410	30.16569	0.83502	gas
RmG	190287	42787	30.21777	0.38664	gas
KbG	172055	20729	30.05418	0.18729	gas

Appendix A.2: Trace element data of carbonates (BU=Buranga; KA=Katwe; MU=Muhokya)

S. ID	Li	Be	B	Na%	Mg%	Al%	K%	Ca%	Sc	V	Cr	Mn
BU-1	4.7	13.9	0	0.094	0.09	0.03	0.02	30.3	0.2	0	1.6	81
BU-2	20.9	12.0	0	0.039	0.38	0.03	0.01	27.8	0.0	0	0.9	65
BU-3	2.7	62.8	0	0.099	0.96	0.01	0.03	28.5	0.2	0	1.6	137
KA-1	18.1	0.2	0	0.481	22.1	0.07	0.29	3.29	0.6	29	2.8	57
KA-2	28.5	0.1	0	0.841	15.8	0.07	0.60	3.54	0.5	37	3.3	120
MU-1	0.0	0.1	0	0.019	0.41	0.00	0.00	22.7	0.0	2	2.0	155
S. ID	**Fe%**	**Co**	**Ni**	**Cu**	**Zn**	**Ga**	**Ge**	**As**	**Se**	**Rb**	**Sr**	**Y**
BU-1	0.14	0.6	5.3	5.93	7.1	0.00	0.9	2.8	0.0	0.8	n.a.	1.47
BU-2	0.10	0.5	5.7	1.85	1.0	1.58	0.3	1.9	0.0	1.1	n.a.	0.67
BU-3	0.23	0.3	7.1	1.09	1.5	0.00	0.0	0.0	0.0	1.1	n.a.	0.75
KA-1	0.10	0.8	19.2	2.62	4.0	0.23	0.0	1.6	0.3	3.4	1230	0.47
KA-2	0.12	1.0	12.8	3.88	6.0	0.17	0.0	0.4	0.2	6.9	1660	0.62
MU-1	0.11	1.2	9.2	1.91	1.6	0.00	0.0	2.5	0.0	0.2	864	0.08
S. ID	**Zr**	**Nb**	**Mo**	**Ag**	**Cd**	**In**	**Sn**	**Sb**	**Te**	**Cs**	**Ba**	**La**
BU-1	4.7	0.7	0.14	0.346	0.0	0.00	2.29	1.85	7.26	0.1	1200.0	
BU-2	1.8	0.5	0.21	0.000	0.0	0.00	0.42	0.48	6.19	0.5	884.0	
BU-3	1.8	0.1	0.07	0.000	0.0	0.00	0.44	0.23	4.56	0.2	772.9	
KA-1	23.4	0.9	0.64	0.000	0.0	0.00	1.11	0.12	0.21	0.0	78.2	1.0
KA-2	43.5	1.5	1.70	0.058	0.0	0.00	0.59	0.20	0.32	0.0	117.4	1.2
MU-1	2.8	0.3	0.19	0.000	0.0	0.00	0.26	0.08	0.08	0.0	34.2	
S. ID	**Ce**	**Pr**	**Nd**	**Sm**	**Eu**	**Gd**	**Tb**	**Dy**	**Ho**	**Er**	**Tm**	**Yb**
BU-1	3.36	0.1	0.42	0.1	-0.1	0.2	-0.1	0.1	-0.1	-0.1	-0.1	-0.1
BU-2	0.92		0.05		-0.1	-0.1	-0.1	-0.1	-0.1	-0.1	-0.1	-0.1
BU-3	3.21		0.18		-0.1	-0.1	-0.1	-0.1	-0.1	-0.1	-0.1	-0.1
KA-1	2.36	0.2	0.71	0.1	-0.1	0.1	-0.1	-0.1	-0.1	-0.1	-0.1	-0.1
KA-2	2.84	0.2	0.78	0.1	-0.1	0.1	-0.1	0.1	-0.1	-0.1	-0.1	0.1
MU-1	1.36		0.08		-0.1	-0.1	-0.1	-0.1	-0.1	-0.1	-0.1	-0.1
S. ID	**Lu**	**Hf**	**Ta**	**W**	**Re**	[ppb] **Au**	**Tl**	**Pb**	**Bi**	**Th**	**U**	
BU-1	-0.1	0.2	-0.05	43.7	-0.001	-0.2	0.23	7.85	0.40	0.1	-0.1	
BU-2	-0.1	-0.1	-0.05	20.5	-0.001	-0.2	2.33	1.74	0.04	0.1	0.5	
BU-3	-0.1	-0.1	-0.05	7.9	0.001	-0.2	0.19	1.32	-0.02	-0.1	-0.1	
KA-1	-0.1	0.6	-0.05	13.5	0.002	-0.2	0.04	1.66	-0.02	0.3	0.7	
KA-2	-0.1	1.0	-0.05	61.0	0.002	-0.2	0.04	1.36	-0.02	0.5	0.8	
MU-1	-0.1	-0.1	-0.05	27.1	-0.001	-0.2	0.09	0.84	-0.02	-0.1	27.4	

Concentrations in ppm (parts per million) except noted. Negative values = not detected at that lower limit.

Appendix A.2 continued: Trace element data of carbonates and carbonatites (XRF)

sample ID	Location and rock type	SiO2	TiO2	Al2O3	Fe2O3	MnO
		%	%	%	%	%
Bu001	Mumbuga 1 travertine	1.22	0.011	0.07	0.08	<0.001
Kbk007	Kibuku 7 calcrete	0.52	0.009	0.13	0.09	0.228
LKa009	Katwe 9 highest travertine mount	2.74	0.016	0.2	0.1	0.006
LKa010	Katwe 10 travertine crater wall	13.62	0.061	0.29	0.24	0.029
Mh015	Kikorongo 15 ornamental travertine	<0.1	0.002	<0.05	0.11	0.019
Bg016	Bugoye 16 travertine	0.36	0.004	0.08	0.07	0.016
Rm018b	Rwimi 18b travertine	3.22	0.008	0.12	2.71	0.097
FPV019	Kigere rim 19 lava	15.7	1.915	3.65	12.84	0.448
FPV020	Gate of National Conservation Area 20 lapilli	15.97	2.156	4.4	11.84	0.352
FPV021	Lake Saka 21 ash (not in situ)	33.11	2.433	8.74	15.27	0.343
Kbk022	Kibuku 22 travertine	6.23	0.112	1.47	0.98	0.023
S24 calcite	Kibiro S24 travertine (received as powder)	5.19	0.107	2.35	1.22	0.111

Appendix A.2 continued: Trace element data of carbonates and carbonatites (XRF)

sample ID	MgO	CaO	Na2O	K2O	P2O5	(SO3)	(Cl)	(F)	LOI	Sum
	%	%	%	%	%	%	%	%	%	%
Bu001	0.55	34.484	0.04	0.01	0.015	0.04	0.046	<0.05	31.90	68.47
Kbk007	1.54	52.94	0.03	0.008	0.054	0.22	0.005	<0.05	43.72	99.52
LKa009	42.17	3.714	0.11	0.059	0.054	0.15	<0.002	<0.05	50.52	99.84
LKa010	19.47	25.616	0.35	0.049	0.059	0.11	0.004	0.10	38.95	98.95
Mh015	0.08	53.734	0.12	<0.005	0.008	0.17	0.005	<0.05	43.94	98.30
Bg016	0.73	53.94	0.10	0.02	0.026	0.53	0.015	0.06	43.28	99.24
Rm018b	3.38	44.983	0.09	0.032	0.209	0.78	0.01	0.06	43.32	99.00
FPV019	8.42	34.154	0.27	0.196	3.17	0.84	0.021	0.28	16.84	98.75
FPV020	5.01	30.848	0.50	0.541	2.476	0.06	0.007	0.15	24.47	98.77
FPV021	6.82	20.842	1.52	0.824	1.505	0.15	0.018	<0.05	7.36	98.96
Kbk022	1.24	48.382	0.15	0.136	0.149	0.19	0.004	<0.05	40.67	99.73
S24 calcite	1.96	46.067	0.06	0.115	0.374	0.28	0.006	0.06	41.47	99.37

Appendix A.2 continued: Trace element data of carbonates and carbonatites (XRF)

sample ID	(As)	Ba	Bi	Ce	Co	Cr	Cs	Cu	Ga	Hf
	mg/kg	mg/kg	mg/kg	mg/kg	mg/kg	mg/kg	mg/kg	mg/kg	mg/kg	mg/kg
Bu001	<2	793	<3	<20	<3	<3	<5	176	<3	<5
Kbk007	<2	96	5	42	<3	<3	<5	49	<3	<5
LKa009	<2	60	<3	<20	<3	23	<5	59	<3	<5
LKa010	<2	545	<3	30	<3	5	<5	62	<3	<5
Mh015	<2	17	7	23	<3	<3	<5	31	<3	<5
Bg016	99	28	<3	37	<3	<3	<5	30	<3	<5
Rm018b	2	118	4	33	<3	<3	<5	53	<3	<5
FPV019	3	2223	4	927	31	67	8	61	10	9
FPV020	7	1956	<3	683	33	77	12	65	12	11
FPV021	<2	1467	4	519	43	64	9	93	15	<5
Kbk022	<2	89	<3	<20	<3	7	<5	26	<3	5
S24 calcite	<2	489	4	23	5	12	<5	28	<3	6

Appendix A.2 continued: Trace element data of carbonates and carbonatites (XRF)

sample ID	La	Mo	Nb	Nd	Ni	Pb	Rb	Sb	Sc	Sm
	mg/kg	mg/kg	mg/kg	mg/kg	mg/kg	mg/kg	mg/kg	mg/kg	mg/kg	mg/kg
Bu001	26	<2	37	<50	<3	65	<2	<5	5	<50
Kbk007	<20	<2	<2	<50	<3	<4	<2	<5	<2	<50
LKa009	<20	<2	3	<50	10	<4	4	<5	<2	<50
LKa010	<20	<2	6	<50	<3	<4	3	<5	3	<50
Mh015	<20	<2	2	<50	<3	<4	7	5	<2	<50
Bg016	<20	<2	9	<50	<3	<4	4	8	<2	<50
Rm018b	<20	<2	10	<50	<3	<4	4	<5	<2	<50
FPV019	498	<2	493	388	28	12	9	<5	16	<50
FPV020	373	<2	384	286	32	13	27	7	16	<50
FPV021	278	<2	279	223	50	22	25	<5	23	<50
Kbk022	<20	<2	7	<50	4	<4	9	8	3	<50
S24 calcite	32	<2	87	<50	12	<4	8	<5	3	<50

Appendix A.2 continued: Trace element data of carbonates and carbonatites (XRF)

sample ID	**Sn**	**Sr**	**Ta**	**Th**	**U**	**V**	**W**	**Y**	**Zn**	**Zr**
	mg/kg	mg/kg	mg/kg	mg/kg	mg/kg	mg/kg	mg/kg	mg/kg	mg/kg	mg/kg
Bu001	3	267753	<5	<5	<3	<5	<5	68	<3	<3
Kbk007	<2	1547	<5	9	<3	<5	<5	<3	6	18
LKa009	2	555	<5	<5	<3	17	<5	<3	6	10
LKa010	4	7074	<5	5	5	150	<5	<3	6	50
Mh015	<2	9598	<5	24	127	<5	<5	<3	<3	1218
Bg016	<2	3869	<5	14	<3	<5	<5	<3	4	19
Rm018b	<2	4707	<5	15	16	8	<5	8	17	144
FPV019	2	4903	18	82	16	314	9	60	176	692
FPV020	<2	4324	19	61	11	259	<5	46	133	574
FPV021	<2	3085	14	62	8	301	<5	42	167	458
Kbk022	<2	231	<5	<5	3	22	<5	<3	14	22
S24 calcite	16	850	57	7	<3	14	<5	6	17	26

Appendix A.2: Mineralogical composition of rock samples (XRD)

Sample ID	Major mineral component	Major-Minor	Minor	Minor-Traces	Traces
Bu-1 (Buranga)	Aragonite-like				Calcite
Bu-2 (Buranga)	Aragonite-like				Calcite
Bu-3 (Buranga)	Calcite, possibly Mg-rich			Aragonite-like	
Ka-1 (Katwe)	Magnesite			Dolomite	Halite, ±Quartz
Ka-2 (Katwe)	Magnesite			Dolomite, Halite	possibly plus unidentified clay minerals
Mu-1 (Muhokya)	Calcite				
Mumbuga 001	Calcite	Strontianite			Magnesite, Quartz
Kibuku 7 (calcrete)	Calcite				
Katwe 9 (highest mount)	Ca-rich Magnesite				Dolomite, Calcite
Katwe 10 (crater wall)	Ca-rich Dolomite			Aragonite	
Kikorongo 15 (ornamental stone)	Aragonite-like				±Calcite
Bugoye 16	Calcite				±Quartz
Rwimi 18b	Mg-rich Calcite				
Kigere rim 19	Calcite			Biotite or similar	Monticellite, Apatite, unidentified sheet silicate
Gate 20	Calcite			Biotite	Apatite, Feldspar?
Lake Saka 21	possibly x-ray amorphous phase	Biotite or similar	Feldspar	Calcite, Hornblende, Quartz, Monticellite	Apatite, possibly plus unidentified phase
Kibuku 22 (swamp)	Calcite				Quartz, Feldspar?
S24 Calcite (Kibiro)	Calcite, possibly Mg-rich				Quartz

Appendix A.3: $\delta^{18}O$ and $\delta^{13}C$ isotopic data of carbonates

Sample ID:	**$\delta^{18}O_{PDB}$ [‰]**	**$\delta^{13}C_{PDB}$ [‰]**
Bu-1 (Buranga; most recent Mumbuga)	-17.10	-3.78
Bu-2 (Buranga; rim of Mumbuga)	-16.04	-2.67
Bu-2(repeat) (Buranga)	-15.95	-2.54
Bu-3 (Buranga; GSMD museum)	-15.21	-3.68
Ka-1 (Katwe)	5.16	1.41
Ka-2 (Katwe)	7.36	2.87
Mu-1 (Muhokya lime stone quarry)	-3.27	0.89

Appendix A.3 continued: $\delta^{18}O$ and $\delta^{13}C$ isotopic data of carbonates (second sample series)

Sample ID	**$\delta^{18}O_{PDB}$ [‰]**	**$\delta^{13}C_{PDB}$ [‰]**
Bugoye 16 (travertine terrace)	-3.38	2.59
Katwe 9 (highest travertine mount)	5.70	3.28
Katwe 10 (crater wall)	3.30	2.60
Kibuku 7 (calcrete)	-4.52	-1.83
Kibuku 22 (swamp sinter)	-6.20	-12.46
Kibiro (powdered sinter S 24)	-3.18	-7.92
Kikorongo 15 (buried aragonite)	-5.47	2.37
Rwimi 18b (travertine mount)	-2.39	3.77
Rwagimba 17 (travertine below water)	-3.76	0.45

Appendix A.4: Water chemistry of hot springs around Rwenzori mountains.

Sample ID	**Name**	**Temp. [°C]**	**pH $_{lab}$**	**Cond.$_{lab}$ [µS/cm]**	**Cond.$_{field}$ [mS/cm]**
BuW001	Mumbuga (Buranga)	94.0	8.7	17900	*18.6
BuW002	Nyansimbe (Buranga)	75.4	8.4	22400	n.a.
BuW003	Kagoro (Buranga)	88.0	8.6	21000	n.a.
BuW004	Well #3 (Buranga)	62.0	8.3	21500	n.a.
LKtW011	Lake Kitagata	64.0	8.7	31300	*29.0
KbW012	Kibenge	42.5	8.2	3580	3.6
MhW013	Muhokya	41.0	8.2	3460	3.6
RwW017	Rwagimba	69.0	8.1	6390	n.a.
RmW018a	near Rwimi	25.9	7.2	3880	4.3
RmW018b	near Rwimi	24.6	7.1	3640	3.8
KbkW023	Kibuku area	25.6	8.3	4720	4.7
Rwe-8 §	Nyakalenjijo	n.a.	6.2	1240	n.a.

* analysed not exactly at sampling site

§ analysed from 50 ml isotope sample

Appendix A.4 continued: Water chemistry of hot springs around Rwenzori mountains.

Sample ID	SiO_2 [mg/l]	Na [mg/l]	K [mg/l]	Ca [mg/l]	Mg [mg/l]	Li [mg/l]	Sr [mg/l]
BuW001	70.0	4716	166	6.24	1.94	1.20	4.83
BuW002	77.4	5991	218	6.55	1.97	1.51	4.89
BuW003	76.6	5561	199	7.01	1.97	1.41	5.58
BuW004	73.5	5738	209	7.11	1.77	1.45	5.17
LKtW011	81.7	9237	634	2.41	0.86	0.048	1.67
KbW012	44.5	550	24.3	226	6.4	0.221	3.15
MhW013	50.9	586	18.8	206	13.1	0.062	1.42
RwW017	62.5	1480	41.6	74.1	5.38	0.452	3.20
RmW018a	92.7	424	60.7	380	198	0.071	8.35
RmW018b	84.8	356	56.8	361	181	0.056	8.21
KbkW023	30.2	1027	34.1	27.4	13.7	0.12	0.51
Rwe-8	18.7	181	7.5	94.1	4.3	n.a.	n.a.

Appendix A.4 continued: Water chemistry of hot springs around Rwenzori mountains.

Sample ID	Fe [mg/l]	Mn [mg/l]	Cl [mg/l]	SO_4 [mg/l]	CO_3 [mg/l]	HCO_3 [mg/l]	BO_2 [mg/l]	Br [mg/l]
BuW001	0.02	0.001	3133	3222	72	2850	14.8	14.9
BuW002	0.02	0.001	4019	4186	60	3630	18.1	18.2
BuW003	0.91	0.017	3735	3842	60	3360	17.2	16.9
BuW004	0.16	0.004	3839	4001	54	3440	17.5	17.3
LKtW011	0.02	0.017	2447	12959	108	4160	3.22	13.4
KbW012	0.30	0.149	585	894		98	1.89	4.2
MhW013	1.05	0.175	460	1075		143	1.42	4.3
RwW017	0.48	0.047	838	1468		800	2.77	4.9
RmW018a	6.42	0.339	232	693		2100	0.94	2.6
RmW018b	6.25	0.299	189	523		2020	0.73	2.0
KbkW023	0.40	0.877	558	973	15	748	2.94	2.5
Rwe-8	n.a.	n.a.	123	373	*	n.a.*	n.a.	0.8

* TIC (total inorganic carbon) = 4.5 mg/l

Appendix A.4 continued: Water chemistry of hot springs around Rwenzori mountains.

Sample ID	Al (OES) mg/l	As (OES) mg/l	Ba µg/l	Be µg/l	Bi µg/l	Cd µg/l	Co µg/l	Cr µg/l
BuW001	0.015	0.23	54.8	5.2	0.21	0.05	0.23	6.0
BuW002	0.020	0.35	63.1	7.4	0.17	0.04	0.08	2.5
BuW003	0.710	0.28	63.4	7.5	0.11	0.03	0.63	4.3
BuW004	0.031	0.36	64.9	5.8	0.09	0.04	0.22	2.4
LKtW011	0.020	0.02	38.5	<0.1	0.07	1.30	0.14	1.0
KbW012	0.163	-0.02	37.9	0.2	0.03	0.05	0.76	0.7
MhW013	0.039	-0.02	21.6	0.2	0.02	0.02	0.22	3.1
RwW017	0.010	0.38	37.7	2.6	0.03	0.05	0.08	1.0
RmW018a	0.154	-0.02	61.8	1.2	0.01	0.08	2.40	8.6
RmW018b	0.031	-0.02	44.0	1.5	0.01	0.05	1.10	29.8
KbkW023	0.353	-0.02	12.7	0.1	0.01	0.07	0.98	11.0

-value and <value = below detection limit

Appendix A.4 continued: Water chemistry of hot springs around Rwenzori mountains.

Sample ID	Cs µg/l	Cu µg/l	Ga µg/l	Hf µg/l	In µg/l	Mo µg/l	Nb µg/l	Ni µg/l
BuW001	93.9	14.3	1.10	0.53	<0.02	6.0	0.07	19.4
BuW002	129	14.5	0.82	0.27	<0.02	12.6	0.08	8.4
BuW003	122	14.9	0.90	0.19	<0.02	8.4	0.20	9.7
BuW004	121	14.9	0.90	0.14	<0.02	16.4	0.04	7.9
LKtW011	5.1	37.9	0.17	0.12	<0.02	1060	0.14	6.6
KbW012	15.5	7.6	0.09	0.01	<0.02	6.6	0.10	8.3
MhW013	4.2	5.5	0.04	0.01	<0.02	7.0	0.02	12.7
RwW017	22.1	7.8	0.19	0.02	<0.02	28.4	0.01	11.2
RmW018a	0.1	5.6	0.07	0.12	<0.02	9.1	2.30	17.9
RmW018b	0.2	3.4	<0.01	0.20	<0.02	8.4	0.13	20.7
KbkW023	0.1	6.5	0.16	0.05	<0.02	16.0	0.08	17.9

<value = below detection limit

Appendix A.4 continued: Water chemistry of hot springs around Rwenzori mountains.

Sample ID	Pb µg/l	Rb µg/l	Sb µg/l	Sc (OES) mg/l	Sn µg/l	Ta µg/l
BuW001	6.8	858	3.9	-0.001	0.21	0.07
BuW002	3.3	1120	5.5	-0.001	0.14	0.06
BuW003	2.7	1050	4.2	-0.001	0.13	0.07
BuW004	2.6	1070	22.3	-0.001	0.10	0.04
LKtW011	2.0	974	0.03	-0.001	0.09	0.07
KbW012	2.8	176	0.02	-0.001	0.07	0.01
MhW013	2.1	88	0.08	-0.001	0.28	<0.01
RwW017	2.8	250	1.5	-0.001	0.05	0.01
RmW018a	3.3	54	0.03	-0.001	0.10	0.02
RmW018b	2.1	44	0.01	-0.001	0.07	<0.01
KbkW023	1.7	17	0.05	-0.001	0.07	0.01

-value and <value = below detection limit

Appendix A.4 continued: Water chemistry of hot springs around Rwenzori mountains.

Sample ID	Th µg/l	Ti (OES) mg/l	Tl µg/l	U µg/l	V (OES) mg/l	W µg/l	Y µg/l	Zn µg/l	Zr µg/l
BuW001	0.40	-0.001	2.9	0.04	-0.005	129	0.05	9.9	1.2
BuW002	0.30	-0.001	4.4	0.13	-0.005	161	0.05	7.0	1.0
BuW003	0.47	0.033	6.6	0.13	-0.005	162	0.25	7.6	1.6
BuW004	0.22	-0.001	114	0.2	0.014	157	0.05	6.6	1.1
LKtW011	0.30	0.002	0.17	57.1	0.006	14.2	0.07	8.5	8.2
KbW012	0.11	0.007	0.22	0.13	-0.005	15.1	0.14	13.0	0.2
MhW013	0.07	0.002	0.05	0.02	-0.005	5.0	0.18	7.5	0.2
RwW017	0.09	-0.001	1.3	1.0	-0.005	6.4	0.34	19.1	0.2
RmW018a	0.61	0.009	0.04	80.0	-0.005	0.35	2.3	14.4	50.4
RmW018b	0.15	0.002	0.09	78.7	-0.005	0.18	2.5	11.2	71.8
KbkW023	0.13	0.008	0.02	4.5	0.009	0.11	0.57	4.9	5.2

-value = below detection limit

Appendix A.4 continued: Water chemistry of hot springs around Rwenzori mountains.

Sample ID	La µg/l	Ce µg/l	Pr µg/l	Nd µg/l	Sm µg/l	Eu µg/l	Gd µg/l
BuW001	0.01	0.04	0.01	0.09	<0.01	0.01	0.02
BuW002	<0.01	0.03	0.01	0.04	<0.01	0.01	<0.01
BuW003	0.73	1.2	0.15	0.68	0.09	0.03	0.10
BuW004	0.04	0.04	0.01	0.09	<0.01	0.01	0.01
LKtW011	0.06	0.11	0.02	0.13	<0.01	<0.01	0.02
KbW012	0.32	0.65	0.07	0.25	0.03	0.02	0.02
MhW013	0.11	0.22	0.02	0.10	<0.01	<0.01	0.02
RwW017	0.04	0.05	0.01	0.10	<0.01	0.01	0.03
RmW018a	5.9	9.0	1.1	3.4	0.42	0.11	0.40
RmW018b	0.31	0.52	0.07	0.32	0.05	0.02	0.17
KbkW023	0.86	1.7	0.19	0.68	0.15	0.03	0.09

<value = below detection limit

Appendix A.4 continued: Water chemistry of hot springs around Rwenzori mountains.

Sample ID	Tb µg/l	Dy µg/l	Ho µg/l	Er µg/l	Tm µg/l	Yb µg/l	Lu µg/l
BuW001	<0.01	<0.01	0.01	<0.01	<0.01	<0.01	<0.01
BuW002	<0.01	0.01	0.02	0.01	<0.01	<0.01	<0.01
BuW003	0.01	0.01	0.02	0.03	<0.01	0.01	<0.01
BuW004	<0.01	<0.01	0.02	0.01	<0.01	<0.01	<0.01
LKtW011	0.01	0.01	0.08	0.01	<0.01	0.02	<0.01
KbW012	<0.01	0.02	0.01	0.01	<0.01	0.01	<0.01
MhW013	<0.01	0.01	0.01	0.01	<0.01	0.01	<0.01
RwW017	<0.01	0.02	0.01	0.02	<0.01	0.03	0.01
RmW018a	0.05	0.25	0.06	0.18	0.02	0.17	0.03
RmW018b	0.03	0.21	0.06	0.17	0.02	0.18	0.03
KbkW023	0.01	0.10	0.02	0.06	0.01	0.04	0.01

<value = below detection limit

Appendix A.5: $\delta^{18}O$ and $\delta^{2}H$ isotopic data of water samples

Sample	Sampling Date	$\delta^{18}O$ in ‰ VSMOW	δD in ‰ VSMOW
Rwe-1 (Muhokya)	19.05.2006	-3.61	-12.64
Rwe-2 (Nyamugasane)	19.05.2006	-3.14	-7.77
Rwe-3 (Kibenge)	19.05.2006	-4.15	-17.00
Rwe-4 (Nyamwamba)	20.05.2006	-3.38	-8.97
Rwe-5 (Rwimi)	20.05.2006	-2.23	-1.94
Rwe-6 (Mubuku)	21.05.2006	-3.63	-11.84
Rwe-7 (Isebwe)	21.05.2006	-3.37	-9.33
Rwe-8 (Nyakalenjijo)	22.05.2006	-4.27	-16.17
Rwe-9 (Rwagimba)	23.05.2006	-4.21	-16.60
Rwe-10 (Rwiimi)	23.05.2006	-3.53	-9.87
Rwe-11 (Nsoja)	24.05.2006	-3.11	-7.72
Rwe-12 (Mpanga)	24.05.2006	-2.72	-5.24
Rwe-13 (Mugunu)	24.05.2006	-1.41	0.78
Rwe-14 (Small stream)	25.05.2006	-2.18	-4.31
Rwe-15 (Wasa)	25.05.2006	-2.24	-4.21
Rwe-16 (*Mumbuga)	25.05.2006	-3.22	-12.51
Rwe-17 (*Mumbuga)	25.05.2006	-3.34	-12.64
Rwe-18 (*Stream)	26.05.2006	-1.99	-2.22
Rwe-19 (*Nkisi)	26.05.2006	-2.39	-4.45
Rwe-20 (*Kirumira)	26.05.2006	-2.06	-1.76
Rwe-21 (*Tokwe)	26.05.2006	-2.79	-5.54
Rwe-22 (*Rugo)	27.05.2006	-3.01	-6.89
Rwe-23 (*Ngitte)	27.05.2006	-3.06	-7.41
Rwe-24 (*Nyauka)	27.05.2006	-3.18	-7.94
Rwe-25 (*Kuka)	27.05.2006	-2.54	-3.69
Rwe-26 (*Ndugutte)	28.05.2006	-2.91	-6.47
Rwe-27 (*Lamia)	28.05.2006	-2.78	-5.40
Rwe-28 (Kisina)	28.05.2006	-2.80	-6.84
Rwe-29 (Itojo)	28.05.2006	-2.05	-2.36
Rwe-30 (Stream)	29.05.2006	-1.97	-0.86
Rwe-31 (*Ssempaya)	29.05.2006	-1.78	-0.41
Rwe-32 (Mitomi)	29.05.2006	-2.98	-6.32
Rwe-33 (Samusenge)	30.05.2006	-2.18	-2.79
Rwe-34 (Mugu)	31.05.2006	-1.24	2.94

Appendix A.6: Gas samples in glass flasks and their major component composition

Sample ID	**Water temp.**	**H_2**	**N_2**	**O_2 + Ar**	**CO_2**	**Methane**	**Ethane**
	[°C]	Vol%	Vol%	Vol%	Vol%	Vol%	Vol%
1. Kibenge 20	45	0.00	94.60	3.98	1.17	0.25	0.0005
1. Kibenge 19	45	0.00	94.39	4.21	1.15	0.24	0.0004
2A Rwimi A 18	27	0.00	4.38	1.36	94.24	0.01	0.00
2A Rwimi A 17	27	0.00	52.94	14.38	32.67	0.005	0.00
2B Rwimi B 16	n.a.	0.00	19.07	5.49	75.43	0.01	0.00
2C Rwimi C 15	n.a.	0.00	15.92	4.39	79.68	0.00	0.00
3a Mumbuga A 14	43	0.00	32.78	3.62	49.59	13.19	0.57
3a Mumbuga A 13	43	0.00	31.53	3.46	51.13	13.09	0.56
3b Mumbuga B 12	34	0.00	10.46	1.13	80.79	7.21	0.32
3b Mumbuga B 10	34	0.00	14.99	2.41	75.13	7.06	0.31
3c Mumbuga C 8	84	0.00	19.70	5.23	73.88	1.11	0.05
3c Mumbuga C 7	84	0.00	18.31	4.74	75.69	1.19	0.05
4a Kagoro A 6	78	0.00	29.85	5.93	57.53	6.24	0.29
4a Kagoro A 5	78	0.00	28.71	5.41	58.43	6.95	0.32
4b Kagoro B 4	n.a.	0.00	21.14	4.19	65.13	9.23	0.26
5a Kibiro A 3	74	0.10	51.38	14.34	1.78	31.96	0.39
5b Kibiro B 2	n.a.	0.09	42.19	11.83	2.90	42.24	0.64

Appendix A.6 continued: Gas samples and their hydrocarbon composition

Sample ID	**Ethene**	**Propane**	**Propene**	**i-Butane**	**n-Butane**	**i-Pentane**	**n-Pentane**
	ppm	ppm	ppm	ppm	ppm	ppm	ppm
KbG 20	0	0	1	0	0	41	31
KbG 19	1	0	1	0	0	49	39
RmG A18	0	0	0	0	0	21	13
RmG A17	0	0	0	0	0	44	21
RmG B16	0	0	0	0	0	33	18
RmG C15	0	0	0	0	0	25	12
BuG1A14	0	1998	0	264	228	30	16
BuG1A13	0	1901	0	240	187	21	9
BuG1B12	0	783	0	112	108	22	15
BuG1B10	0	732	0	110	96	21	13
BuG1 C8	0	146	0	13	19	11	6
BuG1 C7	0	136	0	11	15	7	3
BuG3 A6	0	1156	0	153	191	39	31
BuG3 A5	0	1301	0	180	218	43	33
BuG3 B4	0	477	0	35	13	2	1
Kibiro A3	0	471	0	2	3	2	12
Kibiro B2	0	1096	0	5	22	1	1

Appendix A.6 continued: Gas samples and their C and H isotopic composition

Sample ID	δ^{13}-CH_4	δ^{13}-C_2H_6	δ^{13}-C_3H_8	δ^{13}-CO_2	δD - CH_4
	PDB	PDB	PDB	PDB	SMOW
KbG 20	-22.6	---	---	-19.8	---
KbG 19	-22.6	---	---	-20.5	-64.9
RmG A18	---	---	---	-5.3	---
RmG A17	---	---	---	-5.9	---
RmG B16	---	---	---	-4.5	---
RmG C15	---	---	---	-5.7	---
BuG1A14	-54.1	-29.9	-28.1	-7.3	-218.9
BuG1A13	-53.9	-29.9	-27.9	-7.2	-217.0
BuG1B12	-54.2	-30.4	-27.7	-6.9	-220.7
BuG1B10	-53.9	-30.2	-27.7	-6.6	-221.5
BuG1 C8	-52.7	-30.5	-28.3	-7.2	-216.4
BuG1 C7	-53.8	-30.7	-28.2	-7.2	-219.3
BuG3 A6	-53.3	-30.2	-28.5	-6.5	-219.7
BuG3 A5	-53.4	-30.0	-28.4	-6.6	-218.2
BuG3 B4	-53.1	-28.0	-26.3	-7.0	-217.0
Kibiro A3	-46.6	-27.4	-21.7	-11.6	-137.7
Kibiro B2	-47.7	-27.2	-22.1	-9.9	-139.1

Appendix A.7: Cu tube gas samples and their helium isotopic composition

Sample ID	**T_{H2O} [°C]***	**He4_Nml#**	**He3/He4**	**error_He3/He4**	**Ne/He$**	**R/Ra§**
Mumbuga3-2 A	43	3.00E-02	3.80E-06	1.00E-07	0.002	2.744
Mumbuga3-3 A	43	7.00E-02	3.75E-06	1.00E-07	0.002	2.708
Kagoro A	78	2.00E-02	3.90E-06	1.00E-07	0.002	2.816
Rwimi A	27	5.00E-04	2.10E-06	3.00E-08	0.002	1.516
Kibiro	74	6.00E-03	3.00E-07	1.00E-08	0.002	0.217

*Temperature was measured with an Hg-thermometer

analytical uncertainty = 50% in volume

$ analytical uncertainty = 0.001 in Ne/He ratio

§ calculated with Ra = 1.385 ×10^{-6}

Appendix A.8: Handouts of short course “noble gas geochemistry”

Short Course in

Noble gas geochemistry – An introduction

from 19.7. to 20.7.2005

at GSMD, Entebbe, Uganda

by
Michael Kraml
BGR Hannover, Germany

BGR Bundesanstalt für Geowissenschaften und Rohstoffe

What are the main aims of the course?

- questions of geothermal exploration for which noble gas analyses can deliver important results (with application to Buranga geothermal prospect)
- how noble gas sampling is done and major pitfalls
- reservoirs, origin of noble gases and natural processes which are affecting the isotopic composition of noble gases
- how noble gas isotopes can be analyzed (principles of noble gas mass spectrometry)
- Examples for interpretation of noble gas data (case studies)

BGR Bundesanstalt für Geowissenschaften und Rohstoffe

Why noble gas sampling in Uganda?

- **still hot magma chamber below Buranga geothermal site?**
  a) if yes => high chances for a viable geothermal resource => implications for exploration in Buranga area
  b) if not => exploration at different site with magmatic heat source

- **distinguish between three "end member" conceptual models**
  a) Buranga is fed by basinal brines ("oilfield brines") of the rift
  b) Buranga is fed by meteoric fluids from high Rwenzori mountains
  c) Buranga is fed by magmatic fluids of a hidden magma chamber [or Fort Portal volcanoes via deep reaching E-W trending faults] (in both cases of "c)" together with meteoric fluids of Rwenzori)

- **no noble gas isotope data available from Ugandan waters** => implications for underlying mantle (evidence for mantle plume?) => implications for rifting mechanism (explanation for difference between Eastern and Western branch of East African Rift in sedimentation; volcanic, hydrothermal and seismic activity, …)

BGR Bundesanstalt für Geowissenschaften und Rohstoffe

Hot magma chamber below Buranga?

Pros	Cons
• Geothermal anomaly (hot springs with nearly 100°C at surface) • CO_2 degassing (magmatic?) • Aeromagnetic evidence for large magmatic bodies in Albertine rift (still hot?) • Oxygen and carbon isotopic composition of sinter is similar to carbonatite (re-deposition of carbonate from an "old" carbonatite intrusion?)	• No surface expression of volcanism near Buranga • Chemical and isotopic O and H composition of hot spring water points to a meteoric origin • A magma chamber below Buranga is not necessary to explain the geothermal anomaly (there are alternatives)
=> continue with exploration at Buranga (e.g. deep reaching MT soundings but MT would be nearly impossible due to swamp and dense rain forest)	=> do further exploration at different place where heat source is located (e.g. Fort Portal volcanic field)

BGR Bundesanstalt für Geowissenschaften und Rohstoffe

Difference Eastern & Western branch 1

1) Lakes and sediments

From: Kraml & Bull 2000

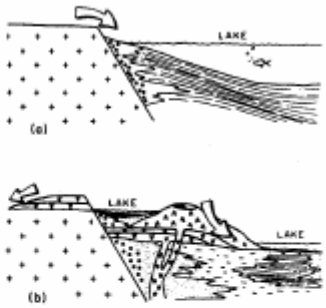

From: Yuretich 1982

Difference Eastern & Western branch 2

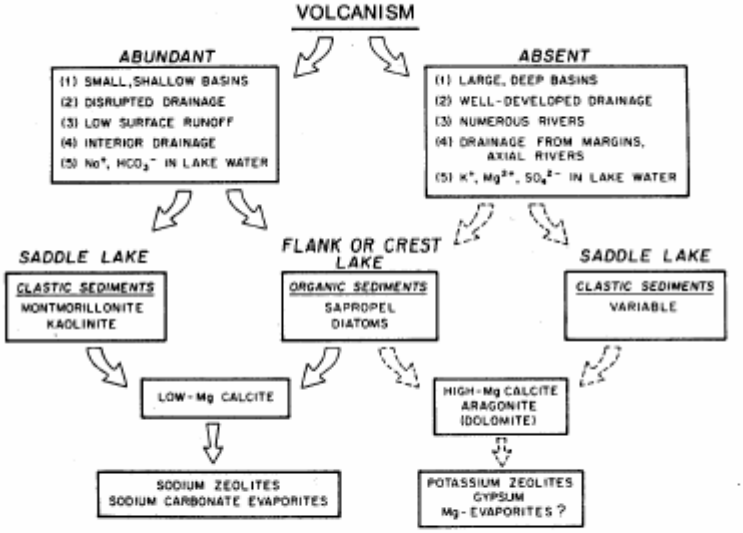

Summary of postulated volcanic influences upon development of lacustrine environments in the East African Rift Valleys. Normalization of climate has been assumed.

From: Yuretich 1982

Difference Eastern & Western branch 3

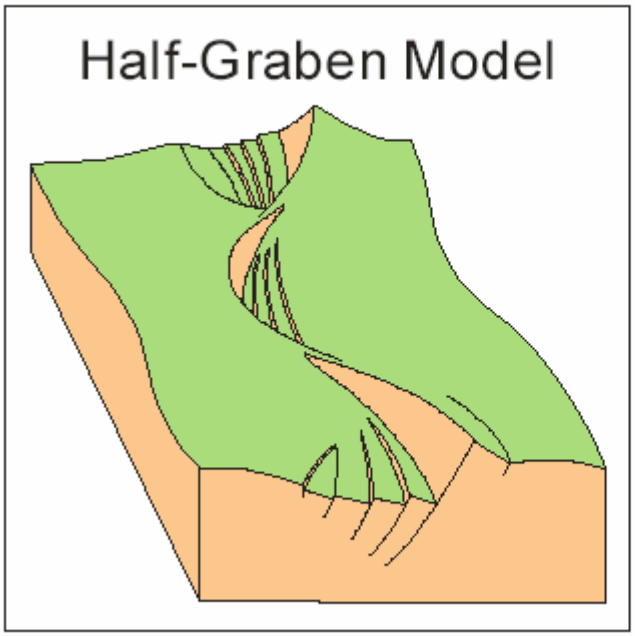

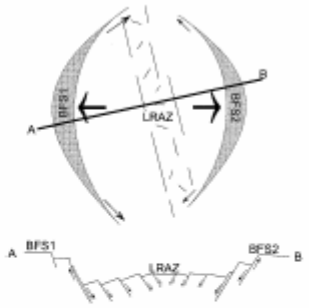

2) Tectonic style

From:
Rosendahl et al. 1986 modified and
Lærdal & Talbot 2002

Difference Eastern & Western branch 4

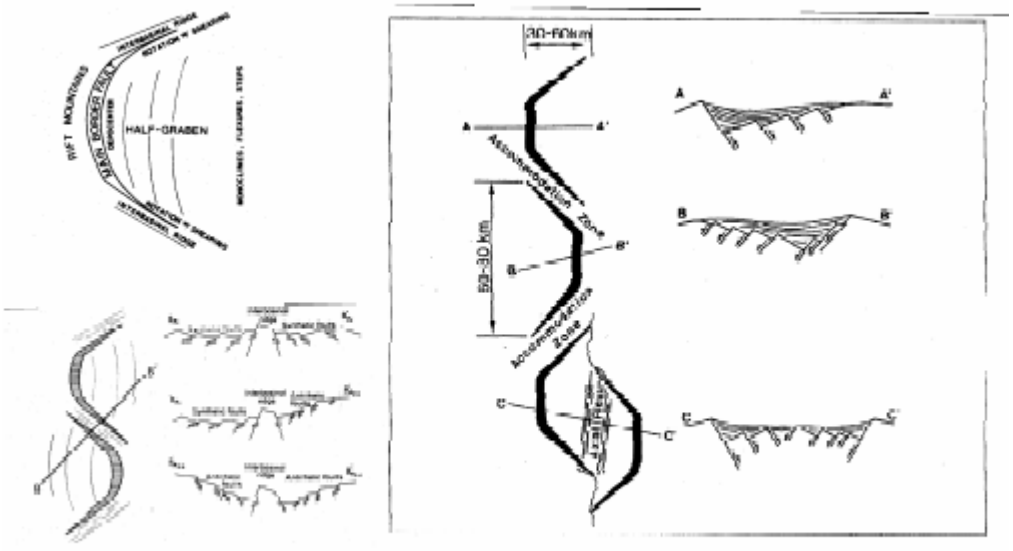

From: Rosendahl et al. 1986 and Rogers & Rosendahl 1989 modified

Difference Eastern & Western branch 4

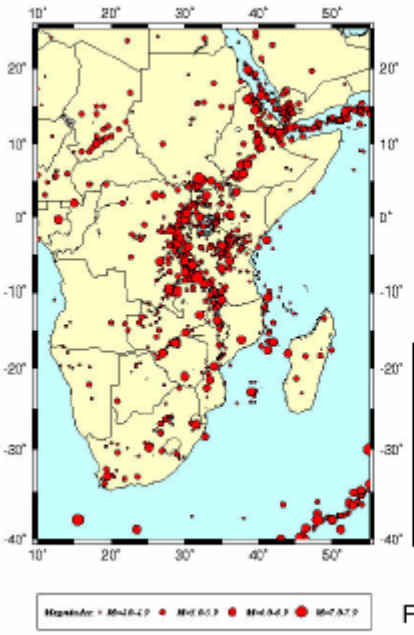

3) Seismic activity

Source zones	Mlow	Mupp	β	λ
6 (West-rift)	4.5	7.8	2.08	3.17
13 (Kenya)	4.5	7.4	1.37	0.14
5 (Ethiopia)	4.5	6.8	1.33	0.39

From: Midzi et al. 1999

BGR Bundesanstalt für Geowissenschaften und Rohstoffe

Difference Eastern & Western branch 5

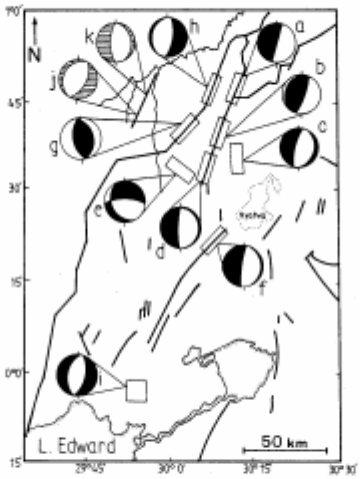

Fault plane solutions in the Rwenzoris Mt region. Plots a-i are upper hemisphere projections, while j & k are lower hemisphere projections. Shaded areas represent compression and rectangles the approximate areas where events for the solutions were located. Note solution c gives a more E-W fault plane solution compared to more common NNE-SSW trend (modified after Maasha 1975 b).

From: Maasha 1975 modified

BGR Bundesanstalt für Geowissenschaften und Rohstoffe

Difference Eastern & Western branch 6

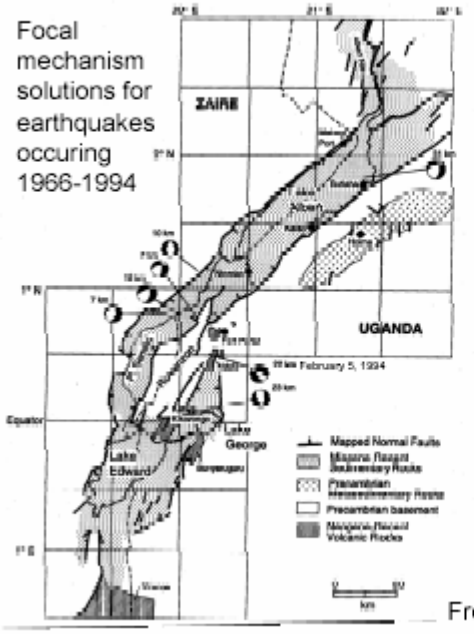

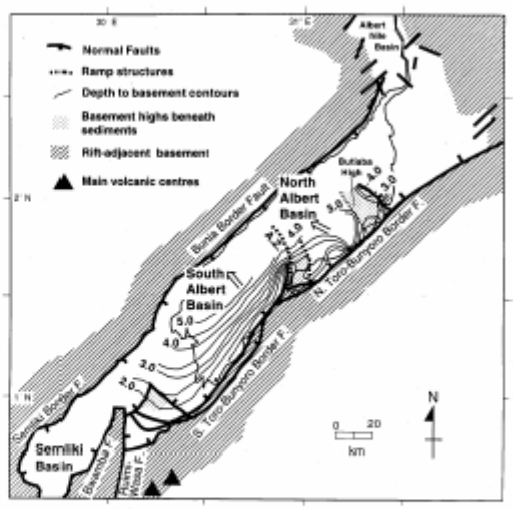

1. Semliki Border F. 2. Bwamba Fault
3. Ruimi Wasa F. 4. S. Toro-Bunyoro Border F.

From: Upcott et al. 1996

Difference Eastern & Western branch 7

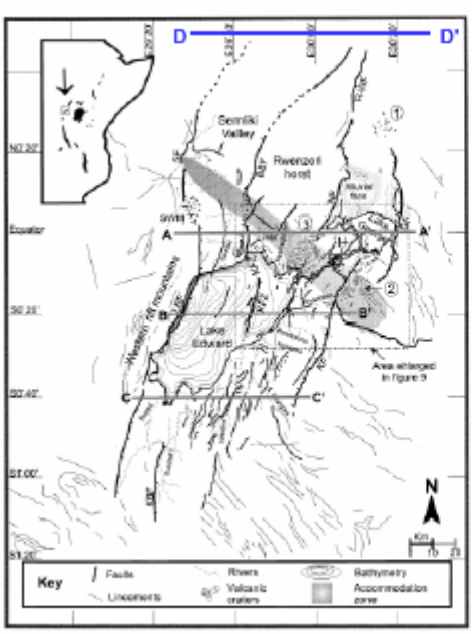

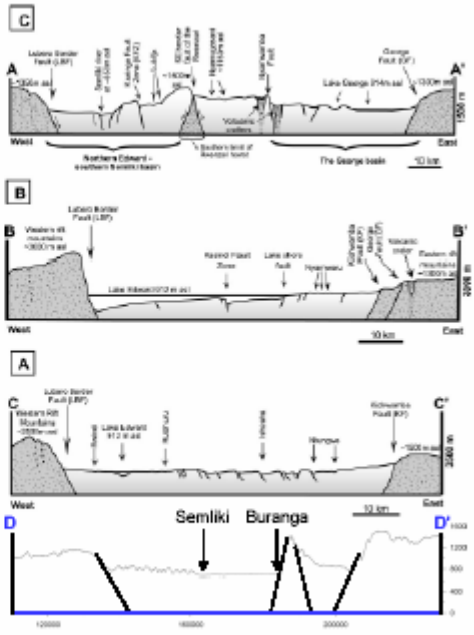

From: Lærdal & Talbot 2002

Difference Eastern and West Rift 8

Observed effects of different combinations of far-field stresses, plume presence and lithospheric thermal state on the style of rifting

Surf. heat flow; Lith. thickness; Lith. strength	Far field compression		Far field extension	
	plume	no plume	plume	no plume
Hot ≥70 m W/m²; ≤100 km; ≤40 TN/m	(1) Diffuse deformation; difficult (no) break-up (Turkana).	(2) Not applicable.	(3) Crust–mantle decoupling; diffuse deformation; difficult (no) break-up (Massif Central).	(4) Crust–mantle decoupling; linear, crustal rifting; no break-up; little extension (Rhine graben).
Intermediate 50–70 mW/m²; 100–150 km; 40–80 TN/m	(5) Whole lithosphere breaks; little extension (Kenya).	(6) Not applicable.	(7) Whole lithosphere breaks; continental break-up (Red Sea).	(8) Once initiated somewhere (plume), a crack propagates through the whole lithosphere (break-up: Red Sea or transform fault: Dead Sea).
Cold <50 mW/m²; >150 km; >80 TN/m	(9) Bending but little inelastic deformation (Tanzania craton).	(10) Not applicable.	(11) Cracks may open and allow magma ascent; no rifting (Nubian shield).	

From: Zeyen et al. 1997

Difference Eastern and West Rift 9

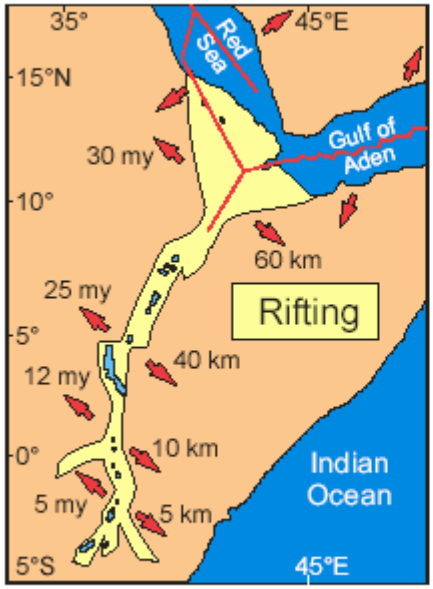

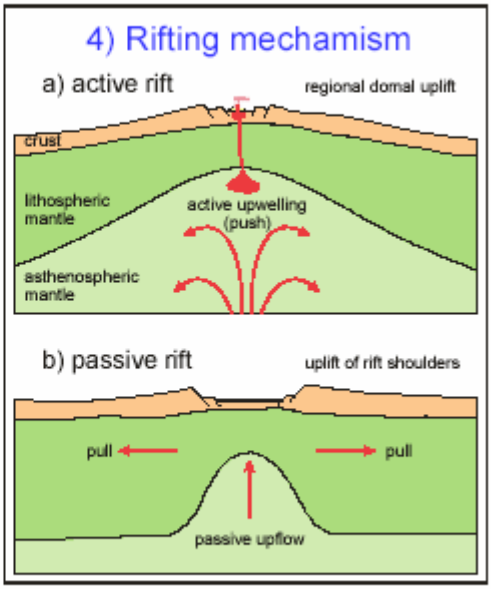

a) From: Strecker & Bosworth 1991 + additional sources b) From: Wilson 1989 modified

Difference Eastern and West Rift 10

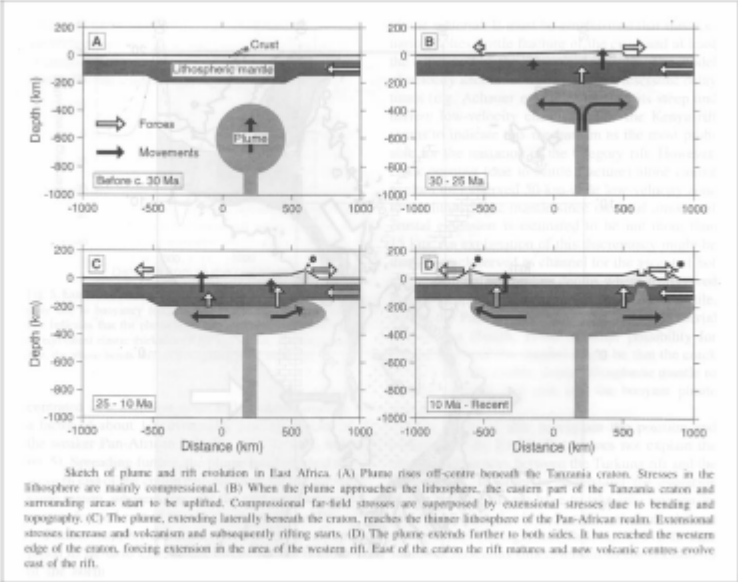

Sketch of plume and rift evolution in East Africa. (A) Plume rises off-centre beneath the Tanzania craton. Stresses in the lithosphere are mainly compressional. (B) When the plume approaches the lithosphere, the eastern part of the Tanzania craton and surrounding areas start to be uplifted. Compressional far-field stresses are superposed by extensional stresses due to bending and topography. (C) The plume, extending laterally beneath the craton, reaches the thinner lithosphere of the Pan-African realm. Extensional stresses increase and volcanism and subsequently rifting starts. (D) The plume extends further to both sides. It has reached the western edge of the craton, forcing extension in the area of the western rift. East of the craton the rift matures and new volcanic centres evolve east of the rift.

From: Zeyen et al. 1997

Difference Eastern and West Rift 11

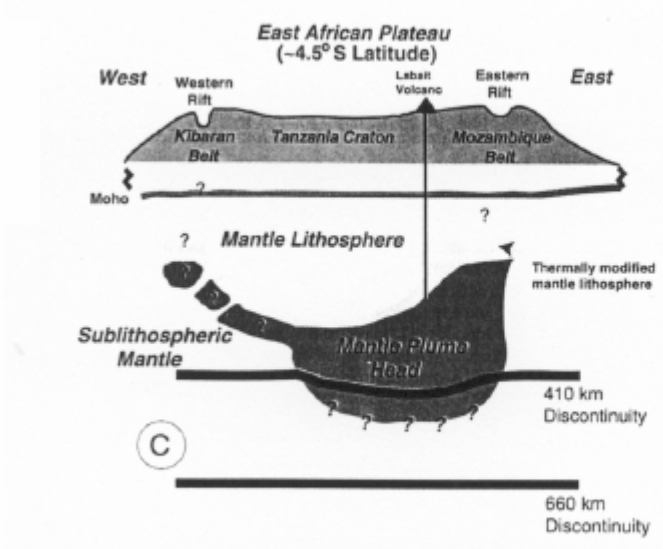

5) Seismology

Schematic cross section derived from S-wave velocity variations in the upper mantle

From: Nyblade et al. 2000

Difference Eastern and West Rift 12

5) Seismology

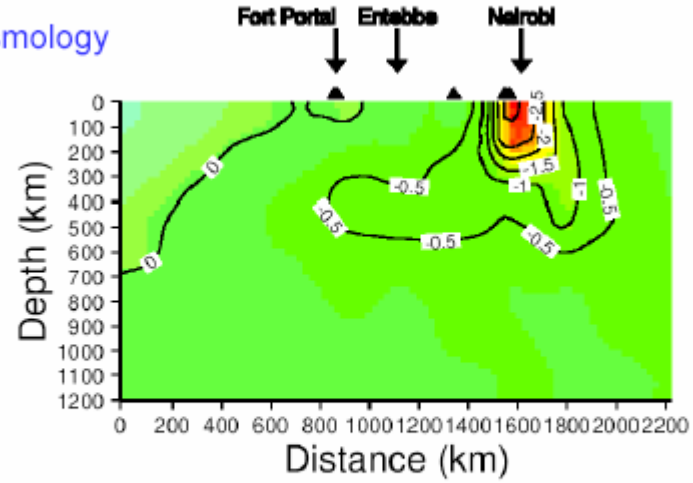

Tomographic (P wave) cross-section.
Contours show percentage P wave velocity differences

From: Bailey & Collier 2000

Difference Eastern and West Rift 13

6) Volcanic activity

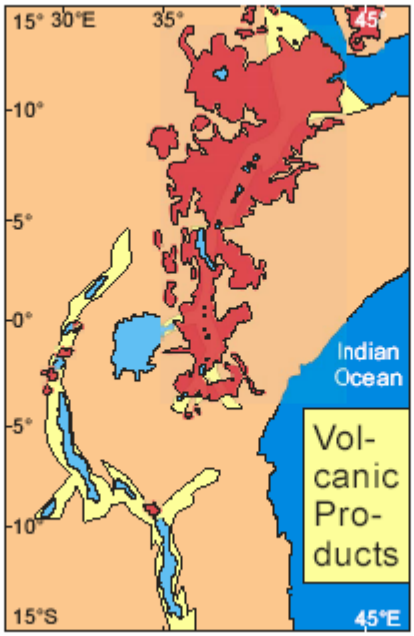

From: Yuretich 1982
and additional sources

Difference Eastern and West Rift 14

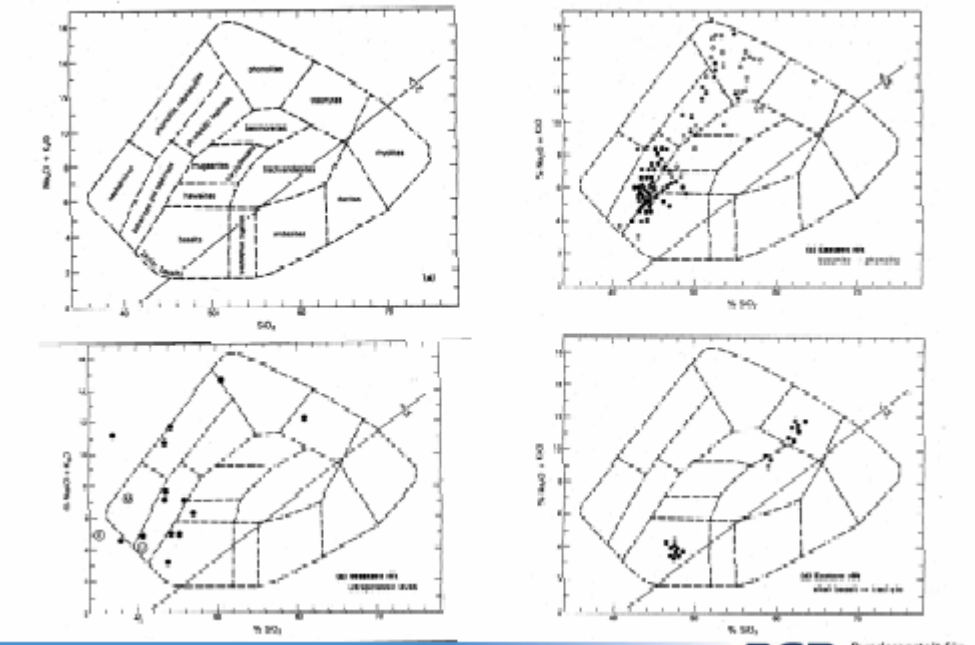

From: Wilson 1989

BGR Bundesanstalt für Geowissenschaften und Rohstoffe

Difference Eastern and West Rift 15

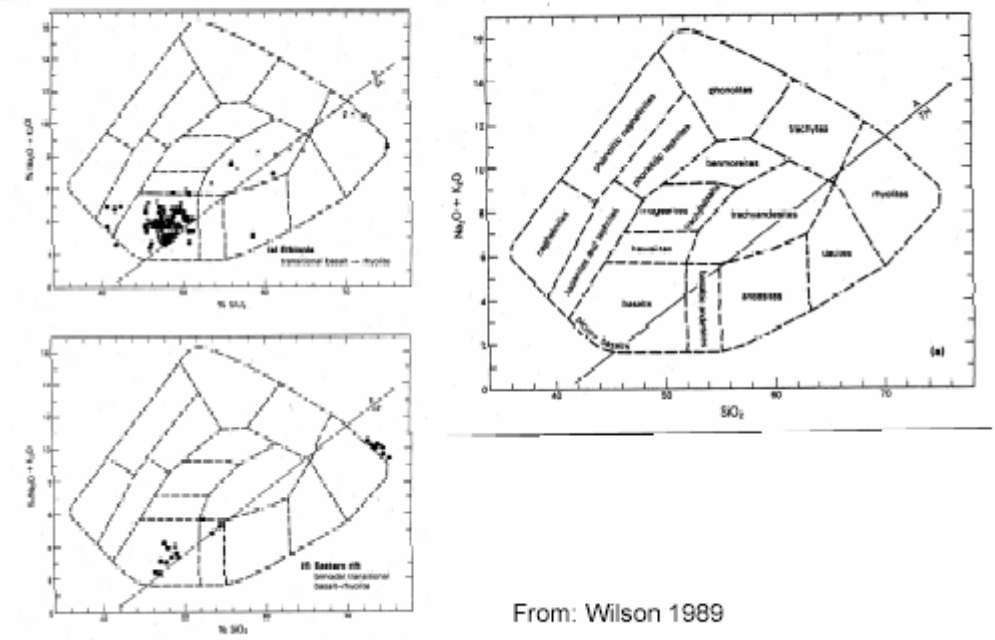

From: Wilson 1989

BGR Bundesanstalt für Geowissenschaften und Rohstoffe

Difference Eastern and West Rift 16

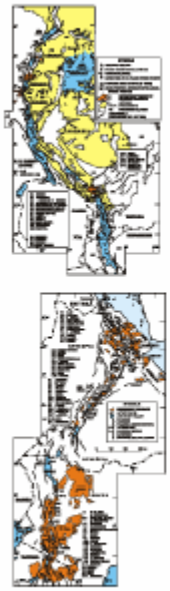

7) Hydrothermal activity

Compared parameter	Western Rift	Eastern Rift
Active volcanoes (active in last 2000 yrs)	4	12
Volcanic hydrothermal systems	0	11
Major hydrothermal systems (Q>10 MW)	7	31
Thermal spring systems (Q<1 MW)	c. 50?	40
Heat discharge rate of all hydrothermal systems and thermal springs (MW)	c. 300	4000
Earthquakes with m_b>5.0 (1965-2002)	c. 115	35 (40 Afar)
Total seismic energy released (PJ)	c. 15	2

From: Hochstein 2005

BGR Bundesanstalt für Geowissenschaften und Rohstoffe

Volcanism in East African Rift 1

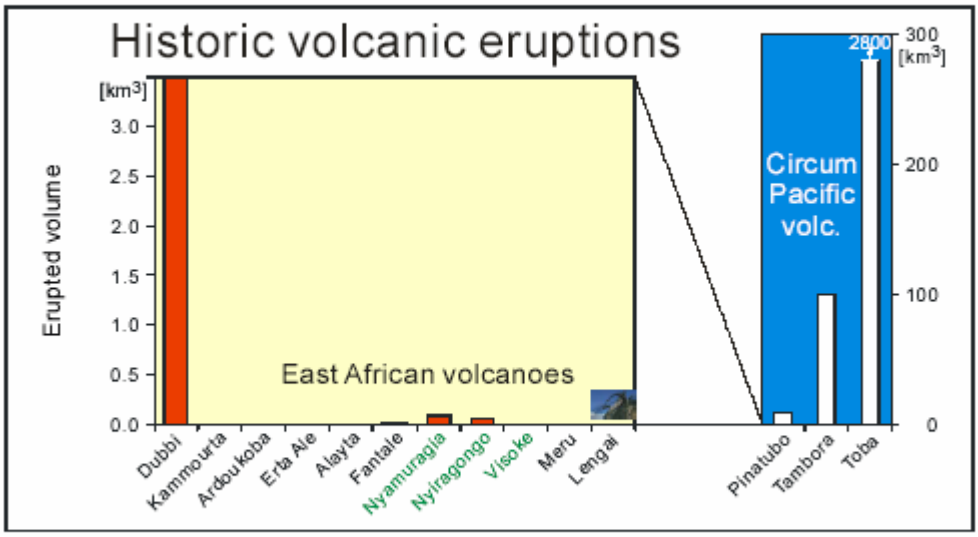

compiled from various sources

BGR Bundesanstalt für Geowissenschaften und Rohstoffe

Volcanism in East African Rift 2

Volcanism in East African Rift 3

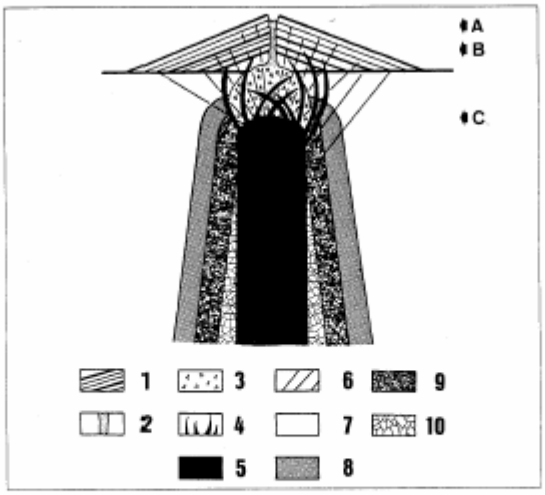

Schematic cross section through a carbonatite complex. East African carbonatites represented by A: Oldoinyo Lengai; B: Napak; C: SE Ugandan carbonatite complexes. 1: Alkalic metavolcanics with phonolite, nephelinite; 2: Natrocarbonatite; 3: Breccia zone; 4: Carbonatite ring dykes; 5: Carbonatite core; 6: Carbonatite cone-sheets; 7: Country rock, fenitized near the contact; 8: Syenite fenite; 9: Nepheline syenite; 10: Ijolite (modified after Kinnaird & Bowden 1991).

From: Kinnard & Bowden 1991 modified

Volcanism in East African Rift 4

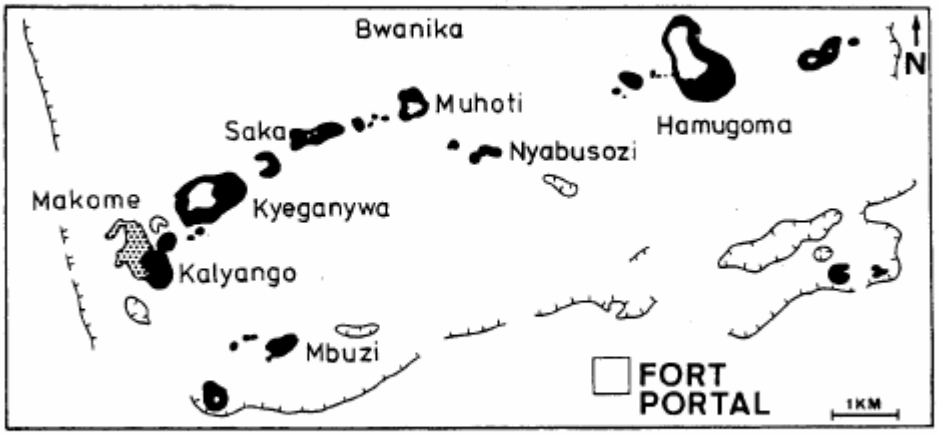

From: Barker & Nixon 1989

Volcanism in East African Rift 5

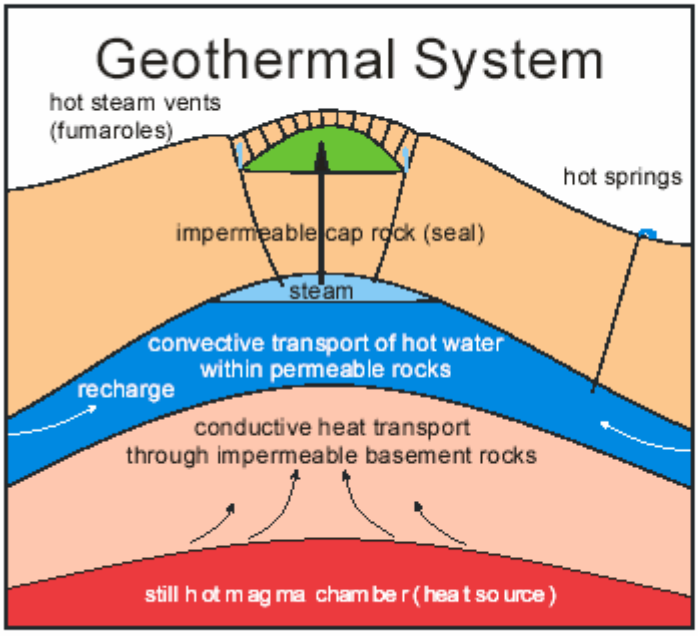

From: Brown 1996
modified

Volcanism in East African Rift 6

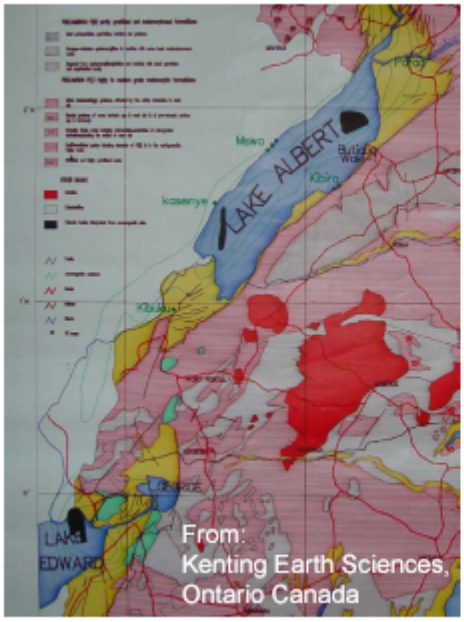

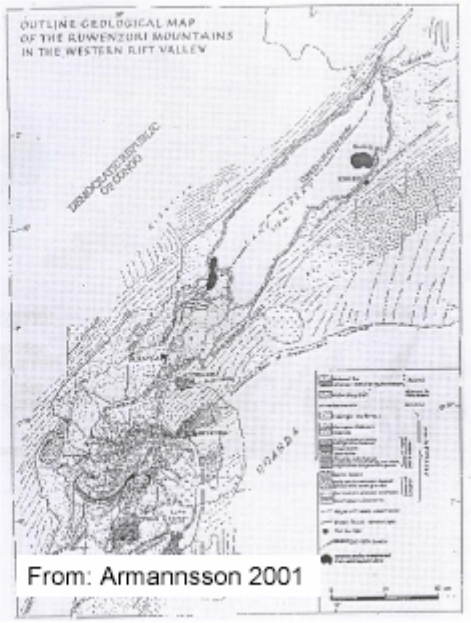

BGR Bundesanstalt für Geowissenschaften und Rohstoffe

Distuinguish between models 0

Theory of cognition (e.g. Popper 1959, 1963)

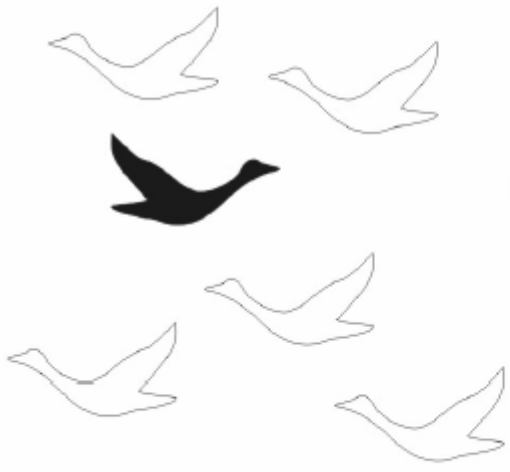

Keep in mind:
a theory, model or scenario
(which is a description of the reality)
cannot finally be proven
but finally be disproven!

BGR Bundesanstalt für Geowissenschaften und Rohstoffe

Distuinguish between models 1

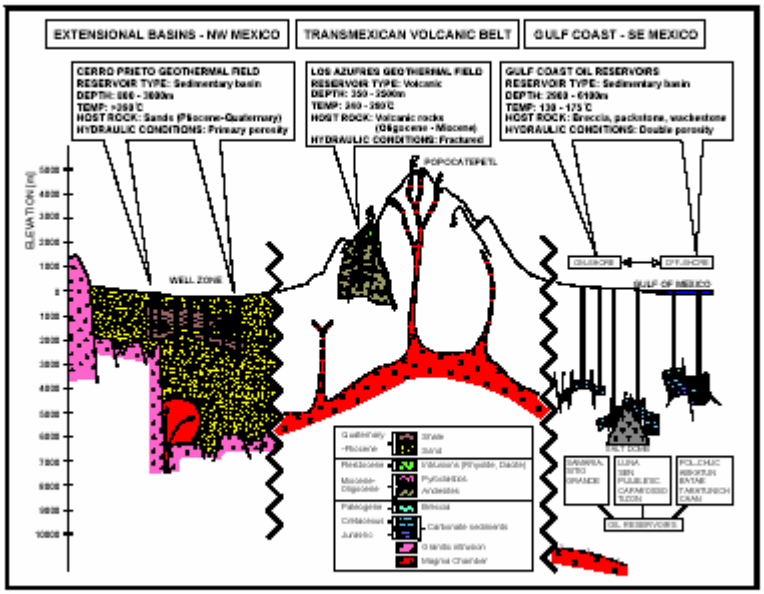

From: Birkle 2005

Distuinguish between models 2

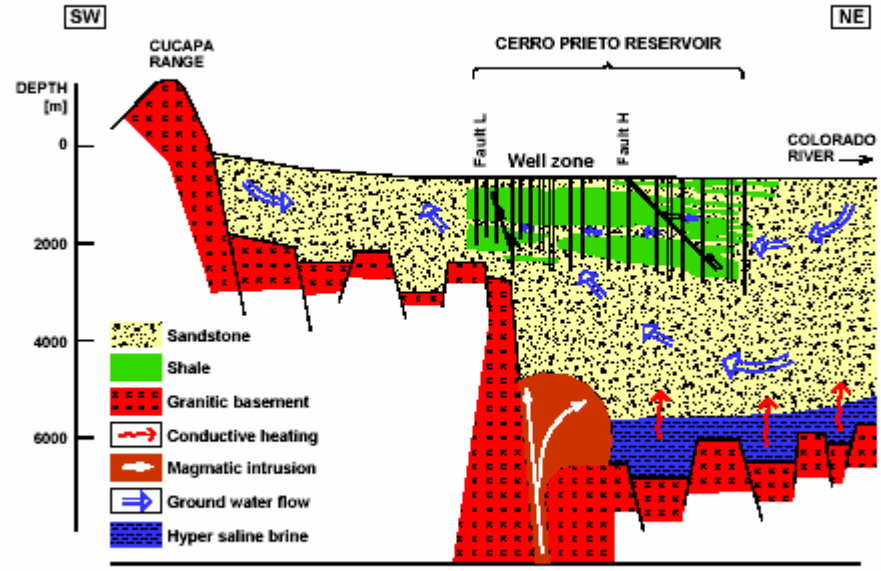

From: Halfman et al. 1984, Lippmann et al. 1991 (In: Birkle 2005)

Distuinguish between models 3

Type of reservoir	Geothermal fluids (Mexico)	Oilfield brines (Mexico)
Host rock	Volcanic + sedimentary	Carbonates
Components	Mixing: Magmatic + meteoric water	Connate (trapped fossil water)
Hydraulic system	Dynamic-convective circulation	Stagnant
Mobility	Medium - high	Low
Recharge	Partially	None

From: Birkle 2005

Distuinguish between models 4

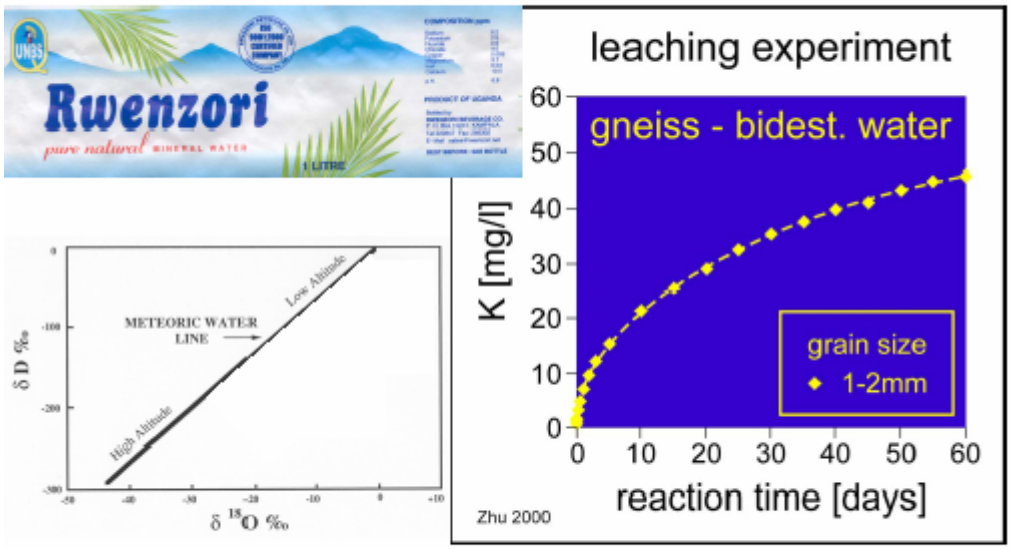

From: Craig 1961, Faure 1986 modified

Where gas sampling in Uganda?

- Buranga (Mumbuga & Kagoro; Nyansimbe is not accessible)
- Kibenge (possible source of recharge for Buranga)
- Rwimi (a & b) at southern end of Kyatwa or Ndale volcanic field

BGR Bundesanstalt für Geowissenschaften und Rohstoffe

Where gas sampling in Uganda (2)?

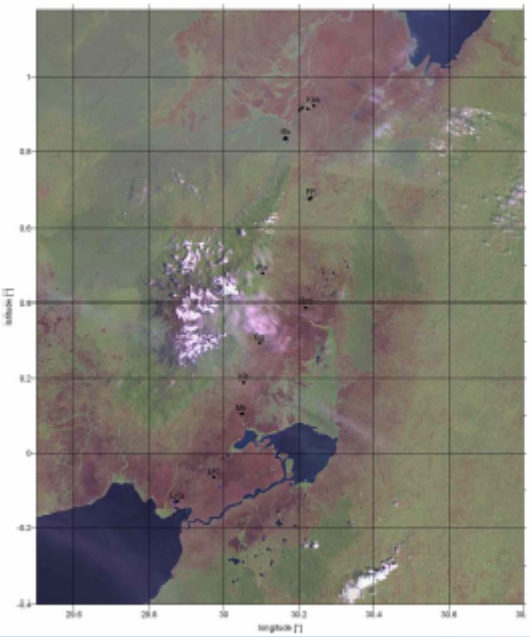

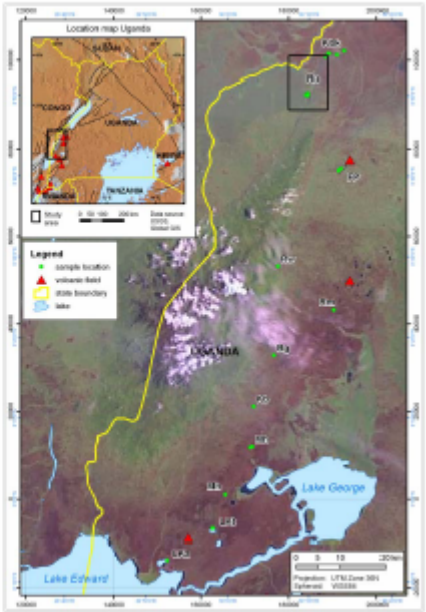

BGR Bundesanstalt für Geowissenschaften und Rohstoffe

How gas sampling?

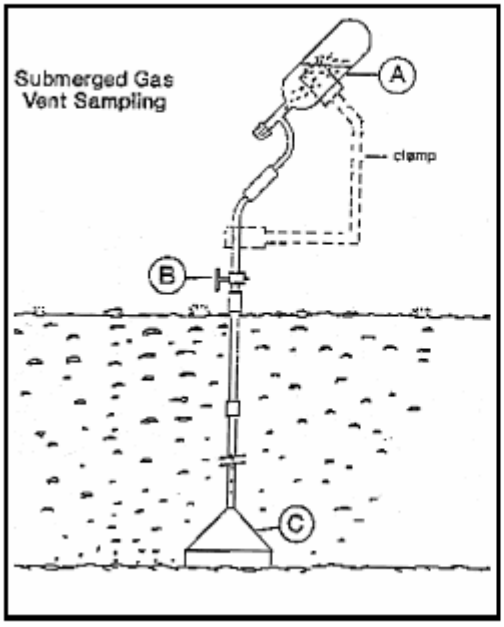

Possibility for gas (=> CO_2) sampling into evacuated flask

A: Evacuated flask
B: Valve
C: Funnel

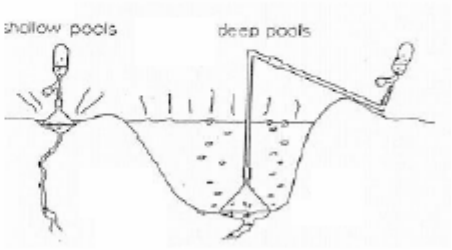

From: Giggenbach & Goguel 1989 and

Glover 1999 In: Armannsson 2001

BGR Bundesanstalt für Geowissenschaften und Rohstoffe

How gas sampling (2)?

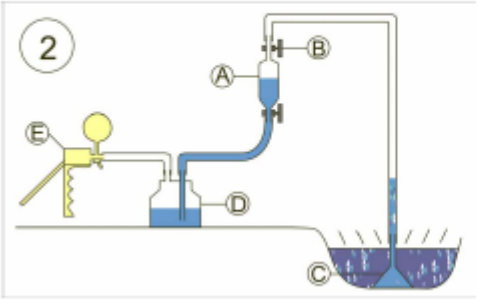

CO_2 sampling procedure
(following Dr. E. Faber, BGR Hannover, Germany)

A: Flask ("gas mouse")
B: Valve
C: Funnel
D: Bottle
E: Hand vacuum pump

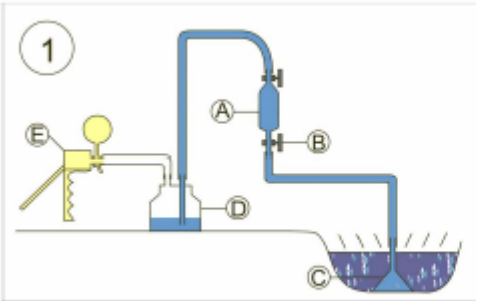

BGR Bundesanstalt für Geowissenschaften und Rohstoffe

How noble gas sampling?

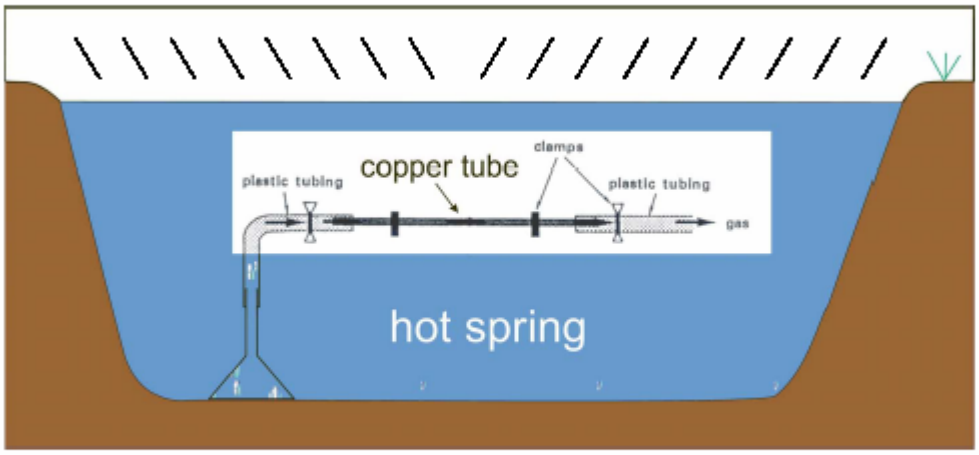

Noble gas sampling procedure
(following Dr. E. Griesshaber, University of Bochum, Germany)

BGR Bundesanstalt für Geowissenschaften und Rohstoffe

Implications for geothermal energy 1

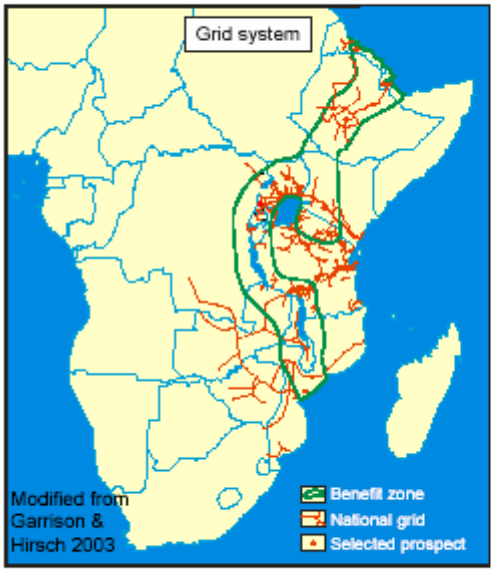

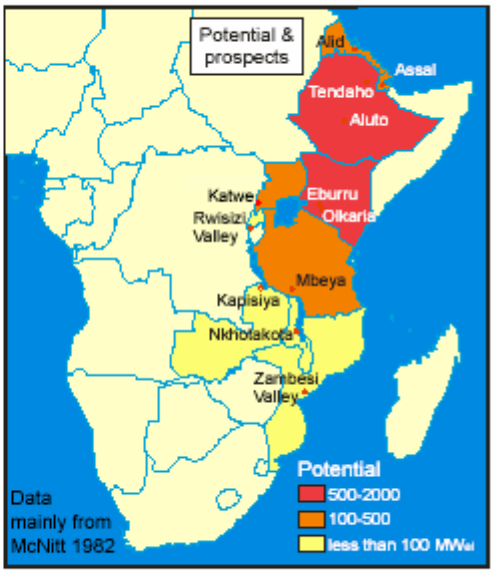

From: Kraml & Ochmann 2004 modified

BGR Bundesanstalt für Geowissenschaften und Rohstoffe

Implications for geothermal energy 2

Digital picture of Olkaria I steam power plant by Norbert Ochmann

BGR Bundesanstalt für Geowissenschaften und Rohstoffe

Implications for geothermal energy 3

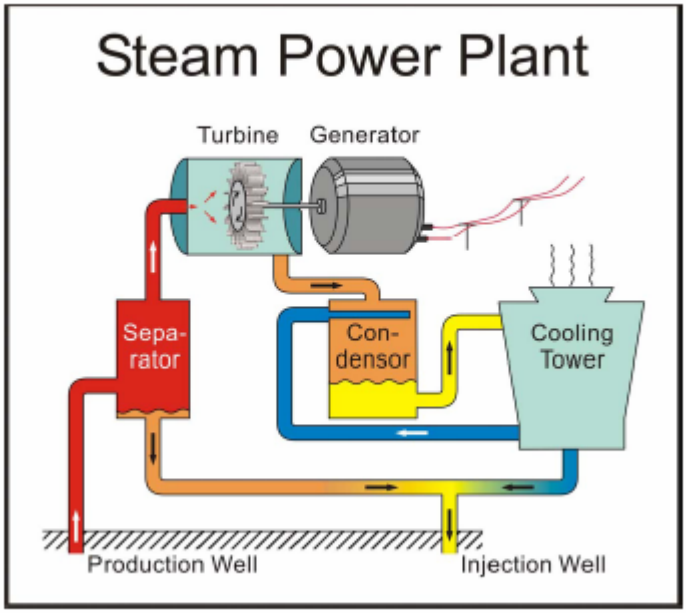

From various sources

BGR Bundesanstalt für Geowissenschaften und Rohstoffe

Implications for geothermal energy 4

Digital pictures of Olkaria binary power plant by Norbert Ochmann

BGR Bundesanstalt für Geowissenschaften und Rohstoffe

Implications for geothermal energy 5

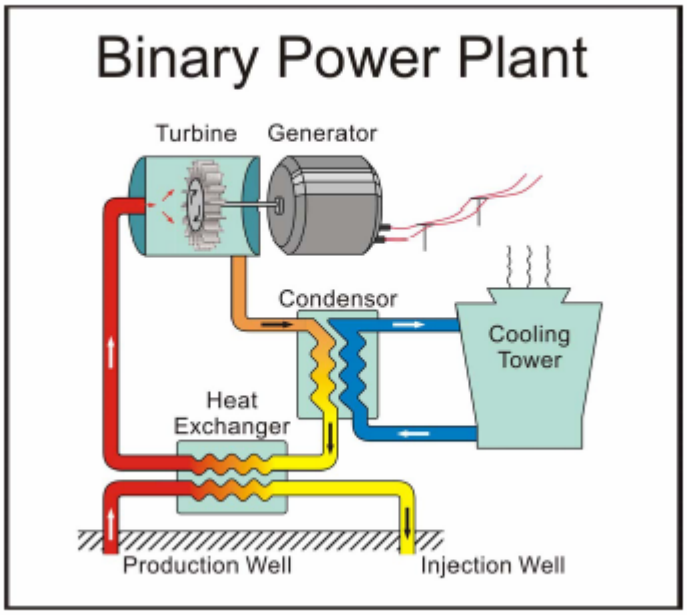

From various sources

BGR Bundesanstalt für Geowissenschaften und Rohstoffe

Implications for geothermal energy 6

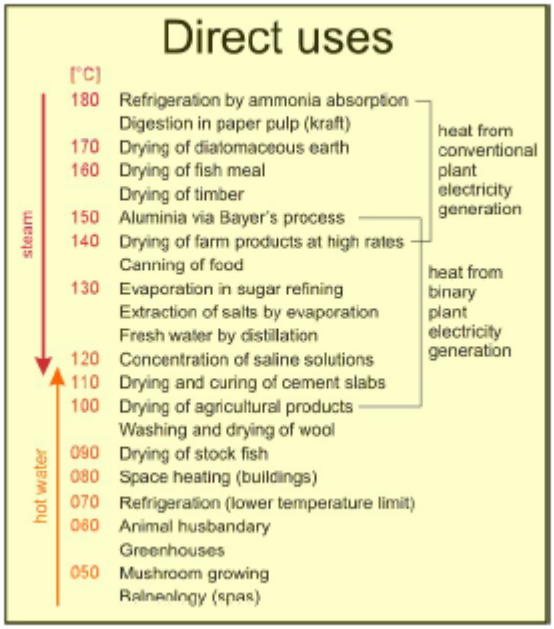

Lindal diagram

From:
Lund 2002
modified

Implications for geothermal energy 7

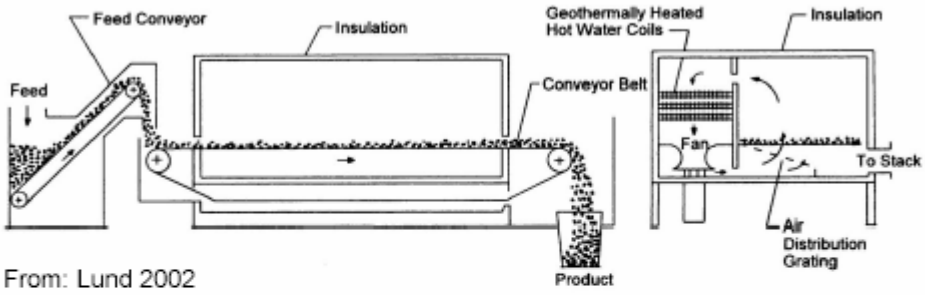

From: Lund 2002

e.g. for drying of cacao beans

Part 2: Introduction to noble gases

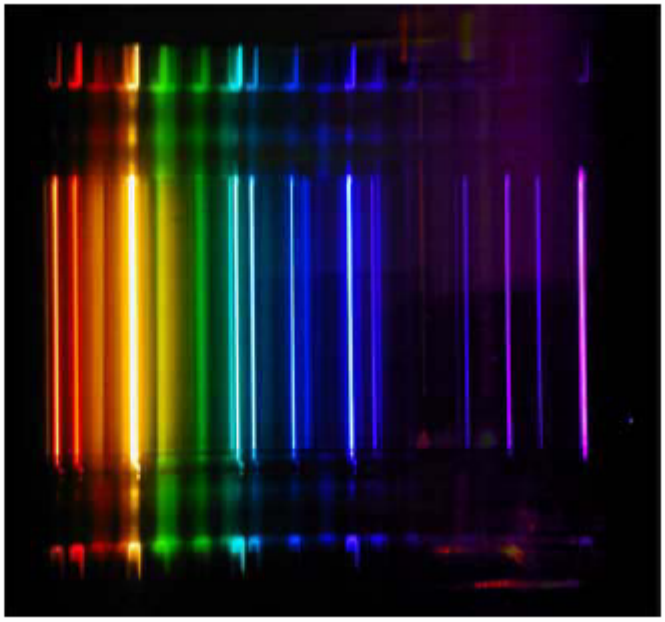

BGR Bundesanstalt für Geowissenschaften und Rohstoffe

Noble Gases Fundamentals 1

- first known experimental indication of noble gas existence by Cavendish in 1784 (gaseous residue after chemical removal of nitrogen and oxygen from air).
- first definitive indication when several observers in 1868 found a previously unknown line in the solar spectrum named helium {= Greek: sun} but no chemical characterization was possible.
- actual "discovery" of the noble gases by Rayleigh and Ramsey started in 1892 (nitrogen prepared from ammonia was less dense than the one prepared from air; during spectroscopic examination of the residue a new element named argon {lazy} was found). Shortly after publishing the discovery of argon in 1894 Ramsey found the helium in 1895 when he heated a uranium mineral.
- In 1898 three new elements were identified by fractional distillation experiments on liquid air: neon {new}, krypton {hidden} and xenon {strange}.
- In 1900-1903 the last noble gas radon {ray} was discovered by analyzing gaseous emanations of thorium and radium.

From: Ozima & Podosek 2002 and additional sources

BGR Bundesanstalt für Geowissenschaften und Rohstoffe

Noble Gases Fundamentals 2

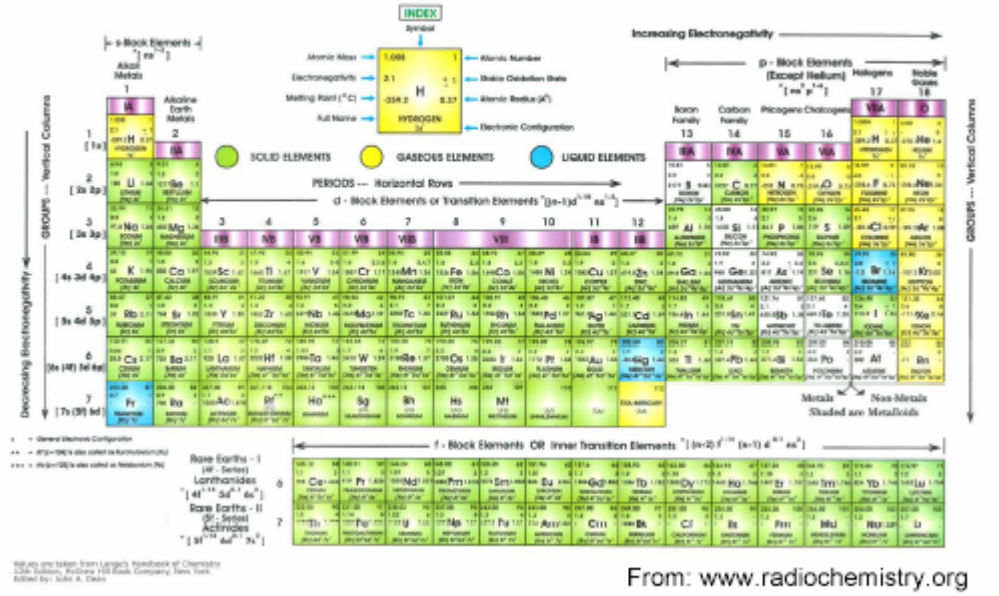

From: www.radiochemistry.org

Noble Gases Fundamentals 3

- development of mass spectrograph by Thomson in 1897

- first demonstration of multiple isotopes of a stable element (neon!) by Thomson in 1912. He found two isotopes of neon, one of mass number 20 and another of mass 22
- first development of mass spectrometer by Dempster in 1918 (first electron impact ion source and magnetic focussing) and Aston in 1919
- further development of mass spectrometer by Nier in 1940 and 1947 suitable for precise isotope ratio measurements ("Nier type" ion source)
- new determination of isotope abundances by Nier 1950 (e.g. atmospheric $^{40}Ar/^{36}Ar$ ratio of 296)
- further development of mass spectrometer by Reynolds in 1956 (static or "Reynolds type" mass spec.) for small gas quantities
- ultra-high-vacuum mass spec. commercially available in early 1980s

From: Ozima & Podosek 2002 and additional sources

Noble Gases Fundamentals 4

Nomenclature of nuclides

- **Atomic number** Z (number of protons which defines the element)
- **Mass number** A (sum of protons and neutrons)
- **Isotopes** (same number of protons, different number of neutrons)
- **Isobars** (same mass number)
- **Isotones** (same number of neutrons, different number of protons)

$$^{14}_{6}C \qquad A = 14,\ Z = 6,\ N = 8$$

From: Faure 1986

Noble Gases Fundamentals 5

Some constants and conversion factors

Avogadro's number (N_A)	6.02217×10^{23} molecules/mole
1 atm (760 torr)	1.01325×10^{5} Pa
1 cm^3 STP	4.465×10^{-5} mole = 2.688×10^{19} molecules
1 amu ($^{12}C \equiv 12$)	1.66053×10^{-24} g
1 eV/molecule	23.06 kcal/mole
1 cal	4.184 J

From: Ozima & Podosek 2002

Noble Gases Fundamentals 6

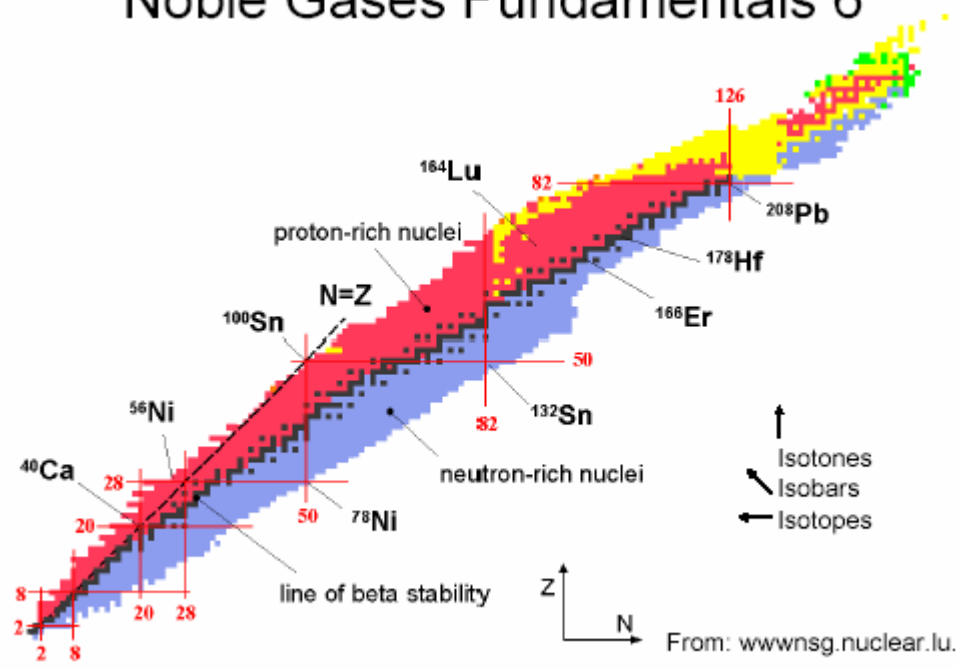

From: wwwnsg.nuclear.lu.se

Noble Gases Fundamentals 7

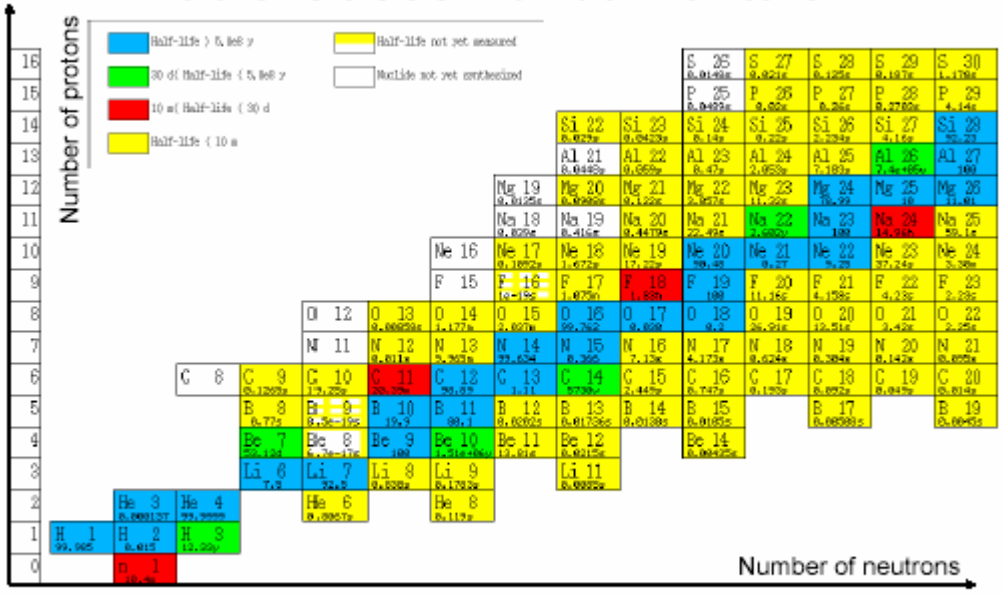

From: wwwndc.tokai.jaeri.go.jp

Noble Gases Fundamentals 8

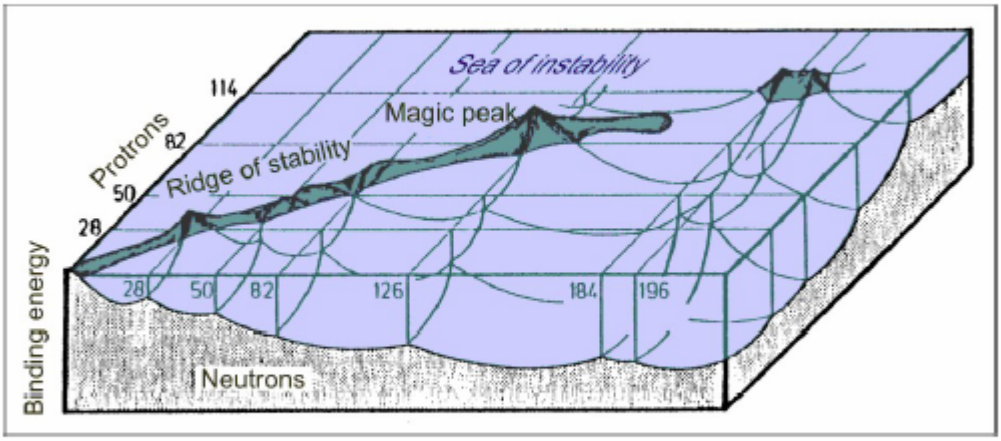

Noble Gases Fundamentals 9

Reservoirs and origin of noble gases

- **Cosmic abundances**
- **Extrasolar noble gases:** (e.g. presolar grains [= stardust] in undifferentiated meteorites)
- **Solar noble gases:** (sun, solar wind …)
- **Planetary noble gases:** (meteorites, atmospheres of planets …)
- **Earths atmosphere**
- **Earth surface waters:** (seawater, meteoric water [rain-, river-, lake-water])
- **Earths crust:** (radiogenic, cosmogenic and nucleogenic production, adsorbed to clay-rich sediments, cosmic dust, groundwater)
- **Earth mantle:** (volcanic rocks, diamonds, volcanic gases [in fumaroles and hot springs], mantle xenoliths)

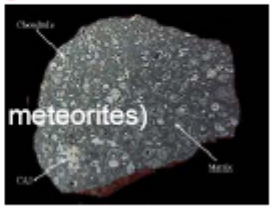

From: Ozima & Podosek 2002

Noble Gases Fundamentals 10

Gas	Molecular weight ($^{12}C \equiv 12$)	Volume fraction	Total inventory grams	Total inventory cm^3 STP
Dry air	28.9644	1	5.119×10^{21}	3.961×10^{24}
N_2	28.0134	0.78084	3.866×10^{21}	3.093×10^{24}
O_2	31.9988	0.20948	1.185×10^{21}	8.298×10^{23}
CO_2	44.0099	3.10×10^{-4}	2.45×10^{18}	1.248×10^{21}
He	4.0026	5.24×10^{-6}	3.707×10^{15}	2.076×10^{19}
Ne	20.179	1.82×10^{-5}	6.484×10^{16}	7.202×10^{19}
Ar	39.948	9.34×10^{-3}	6.594×10^{19}	3.700×10^{22}
Kr	83.80	1.14×10^{-6}	1.688×10^{16}	4.516×10^{18}
Xe	131.30	8.7×10^{-8}	2.019×10^{15}	3.446×10^{17}

Elemental composition of dry air

From: Ozima & Podosek 2002

BGR Bundesanstalt für Geowissenschaften und Rohstoffe

Noble Gases Fundamentals 11

Isotopic composition and abundance of atmosperic He, Ne & Ar

Isotope	Isotopic ratios	Isotopic ratios (alternate)	% atomic abundance	Total abundance§ (cm^3 STP/g)
^3He	0.000001399		0.00014	
^4He	≡1		100	3.473×10^{-9}
^{20}Ne	≡1	9.80	90.5	1.091×10^{-8}
^{21}Ne	0.00296	0.029	0.268	
^{22}Ne	0.1020	≡1	9.23	
^{36}Ar	0.003378	≡1	0.3364	2.083×10^{-8}
^{38}Ar	0.000635	0.188	0.0632	
^{40}Ar	≡1	296.0	99.6	6.166×10^{-6}

§ atmosperic inventory divided by the mass of the earth (5.976×10^{27}g)

From: Ozima & Podosek 2002

BGR Bundesanstalt für Geowissenschaften und Rohstoffe

Noble Gases Fundamentals 12

Models for evolution of atmospheric argon isotopic composition

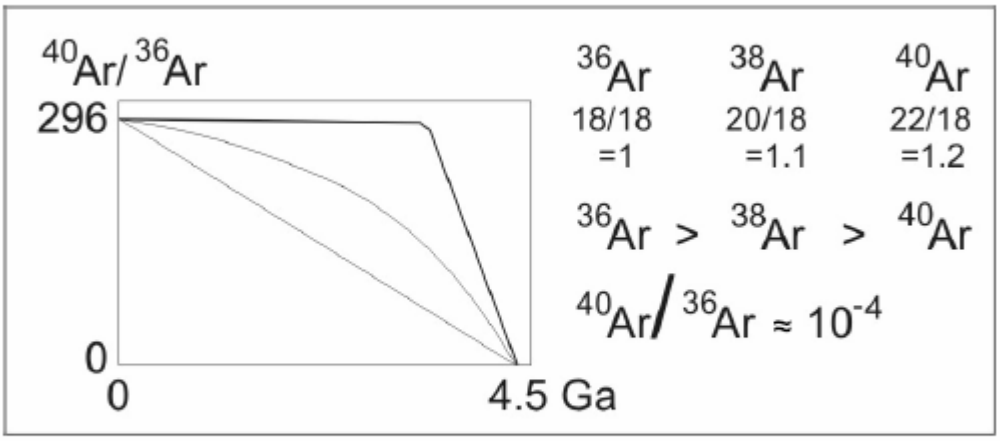

Paleoatmospheric $^{40}Ar/^{36}Ar$ ratio in Devonian (~400 Ma old chert of hot spring system) = 292.1 ± 0.6 (Rice et al. 1995)
and $^{40}Ar/^{36}Ar$ ratio in Precambrian (~2 Ga old C-bearing shungites) = indistinguishable from present-day atmospheric composition (Trieloff et al. 2005)

Noble Gases Fundamentals 13

Modes of decay (α, β⁻, β⁺, sf)

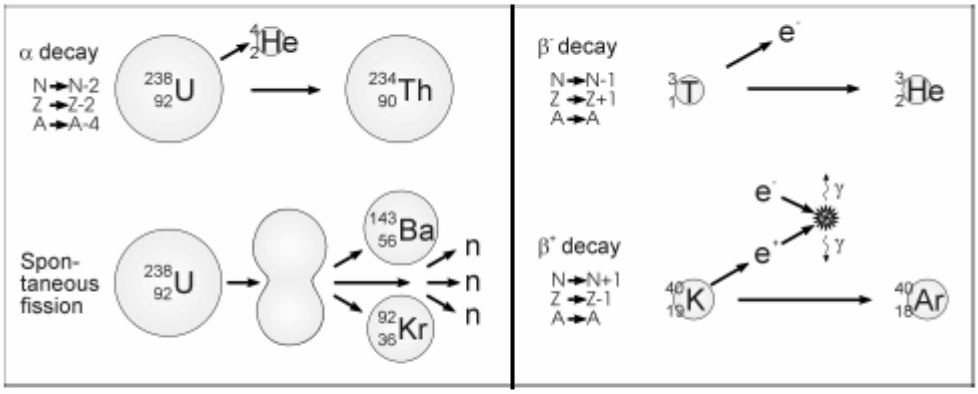

Noble Gases Fundamentals 14

Double beta decay (β+β+):

two neutrons are changed into protons inside the nucleus, emitting two electrons and two antineutrinos (=> Feynman graph)

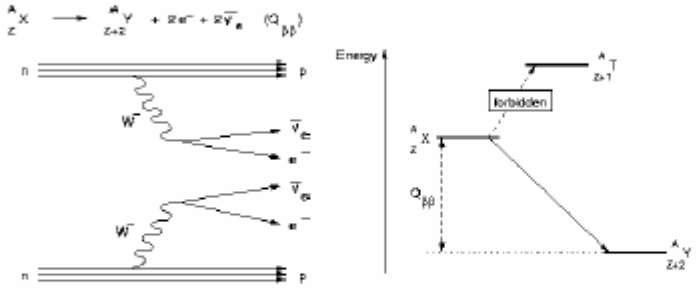

Energy scheme for the double β⁻ decay from parent nucleus ^{A}X to daughter nucleus ^{A}Y. The single β⁻ decay to the intermediate isotope ^{A}T is forbidden by the energy conservation rule.

Parent	Daughter	Qββ [MeV]	Isotopic abundance [%]	Half life [years]
^{82}Se	^{82}Kr	2.995	9.2	~ 1×10^{20} Kirsten et al. 1986

BGR Bundesanstalt für Geowissenschaften und Rohstoffe

Noble Gases Fundamentals 15

Decay chains and branched decay:

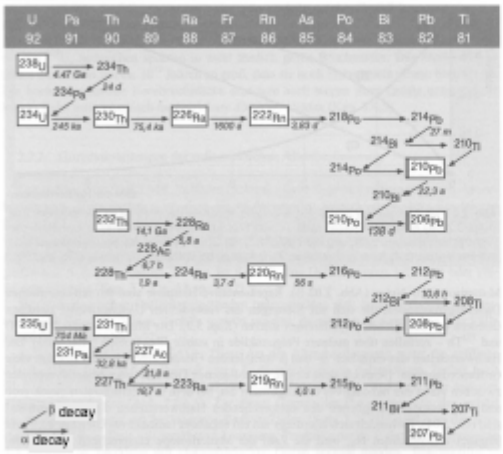

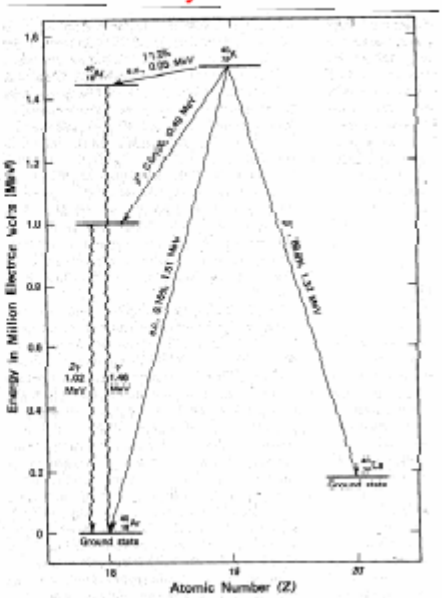

From: Geyh 2005 (left) and Faure 1986 (right)

BGR Bundesanstalt für Geowissenschaften und Rohstoffe

Noble Gases Fundamentals 16

Parent	Half-life [Ga]	Decay	Daughter	Yield
^{238}U	4.468	α	^{4}He	8
^{235}U	0.7038	α	^{4}He	7
^{232}Th	14.01	α	^{4}He	6
^{40}K	1.251	e.c. and β^+	^{40}Ar	0.1048
Other nuclear processes		**Cosmogenic noble gases (produced by cosmic rays)**		
Reaction	Product	Main targets	Isotopes	Half-life (yr)
^{6}Li (n, α)	^{3}He	O, Mg, Si, Fe (N, O)	^{3}H	12.3 (→ ^{3}He)
^{18}O (α, n)	^{21}Ne	O, Mg, Si, Fe (N, O)	^{3}He, ^{4}He	stable
^{19}F (α, n)	^{22}Ne	O, Mg, Si, Fe (N, O)	$^{20; 21; 22}Ne$	stable
^{35}Cl (α, p)	^{38}Ar	Fe, Ca, K	^{36}Ar, ^{38}Ar	stable
		Fe, Ca, K (Ar)	^{37}Ar	35.1 days
		Fe, Ca, K (Ar)	^{39}Ar	269

From: Ozima & Podosek 2002 (selection of natural nuclear processes)

Noble Gases Fundamentals 17

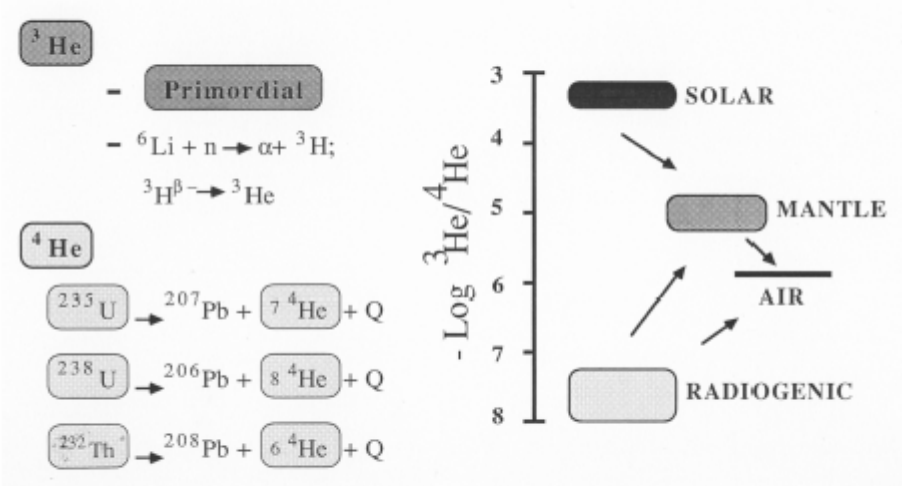

From: Griesshaber 1990

Noble Gases Fundamentals 18

Important processes concerning noble gases

- **Mixing of noble gases from different sources**
- **Solution in fluids (melts, waters, oil) and partitioning into the gas phase (CO_2 bubbles, natural gas)**
- **Crystal-melt partitioning**
- **Diffusion of noble gases in solids**
- **Adsorption of noble gases at sediments (clay minerals) and at the walls of the vacuum system**
- **Trapping of noble gases in meteorites** (neither cosmogenic nor radiogenic production but e.g. implantation of solar wind ions into asteroidal regoliths => solar pattern resembling "cosmic" abundances)
- **Isotopic fractionation in nature and discrimination during mass spectrometric analyses**

From: Ozima & Podosek 2002

BGR Bundesanstalt für Geowissenschaften und Rohstoffe

Noble Gases Fundamentals 19

Mixing

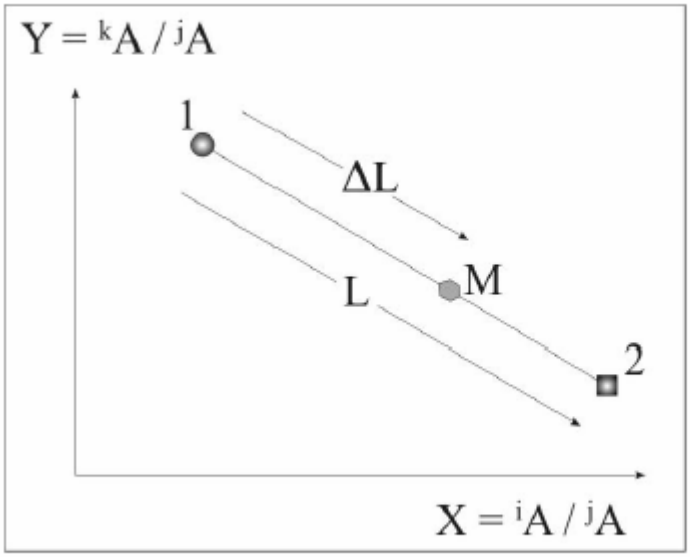

1 and 2 = two components with distinct composition.

Straight line = all mixtures of component 1 and 2.

M = mixture composition.

Ratio of ΔL and L = fractional contribution that 2 contributes to ^{i}A (reference isotope).

Qualitatively, the closer the mixture composition is to component 2, the greater is the contribution of component 2 to the mixture (for the reference isotope).

From: Ozima & Podosek 2002 Three-Isotope diagrams

BGR Bundesanstalt für Geowissenschaften und Rohstoffe

Noble Gases Fundamentals 20

Solubility in water

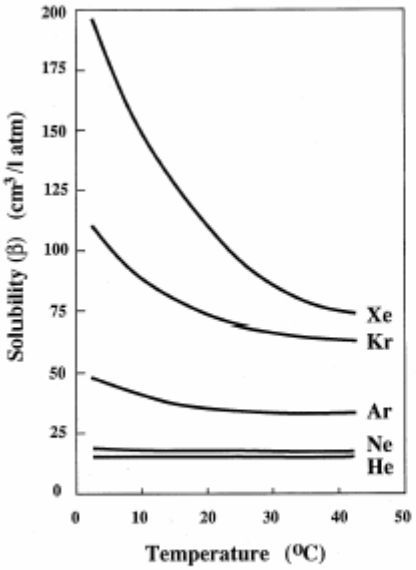

modified from:
Benson and Krause 1976
and Andrews 1992

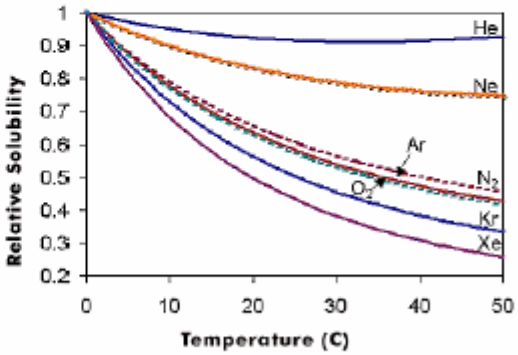

From: Benson & Krause 1976 In: Griesshaber 1990

BGR Bundesanstalt für Geowissenschaften und Rohstoffe

Noble Gases Fundamentals 21

The equilibrium relationship between the atmosphere and the body of water is described in Henry's Law:

$$p_i = k_i(T,S)x_i$$

where p_i is the partial pressure of the noble gas in the gas phase, k_i is a proportionality coefficient (Henry's coefficient, dependent on temperature [T] and salinity [S]), and x_i is the equilibrium concentration of the dissolved gas in water (or other liquid) as a mole fraction. In other words, the equilibrium concentration of the noble gases depends on three parameters: temperature, salinity, and atmospheric pressure.

From: http://www.sahra.arizona.edu/programs/isotopes/noble.html

BGR Bundesanstalt für Geowissenschaften und Rohstoffe

Noble Gases Fundamentals 22

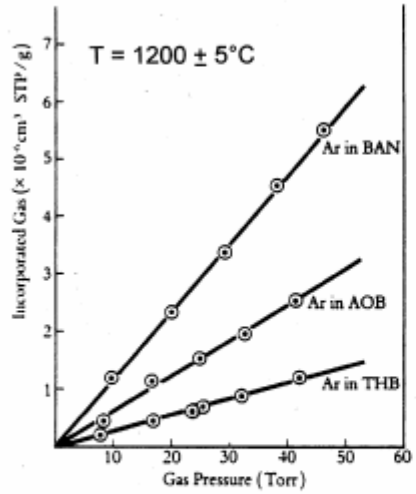

For small incorporated gas amounts Henry's Law is also valid for melts (solubility depends strongly on composition and a little bit on temperature)

From: Lux 1987

Solubility in melts and solids

Solvent	T [°C]	$10^{-5}cm^3STPg^{-1}atm^{-1}$		
Melts: P=1atm (760Torr)		He	Ne	Ar
Tholeitic basalt	1350	64	35	8.7
Alkali olivin basalt	1350	57	26	6.4
Basanite	1350	70	42	12.2
Ugandite	1350	48	21	4.5
Melts: P=15kbar				
Basalt	1600			4.7
Granite	1600			39.1
Solids: P=1kbar				
Anorthite	1300		0.016	0.39
Diopside	1300		0.018	0.35

From: Ozima & Podosek 2002

BGR Bundesanstalt für Geowissenschaften und Rohstoffe

Noble Gases Fundamentals 23

Solubility in different materials – A comparison (example Ar)

Note that due to the volatile nature of the noble gases they have a strong tendency to partition into gas or fluid phases and can therefore be used as inert tracers for the origin and transport of fluids.

Solubility of Ar in sea water (saline fluids): ≈ 400 ppm

Solubility of Ar in silicate melt ≈ 0.02 ppm

Solubility of Ar in solid feldspar (orthoclase): ≈ $5 * 10^{-6}$ ppm

Compiled from various sources, In: Kraml 1997

BGR Bundesanstalt für Geowissenschaften und Rohstoffe

Noble Gases Fundamentals 24

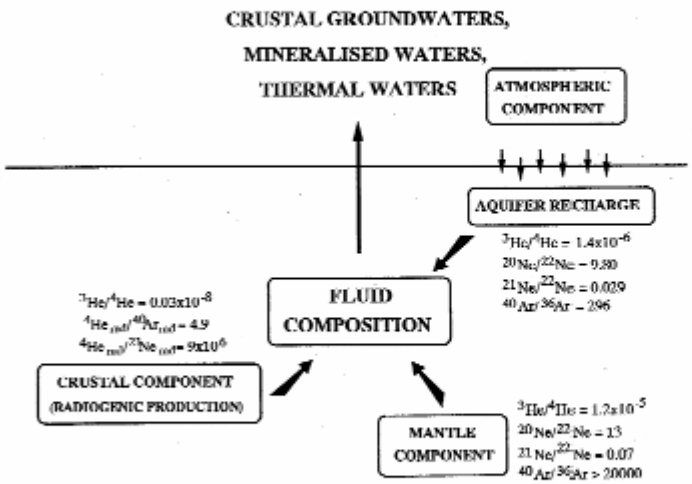

From: Griesshaber 1990

Noble Gases Fundamentals 25

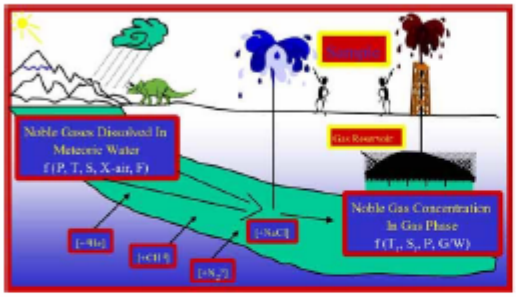

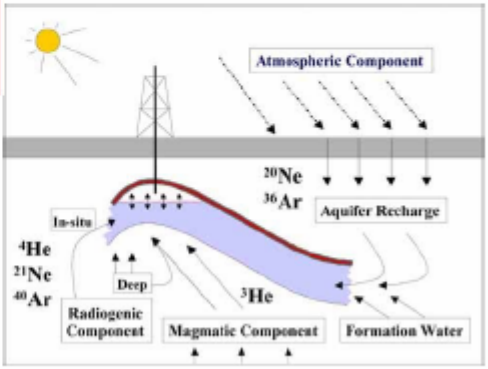

From: www.seaes.manchester.ac.uk

Noble Gases Fundamentals 26

Mantle reservoirs and their isotopic signature (classic model)

3He/4He	R/Ra	20Ne/22Ne	40Ar/36Ar
0.14 *10-5	1	9.80	296
≈ 1.2 *10-5	≈ 8	≈ 12	>30000
≈ 4 *10-5	≈ 29	≈ 12	>3000

$R/Ra = (^3He/^4He)_{sample} / (^3He/^4He)_{atmospheric}$

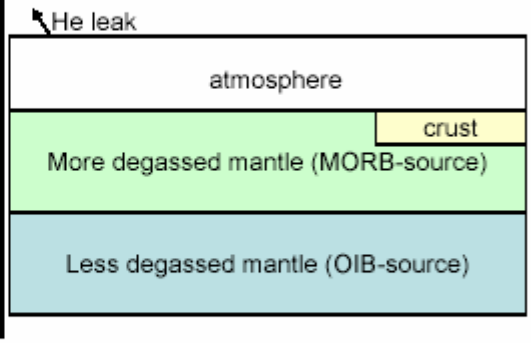

All R/Ra values significantly > 8 indicate a plume component (OIB-source).
Ne & Ar isotopic compositions are used to support this interpretation and to delineate atmospheric contamination.

Mainly from: Ozima & Podosek 2002

R/Ra for Buranga = ? (your prediction)

BGR Bundesanstalt für Geowissenschaften und Rohstoffe

Noble Gases Fundamentals 27

Further reading:

M. Ozima & F.A. Podosek (2002):
Noble Gas Geochemistry.-
Second Edition, Cambridge University Press, 286 pages

D. Porcelli, C.J. Ballentine & R. Wieler (editors 2002):
– Noble Gases – In GEOCHEMISTRY AND COSMOCHEMISTRY.-
In: Reviews in Mineralogy and Geochemistry,
Volume 47, 844 pages

BGR Bundesanstalt für Geowissenschaften und Rohstoffe

Why additional $\delta^{13}C$ analyses?

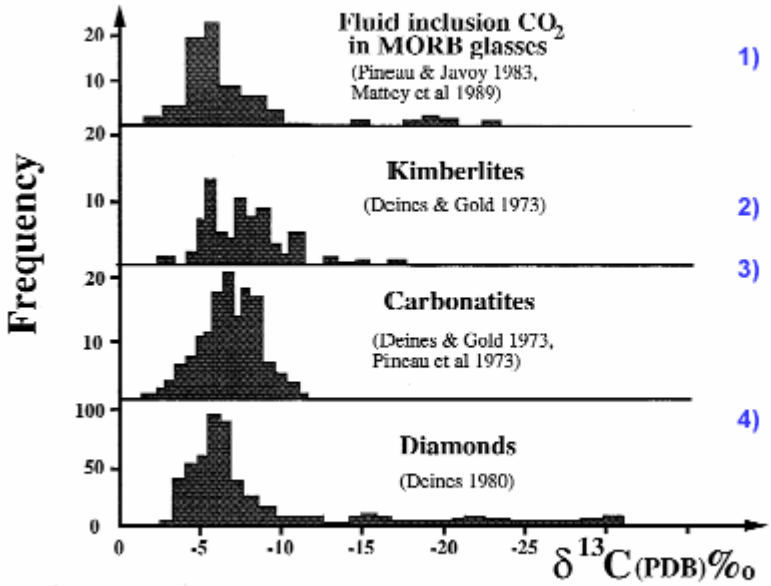

1) Give a good first indication for magmatic or sedimentary origin
2) Can be analysed fast and cheap
3) Are useful for selection of most promising noble gas samples
4) Combined data sets always enhance reliability of interpretation

In: Griesshaber 1990

BGR Bundesanstalt für Geowissenschaften und Rohstoffe

Why additional $\delta^{13}C$ analyses? (2)

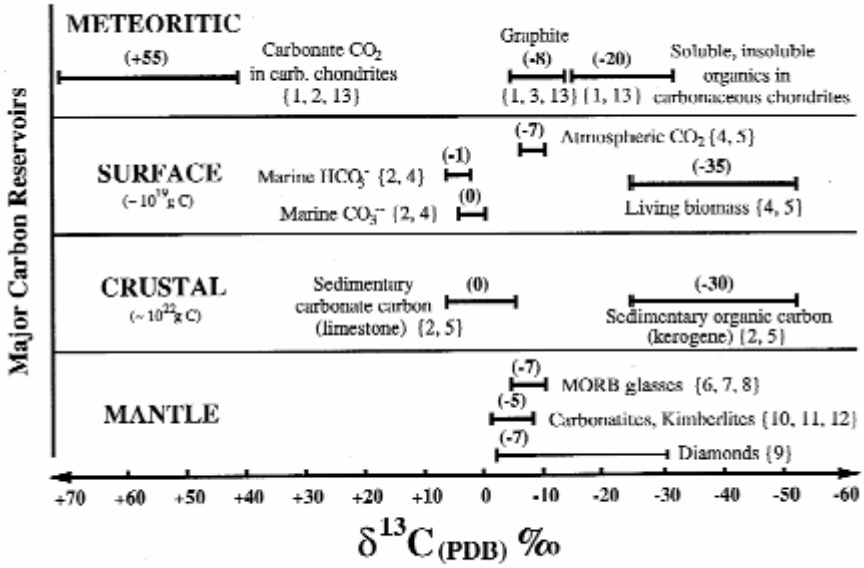

Compiled from various sources In: Griesshaber 1990

BGR Bundesanstalt für Geowissenschaften und Rohstoffe

Why additional $\delta^{13}C$ analyses? (3)

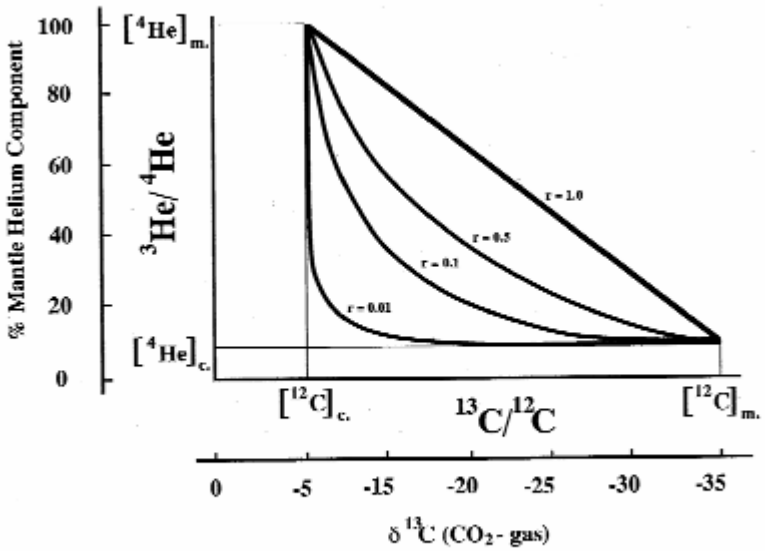

From: Griesshaber 1990

Why additional $\delta^{13}C$ analyses? (4)

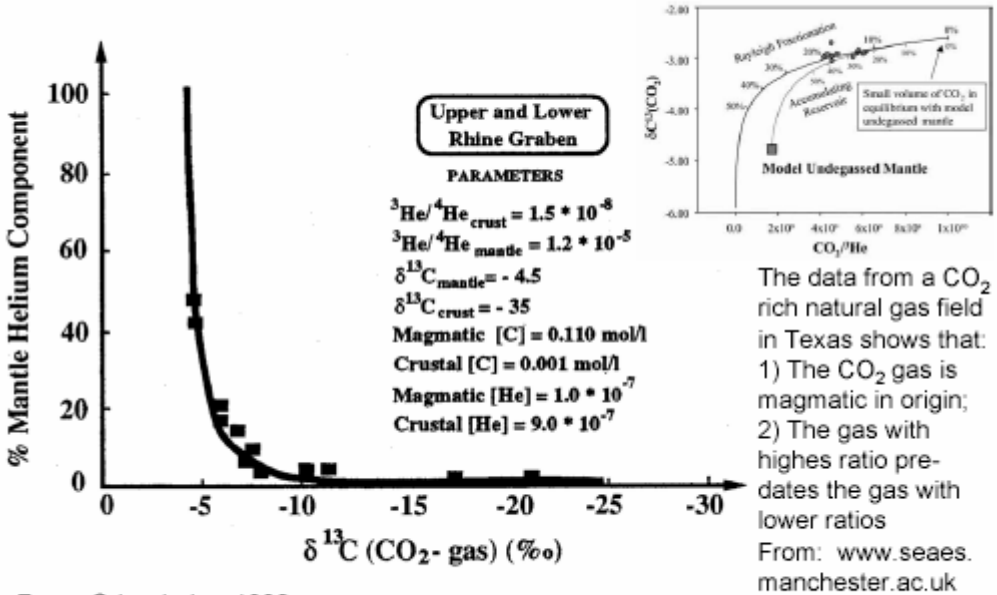

The data from a CO_2 rich natural gas field in Texas shows that:
1) The CO_2 gas is magmatic in origin;
2) The gas with highes ratio pre-dates the gas with lower ratios
From: www.seaes.manchester.ac.uk

From: Griesshaber 1990

Part 3: Analytical techniques

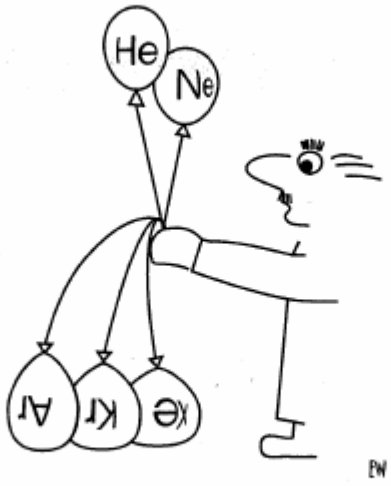

Separating the light from the heavy noble gases.

BGR Bundesanstalt für Geowissenschaften und Rohstoffe

Mass Spectrometry 1

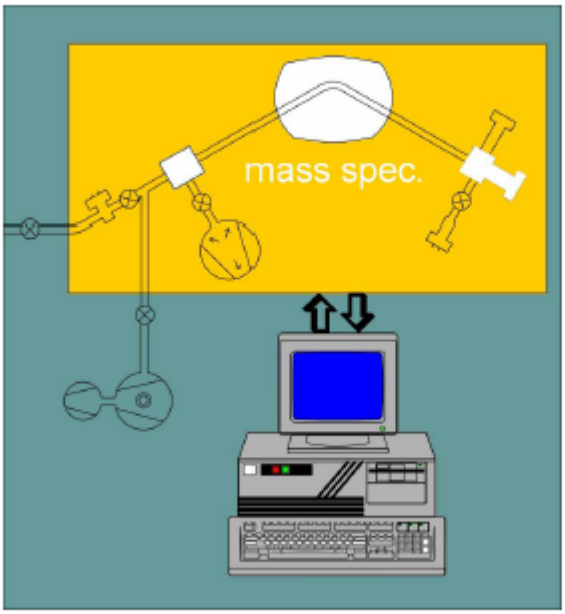

Principal components

a) Ion source
b) Magnet
c) Detector

From:
Kraml 1997
simplified

BGR Bundesanstalt für Geowissenschaften und Rohstoffe

Mass Spectrometry 2

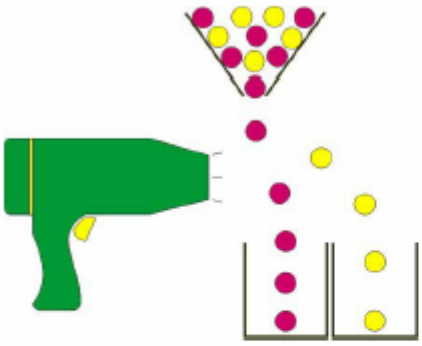

$m/e = B^2r^2/2V$

$B = 143{,}9/r\sqrt{(m/e)*V}$

$B = 143{,}9/18\sqrt{(40/1)*4000}$

B = 3198 Gauss (3034 G for ^{36}Ar)

m = Mass in amu; e = Charge; V = Potential difference in Volt
B = Magnetic field strength in gauss; r = Radius in cm;

Better name for the instrument: mass/charge ratio spectrometer

i.e. CO_2^+ => m/e = 44
CO_2^{++} => m/e = 22 (contributes to ^{22}Ne peak)
i.e. $^{40}Ar^+$ => m/e = 40
$^{40}Ar^{++}$ => m/e = 20 (contributes to ^{20}Ne peak)

Equation from: Faure 1986

BGR Bundesanstalt für Geowissenschaften und Rohstoffe

Mass Spectrometry 3

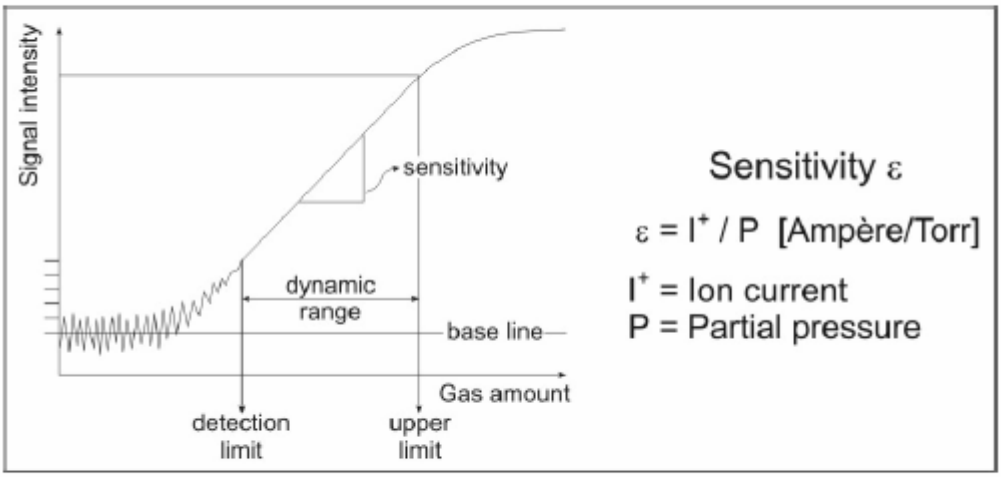

Sensitivity ε

$\varepsilon = I^+ / P$ [Ampère/Torr]

I^+ = Ion current
P = Partial pressure

BGR Bundesanstalt für Geowissenschaften und Rohstoffe

Mass Spectrometry 4

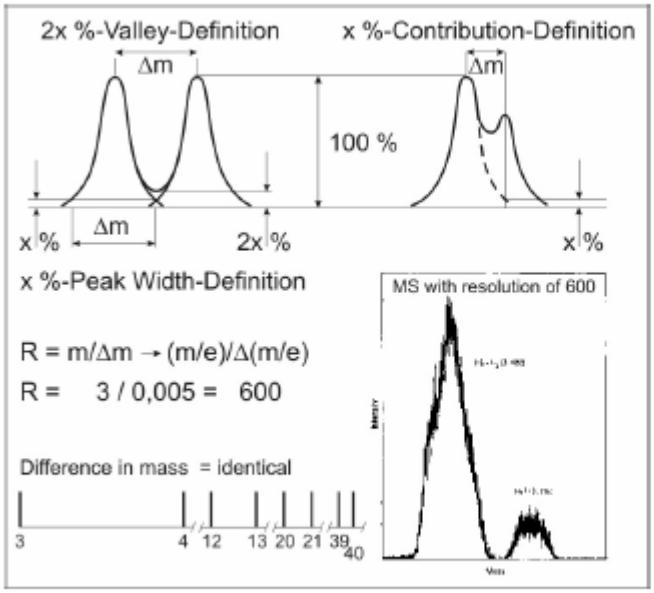

Resolution R

Inset picture with 3He peak from: Dickin 1997

Mass Spectrometry 5

Abundance sensitivity:
example TIMS

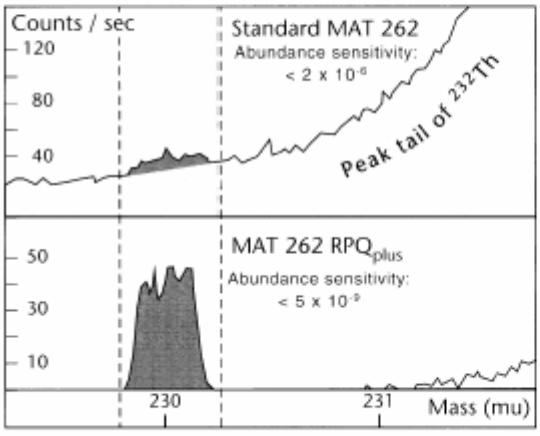

e.g. Finnigan MAT 262 RPQ
4 moveable Faraday detectors
1 Electron-Multiplier with Retarding Potential Quadrupole Filter

Mass Spectrometry 6

Abundance sensitivity: example noble gas MS

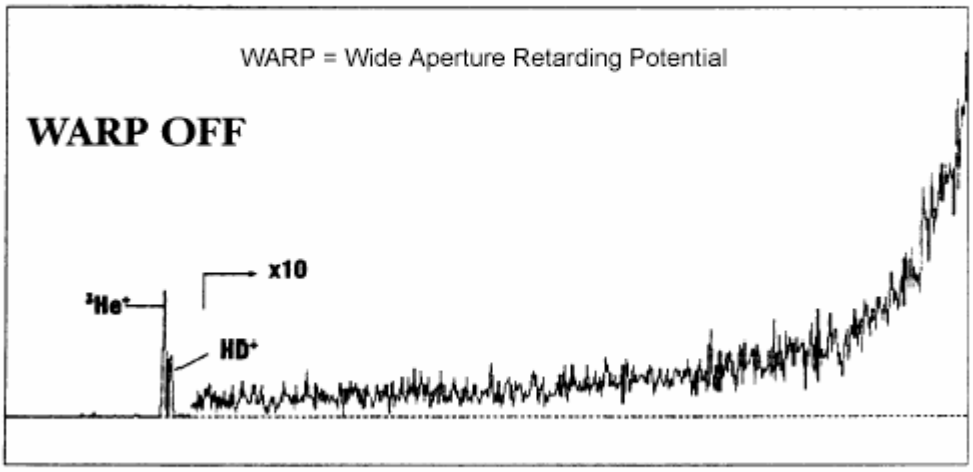

From: C. Haines Technical Note 400; now GV Instruments

Mass Spectrometry 7

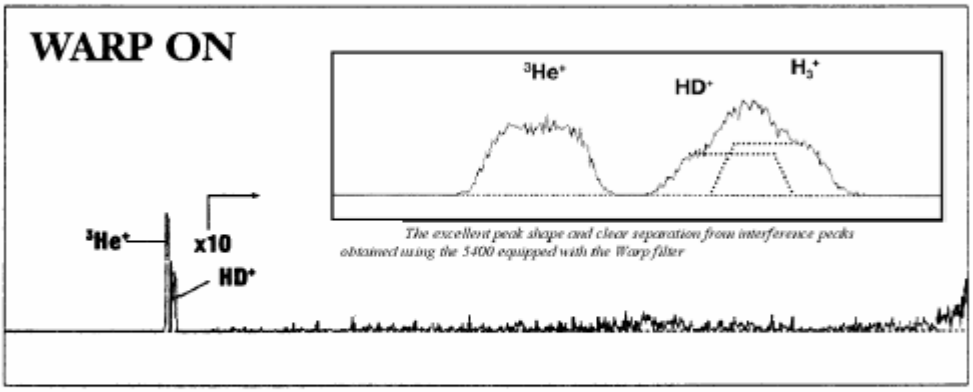

From: C. Haines Technical Note 400; now GV Instruments
(http://www.gvinstruments.co.uk/Noble_Gas_MS.htm)

Mass Spectrometry 8

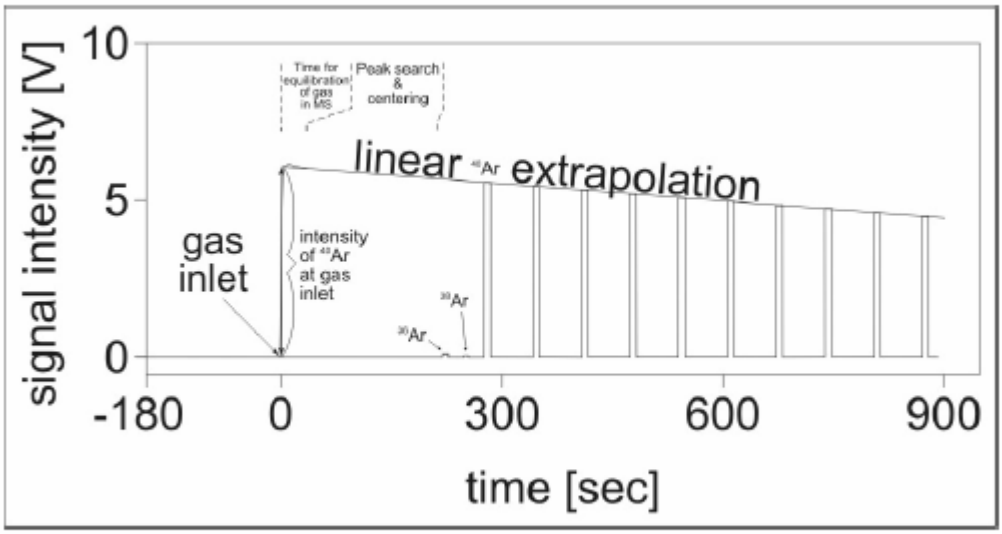

From: Kraml 1997 modified

Mass Spectrometry 9

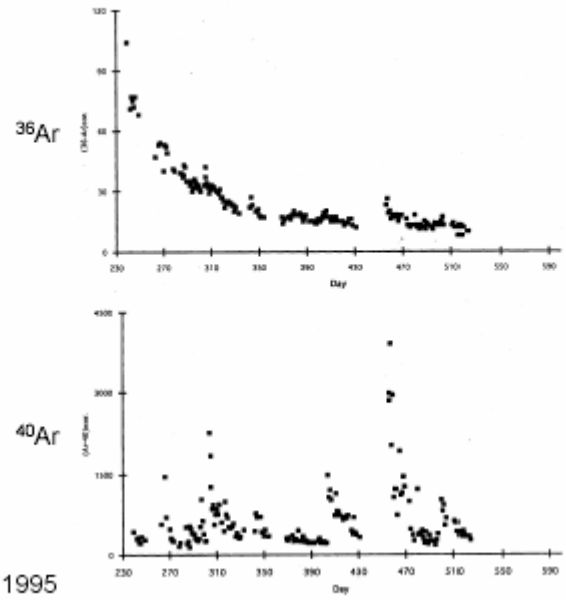

Blank

From:
Wijbrans et al. 1995

Mass Spectrometry 10

Precision and accuracy
example: calculated atmospheric $^{40}Ar/^{36}Ar$ ratio

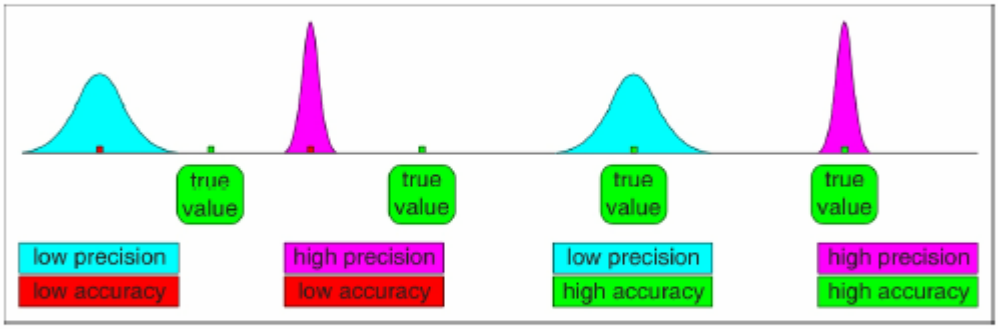

Air standard (pipette system) needed for determination of instrument's discrimination

Mass Spectrometry 11

The fascinating world of „nothing“

Vacuum

	Pressure [hPa] or [mbar]	N per cm^3	Ø free path	Rate of re-adsorption
Atmospheric pressure	1Atm=1000	$3*10^{19}$	0.066 µm	
Low-medium vacuum	$>10^{-3}$	$>3*10^{13}$	<10 cm	<0.001 sec
High vacuum	10^{-3}-10^{-7}			
Ultrahigh vacuum	$<10^{-7}$	<3 Mrd	>1 km	>10 seconds
TV	$<10^{-6}$	13 Mrd	134 m	>1 second
Mass spectrometer	10^{-9}	30 mio	67 km	16.7 minutes
Cern	$<10^{-10}$	2 mio	1000 km	4.6 hours
Interstellar space	10^{-16}	3	670 Million km	317 years
Intergalactic space	$<10^{-23}$	1 per 10 m^3	$1.7*10^9$ Billion km =180000 light-years	10.6 Ga

viscous flow: depends on pressure difference

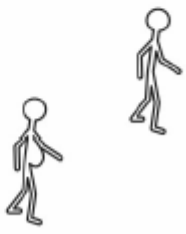

molecular flow: depends on mass

Mass Spectrometry 12

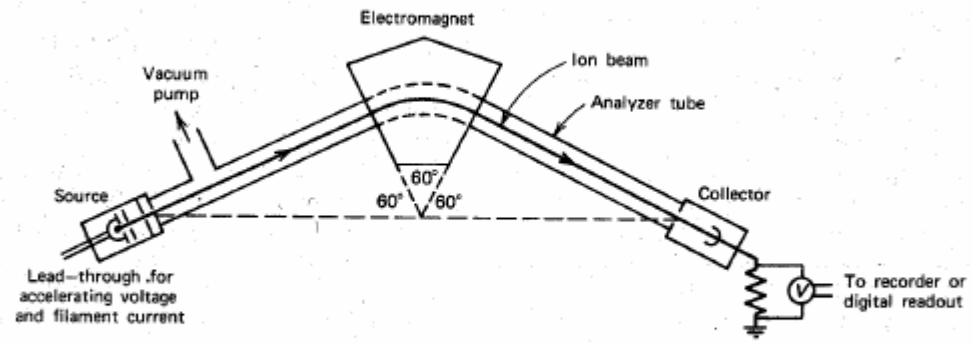

From: Faure 1986

Mass Spectrometry 13

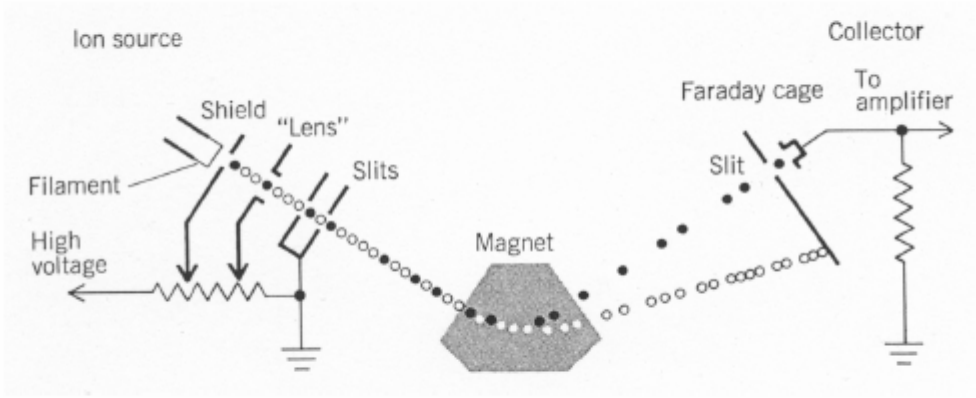

From: Dickin 1997 (after Faul 1966)

Mass Spectrometry 14

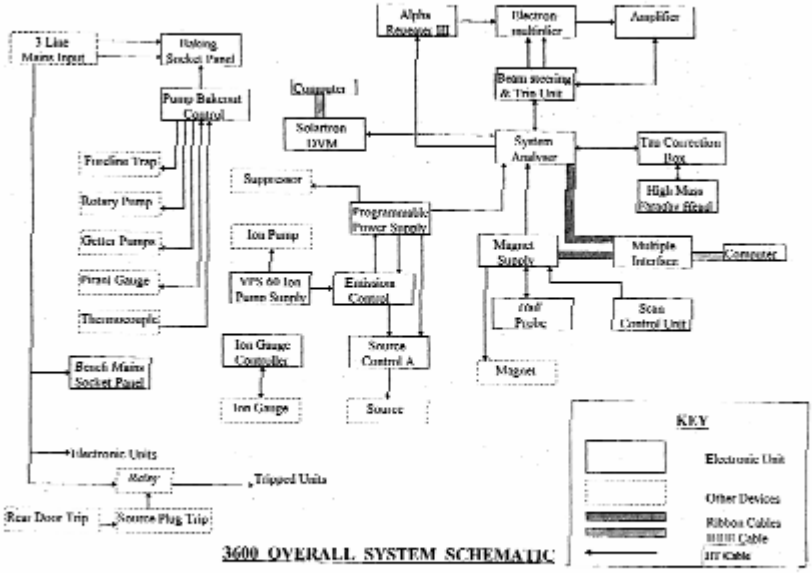

From: VG3600 Instrument manual

Mass Spectrometry 15

How to get the gas
(or gas-containing water)
out of the Cu tube?

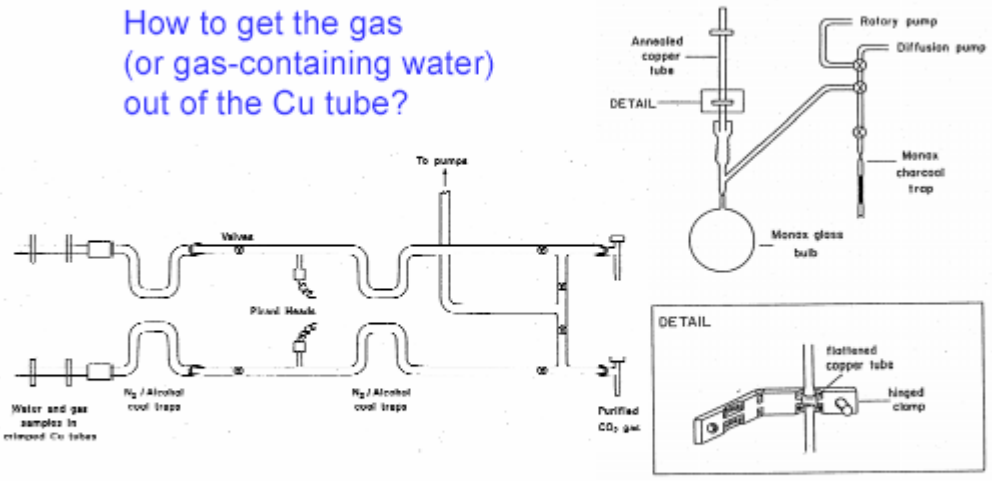

From: Griesshaber 1990

Mass Spectrometry 16

How to clean the gas?

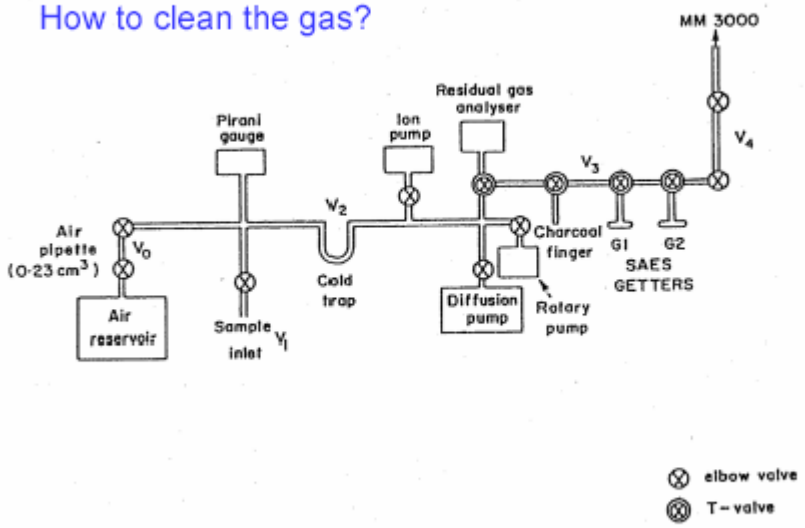

From: Griesshaber 1990

Mass Spectrometry 17

Examples for further development of MS enhancing sensitivity

Ion sources	Detectors
Nier type	Faraday cup
Baur-Signer	Electron-Multiplier
Compressor	Channeltron

Mass Spectrometry 18

Modern noble gas lab of GFZ Potsdam, Germany

From: http://www.gfz-potsdam.de/pb4/pg2/equipment/edelgas/mswebpage.html

Mass Spectrometry 19

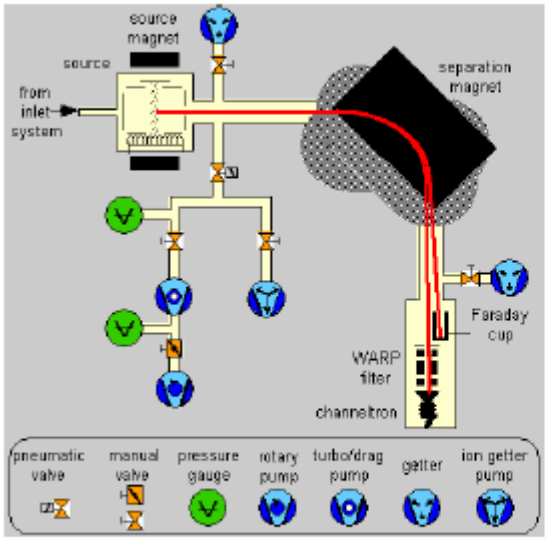

From:
homepage of GV Instruments

From:http://www.ldeo.columbia.edu/~etg/ms_ms/Mass_spectrometer.html

Mass Spectrometry 20

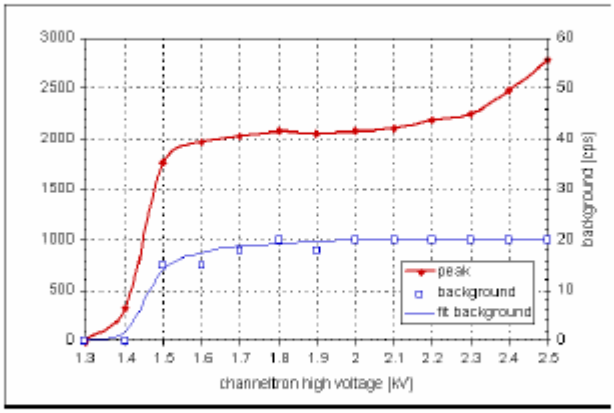

From:http://www.ldeo.columbia.edu/~etg/ms_ms/Mass_spectrometer.html

Mass Spectrometry 21

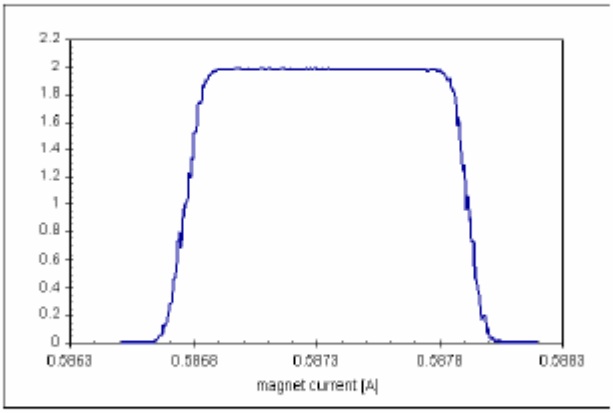

From:http://www.ldeo.columbia.edu/~etg/ms_ms/Mass_spectrometer.html

Mass Spectrometry 22

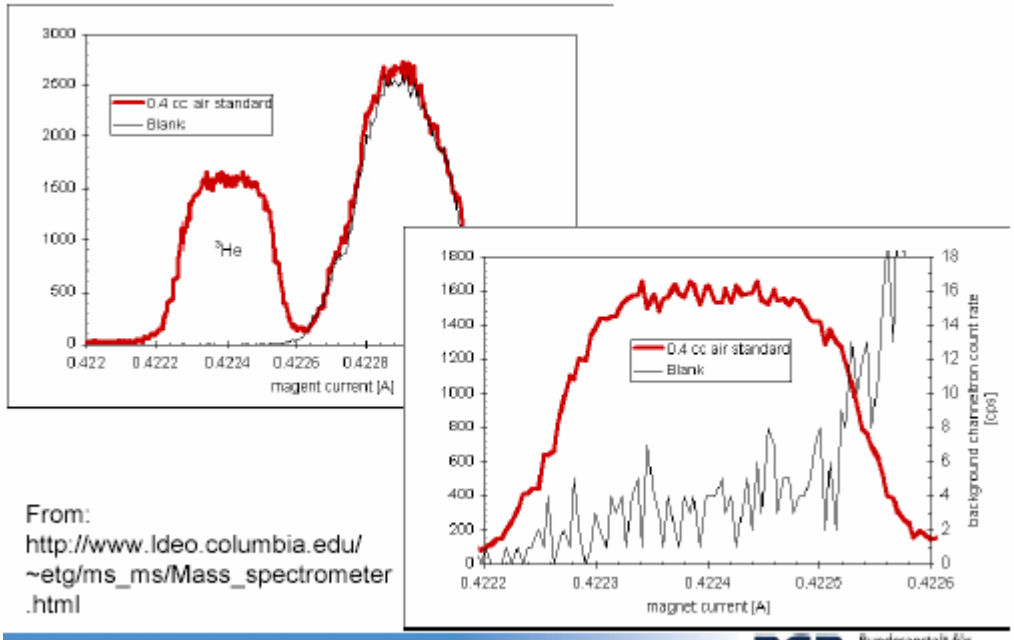

From:
http://www.ldeo.columbia.edu/~etg/ms_ms/Mass_spectrometer.html

Mass Spectrometry 23

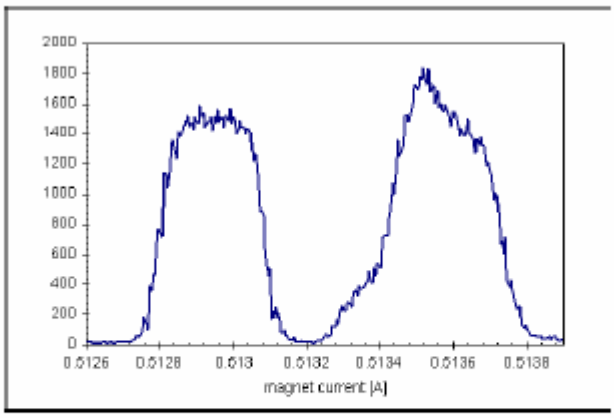

3He and HD/H3 peaks measured with a channeltron 3 days after a bakeout

From: http://www.ldeo.columbia.edu/~etg/ms_ms/Mass_spectrometer.html

Mass Spectrometry 24

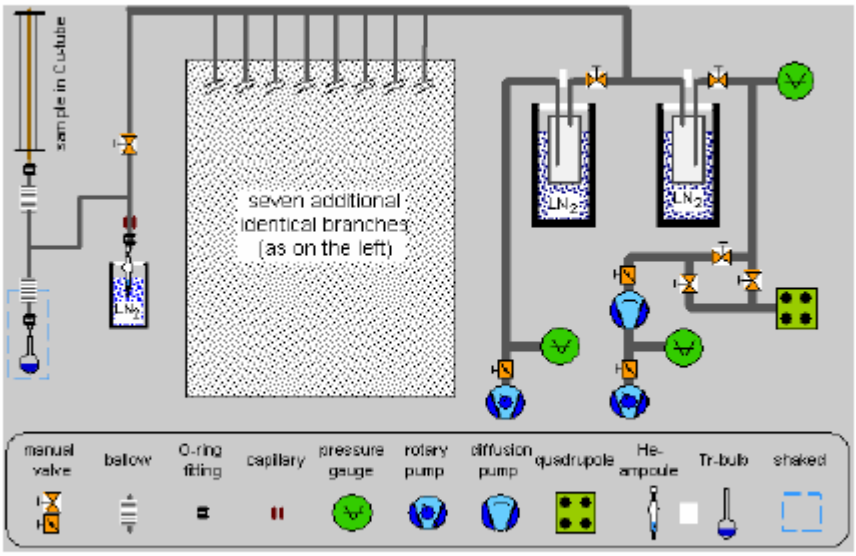

From:http://www.ldeo.columbia.edu/~etg/ms_ms/Mass_spectrometer.html

Mass Spectrometry 25

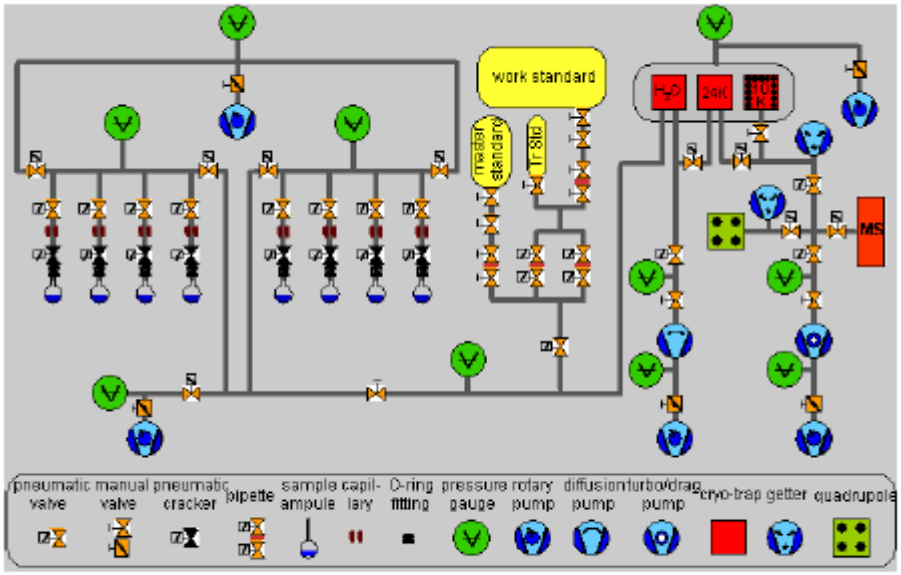

From:http://www.ldeo.columbia.edu/~etg/ms_ms/Mass_spectrometer.html

Mass Spectrometry 26

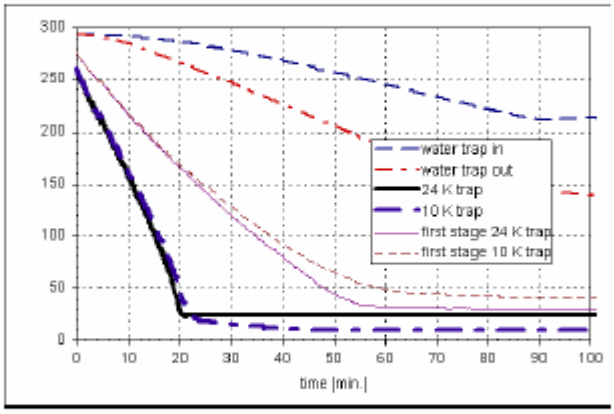

From:http://www.ldeo.columbia.edu/~etg/ms_ms/Mass_spectrometer.html

Mass Spectrometry 27

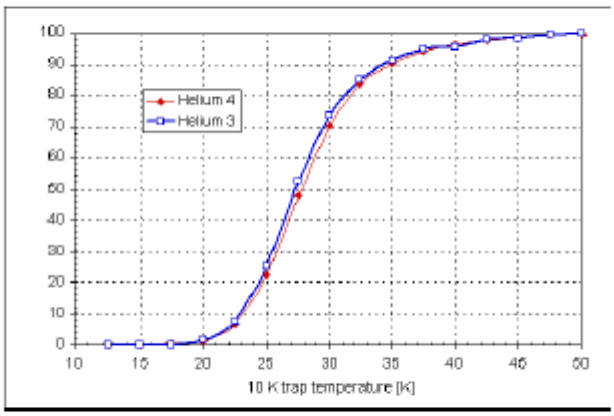

From:http://www.ldeo.columbia.edu/~etg/ms_ms/Mass_spectrometer.html

Mass Spectrometry 28

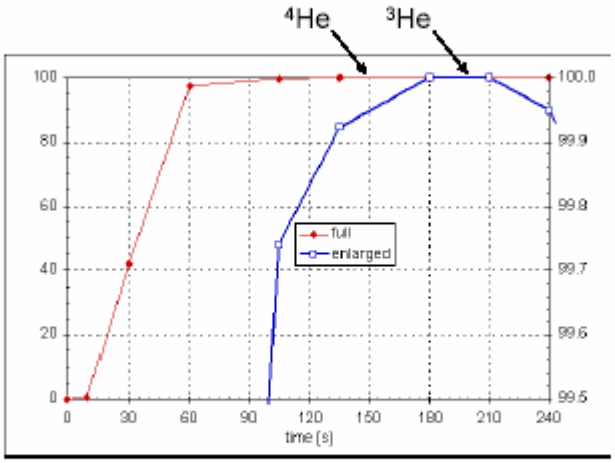

From:http://www.ldeo.columbia.edu/~etg/ms_ms/Mass_spectrometer.html

Mass Spectrometry 29

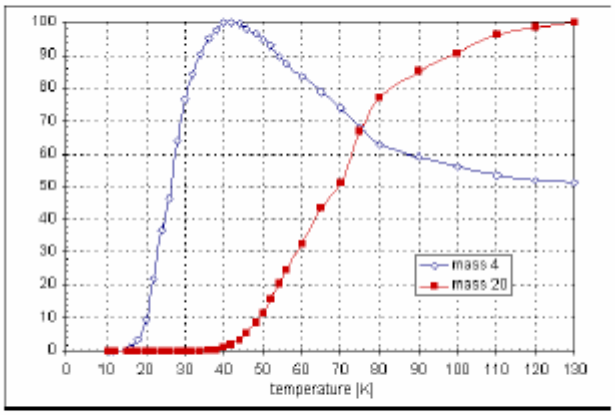

From:http://www.ldeo.columbia.edu/~etg/ms_ms/Mass_spectrometer.html

Mass Spectrometry 30

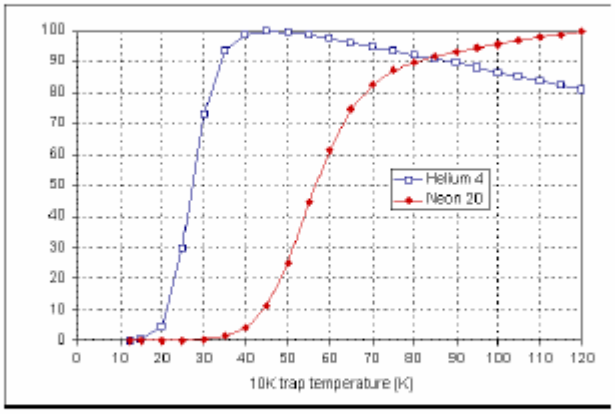

From:http://www.ldeo.columbia.edu/~etg/ms_ms/Mass_spectrometer.html

Mass Spectrometry 31

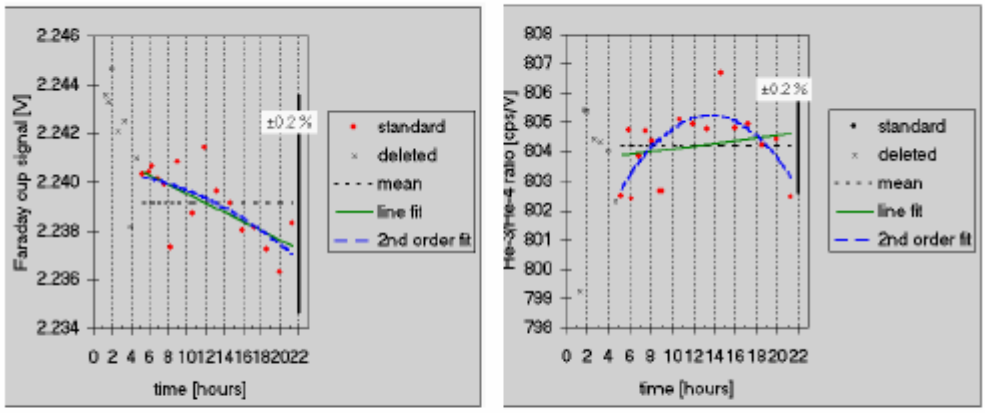

From:http://www.ldeo.columbia.edu/~etg/ms_ms/Mass_spectrometer.html

Mass Spectrometry 32

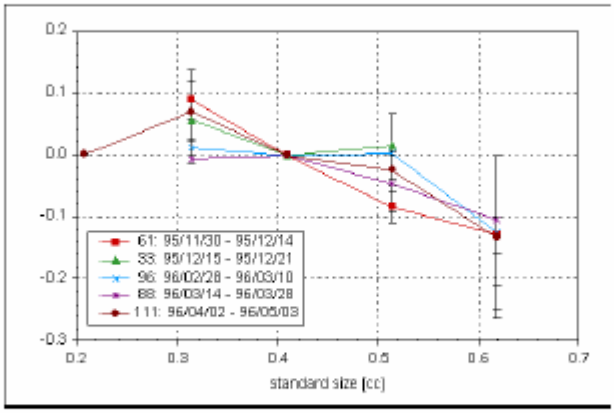

From:http://www.ldeo.columbia.edu/~etg/ms_ms/Mass_spectrometer.html

Mass Spectrometry 33

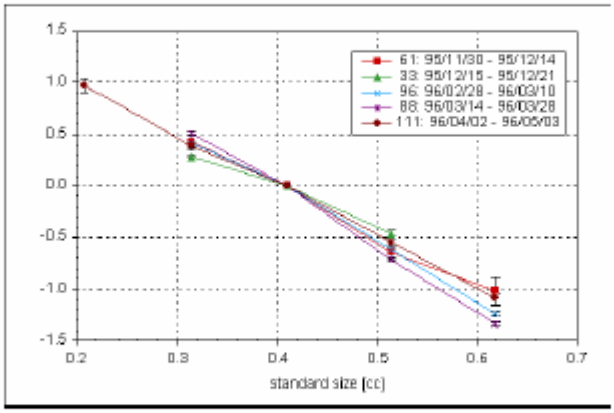

From:http://www.ldeo.columbia.edu/~etg/ms_ms/Mass_spectrometer.html

Mass Spectrometry 34

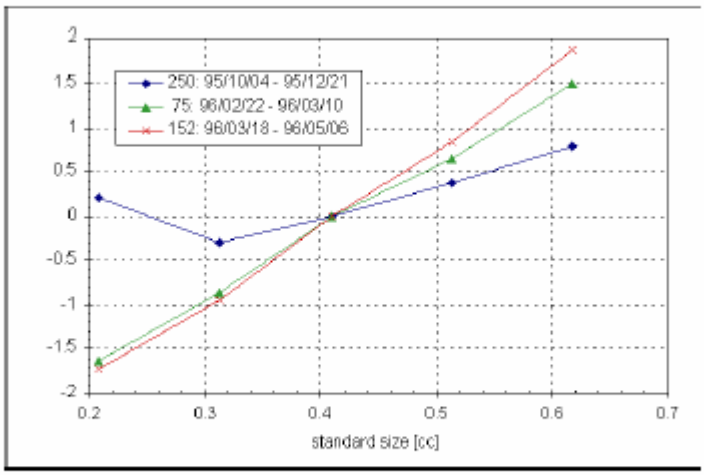

From:http://www.ldeo.columbia.edu/~etg/ms_ms/Mass_spectrometer.html

Mass Spectrometry 35

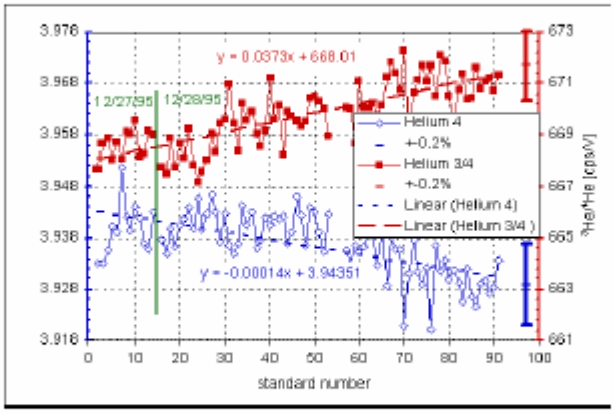

From:http://www.ldeo.columbia.edu/~etg/ms_ms/Mass_spectrometer.html

Mass Spectrometry 36

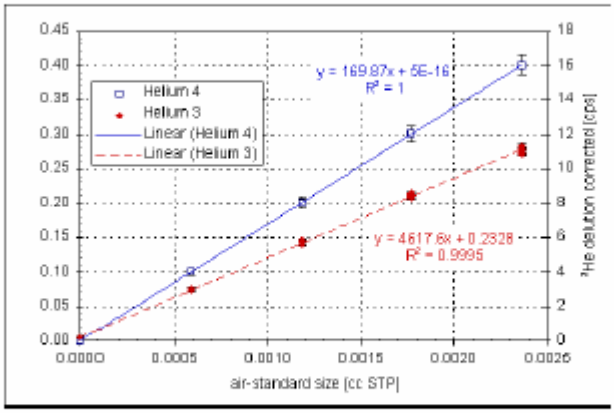

From:http://www.ldeo.columbia.edu/~etg/ms_ms/Mass_spectrometer.html

Part 4: Case Studies

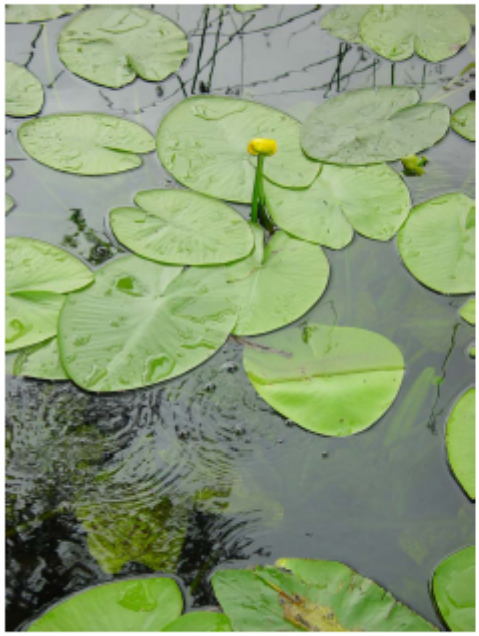

European sampling sites

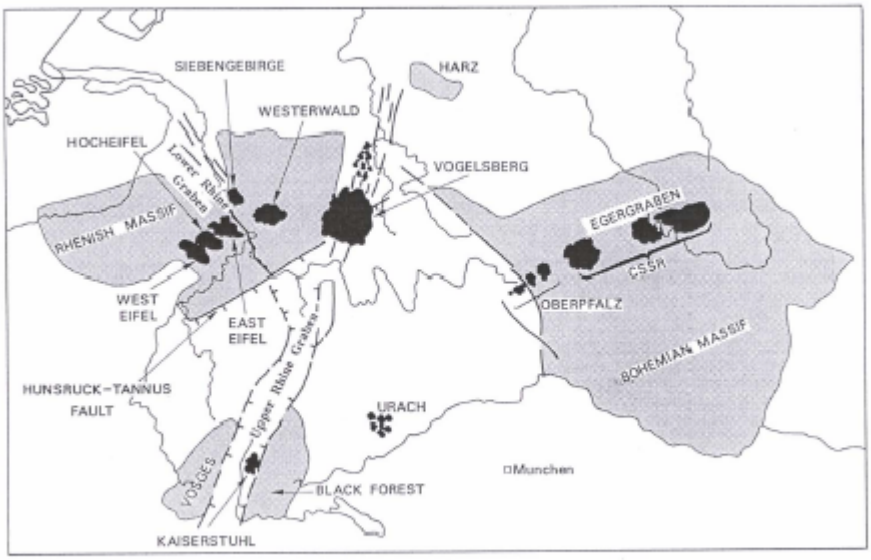

From: Griesshaber 1990

Case Study Eger Rift 1

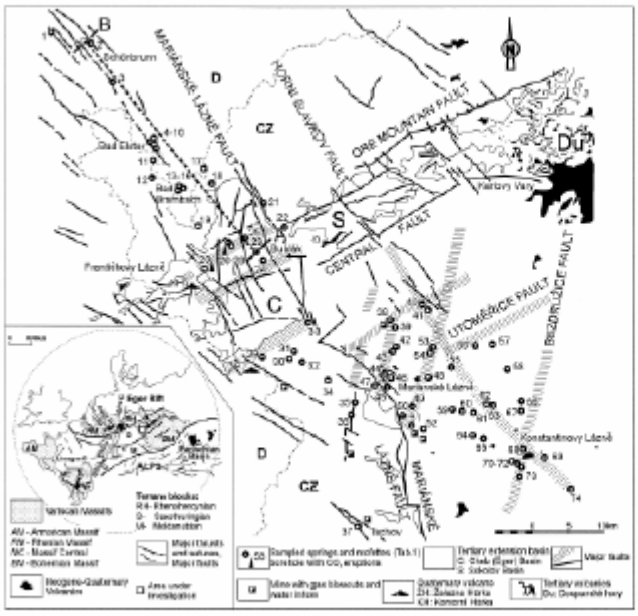

From: Weinlich et al. 1999

Case Study Eger Rift 2

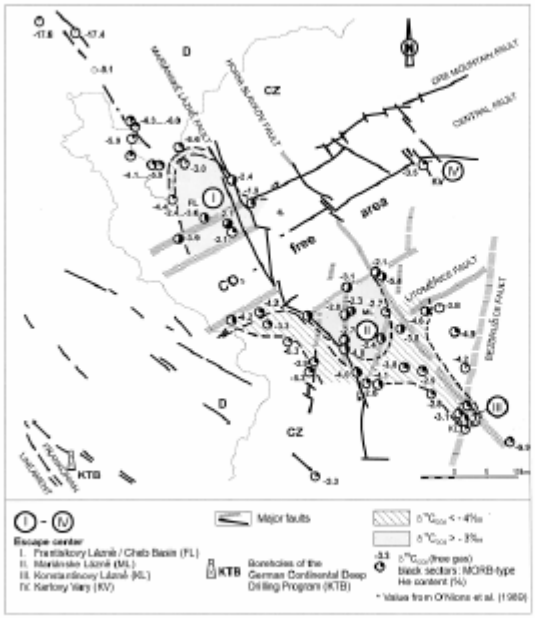

From: Weinlich et al. 1999

Case Study Eger Rift 3

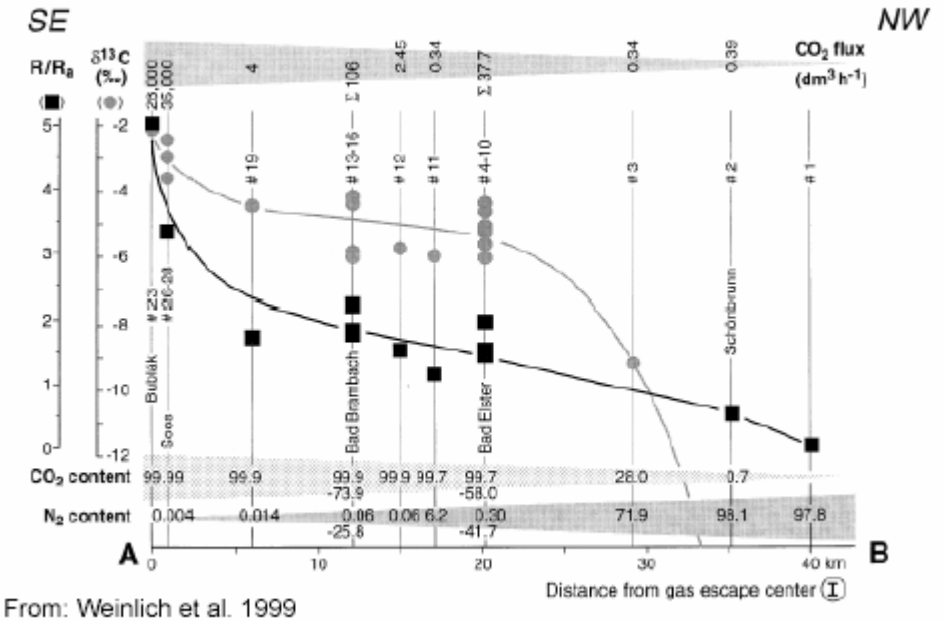

From: Weinlich et al. 1999

Case Study Eger Rift 4

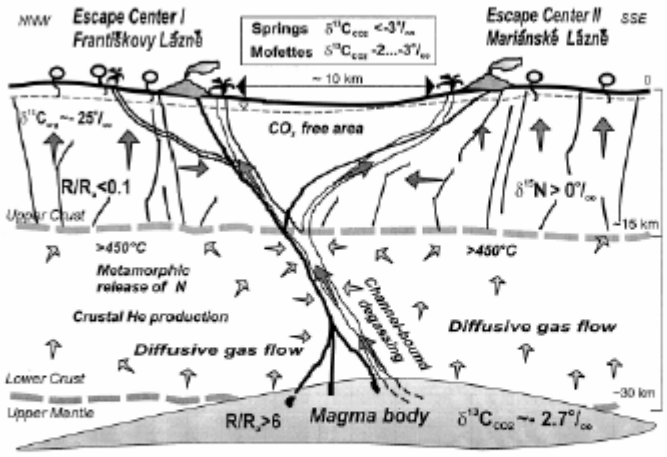

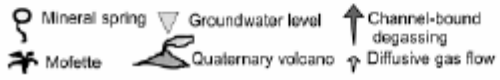

From:
Weinlich et al. 1999

Case Study Upper Rhine Graben Rift 1

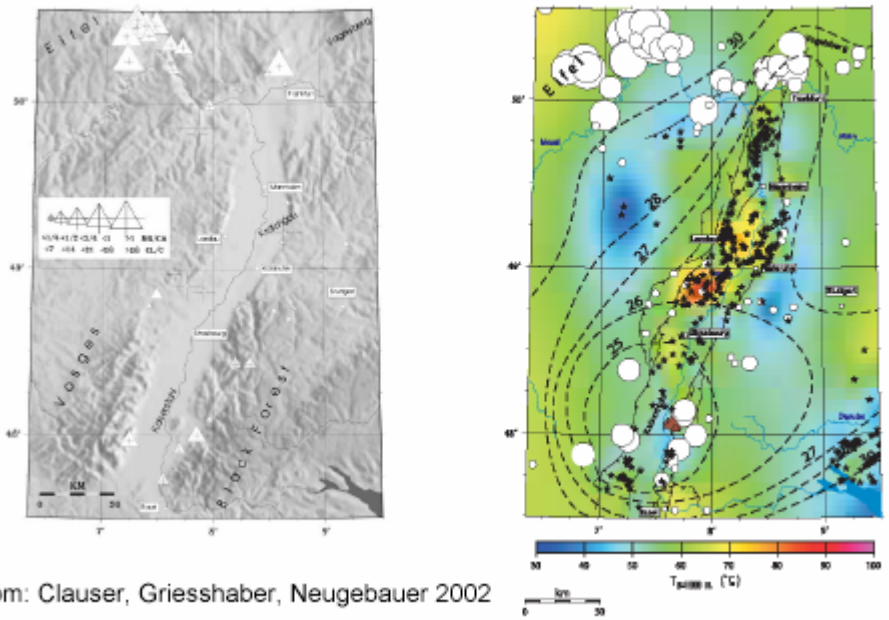

From: Clauser, Griesshaber, Neugebauer 2002

Case Study Upper Rhine Graben Rift 2

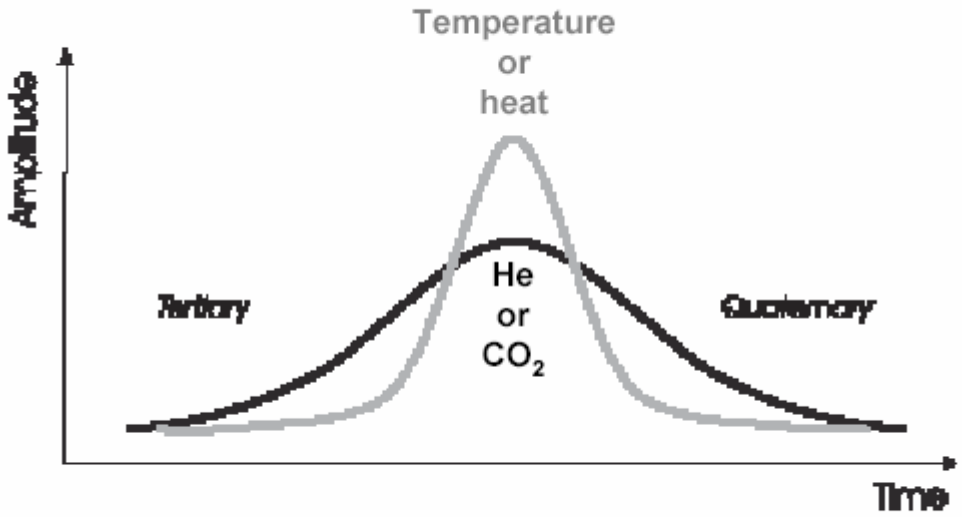

From: Clauser, Griesshaber, Neugebauer 2002

Case Study Upper Rhine Graben Rift 3

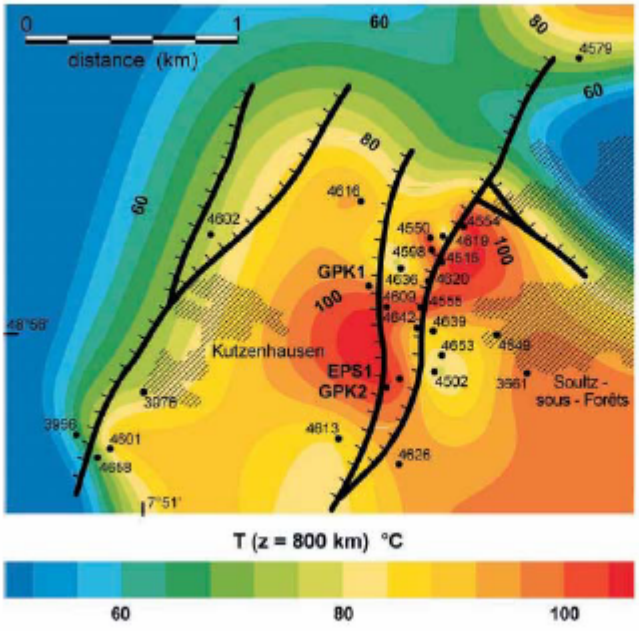

From: Clauser, Griesshaber, Neugebauer 2002

BGR Bundesanstalt für Geowissenschaften und Rohstoffe

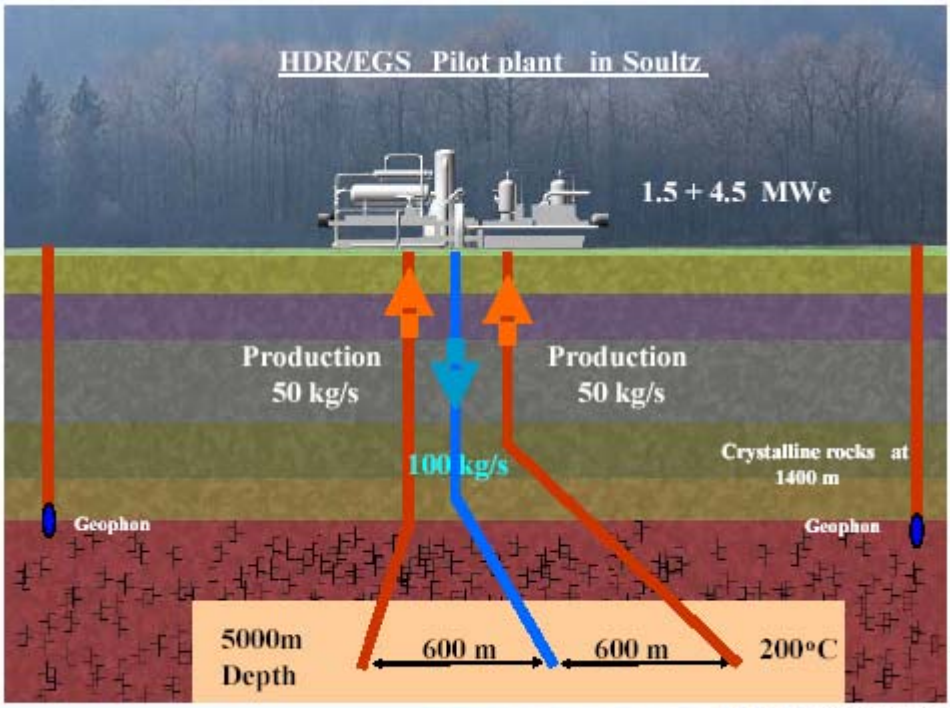

BGR Bundesanstalt für Geowissenschaften und Rohstoffe

Case Study Upper Rhine Graben Rift 4

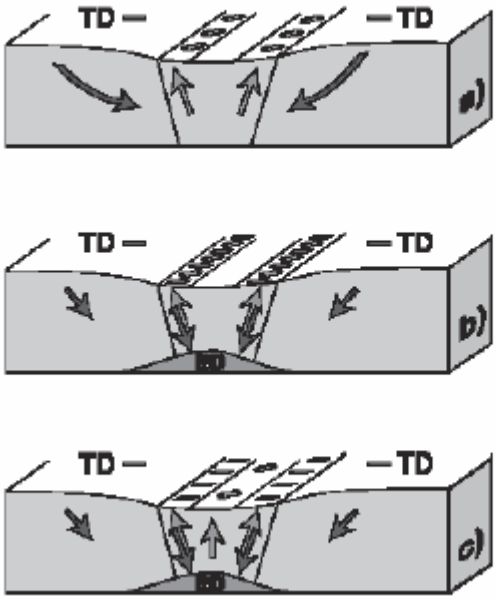

From: Clauser, Griesshaber, Neugebauer 2002

Case Study Cascades 1

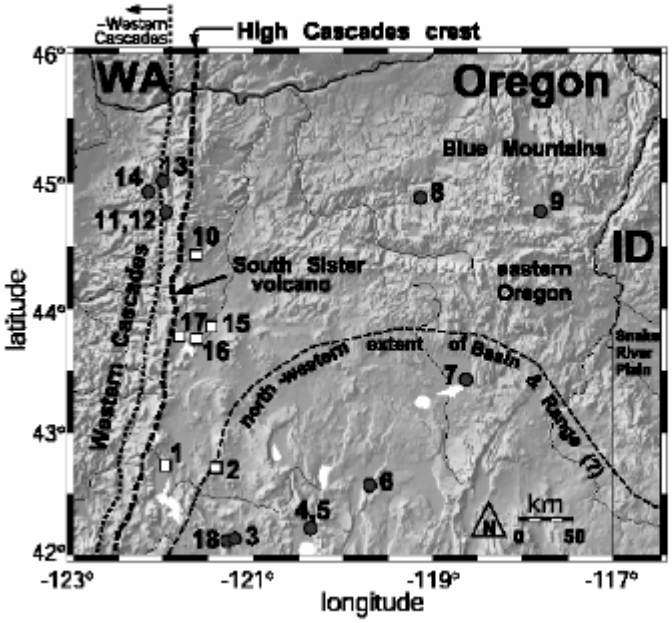

From: Saar et al. ????

Case Study Cascades 2

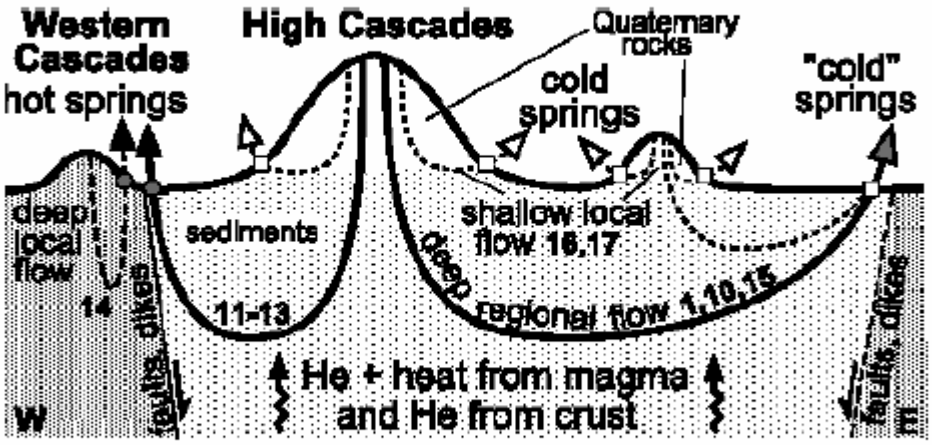

From: Saar et al. ????

Case Study East African Rift Kenya 1

See also: Scarsi & Craig and Marty et al. 1996 for Ethiopian plume

From: Darling, Griesshaber, Andrews, Armannsson & O'Nions 1995

Case Study Aegean Arc 1

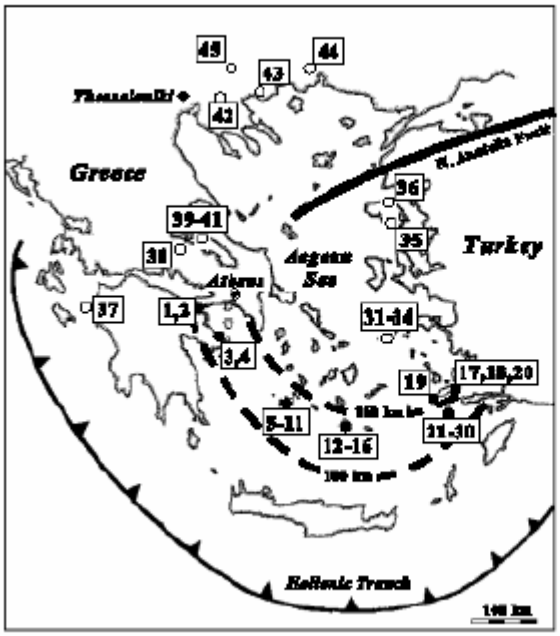

From: Shimizu et al. 2005

Case Study Aegean Arc 2

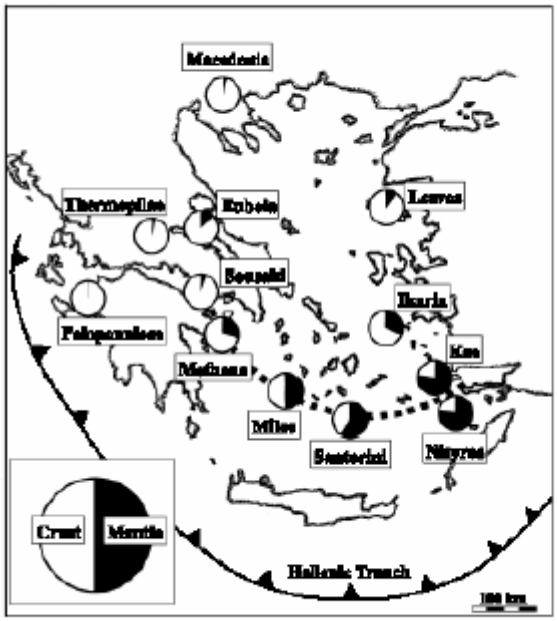

From: Shimizu et al. 2005

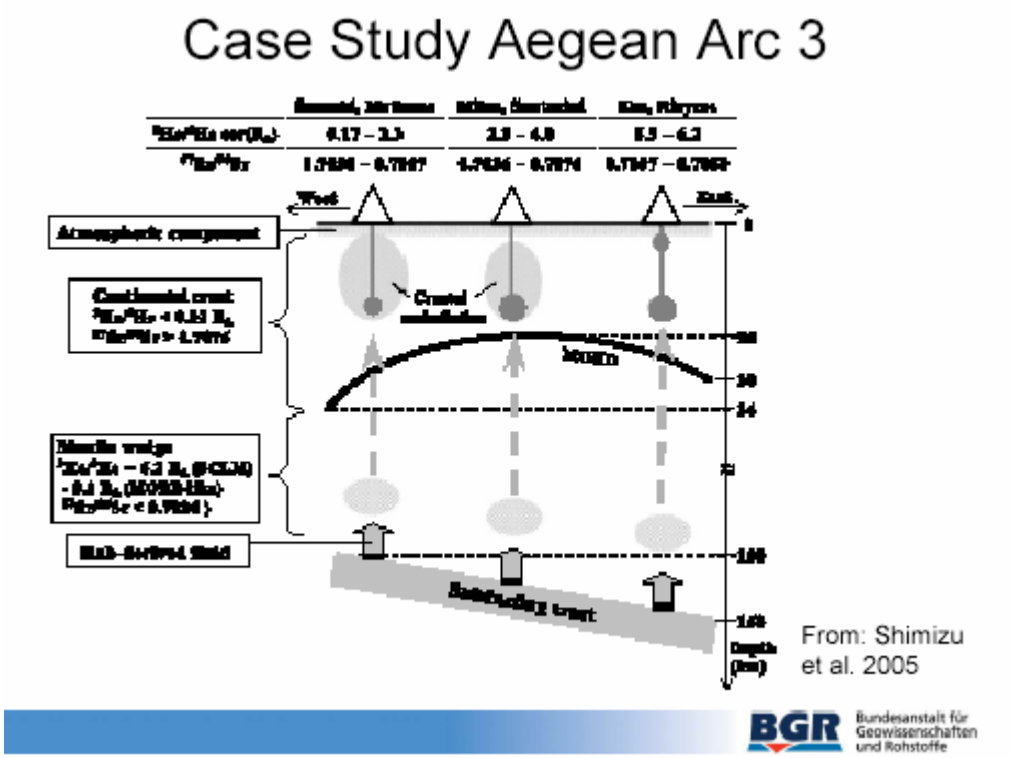
Case Study Aegean Arc 3
From: Shimizu et al. 2005
BGR
Bundesanstalt für Geowissenschaften und Rohstoffe

Case Study Flores Indonesian Arc 1

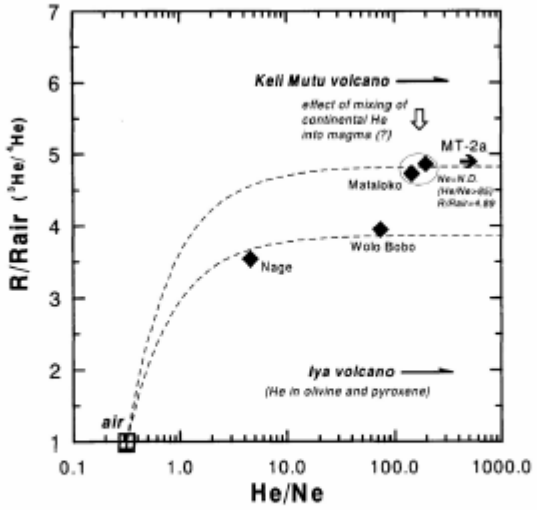

Plots of R/Rair ($^3He/^4He$) vs. He/Ne. The data for the MT-2 steam is not able to be plotted due to indeterminable of its He/Ne ratio because of low Ne concentration not detected in chemical analysis.

From: Matsuda et al. 2002

Case Study Flores Indonesian Arc 2

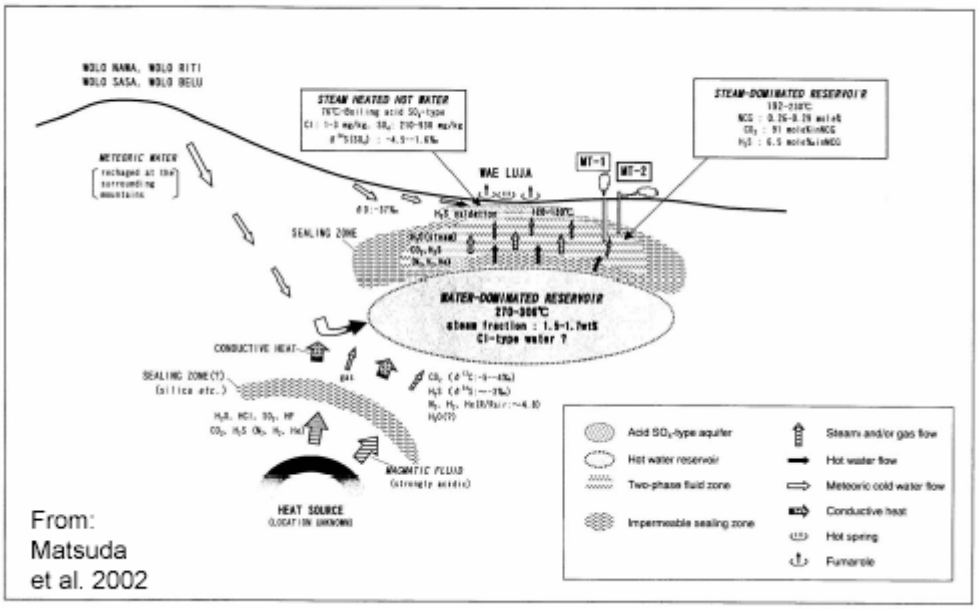

From: Matsuda et al. 2002

Appendix B.1: Schlumberger soundings

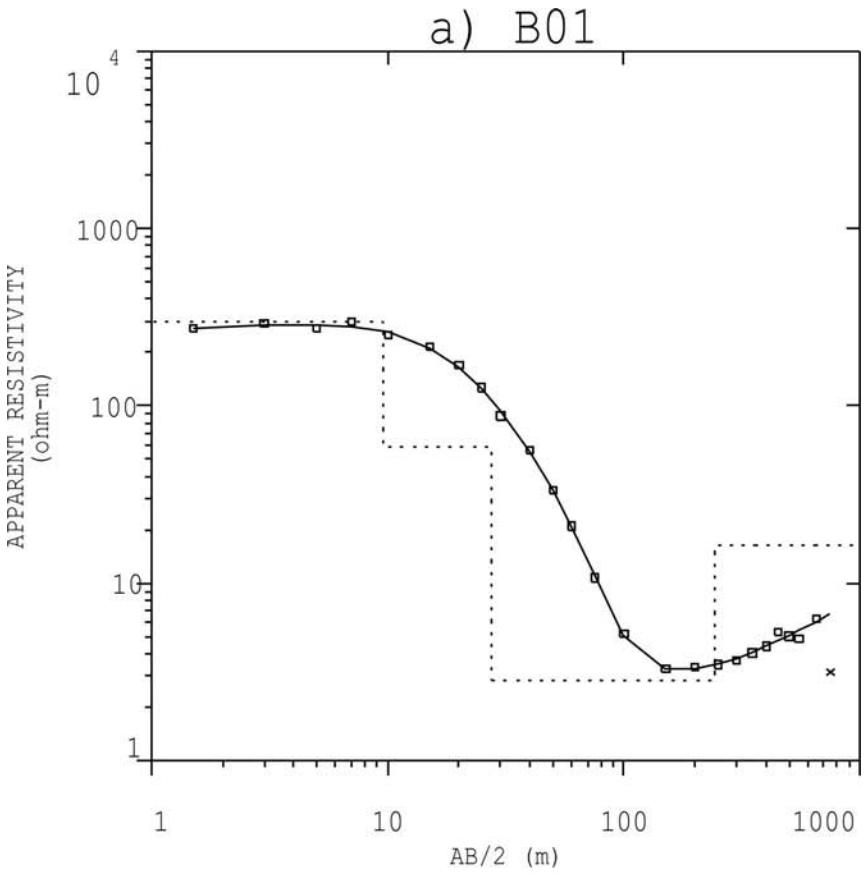

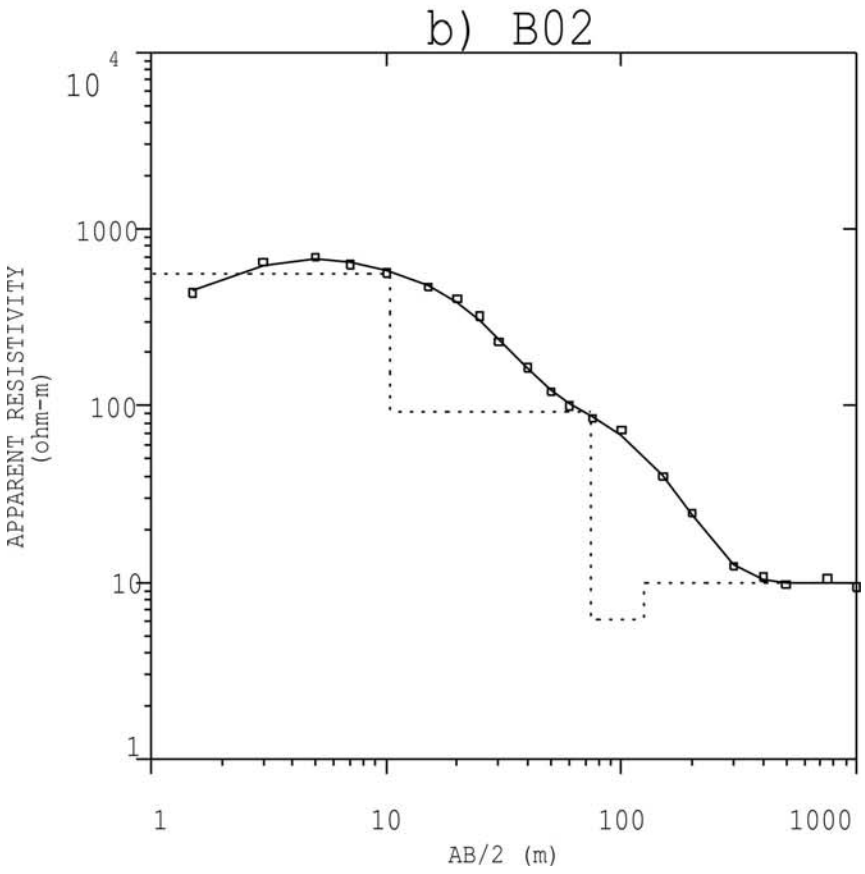

Appendix B.1: Schlumberger soundings

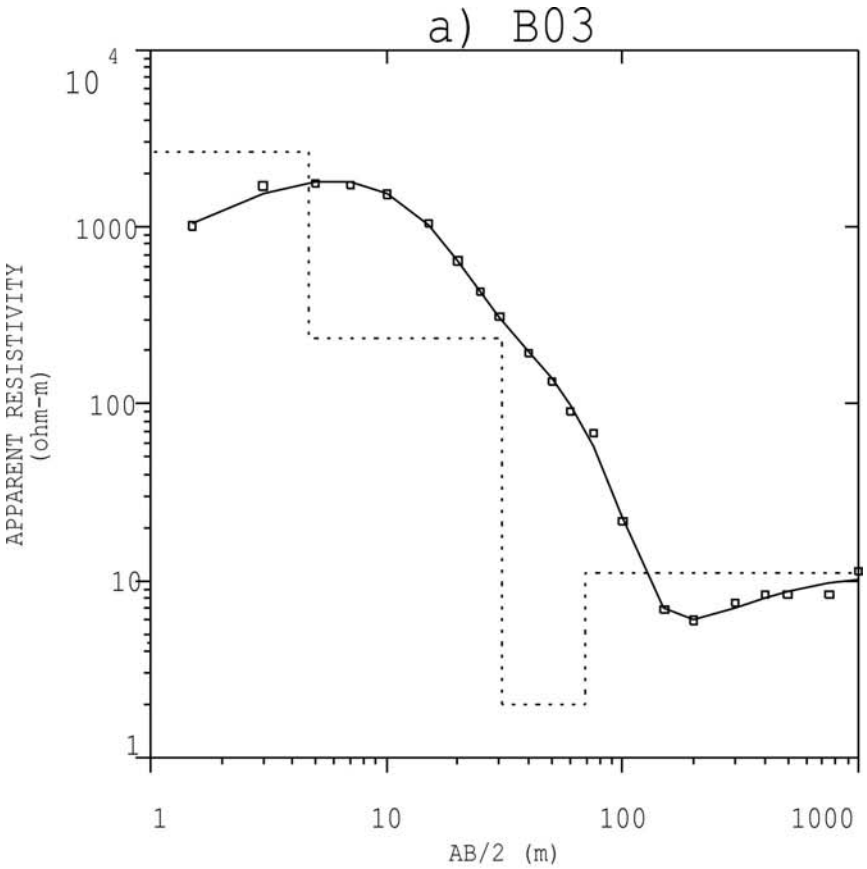

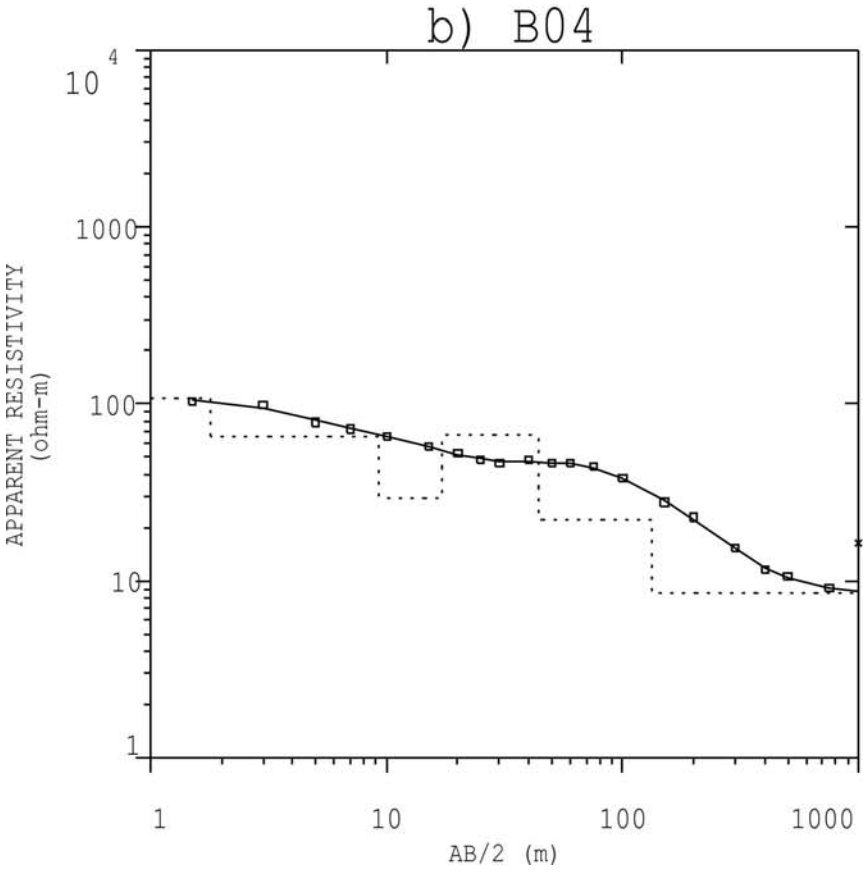

Appendix B.1: Schlumberger soundings

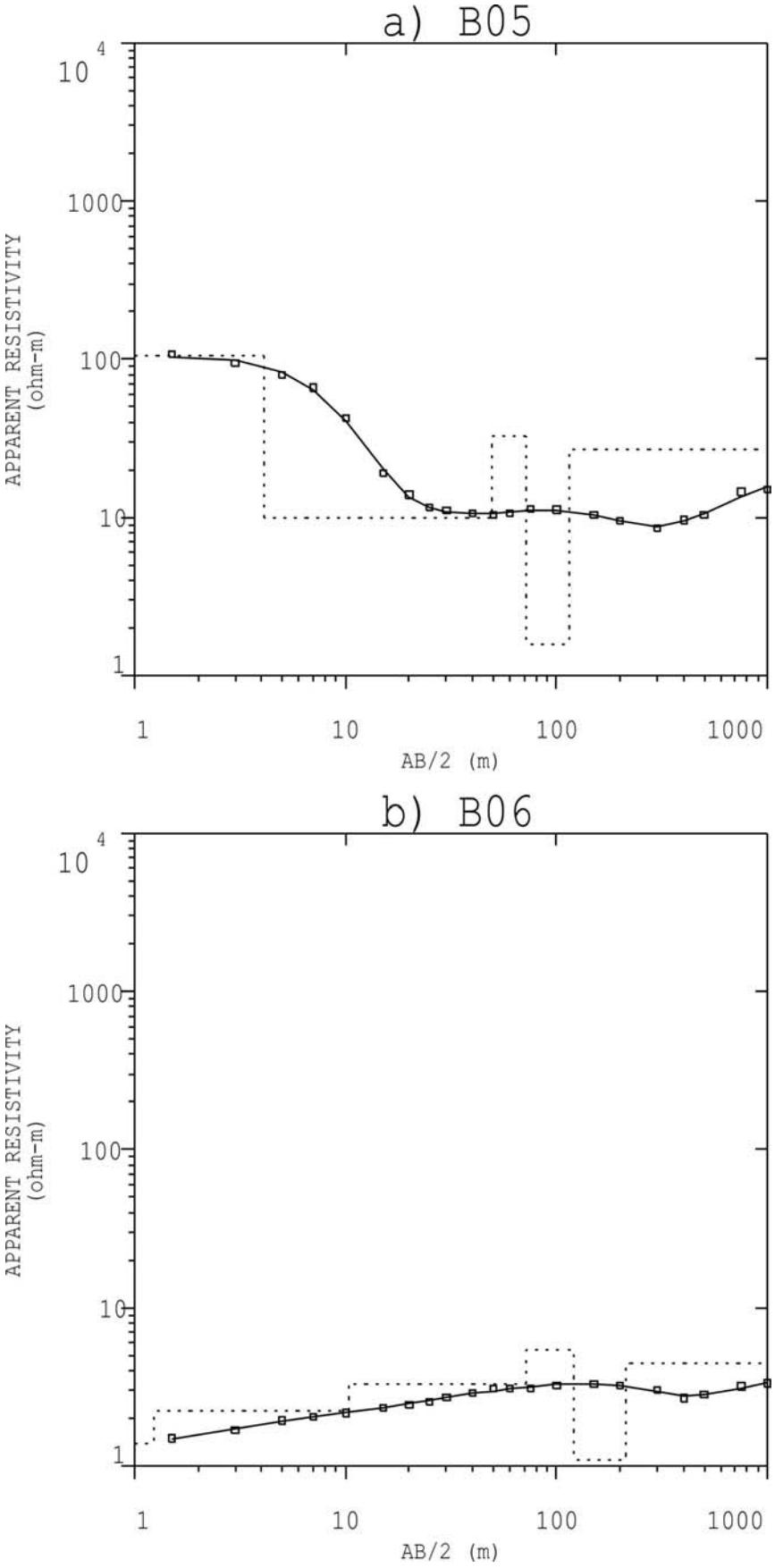

Appendix B.1: Schlumberger soundings

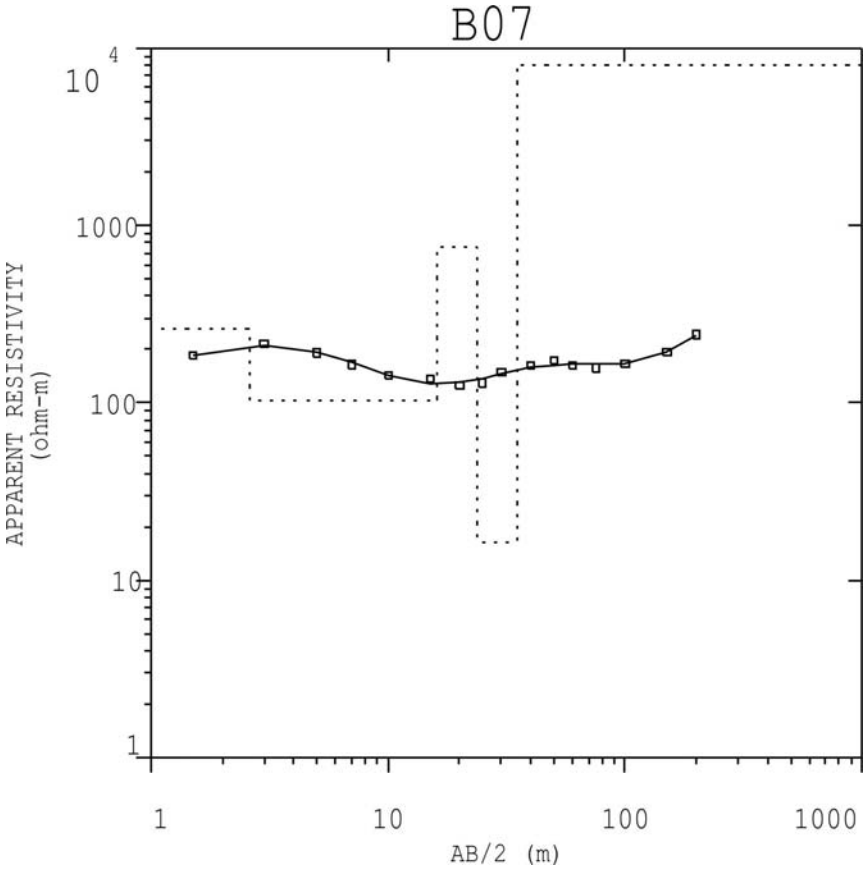

Appendix B.2: Test dipole/dipole-mapping with an electrode separation of 10 m at the Sempaya visitor centre

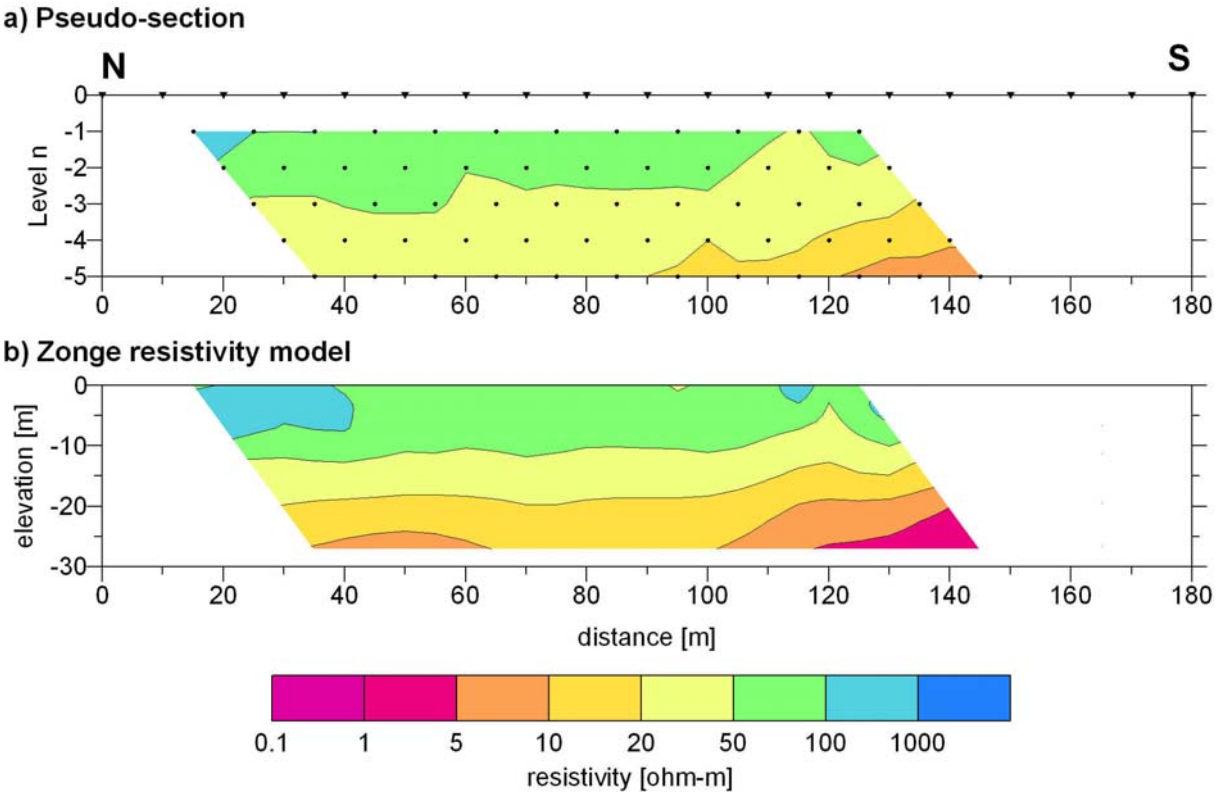

Appendix B.3: TEM soundings (sorted from N to S)

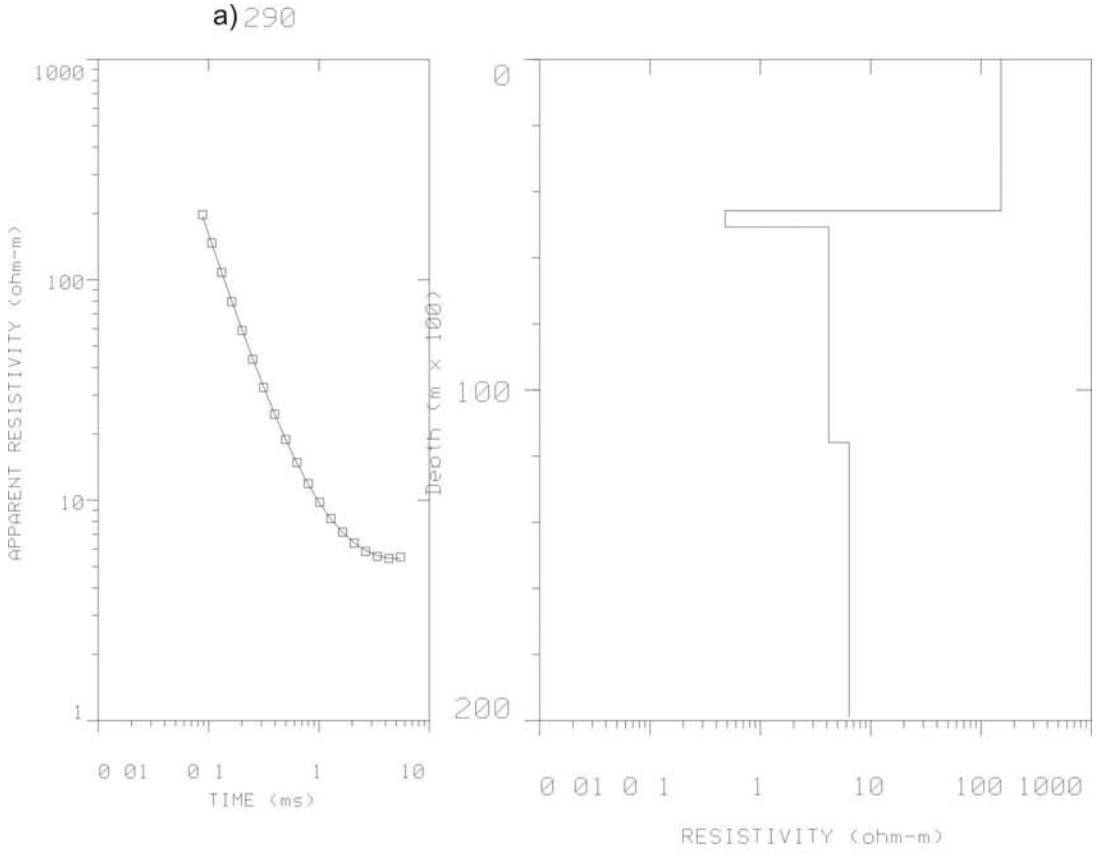

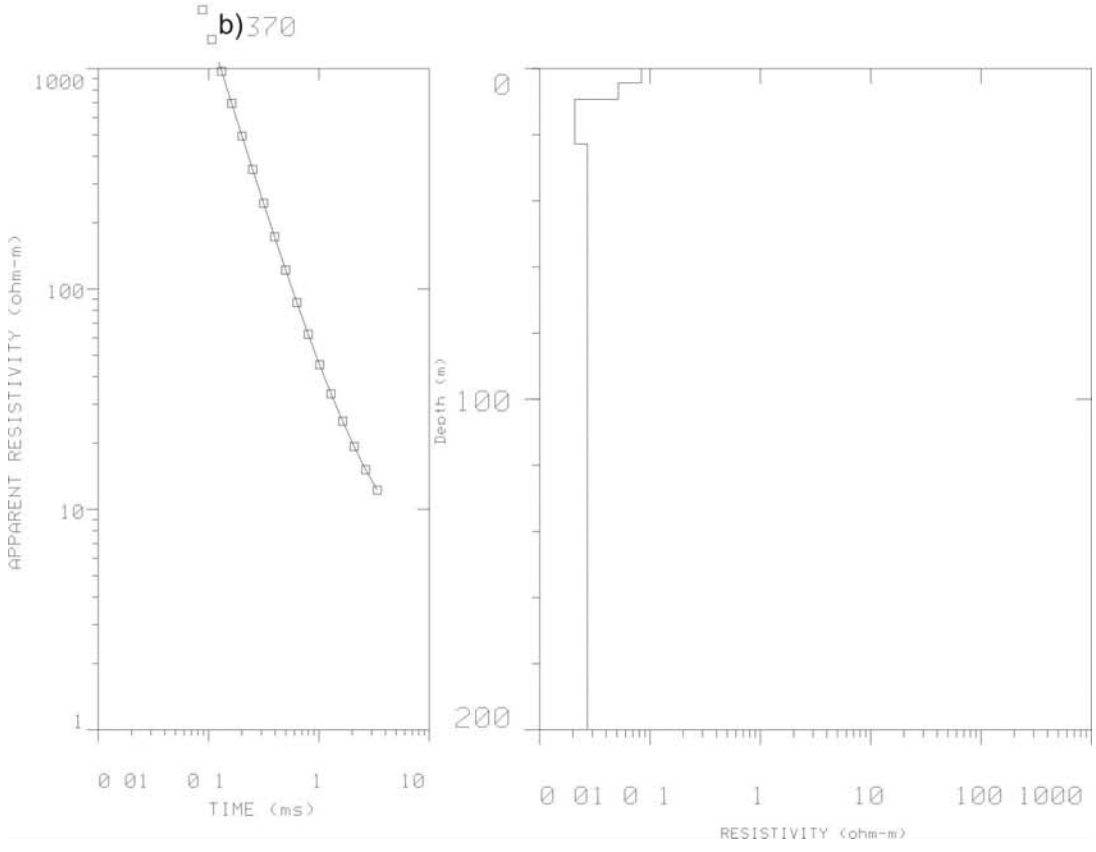

Appendix B.3: TEM soundings

a) 360

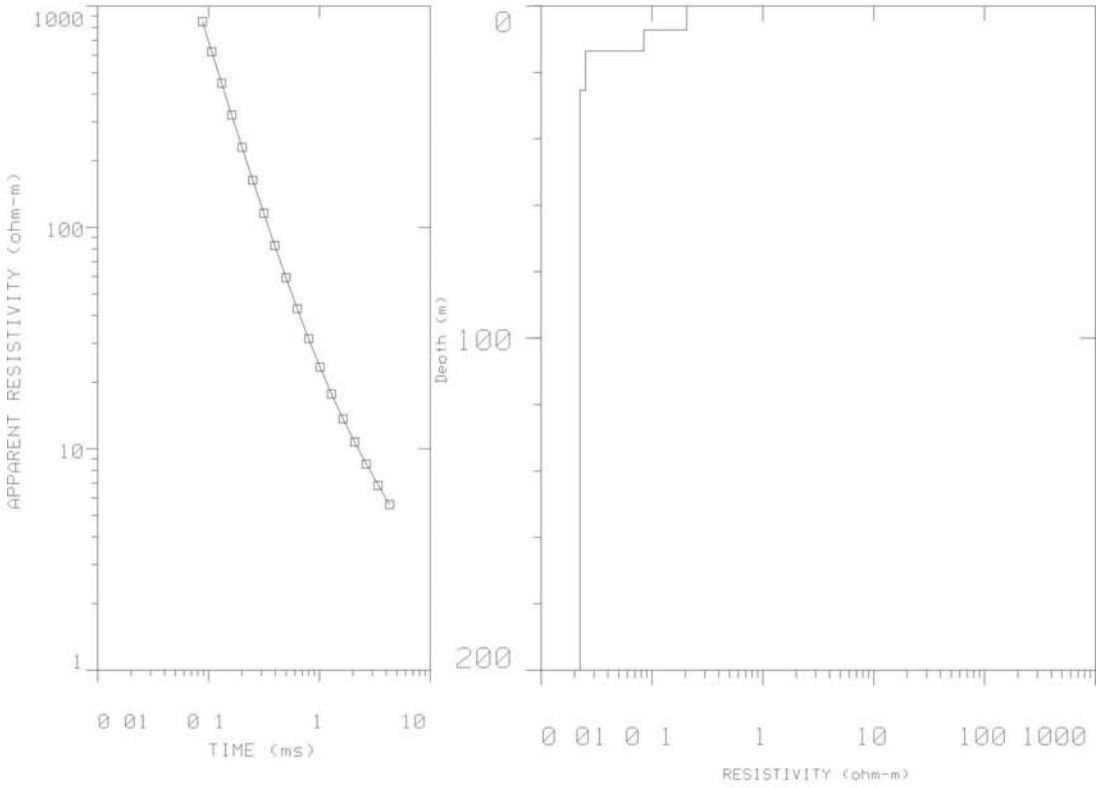

b) 350

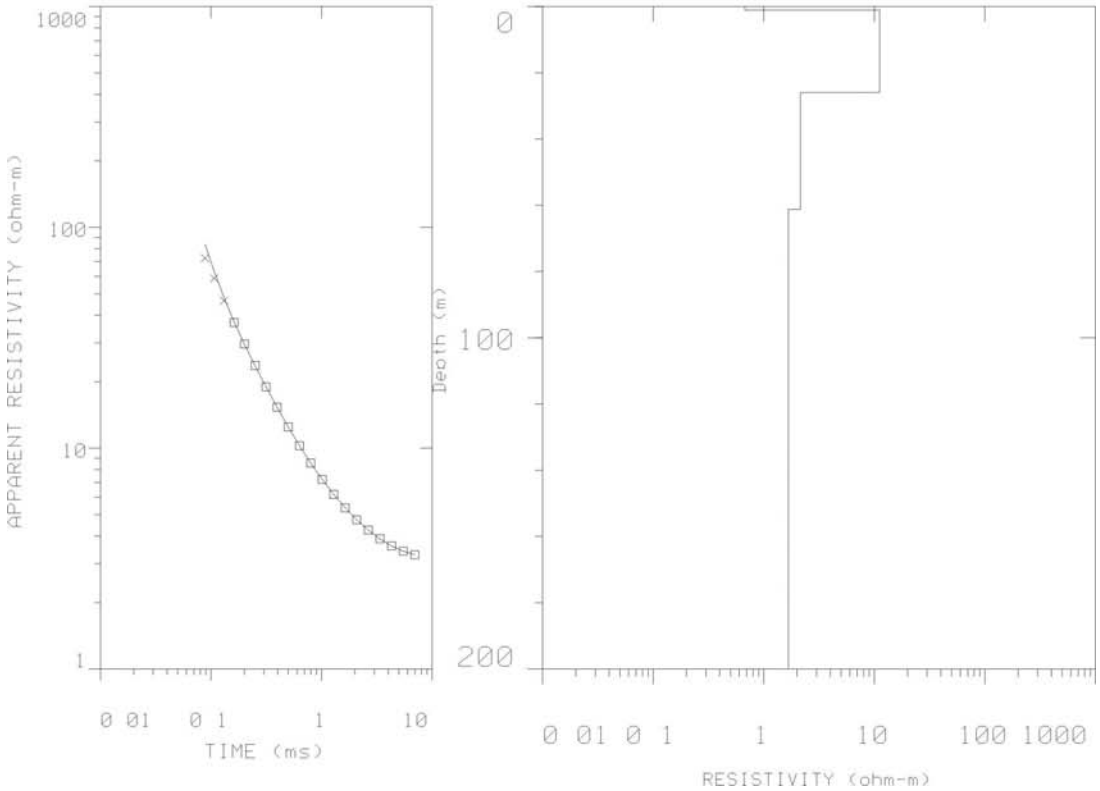

Appendix B.3: TEM soundings (sorted from N to S)

a) 160

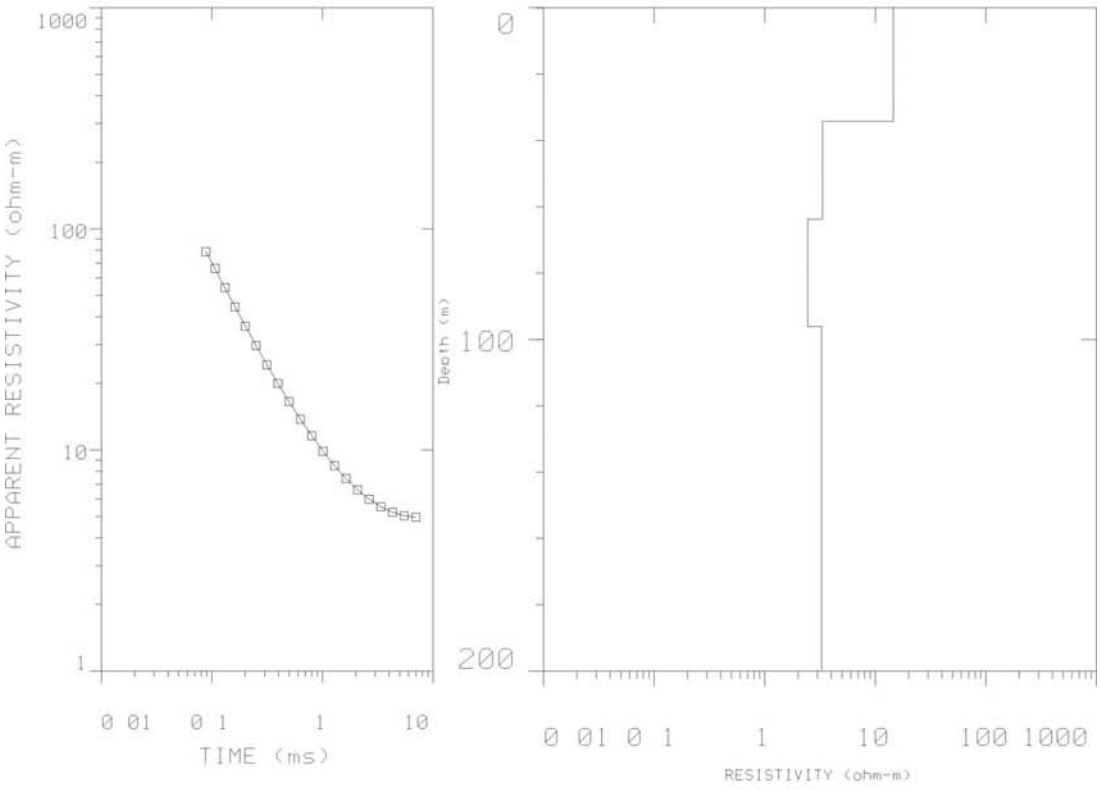

b) 216

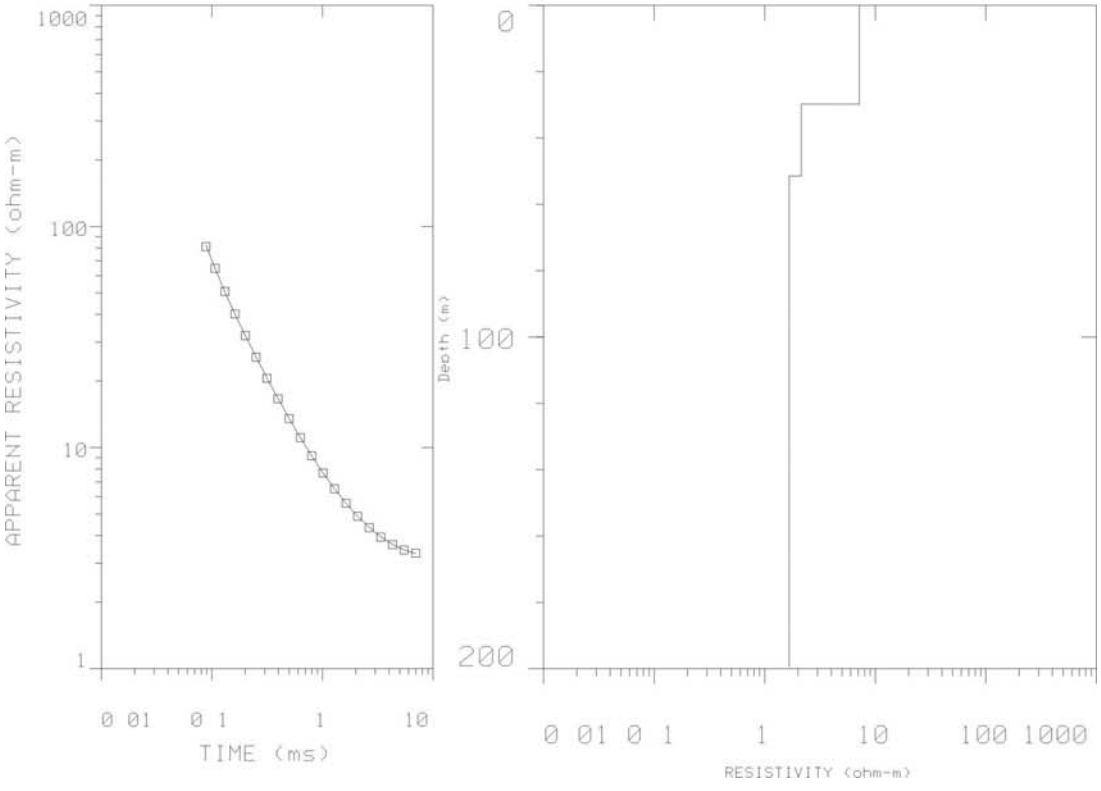

Appendix B.3: TEM soundings (sorted from N to S)

a) 250

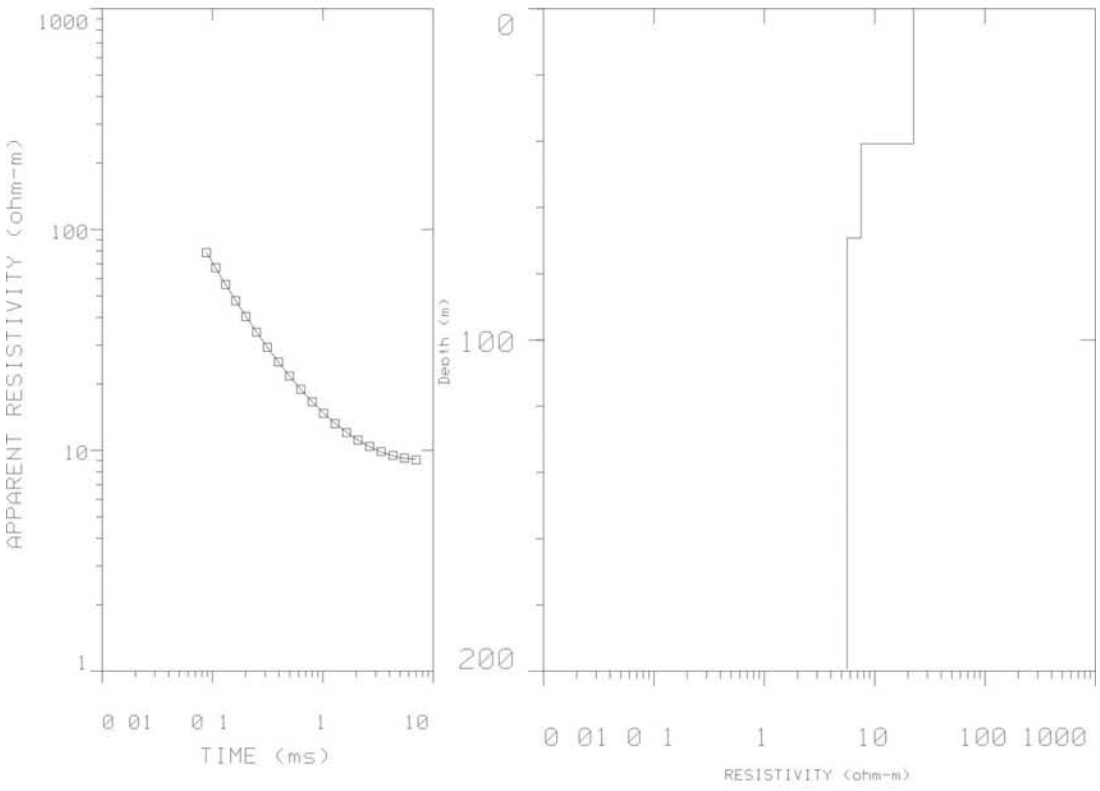

b) 115

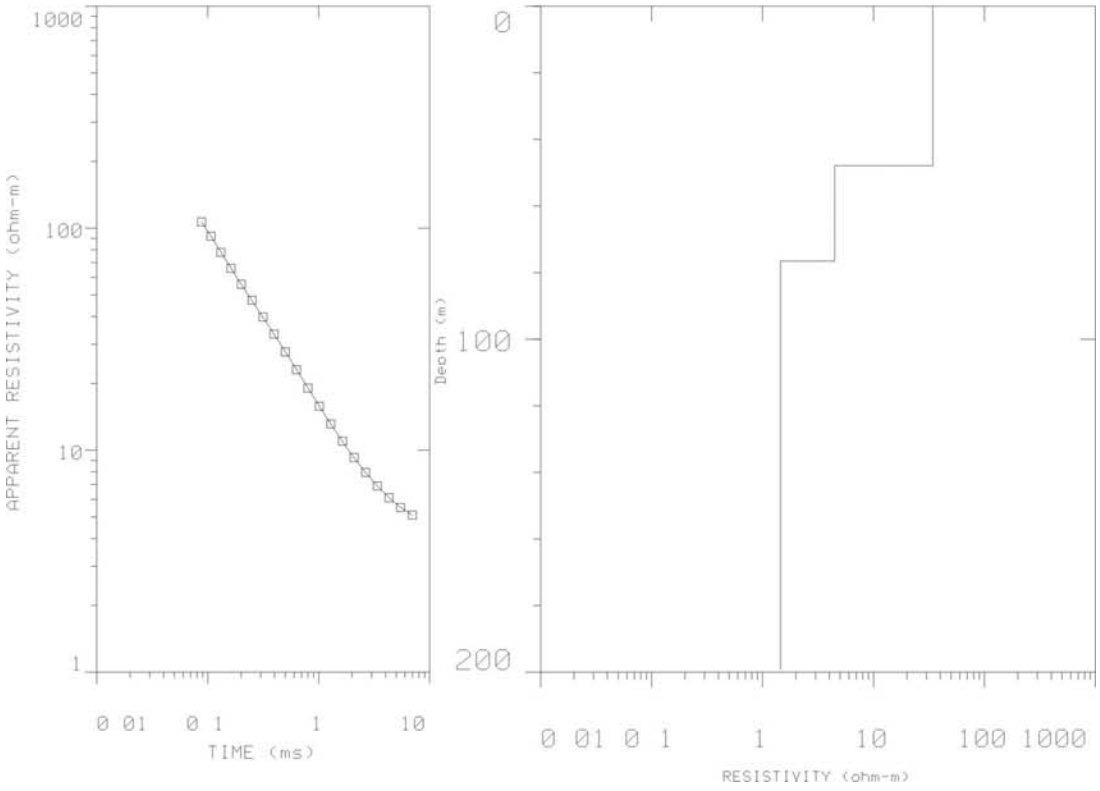

Appendix B.3: TEM soundings (sorted from N to S)

a) 130

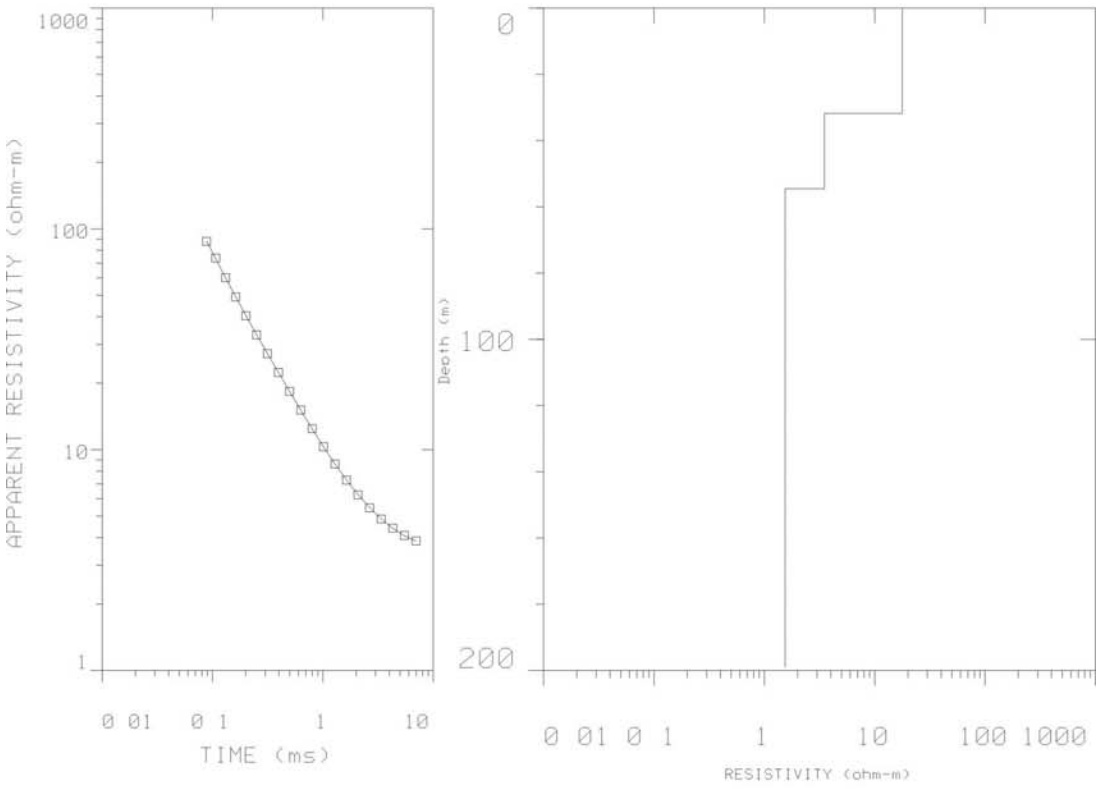

b) 120

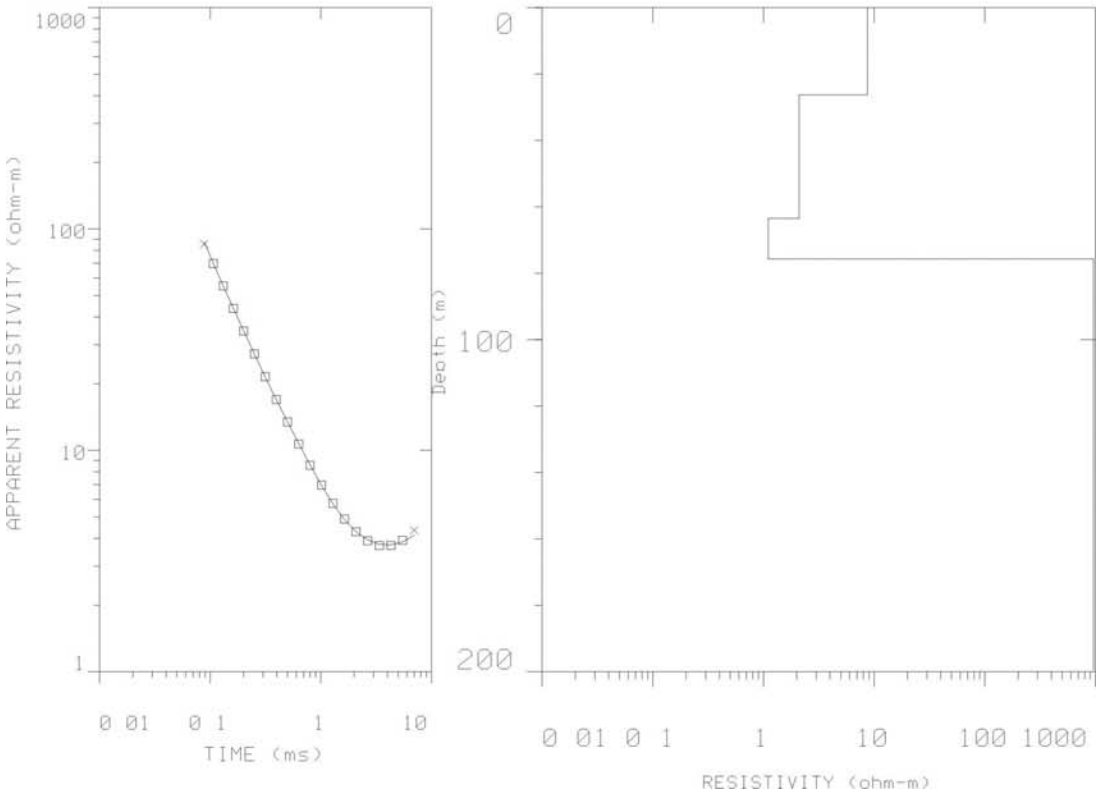

Appendix B.3: TEM soundings (sorted from N to S)

a) 110

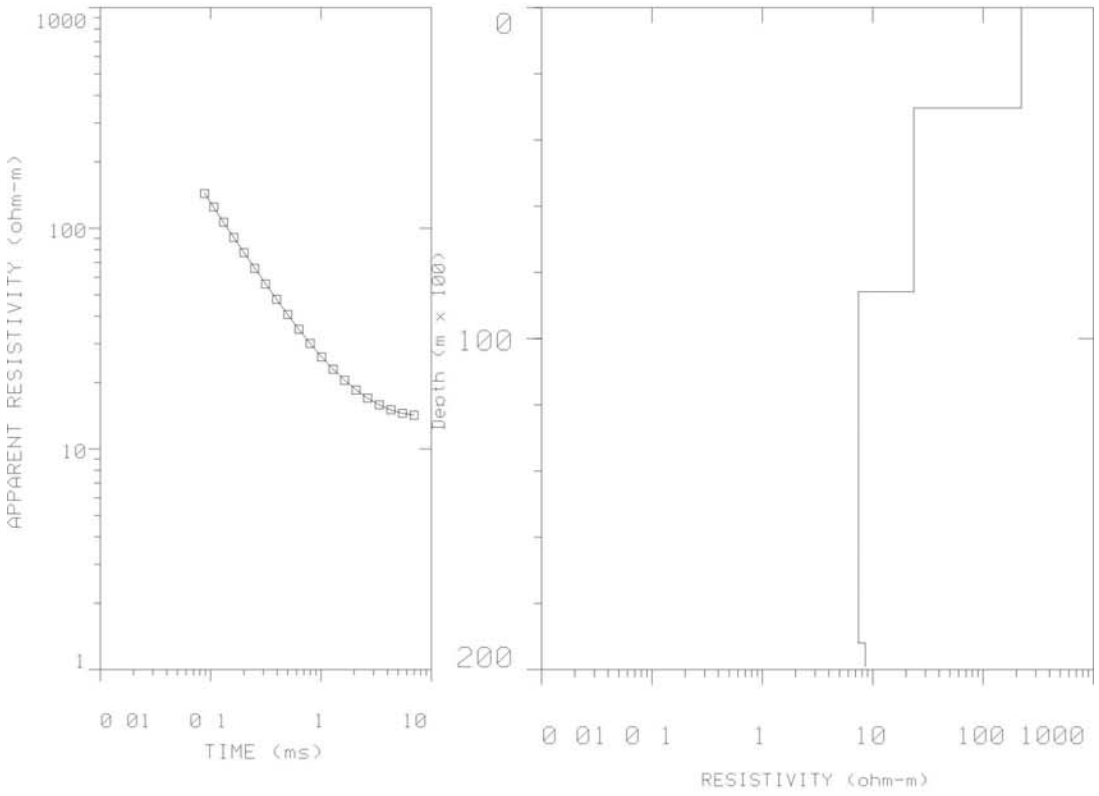

b) 090